

**Systematic irradiation studies and
Quality Assurance of silicon strip sensors
for the CBM Silicon Tracking System**

Dissertation
zur Erlangung des Doktorgrades
der Naturwissenschaften

vorgelegt beim Fachbereich Physik
der Johann Wolfgang Goethe-Universität
in Frankfurt am Main

von
Pavel Larionov
aus Cheboksary, Russland

Frankfurt am Main 2016
(D 30)

vom Fachbereich Physik der Johann Wolfgang Goethe-Universität
als Dissertation angenommen.

Dekan: Prof. Dr. René Reifarth

Gutachter: Prof. Dr. Peter Senger
Prof. Dr. Joachim Stroth

Datum der Disputation: October 2016

*To my mother
In loving memory of my grandmother*

Abstract

The Compressed Baryonic Matter (CBM) experiment at the upcoming Facility for Antiproton and Ion Research (FAIR) is designed to investigate the phase diagram of strongly interacting matter at neutron star core densities under laboratory conditions. This work is a contribution to the development of the main tracking detector of the CBM experiment - the Silicon Tracking System (STS), designed to provide the tracking and the momentum information for charged particles in a high multiplicity environment. The STS will be composed of about 900 highly segmented double-sided silicon strip sensors and is expected to face a harsh radiation environment up to $1 \times 10^{14} \text{ cm}^{-2}$ in 1 MeV neutron equivalent fluence¹ after several years² of operation. The two most limiting factors of the successful operation of the system are the radiation damage and the quality of produced silicon sensors. It is therefore of importance to ensure both the radiation tolerance of the STS sensors and their quality during the production phase.

The first part of this work details the investigation of the radiation tolerance of the STS sensors. Series of irradiations of miniature sensors as well as full-size prototype sensors were performed with reactor neutrons and 23 MeV protons to a broad range of fluences, up to $2 \times 10^{14} \text{ n}_{eq}/\text{cm}^2$. The evolution of the main sensor characteristics (leakage current, full depletion voltage and charge collection) was extensively studied both as a function of accumulated fluence and time after irradiation. In particular, charge collection measurements of miniature sensors demonstrated the ability of the sensors to yield approx. 90% to 95% of the signal after irradiation up to the lifetime fluence, depending on the readout side. First results on the charge collection performance of irradiated full-size prototype sensors have been obtained, serving as an input data for further final signal-to-noise evaluation in the whole readout chain. Operational stability of these prototype sensors, irradiated to twice the lifetime fluence, was monitored for time periods up to several weeks, showing excellent stability at uniform environmental conditions.

The second part of the thesis describes a contribution to the quality assurance of the STS sensors, in particular, the development of a test stand for an efficient automated quality evaluation of each sensor strip. The test setup, comprising a probe station, measurement units and a switching matrix, is managed by a dedicated software developed by the author, and allows for an efficient strip quality evaluation by determination of strip failures originating from the manufacturing or handling. The test stand will be used during the sensor series production and module assembly periods.

¹Defined as the lifetime fluence. Expected in the innermost regions of the system.

²Depending on the physics program.

Contents

Abstract	vii
1 Introduction	1
1.1 CBM experiment	2
1.1.1 Physics program	2
1.1.2 Detector setup	5
1.2 Silicon Tracking System	7
1.2.1 Detector concept	7
1.2.2 Expected performance	9
1.3 Double-sided silicon strip sensors	10
1.3.1 Principle of operation	10
1.3.2 Double-sided silicon strip sensors of the STS	12
1.4 Structure of the thesis	14
2 Radiation damage in silicon detectors	15
2.1 Damage mechanism	15
2.2 The NIEL scaling of radiation damage	16
2.3 Classification of defects	17
2.4 Change in the macroscopic detector properties	19
2.5 Implications on the performance of the STS sensors	25
3 Investigation on the radiation tolerance of STS sensors	27
3.1 Sensors under study	27
3.2 Irradiation facilities	29
3.2.1 Irradiation with neutrons	29
3.2.2 Irradiation with protons	30
3.3 Experimental methods	32
3.3.1 I-V and C-V measurements	32
3.3.2 Charge collection measurements	33
3.3.3 Setup used for annealing studies	37
3.3.4 Setup for long-term stability measurements	39

3.4	Measurements on miniature STS sensors	40
3.4.1	Sensors before irradiation	40
3.4.2	Results after irradiation: leakage current density and full depletion voltage	41
3.4.3	Charge collection results	44
3.4.4	Comparative analysis of charge collection for p - and n -side readout at various levels of irradiation	48
3.4.5	Charge collection as a function of the fluence	53
3.5	Measurements on miniature STS sensors: annealing studies	53
3.5.1	Sensors involved in the annealing studies	54
3.5.2	Annealing procedures	54
3.5.3	Annealing of the leakage current	55
3.5.4	Annealing of effective impurity concentration	55
3.5.5	Parametrization of annealing data for effective impurity concentration	58
3.5.6	Charge collection as a function of annealing time	62
3.6	Measurements on prototype sensors	62
3.6.1	Sensors selected for irradiation	63
3.6.2	Results after irradiation	63
3.7	Long-term stability performance of prototype sensors	68
3.7.1	Measurement results of long-term stability	68
3.7.2	Operational stability under changing environmental conditions	72
3.8	Discussion on measurement results	74
4	Quality Assurance of the STS sensors	83
4.1	Production and distribution of the STS sensors	83
4.2	Quality assurance program at the Quality Test Centers	84
4.3	Infrastructure and laboratory equipment	86
4.3.1	Testing conditions	86
4.3.2	Storage conditions	86
4.3.3	Sensor handling	86
4.3.4	Equipment and testing tools	87
4.4	Quality assurance tests on a sensor level	90
4.4.1	Optical inspection	90
4.4.2	Current-voltage (I-V) test	92
4.4.3	Capacitance-voltage (C-V) test	93
4.5	Long-term stability tests	98
4.6	Microscopic electrical tests	99
4.6.1	Coupling capacitance	99
4.6.2	Interstrip capacitance	101

4.6.3	Interstrip resistance	103
4.6.4	Bias resistance	105
4.7	Strip diagnostic tests	106
4.7.1	“Pinhole” test	106
4.7.2	Readout strip short circuit test	109
4.7.3	Strip leakage current test	110
4.8	Quality of the sensors	111
5	Development of the test stand for automated strip diagnostic tests	115
5.1	Remote control of the probe station electronics	115
5.2	Software tools for remote control of the probe station and the measurement units	116
5.3	Concept of the automated test system	117
5.4	Automation of the probe station operation	119
5.5	Remote control of the measurement instruments	119
5.6	Development of an automated pinhole and readout strip short circuit test system	120
5.7	Development of an extention for a strip current measurement	122
5.8	Optimization of the measurement setup by using a switching matrix	123
5.9	Optimization of the measurement sequence	126
5.10	Optimization of the measurement speed	127
5.11	Development of the software interface	129
5.12	Components of the developed test stand	130
5.13	Output of the automated strip diagnostic scan	130
5.14	Experience with automated testing	132
	Summary and Conclusion	133
	Zusammenfassung	139
A	Additional plots and figures	145
A.1	Hamburg model parametrization	145
A.2	Long-term stability measurements	146
B	Interfaces of the developed LabView software	149
B.1	Software interface for temperature corrected I-V measurements	150
B.2	Software interface for long-term stability measurements	151
B.3	Software interface for C-V measurements	152
B.4	Software interface for automated strip diagnostic tests	153
C	Communication/data transfer protocol for the test stand	157

D Parameters of the Hamburg model used for calculations	161
Bibliography	163
Acknowledgement	171
Curriculum Vitae	173

Chapter 1

Introduction

In the last decades, technological progress in realizing complex experimental facilities supported and motivated by theoretical research opened a new era of studying strongly interacting matter under extreme conditions. The strong interaction is the fundamental interaction between quarks and gluons. It is described by Quantum Chromodynamics (QCD), a part of the Standard Model of particle physics. Figure 1.1 illustrates the phase diagram of strongly interacting matter, i.e., its possible phases as a function of temperature T and baryon chemical potential μ_B . Here, the region of the phase diagram of very high temperatures and almost zero baryon chemical potential is being investigated via heavy-ion collisions at LHC and top RHIC energies. Matter at such conditions is believed to exist shortly after the Big Bang. Up to date, interesting results were obtained in this direction: the conditions of the chemical freeze-out were identified experimentally in the range of 155 - 165 MeV [2], which coincides with the range of critical temperatures predicted by the lattice QCD calculations [3],[4]. The phase transition from partonic to hadronic matter in this case is found to be a rapid crossover [5].

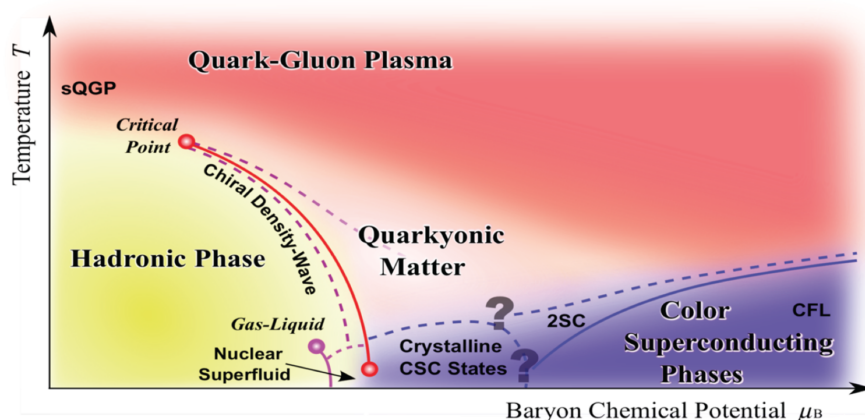


Figure 1.1: Sketch of the phase diagram of strongly interacting matter [1].

Up to date, the region of the phase diagram at lower temperatures and higher net-baryon densities has been only poorly investigated. According to the QCD model calculations, the phase diagram in this region features rich structures such as a first order phase transition from hadronic to quarkyonic phase, a critical endpoint separating the regions with different phase transitions, a new state - quarkyonic matter, located beyond the first order phase transition at large baryon chemical potentials and moderate temperatures, and others [6]. So far, lattice QCD calculations are not yet suited for making predictions in the region of large baryon chemical potentials. Therefore, the experimental investigation of these features of the phase diagram is very important for better understanding of QCD matter at high net-baryon densities.

Several experimental facilities worldwide already study or plan to study the QCD phase diagram at high net-baryon densities, such as STAR at RHIC [7], NA61/SHINE at CERN-SPS [8] and NICA at Nuclotron in JINR [9]. However, due to luminosity or/and detector limitations, these research programs will be able to investigate mainly the abundantly produced bulk observables created at the freeze-out.

In contrast to that, the Compressed Baryonic Matter (CBM) experiment will investigate the region of the phase diagram of high net-baryon densities by focusing its program on observation of rare diagnostic probes carrying the information of the dense stage of the fireball evolution. CBM will run in a fixed-target mode, starting with so-called FAIR Modularized Start Version that comprises the SIS100 synchrotron providing high-intensity beams up to 11 A GeV for heavy nuclei, up to 14 A GeV for light nuclei, and up to 30 GeV for protons. With the upgraded version, featuring the SIS300 synchrotron, the energy range will be enlarged to up to 45 A GeV for heavy nuclei and up to 90 GeV for protons.

1.1 CBM experiment

1.1.1 Physics program

Investigation of the properties of matter at high net-baryon densities and moderate temperatures is the primary focus of the CBM physics program. The fundamental questions to be addressed are:

- What is the equation of state at neutron star core densities and what are the relevant degrees of freedom at such conditions?
- Does the phase transition from hadronic to quarkyonic matter or exotic states like quarkyonic matter exist?
- Is the chiral symmetry restored at high net-baryon densities?

- Does strange matter exist in the form of heavy multi-strange objects?

These and many other related questions are under speculation at the moment as no experimental data is available to answer them.

According to transport model calculations, already at top SIS100 energies in central Au-Au collisions, the fireball will be compressed to densities of more than 8 times the saturation density ρ_0 (Fig. 1.2a). In accordance to non-local 3-flavor Nambu Jona-Lasinio model [10], at such densities a mixed state of quarks and hadrons is predicted (Fig. 1.2b), while above 9 times the saturation density, pure quark matter is formed. The experimental challenge is to identify the diagnostic probes of the dense phase of the fireball, such as multi-strange hyperons and anti-hyperons, light vector mesons, and hadrons containing charm quarks. Most of such probes have very low production cross sections, therefore, cannot be efficiently studied by other experimental programs in the region of high net-baryon densities (e.g., only approx. 300 Ξ^- hyperons have been measured in Au+Au collisions at 6 A GeV [11]). In experiments realized so far, including AGS at SPS and STAR/PHENIX at RHIC, mostly those particles have been measured, which are abundantly produced at the freeze-out already below the saturation density. CBM is designed to study the following physics cases:

- **Equation of state of nuclear matter at neutron star core densities.** The relevant observables are multi-strange (anti-) hyperons. According to hadronic transport models, they are produced in sequential collisions involving kaons and Λ s, therefore, are sensitive to the density in the fireball. CBM will measure the excitation function of yields of multi-strange (anti-) baryons in A+A collisions with different A values. In addition to that, measurements of the collective flow of hadrons, which reflects the pressure created in the early fireball, will be performed and investigated event-by-event. So far, AGS have measured only the proton flow excitation function [12].
- **Possible signatures of the chiral symmetry restoration.** In-medium properties of hadrons, in particular, ρ -meson spectral functions, are expected to be modified due to restoration of the chiral symmetry in dense baryonic matter [14]. Precise measurements of the invariant mass distributions of the vector mesons' decay products, lepton pairs, will be performed for different collision systems. Additionally, yields and transverse mass distributions of charmed mesons will be investigated as a function of energy for the first time at FAIR energy ranges.
- **Phase transitions from hadronic matter to quarkyonic or partonic matter at high net-baryon densities, existence of the critical point of QCD matter.** Measurements of excitation functions of yields, spectra,

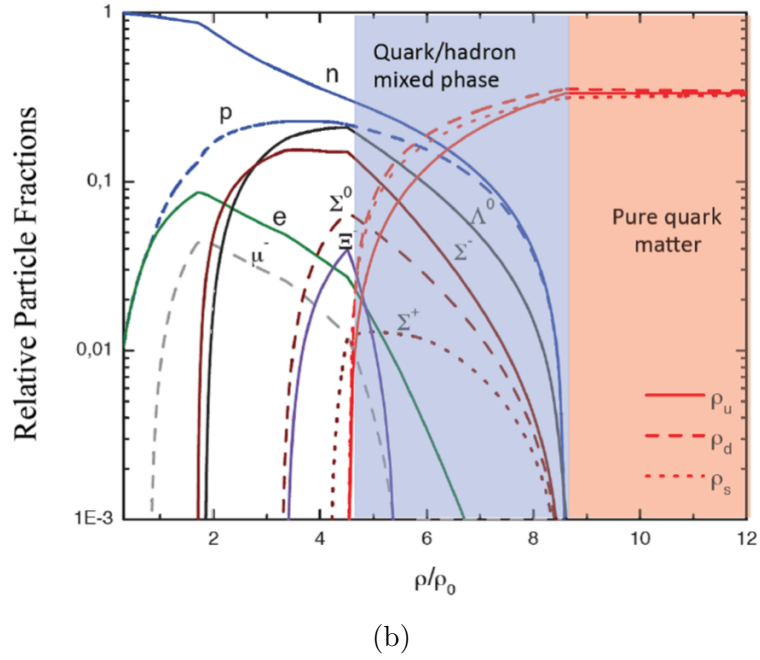
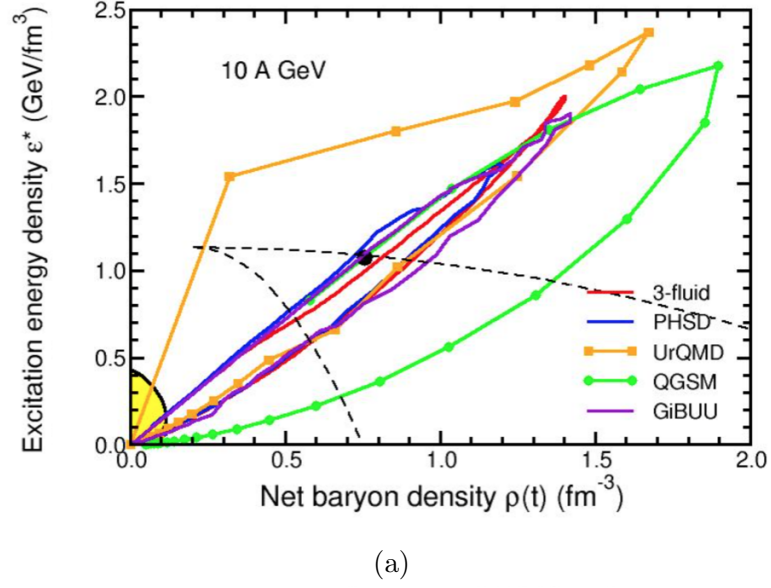


Figure 1.2: (a) Time evolution of the excitation energy density and the net-baryon density in the center of the fireball for central Au+Au collisions at 10 A GeV, calculated by several transport codes and a hydrodynamic model [13]; (b) Relative particle fractions as a function of density in a neutron star of 2 solar masses, according to non-local 3-flavor Nambu Jona-Lasinio model [10].

and collective flow of strange and charmed particles will be performed for various collision systems and different energies. Up to date, only a few data is available for strange particles from AGS, SPS-NA49, and from the RHIC beam energy scan while for charmed observables no data is available at all. Systematic, high-precision measurements of these observables is a very promising tool for the detailed investigation of phase transitions or phase coexistence.

- **Hypernuclei, strange dibaryons and massive strange objects.** Theoretical models predict that at SIS100 energies such complex objects as single and double hypernuclei, strange dibaryons and other short-lived multi-strange objects are produced in heavy-ion collisions with the maximum yield. Therefore, CBM will have a unique opportunity to study these observables with high precision and statistics. The decay chains of single and double hypernuclei in heavy-ion collisions at SIS100 energies will be measured. Also, exotic, meta-stable strange objects like di-baryons will be investigated via their decay products (charged hadrons including hyperons).
- **Mechanisms of charm production, charm propagation and in-medium properties of charged particles in dense nuclear matter** will be studied with high precision for the first time at SIS100/300 energies by measuring cross sections, momentum spectra and collective flow of charmed mesons (D -mesons), charmed baryons and charmonium (J/ψ). Moreover, the propagation of open and hidden charm in cold nuclear matter will be studied in p+A collisions. Up to now no charm data is available at FAIR energies.

The details of the CBM physics program can be found in CBM Physics Book [15], and also in [16], [18], [19], [20].

1.1.2 Detector setup

The CBM detector is a multi-purpose device designed to operate at extremely high interaction rates, several orders of magnitudes higher than any other existing or planned heavy-ion experiment. It is composed of a set of detector systems for effective measurements of various particles produced in beam-target interactions, covering a large part of mid- and forward rapidities.

Because of the complex signatures of various observables, no simple hardware trigger can be generated. The data, read-out from the detector systems, will be delivered to the high performance computing cluster, the so-called “Green-IT cube”, where the First Level Event Selector system will perform online data processing and selection. The readout chain is therefore based on free-streaming

readout electronics, where the signals produced in various detectors are delivered with individual time stamps without event correlation, with further processing by the reconstruction algorithms.

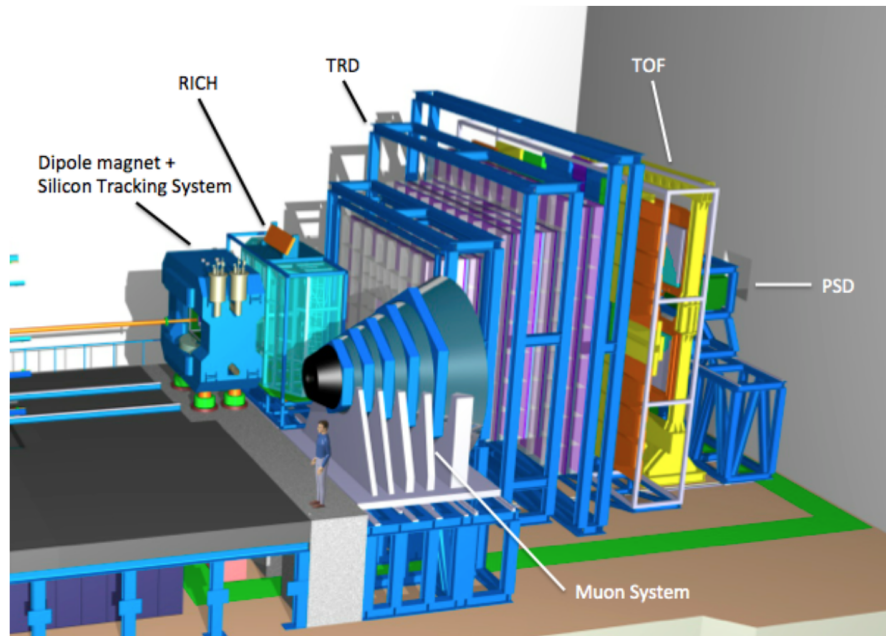


Figure 1.3: Schematic view of the CBM experimental setup, in its hadron-electron configuration.

Figure 1.3 illustrates the CBM detector setup. The main tracking device of the experiment, the Silicon Tracking System (STS), will deliver tracking and momentum information of traversing charged particles. The system is located inside a superconducting dipole magnet. The STS features a double-sided silicon strip sensor technology, custom-designed microcables and readout electronics. For determination of decay vertices of short-lived particles like D -mesons with a high spacial resolution, a Micro-Vertex Detector (MVD), featuring a Monolithic Active Pixel Technology (MAPS), is installed just 5 cm after the target in front of the STS. CBM will have the opportunity of independent identification of di-electron and di-muon decay channels, performed by the Ring Imaging Cherenkov Detector (RICH) and the Muon Chamber System (MUCH), respectively. Both systems are interchangeable via a common rail system. The MUCH system comprises several hadron absorber layers and a set of gaseous micro-pattern chambers located in triplets behind each absorber. By measuring both electrons and muons, the systematic errors will be dramatically reduced due to the background subtraction. The Transition Radiation Detector (TRD) will provide identification of electrons and positrons with momenta > 1.5 GeV/c. It will also serve as an intermediate tracking detector between the STS and the Time Of Flight (TOF) wall. The latter,

consisting of an array of multi-gap resistive plate chambers, covering an active area of 120 m^2 , will identify hadrons by measuring their time-of-flight with a resolution of 80 ps. In order to determine the collision centrality and the reaction plane orientation, the Projectile Spectator Detector (PSD), basically a forward hadron calorimeter, will be installed, consisting of modules with lead/scintillator layers.

The Technical Design Reports for most of the detector systems can be found in [17].

1.2 Silicon Tracking System

1.2.1 Detector concept

The Silicon Tracking System is the core tracking detector of the CBM experiment. Its task is to reconstruct the tracks of charged particles created in beam-target interactions and to determine their momenta. STS is designed to satisfy the following constraints [21]:

- Rapidity coverage from center-of-mass to close to beam;
- Track reconstruction efficiency $> 95\%$ (for tracks with momenta $> 1 \text{ GeV}/c$), hit detection efficiency close to 100% ;
- Momentum determination with a resolution of $\delta p/p \approx 1\%$ (for tracks with momenta $> 1 \text{ GeV}/c$);
- Pile-up free readout at interaction rates from 100 kHz to 10 MHz;
- Radiation tolerant sensors up to a maximum fluence of $1 \times 10^{14} \text{ cm}^{-2}$ in 1 MeV neutron equivalent;

The detector system will comprise 8 tracking stations located between 30 cm and 1 m downstream of the target, inside the superconductive dipole magnet. Such layout will allow for an efficient track point measurement along the particle trajectories, identification of in-detector decays, location of secondary vertices and extrapolation of their trajectories to the Micro-Vertex Detector.

The required rapidity coverage of the STS is determined by the polar angle acceptance from 2.5° to 25° (Fig. 1.4). According to simulations, 800 out of 1000 charged particles, created per central interaction in 25 A GeV Au+Au collisions, will be captured by the detector's acceptance [22]. In order to enhance the detection of low-momentum tracks, the four upstream stations are additionally extended to a 35 degree aperture along the horizontal axis.

With the double-sided microstrip sensors, featuring a strip pitch of $58 \mu\text{m}$, the single-hit resolution in the bending plane is approx. $25 \mu\text{m}$, which will provide the momentum resolution at the required level.

In the inner parts of the stations, the hit rates up to $10 \text{ MHz}/\text{cm}^2$ are expected. Sensors of four different sizes are implemented in different areas of the stations, in order to keep the maximum strip occupancy at the level of a few percent. The

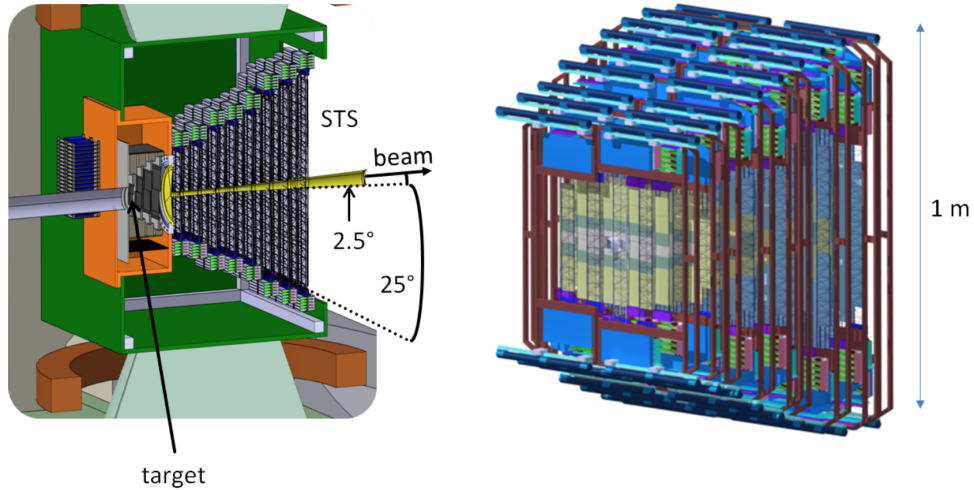


Figure 1.4: Cut-through view of the Silicon Tracking System, located inside the dipole magnet, showing its conceptual details (left); Full-component engineering model of the STS (right).

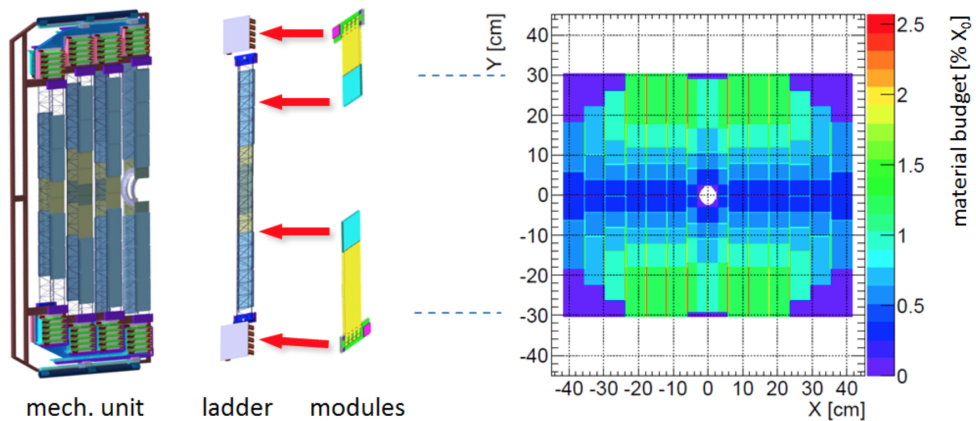


Figure 1.5: Concept of assembly of the modules into ladders and, sequentially, into stations (left); Material budget in various areas of a station (right).

sensors will be read-out via ultra-thin microcables with the readout electronics located outside of the active area, restraining the maximum material budget of

about 1% X_0 (Fig. 1.5). The front-end readout electronics is based on a custom designed ASIC with self-triggering data streaming, the STS-XYTER. The electronics architecture is tailored in order to accept the capacitive load of the sensors and the connecting cables, and to handle the rates expected in the tracking system.

A high level of radiation damage is expected to impact on the sensors' performance. The sensors have to withstand an exposure of $1 \times 10^{14} \text{ cm}^{-2}$ in 1 MeV neutron equivalent as expected in the innermost regions. The sensors which will accumulate higher fluences will be replaced. In order to suppress the radiation-induced reverse currents, the system is expected to run at temperatures of $-5 \text{ }^\circ\text{C}$ or lower.

1.2.2 Expected performance

A detailed version of the detector geometry, besides the sensors themselves, including the readout components and the support and integration structures was realized and implemented into the CBMROOT framework. The particle flow obtained from the URQMD [23] modeling of interactions at corresponding collision energies, was transported through the detector volume using a GEANT3 transport code [24]. The response of the sensors at the microscopic level, including the charge carriers production and propagation in the presence of the magnetic field, was modelled by digitizers. Then, the track reconstruction was performed with the Cellular Automaton (CA) track finder algorithm, using the hit information from digitizers. The Kalman Filter (KF) based track fit is used for precise estimation of the track parameters.

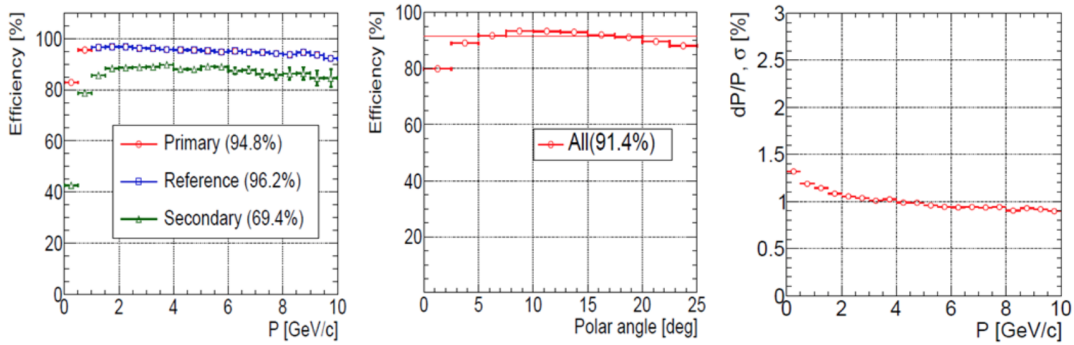


Figure 1.6: Track reconstruction efficiency as a function of particle momentum (left) and polar angle (middle); Momentum resolution as a function of particle momentum (right), obtained for central Au+Au collisions at 25 A GeV.

The reconstruction efficiency is defined as a ratio of reconstructed particles to the reconstructible ones, i.e. the particles intersecting at least four stations,

according to the algorithm. Figure 1.6 exhibits the track reconstruction efficiency and momentum resolution of charged particles as a function of particle momentum and polar angle, obtained using the CBMROOT framework with the CA and KF packages implemented, for central Au+Au collisions at 25 A GeV. Here, the primary tracks are those which originate from the primary vertex, secondary – from the secondary one. The reference tracks have a momentum higher than 1 GeV/c. The track reconstruction exhibits good performance with an average efficiency close to 95% for primary tracks, and up to almost 90% for secondary ones. The momentum resolution is achievable at a 1% level for tracks with high momentum. As a function of the polar angle, i.e. the emission angle of the particle w.r.t. the beam direction, the efficiency varies from 80% to higher than 90% level, in case of all tracks considered.

1.3 Double-sided silicon strip sensors

1.3.1 Principle of operation

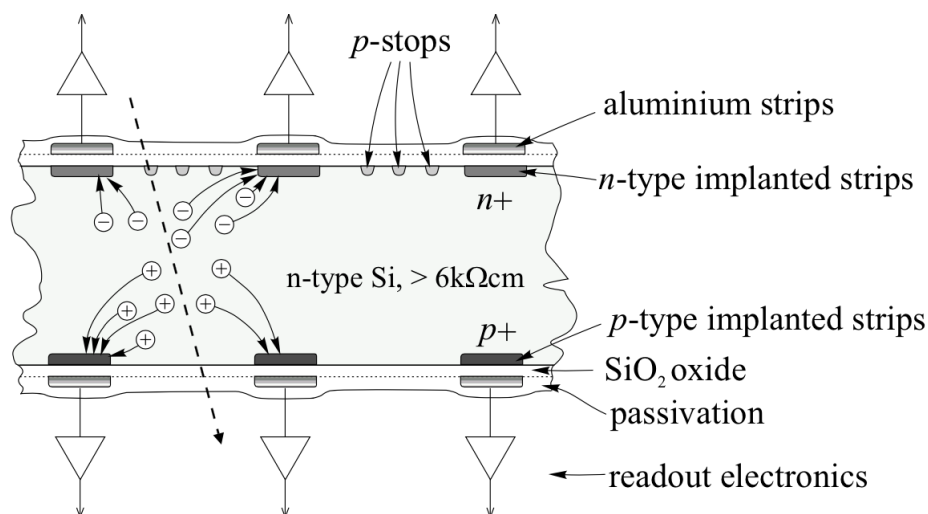


Figure 1.7: Schematic view of the operational principle of a double-sided detector. Taken from [25].

The principle of operation of silicon detectors is based on registration of the primary ionization caused by the energy loss of incident charged particles traversing the detector bulk. In a double-sided silicon detector, the electric field, established by applying a potential difference to segmented electrodes - strips, p^+ and n^+ doped, depletes the detector bulk of free charges.

When traversing through the depleted bulk, a charged particle ionizes the Si

atoms and creates a number of electron-hole pairs along its track¹ (Fig. 1.7). Due to the presence of an electric field, the carriers drift in the opposite directions. When drifting, the charge carriers induce a current pulse which is registered by the readout electronics connected to the aluminum readout lines² which are capacitively coupled to the strips. The signal induction stops when all the carriers reach the corresponding electrodes.

The mean energy loss of electrons³ in silicon, described by the Bethe-Bloch formula [26], is depicted in Fig. 1.8a. Here, the particles with energies corresponding to a minimum value of the mean energy loss are called minimum ionizing particles (MIP). If a sensor is able to detect a signal from a MIP, it will be able to detect signals from other stronger ionizing particles.

Due to statistical fluctuations of the energy loss, the *most probable value* (MPV) of the energy loss distribution, which defines the *charge collection*⁴ in silicon detectors, is approx. 30% lower than its mean value (Fig. 1.8b). The most probable charge deposition of a minimum ionizing particle in 300 μm silicon detector is approximately 21.6 ke^- , when considering 72 electron-hole pairs created per μm [27].

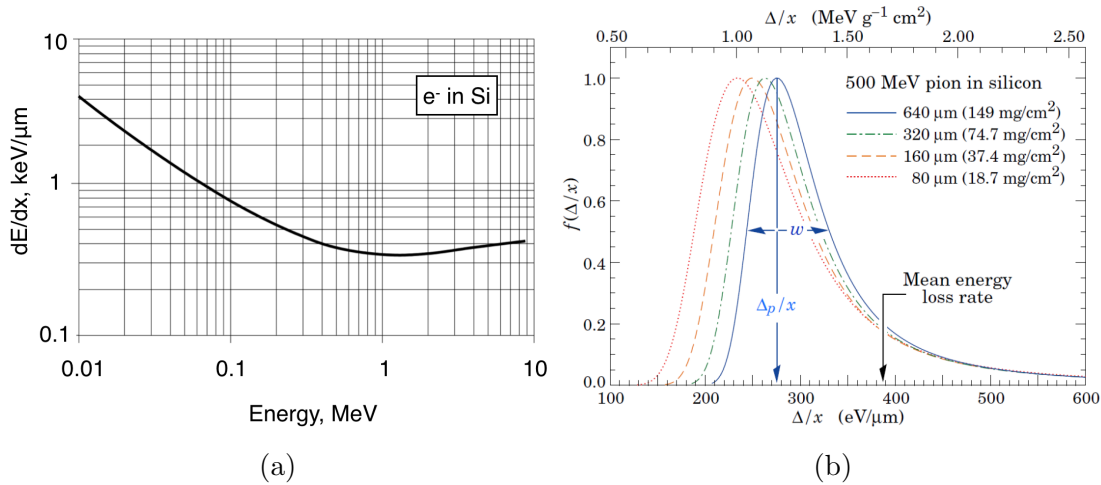


Figure 1.8: (a) Mean energy loss of electrons in silicon. The minimum energy loss corresponds to a 1.5 MeV energy. The particles of this energy are called minimum ionizing particles [28]; (b) Straggling function for 500 MeV pions in silicon, normalized to unity at the most probable value Δ_p/x [29].

Both electrons and holes contribute to the signal “seen” at the opposite electrodes. In case the particle track is not perpendicular to the detector surface,

¹The average energy required for creation of one electron-hole pair is approx. 3.66 eV.

²Also called the *readout strips*.

³A similar dependence is observed for other charged particles.

⁴Also, *most probable charge*.

the carriers are collected at two or more strips, therefore, the full signal is shared among them. However, the position of the particle can be determined more precisely in case when the signal is shared among several strips by either calculation of the “center of gravity” or by using an algorithm that takes into account the actual shape of the charge distribution [26].

1.3.2 Double-sided silicon strip sensors of the STS

The STS stations will be populated with double-sided silicon microstrip sensors. Up to date, several generations of prototype sensors have been and are being produced by two manufacturer companies⁵, namely CiS Research Institute for Microsensors, Germany and Hamamatsu Photonics Company (HPK), Japan. The sensors have been produced in three different sizes keeping the uniform layout. A standard size is $6.2 \times 6.2 \text{ cm}^2$. For the innermost parts of the stations, the sensors of a $6.2 \times 2.2 \text{ cm}^2$ and a $6.2 \times 4.2 \text{ cm}^2$ size will be used in order to keep the strip occupancy at a required level. For the outermost areas, either two sensors of standard size will be daisy-chained or a stand-alone $6.2 \times 12.4 \text{ cm}^2$ sensor⁶ will be used.

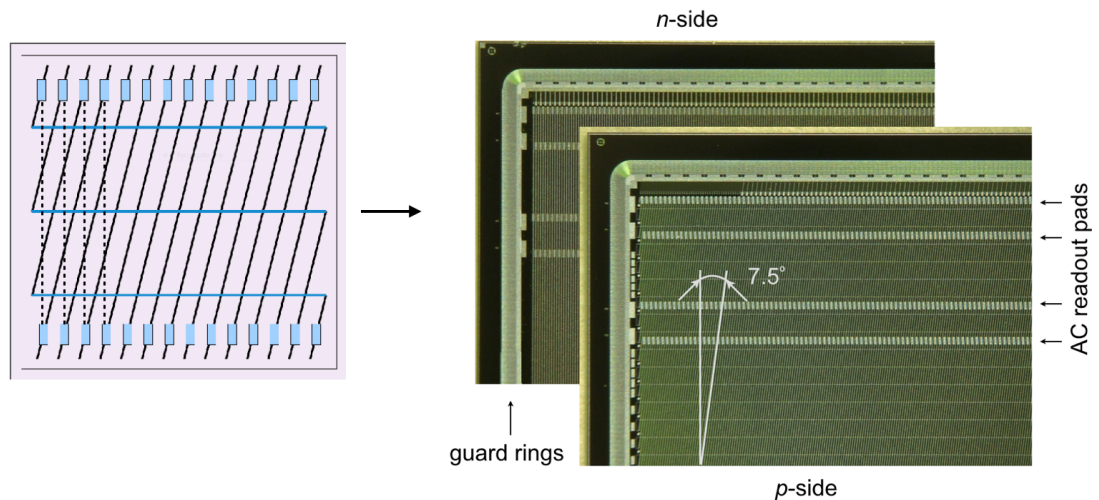


Figure 1.9: Corner view of the STS double-sided prototype sensor, showing the design details (right).

The sensors are produced using standard float-zone silicon wafers of an approx. $2 \text{ k}\Omega\cdot\text{cm}$ to $6 \text{ k}\Omega\cdot\text{cm}$ resistivity. CiS uses a $285 \pm 15 \mu\text{m}$ thick wafers while in case of Hamamatsu the substrates are $320 \pm 15 \mu\text{m}$ thick.

⁵Considered as suppliers at the moment of completing this work.

⁶The prototype of this size is currently under production.

1.3 Double-sided silicon strip sensors

The sensor bulk is of an n -type silicon with a segmentation into 1024 implanted strips on both sides. The p^+ strips at one side (also called p -side) establish the pn -junction. The opposite side strips are of an n^+ type (n -side). The strips at the n -side are isolated using a p -spray technology.

One of the design specifics of the STS sensors is the inclination of the p -side strips by 7.5° with respect to the n -side, where the strips are positioned vertically. At both sides the strip pitch is $58 \mu\text{m}$. This layout gives the optimal position resolution along the bending plane (horizontal) of an approx. $25 \mu\text{m}$ and minimizes the combinatorial uncertainties [30]. Because of such a strip orientation at the p -side, some strips are reduced in length, which decreases towards the corner of the sensor (Fig. 1.9). These “short” or “corner” strips must be interconnected as by design the readout will be performed from one edge of the sensor [31]. At the time of completing this work, two technologies were considered for the interconnection of the corner strips: a “double-metal” interconnection, implemented during fabrication as an additional metal layer, or an interconnection scheme via an external microcable (Fig. 1.10) [32].

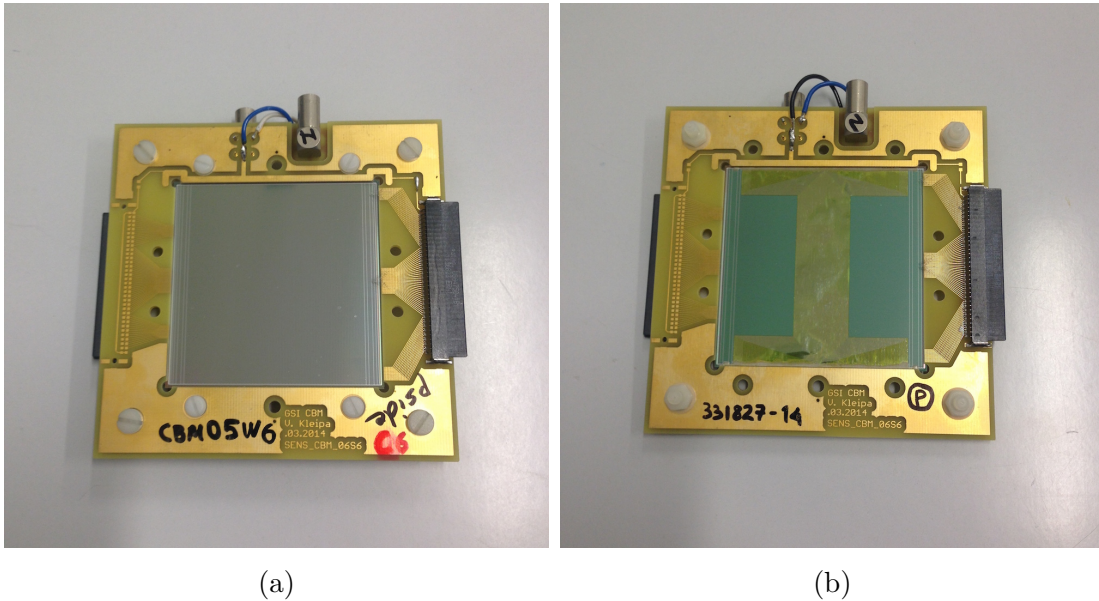


Figure 1.10: General view of the $6.2 \times 6.2 \text{ cm}^2$ prototype CiS sensors featuring the double-metal (a) and the external microcable (b) strip interconnection design, clamped in the printed circuit boards (PCB).

The strips are capacitively coupled to the readout electronics (AC-coupling) via a thin insulation layer. Each strip is connected to a common bias ring at the corresponding side via a $poly-Si$ resistor. For each strip, two pairs of AC readout pads are produced at both edges. A series of guard rings is implemented around the bias ring in order to suppress the surface currents and to focus the electric

field in the close-to-the-edge area.

1.4 Structure of the thesis

This work contributes to the development of the CBM Silicon Tracking System, in particular, it's main units - double-sided microstrip sensors. Considering that radiation damage is the most limiting factor for operation of silicon sensors in high-energy physics experiments, it has to be ensured that the STS sensors are able to withstand the radiation conditions expected during the run of the experiment. According to simulations⁷, the sensors in the innermost regions of the STS stations will face a harsh radiation environment, reaching up to $1 \times 10^{14} \text{ cm}^{-2}$ in 1 MeV neutron equivalent (defined as the lifetime fluence), after several years of running depending on the physics program. Such a radiation environment is expected to have a negative impact on the sensors' performance. Other components of the system (readout cables and electronics) are expected to be damaged in a smaller degree under irradiation. Therefore, evaluation of the sensors' performance after irradiation is a crucial demand for successful operation of the system in the future. Chapter 2 gives an introduction to radiation damage in silicon detectors and it's consequence on detector operation. Chapter 3 details the investigation of the radiation tolerance of the STS sensors.

Another limiting factor of the performance of the system is the quality of it's components, in particular, the silicon sensors. Thus, the produced sensors are being tested for several types of defects at the manufacturer sites. However, during shipping, handling and assembly procedures a potential risk of damaging the sensors is expected. Therefore, their quality needs to be ensured at each step of the system assembly. In particular, the quality of each strip has to be evaluated using automated, time-efficient procedures. Chapter 4 considers characterization methods of bulk and strip parameters of the sensors as a part of the quality assurance program. Chapter 5 describes the development of the quality assurance test stand for automated strip diagnostic tests.

⁷FLUKA simulations of the non ionizing energy loss [31].

Chapter 2

Radiation damage in silicon detectors

The damage caused by radiation can be divided into the surface and bulk damage. Surface damage is produced due to accumulation of the positive charge close to the $Si-SiO_2$ interface and can be controlled to a certain extent by proper design and manufacturing process [33]. Bulk damage, produced due to displacement of the Si atoms and a consequent formation of lattice defects, is the main reason of semiconductor detector degradation in high-energy physics experiments. In this chapter, the mechanism of the bulk damage generation is considered with a further overview of its consequences on the silicon detector operation.

2.1 Damage mechanism

The main reason of the radiation caused bulk damage is the displacement of the lattice atoms out of their native position due to interaction with the incident particles. When charged hadrons traverse through the bulk, they interact with the lattice atoms via the Coulomb interaction (or Rutherford scattering). Neutrons interact only with the nuclei, therefore, the displacements are produced mainly via elastic scattering¹. In each displacement a pair of point defects² is produced, consisting of a vacancy (V) and an interstitial atom (I). The minimum amount of energy required for production of a Frenkel pair is approximately 25 eV [34]. However, the energy that the particles can transfer to a recoil atom can be much higher. The maximum recoil energy can be written as³:

$$E_{R,max} = 4E_p \frac{m_p m_{Si}}{(m_p + m_{Si})^2}, \quad (2.1)$$

¹Also via nuclear reactions, e.g. $^{30}Si + n \rightarrow ^{31}Si + \gamma$; $^{31}Si \rightarrow P + e^- + \bar{\nu}$ [35].

²So called Frenkel's pairs.

³In case of elastic scattering (non-relativistic kinematics).

where E_p and m_p is the energy and the mass of an incident particle. In case when the recoil energy is higher than the displacement threshold, the displaced interstitial atom will produce further vacancy-interstitial pairs. For instance, for

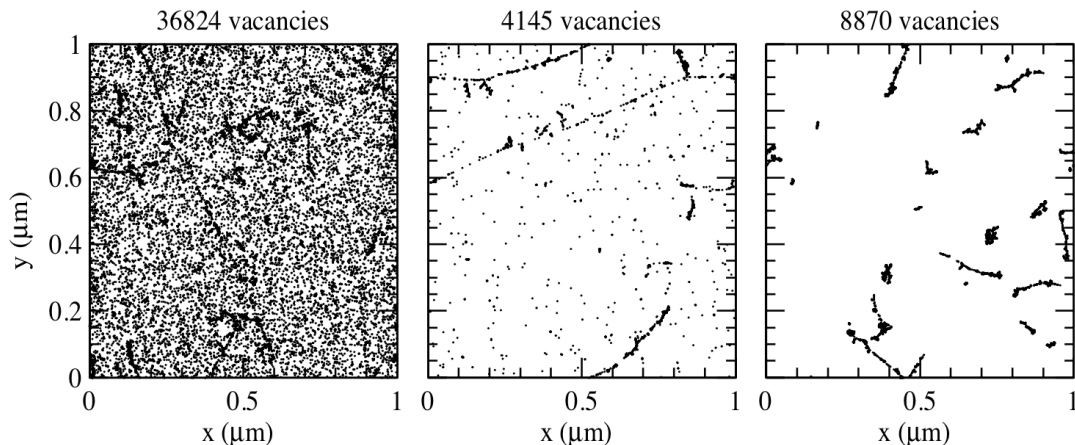


Figure 2.1: Simulated initial distributions of vacancies produced by 10 MeV protons (left), 24 GeV protons (middle) and 1 MeV neutrons (right) corresponding to the equivalent fluence of 10^{14} cm^{-2} [36].

a 1 MeV neutron the average recoil energy is about 50 keV. Simulations have shown that approx. 1000 vacancy-interstitial pairs are produced by the *primary knock on atom* (PKA) of this energy [36]. In the end of the path of a high-energy PKA a region with high concentration of defects is formed (*cluster* of defects) [37]. Figure 2.1 shows a simulation of initial distributions of vacancies produced by 10 MeV and 24 GeV protons and 1 MeV neutrons. As seen from the plot, low energetic protons produce more point defects while high energy protons and 1 MeV neutrons mostly produce clusters of defects due to higher imparted energies.

2.2 The NIEL scaling of radiation damage

The basic assumption of the *Non Ionizing Energy Loss* (NIEL) scaling hypothesis is that the radiation induced change in the material properties scales with the imparted energy irrespective of the initial spatial distribution of the displacement defects in one PKA cascade, and irrespective the of the annealing sequences after the initial damage event [38]. The damage produced by various particles is usually given in terms of the damage caused by 1 MeV neutrons, where the latter is described by the *displacement damage function* $D(E)$ and standartized as $95 \text{ MeV}\cdot\text{mb}^4$. The displacement damage function is calculated over all possible

⁴Millibarn, $1 \text{ mb} = 10^{-27} \text{ cm}^2$.

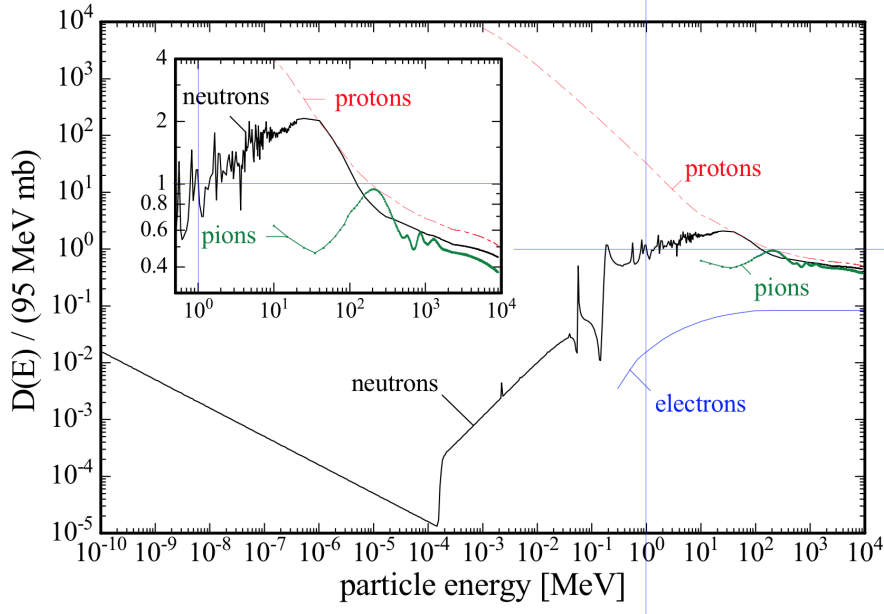


Figure 2.2: Displacement damage functions normalized to 95 MeV·mb for different particles [48].

interactions with the incident particle of energy E with a cross section of i -th interaction $\sigma_i(E)$, a probability $f_i(E, E_R)$ of generation of a PKA with a recoil energy E_R and a fraction of energy $P(E_R)$ that goes into the displacement of a silicon atom (also called *Lindhard partition function*):

$$D(E) = \sum_i \sigma_i(E) \cdot \int_0^{E_{R,max}} f_i(E, E_R) P(E_R) dE_R, \quad (2.2)$$

Figure 2.2 illustrates the displacement damage functions calculated for various types of particles. Using the displacement damage function, the *hardness factor* κ is used to compare the damage produced by various radiation sources in terms of the damage caused by 1 MeV neutrons:

$$\kappa = \frac{\int D(E) \Phi(E) dE}{D(E_{n(1\text{ MeV}})}) \cdot \int \Phi(E) dE \quad (2.3)$$

Thus, the equivalent fluence of 1 MeV neutrons is calculated by:

$$\Phi_{eq}(1\text{ MeV neutrons}) = \kappa \cdot \Phi \quad (2.4)$$

2.3 Classification of defects

If a displaced interstitial atom is located within the lattice constant, it will most likely recombine with the vacancy. According to [39], this is the case for $\approx 60\%$

of produced Frenkel pairs. At temperatures higher than 150 K, the defects that did not recombine can easily migrate through the material [37]. While migrat-

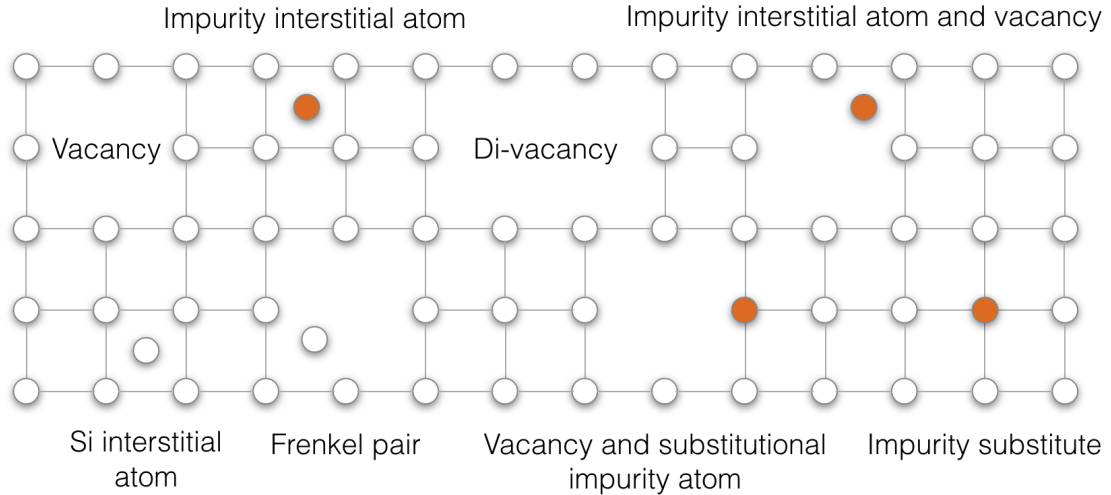


Figure 2.3: Various basic configurations of point defects and defect complexes.

ing, they interact with each other or with other impurities that are present in the material (e.g., oxygen, carbon, phosphorus) and form stable defects with different energy levels and charge states. Moreover, complex defects can dissociate. Both mechanisms lead to *annealing* of defects. The relevant defect kinetics can be found in [40]. Several techniques such as *Deep Level Transient Spectroscopy* (DLTS) [41], *Transient Current Technique* (TCT) [42] and *Thermally Stimulated Current* (TSC) [43] are used to characterize the produced defects and to study their properties and the impact on the detector operation.

Figure 2.3 illustrates various configurations of defects, indicating point defects and defect complexes, comprising two or more defects that were identified using the above mentioned methods. Figure 2.4 illustrates the variety of defect complexes, their energy levels and charge states. Herewith, some of the defects have their energy levels close to the intrinsic Fermi level. Such defects are called *deep level* (DL) defects. DLs can affect the properties of the detector in the following way:

- Capture and emit electrons or holes, thus generating additional leakage current in the bulk of the reverse biased detector;
- Change the space charge density and influence the full depletion voltage;
- Act as trapping centers for carriers created by ionization, reducing the carrier lifetimes and the charge collection efficiency.

In the following sections, the implications of deep levels on the detector performance is described.

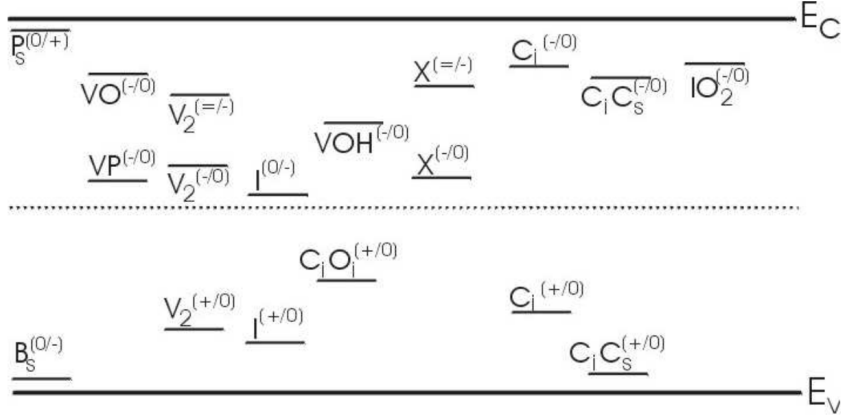


Figure 2.4: Energy levels and charge states of selected defects in the band gap [44].

2.4 Change in the macroscopic detector properties

Leakage current

Experimental data have shown a linear increase of the leakage current with irradiation (Fig. 2.5). This increase is caused due to an additional generation of charge carriers in the sensor bulk by the defect levels having their energy level close to the intrinsic level in the forbidden band gap. Those defect levels can capture and emit electrons or holes. This processes are described by the Shockley-Read-Hall statistics [45]. An additional electrical current is generated in the detector bulk under applied electric field due to the drift of emitted carriers in opposite directions. In [33] it was shown that the current induced by drifting carriers is proportional to the carrier generation rate which is proportional to the concentration of the deep level defects, therefore, proportional to the fluence. Thus, the increase of the leakage current under irradiation is proportional to the accumulated fluence:

$$\frac{\Delta I}{V} = \alpha \cdot \Phi_{eq} \quad (2.5)$$

where α is the current related damage rate, $\Delta I = (I - I_0)$ is the difference in the leakage current before and after irradiation, V is the detector volume. Being a parameter of the leakage current, α exhibits a strong temperature dependence. Measured directly after irradiation, it usually ranges from 10^{-17} to 10^{-18} A/cm.

The time evolution of α at various temperatures due to annealing of the radiation-induced defects has shown a decreasing behaviour of α (i.e., the leakage current of the detector) with time (Fig. 2.6). In [37], the following parametrization

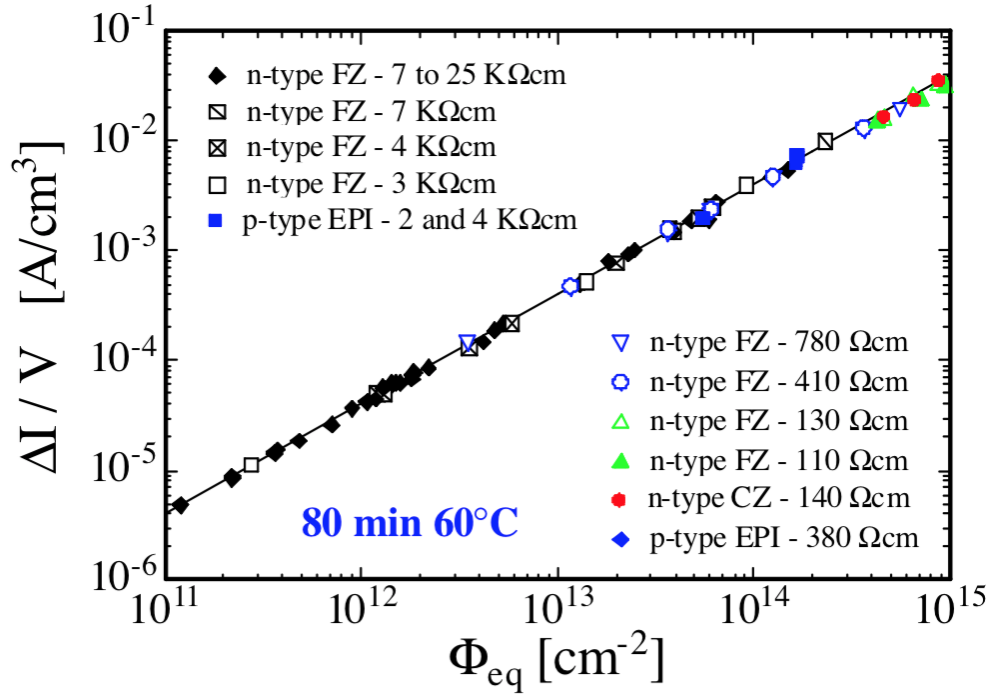


Figure 2.5: Fluence dependence of the leakage current density for various materials [46].

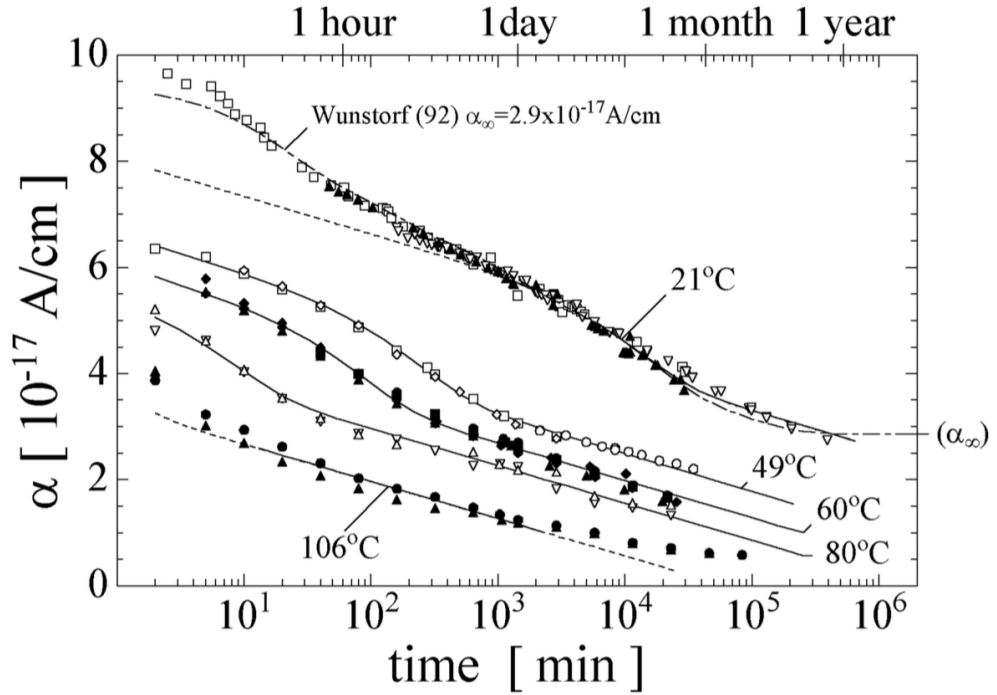


Figure 2.6: Time evolution of the current related damage rate at various temperatures [37].

is given to describe the time evolution of α based on experimental data:

$$\alpha(t) = \alpha_I \cdot \exp\left(-\frac{t}{\tau_I}\right) + \alpha_0 - \beta \cdot \ln(t/t_0), \quad (2.6)$$

where $\alpha_I \approx 1.23 \times 10^{-17}$ A/cm, $\beta \approx 3 \times 10^{-18}$ A/cm, $t_0 = 1$ min.

Most frequently the current related damage rate is represented after 80 min. of annealing at 60 °C. The averaged value based on experimental data for various detector materials is $\alpha_{80/60} \approx 3.99 \times 10^{-17}$ A/cm with a 1σ uncertainty of 0.24×10^{-17} A/cm in the fluence range up to 10^{14} n_{eq}/cm² [37].

Effective impurity concentration N_{eff} and full depletion voltage V_{fd}

Experimental results have shown a considerable evolution of the effective doping concentration⁵ with irradiation⁶. For detectors with positive space charge (*n-type*), N_{eff} decreases with irradiation until it reaches a minimum and rapidly increases with further irradiation (Fig. 2.7). Two processes are responsible for this evolution. Removal of donors takes place (e.g., reaction $V + P = VP$), as the VP defect is more electrically neutral, while many newly introduced deep level defects are more acceptor-like [38]. As a result, the sign of the space charge changes from positive to negative at the point of *type inversion* or *space charge sign inversion* (SCSI). However, this does not mean that all the donors are removed. As the effective doping concentration is an absolute difference of concentration of donors and acceptors, the SCSI occurs when the concentration of acceptor-like impurities becomes equal to concentration of donor-like ones. In [47] it has been reported that for neutron irradiated samples the donor removal is incomplete while for charge hadrons the complete removal takes place. After the SCSI, the space charge remains positive and N_{eff} increases proportionally to the fluence. For a silicon sensor of *n-type*, the SCSI practically reflects in relocation of the *pn*-junction to the opposite side of the sensor (from the *p*-side to the *n*-side), from where the space charge region will develop under the reverse bias voltage applied.

Based on experimental results the following parametrization of the change in N_{eff} was proposed by the Hamburg group (so-called *Hamburg model* [38], [37]). Considering that the absolute change in effective impurity concentration is a difference between the initial effective impurity concentration before irradiation and the one after irradiation, $\Delta N_{eff}(\Phi_{eq}, t) = N_{eff,0} - N_{eff,SCR}(\Phi_{eq}, t)$, the evolution of the latter is given by:

$$\Delta N_{eff}(\Phi_{eq}, t) = N_C(\Phi_{eq}, t) + N_A(\Phi_{eq}, t) + N_Y(\Phi_{eq}, t), \quad (2.7)$$

⁵Also, *effective impurity concentration* and *space charge density*.

⁶By monitoring the depletion voltage at various fluences.

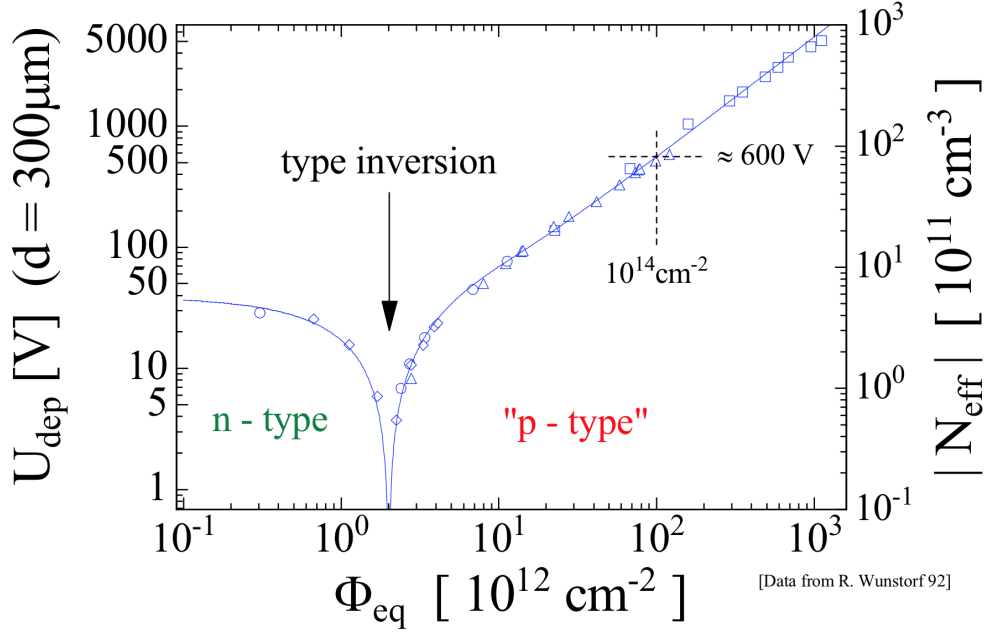


Figure 2.7: Fluence dependence of effective impurity concentration N_{eff} and depletion voltage V_{fd} of an n -type detector, measured immediately after irradiation [48].

where $N_C(\Phi_{eq}, t)$ is the *stable damage* term, $N_A(\Phi_{eq}, t)$ represents the *short-term annealing* and $N_Y(\Phi_{eq}, t)$ is the *long-term* or *anti-annealing* component. The stable damage component does not change in time. It comprises two components responsible for removal of donors and for introduction of stable acceptors:

$$N_C(\Phi_{eq}, t) = N_{C,0}(1 - \exp(-c \cdot \Phi_{eq})) + g_c \cdot \Phi_{eq}, \quad (2.8)$$

where $N_{C,0}$ represents the initial concentration of donors. The left-hand exponential term represents the removal of donors where c is the donor removal constant. The right-hand term is responsible for introduction of stable acceptors and it is proportional to the fluence. The N_C component determines the overall trend of the N_{eff} evolution and therefore has the most significant impact on the detector operation.

The short-term annealing takes place during about 10 days at room temperature. During this stage, the V_{fd} of type-inverted detectors was observed to decrease. Therefore, it is also called *beneficial* annealing. It corresponds to decrease of the N_{eff} . For the detectors which did not undergo the SCSI, the depletion voltage increases which corresponds to the space charge to become more positive. Thus, this stage is usually attributed to partial removal of acceptor-like defects. The parametrization of the short-term annealing is given by:

$$N_A(\Phi_{eq}, t) = \Phi_{eq} \sum_i g_{a,i} \exp\left(-\frac{t}{\tau_{a,i}}\right), \quad (2.9)$$

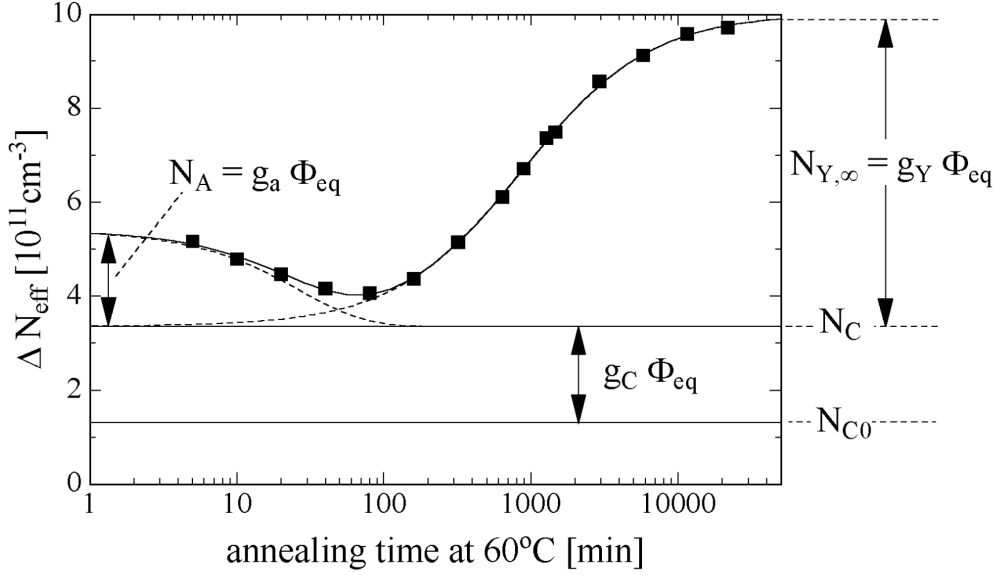


Figure 2.8: Annealing behaviour of the radiation induced change in effective impurity concentration at 60 °C [37].

where g_a depends on the material, τ_a is the time constant that depends on the temperature. Here it should be noted that as the N_A is directly proportional to the fluence, the effect of short-term annealing expressed in decrease⁷ of the depletion voltage is higher for the sensors irradiated to higher fluences.

The reverse annealing was observed when the full depletion voltage started to grow⁷ after reaching the minimum. In terms of the ΔN_{eff} an increase is expected in both cases before and after type inversion due to the fact that it is expressed in absolute values (Fig. 2.8). The possible process which drives the reverse annealing is the reaction between electrically neutral defects, resulting in a new electrically active defect. Here, for type-inverted detectors this results in continuous increase of the V_{fd} . For detectors not experienced the type inversion, reverse annealing leads to decrease of V_{fd} until the inversion of the space charge occurs. A parametrization of the reverse annealing is given by:

$$N_Y(t) = N_{Y,\infty} \left(1 - \frac{1}{1 + t/\tau_Y} \right), \quad (2.10)$$

where $N_{Y,\infty} = \Phi_{eq} \cdot g_Y$ is the reverse annealing amplitude, $g_Y = (5.16 \pm 0.09) \times 10^{-2} \text{ cm}^{-1}$ is the average introduction rate which is material dependent and τ_Y is the reverse annealing time constant given as:

$$\frac{1}{\tau_Y} = k_{0Y} \cdot \exp\left(-\frac{E_Y}{k_B T_a}\right), \quad (2.11)$$

⁷For type-inverted detectors.

where $E_Y = (1.33 \pm 0.03)$ eV is the activation energy for dissociation or migration of defects, $k_{0Y} = 1.5^{+3.4}_{-1.1} \times 10^{15}$ cm⁻¹ is the frequency factor in the corresponding Arrhenius relation [37].

Trapping probability and charge collection

Charge collection is an important parameter of silicon detectors which determines their performance. Therefore, it has to be kept at the maximum possible level. The induced charge that is integrated into the readout electronics depends on the amount of charge carriers⁸ and their drift path. The deep level states that are located above the intrinsic level can trap electrons, while the levels located below the intrinsic level can act as a hole trap [49]. Here, the probability of trapping of the

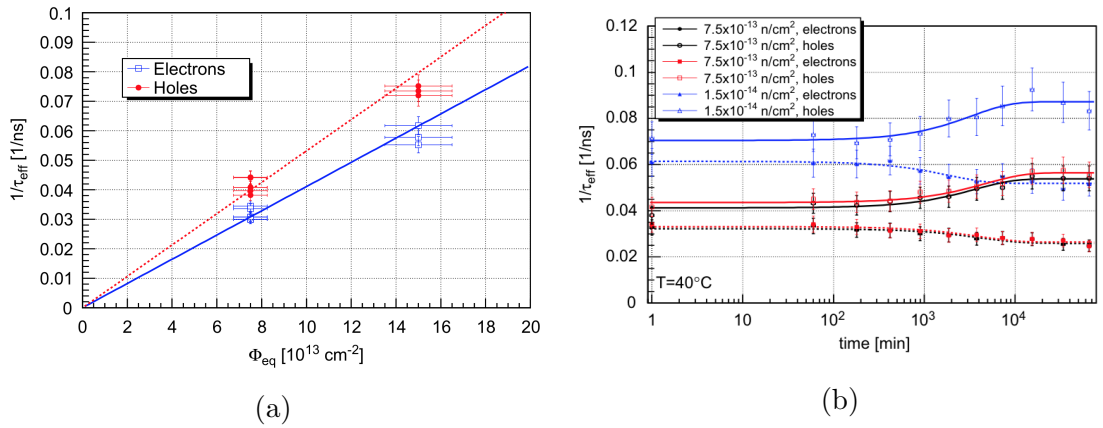


Figure 2.9: (a) Dependence of effective trapping probability of holes and electrons on fluence for all irradiated samples after the completion of beneficial annealing of N_{eff} . The lines represent the linear fit to the data; (b) Annealing of the effective trapping probability $1/\tau_{eff}$ for holes and electrons. Both figures are taken from [50].

carriers depend on their mobility and the trapping cross section, therefore, is higher in the regions where the electric field is lower. If the charge carriers were trapped, they are not drifting thus they do not produce an electrical current and do not contribute to the read-out signal. Therefore, the charge collection in the presence of trapping levels is reduced (Fig. 2.10). The charge collection of irradiated sensors is attributed to the *effective carrier lifetime* τ_{eff} or to *effective trapping probability* equal to $1/\tau_{eff}$. When the deep level traps capture the drifting carriers they re-emit them with a delay. Usually, this delay is longer than the integration time of the readout electronics. Therefore, re-emitted carriers do not contribute to the

⁸Electron-hole pairs.

read-out signal. The effective trapping probability is given by [50]:

$$\frac{1}{\tau_{eff,e,h}} = \Phi_{eq} \sum_k g_k (1 - P_k^{e,h}) \sigma_{k_e,h} v_{th_e,h} = \beta_{e,h}(t, T) \Phi_{eq}, \quad (2.12)$$

where in the sum over all defects $v_{th_e,h}$ is the thermal velocity of carriers, g_k is the introduction rate of the defect k with occupation probability $P_k^{e,h}$, and $\sigma_{k_e,h}$ is the cross section for capturing electrons and holes. Using the transient current technique it has been shown that the effective trapping probability increases as a function of the fluence more for holes than for electrons [33], [50]. Furthermore, the time evolution of the effective trapping probabilities is such that the $1/\tau_{eff,e,h}$ increases by 20% for holes and decreases by 40% for electrons (Fig. 2.9b).

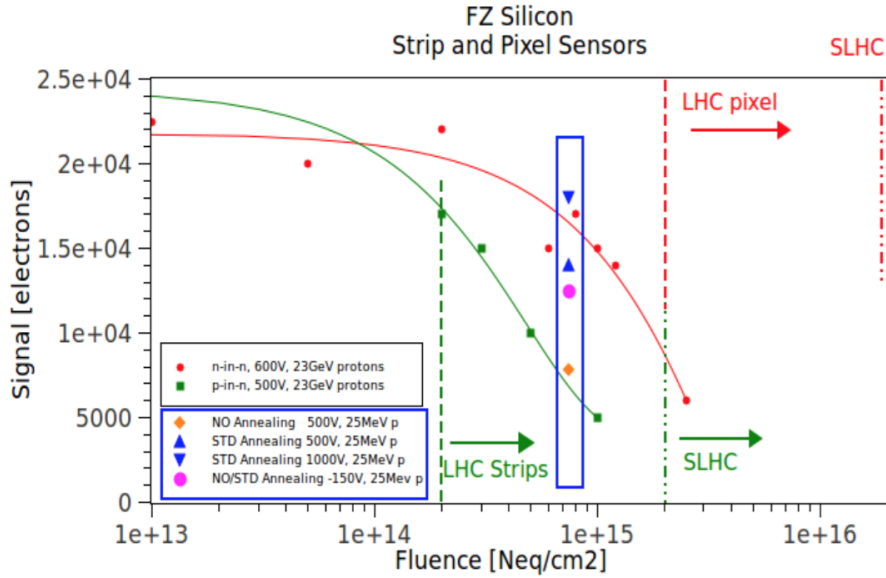


Figure 2.10: Charge collection as a function of the fluence. Taken from [51].

2.5 Implications on the performance of the STS sensors

The STS sensors' performance will be affected by the radiation damage. The simulated NIEL shows that for the sensors located in the innermost regions of the stations the equivalent fluence reaches 1×10^{14} n_{eq}/cm^2 after several years of running. In this case, an increase in the leakage current can deteriorate the signal to noise ratio and, as a result, the track reconstruction efficiency. Moreover, high values of the leakage current may lead to a thermal runaway and an instability of behaviour of the sensors. Most sensitive to that are the sensors with large areas,

$6.2 \times 12.4 \text{ cm}^2$ and $6.2 \times 6.2 \text{ cm}^2$. The level of the leakage current increase has to be identified to be able to predict the sensor behaviour at a certain operational period and to determine the signal-to-noise scenario of the detector operation. Also, operational stability of the sensors after high levels of radiation exposure has to be evaluated at real operational conditions of the CBM experiment.

The evolution of the space charge density will cause a rapid increase of the depletion voltage after the space charge sign inversion. Therefore, the parameters of the space charge density evolution and the inversion point has to be identified. As the inversion point can be focused by tuning the initial resistivity of the sensors, it has to be selected such that the V_{fd} level after the exposure to the lifetime fluence is as low as possible.

The introduction of the radiation induced deep level trapping centers will reduce the effective carrier lifetimes and the charge collection efficiency. The evolution of the charge collection efficiency has to be monitored at different levels of irradiation corresponding to operational scenario up to the lifetime fluence. The inversion of the space charge will lead to a relocation of the pn -junction to the n -side. In this case the charge collection efficiency for both p - and n -side readout sides has to be evaluated.

As the CBM operational scenario implies 2 months of annual operation, annealing effects have to be considered as willing to take place during the maintenance periods. Possible implications of the long-term annealing has to be evaluated for the sensors experienced different irradiation levels. The next chapter details the investigation on the radiation tolerance of the STS sensors.

Chapter 3

Investigation on the radiation tolerance of STS sensors

The operation of the CBM experiment at high interaction rates with beam intensities up to 10^9 heavy ions per second, produces a harsh radiation environment for the STS detector. The variety of particles created in beam-target interactions includes pions, neutrons, protons and others. These particles will produce damage of the silicon bulk via the non-ionizing energy loss. According to the CBM operation scenario, the sensors located in the innermost regions of the STS stations are expected to accumulate an equivalent fluence up to $1 \times 10^{14} \text{ cm}^{-2}$, after several years of operation [31]. Irradiation at such a level will impact on the operational performance of the sensors. In order to investigate the performance of the STS sensors after irradiation, several sets of the STS sensors, including miniature and prototype sensors, were irradiated with either reactor neutrons, or 23 MeV protons to a broad range of fluences.

In Section 3.4 of this chapter, the performance of the STS miniature sensors is studied after various levels of neutron irradiation. In Section 3.5, annealing studies were performed at different temperatures in order to investigate the performance of irradiated STS sensors during the maintenance period and their possible treatment. In Section 3.6, the performance of the STS prototype sensors is evaluated after proton irradiation to twice the lifetime fluence. In Section 3.7, the long-term stability performance and the environmental impact on the latter is considered for irradiated prototype sensors.

3.1 Sensors under study

Studies were performed on the CBM05 and CBM06 prototype sensors fabricated by CiS and Hamamatsu (or HPK), and two sets of miniature sensors fabricated by CiS within the same wafers as the CBM05 prototype sensors. The sensors are

double-sided, $p^+n^-n^+$ devices built on a $\langle 111 \rangle$ oriented float-zone silicon. The strips at the p -side are tilted by 7.5° for the prototype sensors and by 90° for the miniature devices. The strips at the n -side are isolated with implemented p -spray structures. General properties of the sensors are listed in Tab. 3.1.

Acronym	Vendor	Thickness [μm]	Size [cm^2]	$V_{fd,0}$ ¹ [V]	Strip pitch [μm]	Fluence [$\text{n}_{eq}/\text{cm}^2$]
---------	--------	--------------------------------	---------------------------	----------------------------------	----------------------------------	--

Irradiated *batch A*: miniature STS sensors irradiated with **neutrons** (Section 3.4):

w06				85		0
w1sn5				88		3×10^{13}
w2sn5				82		3×10^{13}
w2sn3				82		5×10^{13}
w8sn2				83		5×10^{13}
w7sn1	CiS	290	1.2×1.2	85	50	8×10^{13}
w7sn4				80		8×10^{13}
w1sn2				90		1×10^{14}
w2sn1				85		1×10^{14}
w2sn2				85		2×10^{14}
w8sn1				80		2×10^{14}

Irradiated *batch B* miniature STS sensors irradiated with **neutrons** (Section 3.5):

w25				85		1×10^{13}
w12sn2				80		5×10^{13}
w6sn2	CiS	290	1.2×1.2	85	50	1×10^{14}
w6sn1				83		1×10^{14}

Full size prototype STS sensors involved in **proton** irradiation (Sections 3.6 and 3.7):

CBM05w10-DM ²	HPK	330	6.2×4.2	74		2×10^{14}
CBM05w18-SMwC ³	HPK	330	6.2×4.2	69		2×10^{14}
CBM05w6-DM	CiS	290	6.2×6.2	86		2×10^{14}
CBM06w14-SMwC	CiS	290	6.2×6.2	73	58	2×10^{14}
CBM05w13-DM	HPK	330	6.2×4.2	74		0
CBM05w24-SM	HPK	330	6.2×4.2	72		0

Table 3.1: Properties of the sensors under study.

¹Depletion voltage before irradiation.

²Double-metal strip interconnection.

³External microcable strip interconnection design (**Single Metal with Cable**).

3.2 Irradiation facilities

3.2.1 Irradiation with neutrons

The neutron irradiation of the sensors was performed at the Jozef Stefan Institute in Ljubljana, Slovenia, with reactor neutrons from the TRIGA type nuclear reactor [52], featuring a maximum power of 250 kW. The irradiation was conducted by lifting the objects down into the core of the reactor through a special irradiation tube which occupies a position of a fuel rod (Fig. 3.1a). The tube has an elliptical shape with dimensions of 7.5 cm×4.5 cm, a 5 m length, and it curves just above the core to prevent the radiation escape through it [53]. After lifting down, the object occupies the irradiation position having a range of 15 cm in length.

The reactor group used the neutron energy spectrum (Fig. 3.1b), measured using different activation foils, and hardness factors [54] in order to calculate the equivalent fluence in 1 MeV neutrons. Then, the irradiation time for each fluence was determined according to the reactor power as the neutron flux is linearly proportional to the latter.

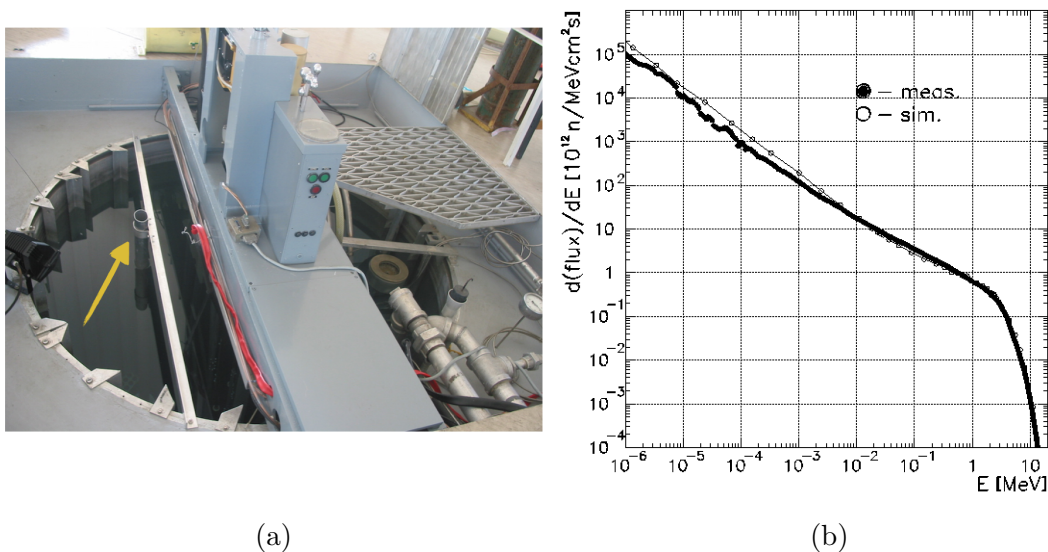


Figure 3.1: (a) Neutron energy spectrum in the irradiation tube; (b) General view of the JSI irradiation facility; location of the irradiation tube is pointed with an arrow.

The equivalent neutron flux inside the irradiation tube equals to $8.8 \times 10^9 \text{ n}_{eq}/\text{kW} \cdot \text{cm}^2 \cdot \text{s}$. Two batches of miniature sensors were irradiated to equivalent fluences from $1 \times 10^{13} \text{ cm}^{-2}$ to $2 \times 10^{14} \text{ cm}^{-2}$ (Table 3.1). In each case, the reactor power was selected such that the irradiation time exceeds two minutes

in order to keep the irradiation time error at the level of a few seconds (approx. 0.17%). However, the major contribution to the total irradiation error is the 10% error of the fluence.

The irradiated devices were sent to GSI either in a sealed box filled with dry ice and featuring the temperature and humidity monitoring system (*batch B*), or transported within several hours by plane (*batch A*).

3.2.2 Irradiation with protons

Proton irradiation of the STS prototype sensors was performed at KIT, Karlsruhe, Germany, with protons from a Compact Cyclotron at the KIT Irradiation Center [55]. The main parameters of the irradiation facility are:

- Proton energy ~ 23 MeV (25.3 MeV at extraction);
- Typical proton current ~ 1.5 μA ;
- Temperature in the sample box ~ -40 °C;
- Typical beam spot size ~ 7 mm;
- Proton flux $\sim 2.5 \times 10^{13}$ p/cm²·s;
- Nominal scanning speed $\nu_x = 115$ mm/s;

The irradiation setup is shown in Fig. 3.2. The objects for irradiation were fixed on a custom-made metal frame made from pure aluminum (Fig. 3.3a), located inside an insulated sample box having a window of two kapton foils. The box is located on a base equipped with motors for scanning in X and Y directions along the beam. Dry nitrogen of -40 °C was flooded to the sample box continuously in order to avoid annealing effects.

With the beam spot size of approximately 7 mm, the sensors were scanned in rows using the motors of the sample box (Fig. 3.3b). The average proton energy entering the samples after two layers of kapton and a layer of nickel is approx. 22.9 MeV according to SRIM [56]. In order to achieve the equivalent fluence of 2×10^{14} cm⁻², the scanning time and speed was adjusted by the irradiation team and the hardness factor $\kappa = 1.85$ was used for the NIEL scaling of the equivalent fluence. Here, the error of the fluence estimated in [56] is approx. 20%. After irradiation, the sensors were kept at -20 °C at KIT for approx. one week in order to suppress the activation of the PCBs, then transported to GSI.

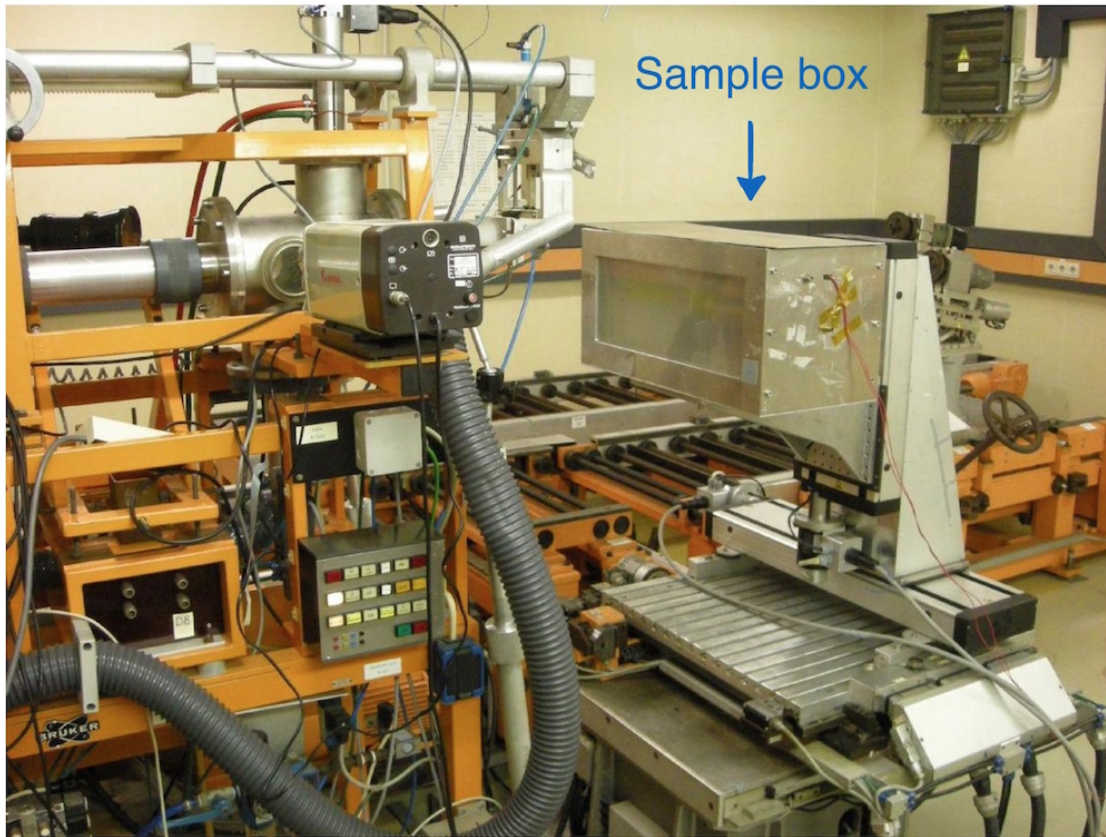
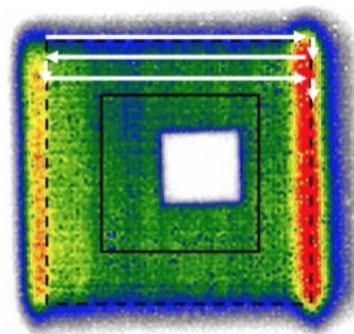


Figure 3.2: General view of the proton irradiation setup [55].



(a)



(b)

Figure 3.3: (a) Aluminum frame for mounting of sensors for irradiation inside the sample box; (b) Autoradiographic image of a large Ni-foil scanned showing the scanning movements [56].

3.3 Experimental methods

3.3.1 I-V and C-V measurements

Measurements of both I-V and C-V curves for irradiated objects were performed at $-5\text{ }^{\circ}\text{C}$ within the setup described in Section 3.3.2, using the methods and the equipment as described in Section 4.4.2 and Section 4.4.3. The measurements of non-irradiated sensors were performed at room temperature. Due to the temperature variation inside the test box hosting the sensor under test inside the refrigerator, the temperature and humidity values were recorded during the measurement.

As the temperature variations influence the measured values of the leakage current, a software for a temperature normalized I-V measurement was developed. The software uses a temperature monitoring system inside the test box and provides an automatic correction of the I-V curve by normalizing the leakage current values to a fixed temperature of $-5\text{ }^{\circ}\text{C}$. The interface of the software is presented in Appendix B.

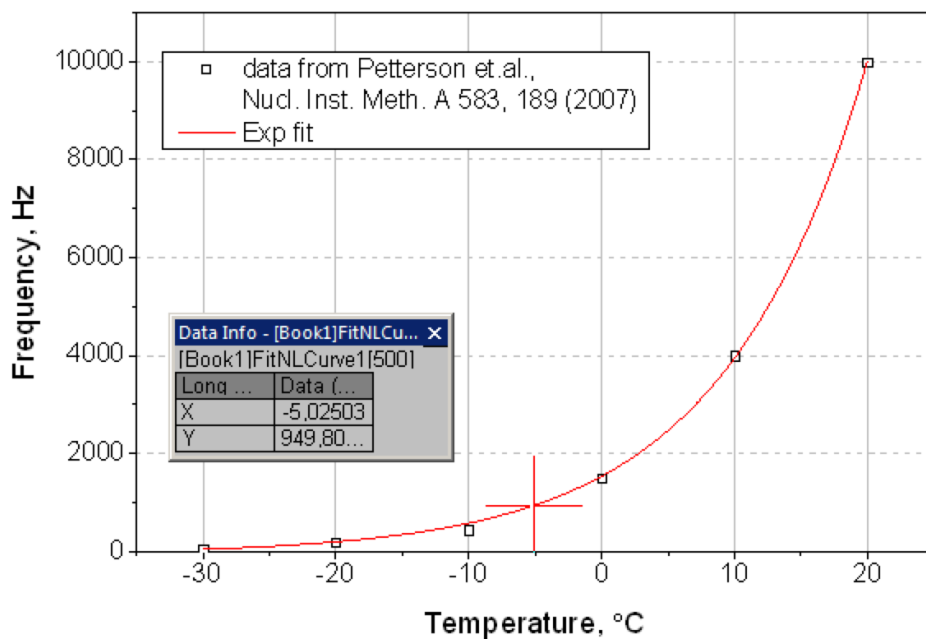


Figure 3.4: Frequency-temperature dependence recommended for C-V measurements [58]. The data window shows the frequency corresponding to $T = -5\text{ }^{\circ}\text{C}$.

The values of full depletion voltages V_{fd} for irradiated sensors extracted from the $1/C^2$ -V plot (see Section 4.4.3) show a frequency and a temperature dependence [57]. In [58], a model has been proposed to describe these dependences. The data points from this model were fitted with an exponential function (Fig. 3.4) and the test frequency corresponding to a $-5\text{ }^{\circ}\text{C}$ temperature has been found to be

approximately 950 Hz. Thus, the measurements of the V_{fd} were performed at this frequency⁴.

3.3.2 Charge collection measurements

Measurement conditions

The schematic representation of the measurement setup for charge collection tests, performed in this chapter, is illustrated in Fig. 3.5. The measurements are performed at -5 °C, inside a refrigerator, in order to reproduce real operational conditions of the CBM experiment. A special test box for housing the sensors under test has been assembled, serving as an electromagnetic shield inside the refrigerator itself and as an additional stabilizer⁵ of the environmental conditions. Figure 3.5b shows a schematic view of the test box with a sensor under test mounted inside. The test box is built from 3 mm thick steel plates. It is equipped with both temperature and humidity monitoring systems, based on PT100 and HIC-3602-C, respectively [59]. Both systems provide linear voltage output versus the measured parameter. The read-out is performed via a 14 bit NI-USB 6009 data acquisition system [60] using a LabView software. The monitoring sensors are shielded from the sensor under test inside the test box with a metallic net. In order to control the humidity inside the test box, dry nitrogen is supplied with a flow of up to 250 liters per hour. Before entering the test box, the gas is cooled by passing through a coil pipe located inside the refrigerator. The temperature variation inside the test box is ± 0.5 °C while for the refrigerator it is equal to ± 1 °C.

Printed circuit boards for the sensors under test

Sensors under test are clamped inside two printed circuit boards, designed by the STS-GSI group, in order to supply the bias voltage and to perform the readout of the signals from the strips. The strips are connected to the readout lines of the PCB via micro-wire bonds (Fig. 3.7a). Each board features 32 golden coated readout lines for transferring the signals to the readout electronics. When assembled and bonded, the PCB is plugged directly to the ERNI slot of the front-end electronics board (FEB) (Fig. 3.6). The present PCB design allows to readout a maximum of 32 strips per side.

Micro-wire bonding of the power connections and the readout strips was performed manually, using the MEI 1204W Hybrid Wedge Bonder with a 25 μm thick aluminum wire [61]. Due to the difference in pitch for the sensor's strips and the

⁴The C-V measurements of non-irradiated sensors were performed at room temperature and a 10 kHz frequency.

⁵As the temperature variation inside the test box is lower than inside the refrigerator itself.

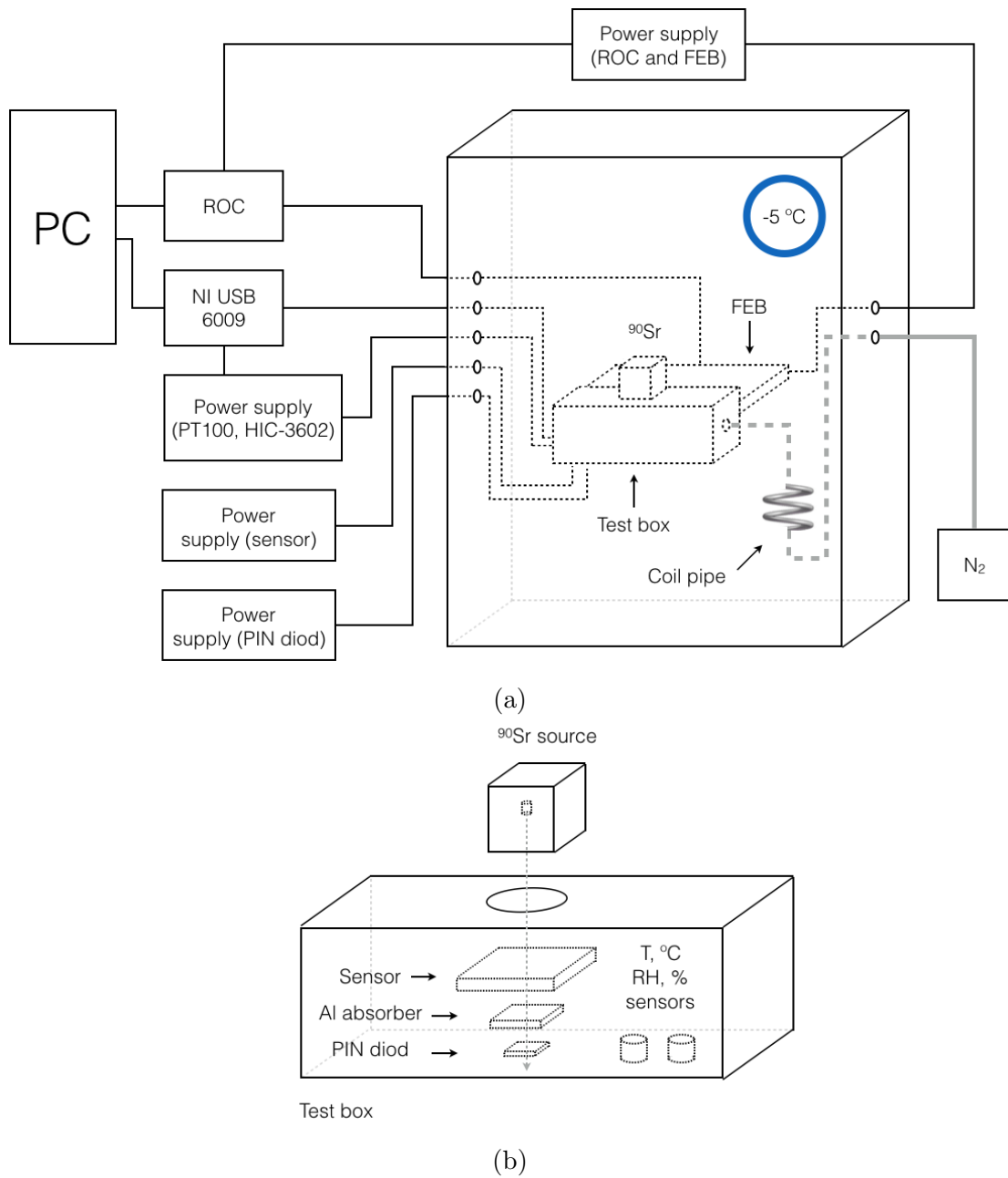


Figure 3.5: (a) Schematic view of the setup for charge collection measurements; (b) Detailed view of the test box for charge collection measurements.

3.3 Experimental methods

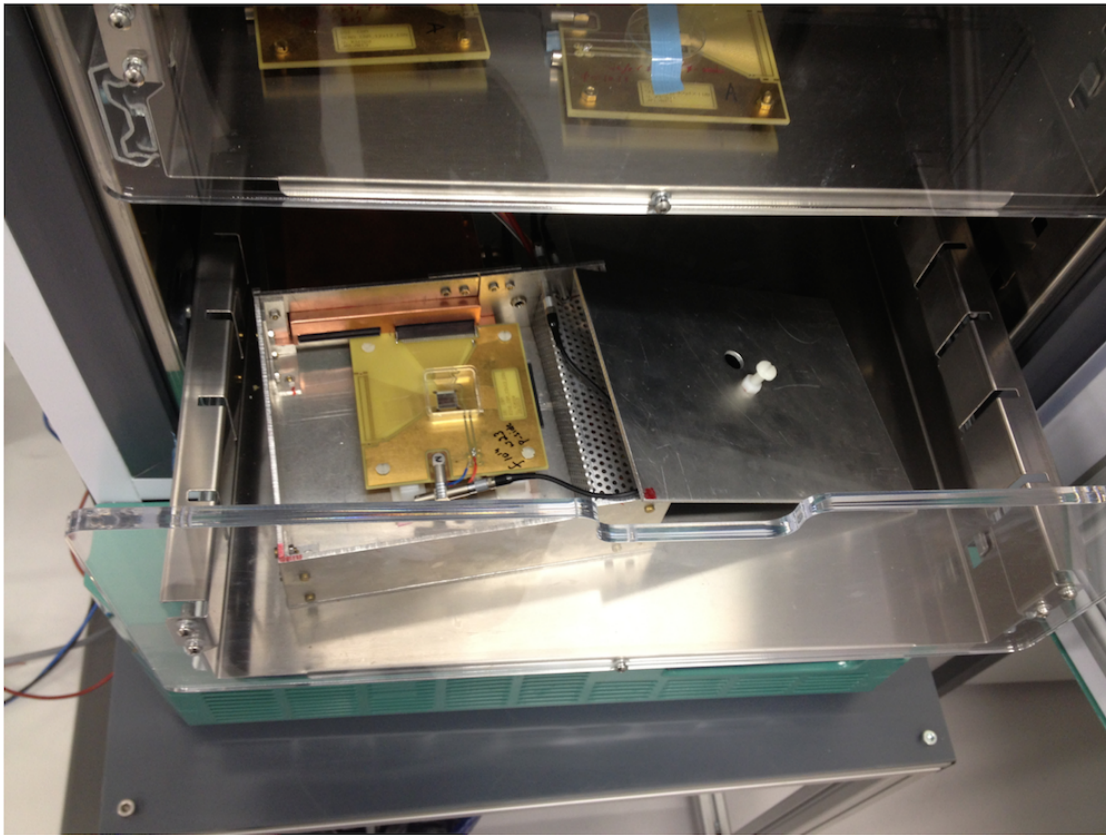


Figure 3.6: General view of the test box inside the refrigerator with a sensor under test mounted inside.

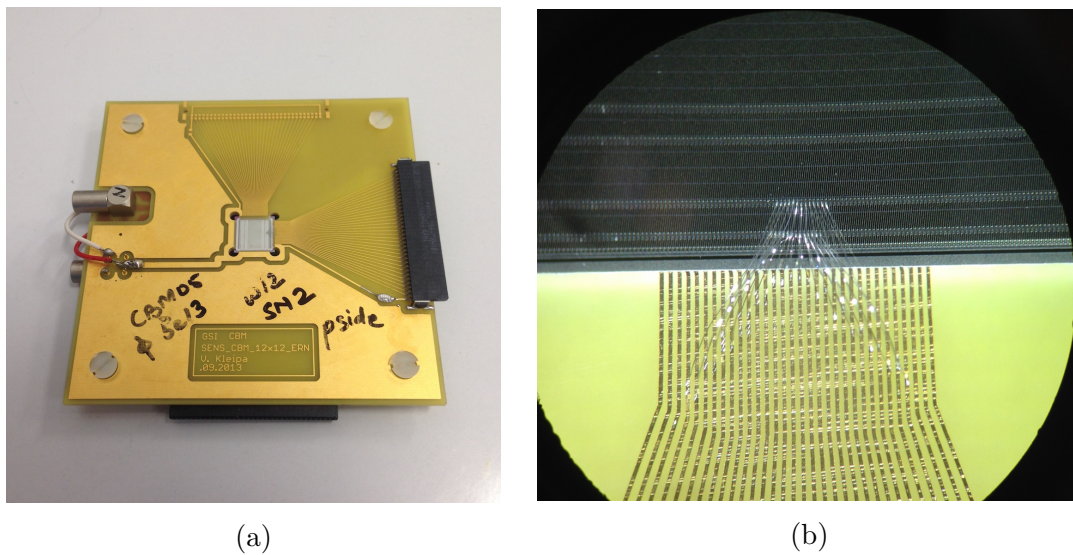


Figure 3.7: (a) General view of the STS miniature sensor mounted on the PCB; (b) Microscopic view of the micro-wire readout bonds.

PCB readout lines, wire bonding of the outermost channels was performed under an angle. In this case, the outermost bonds become longer and special attention is paid during bonding to prevent touching of the neighbouring wires. For the majority of the sensors, wire-bonding of all 32 possible channels was performed. Figure 3.7b exhibits a microscopic view of the micro-wire bonding of the readout strips.

Readout chain and data acquisition

In order to mimic minimum ionizing particles (MIP) in the laboratory conditions, a 37 MBq ^{90}Sr source is used providing a flux of β^- particles with a maximum energy of 2.28 MeV (coming from the daughter product: ^{90}Zr). The source is sealed inside a plastic cube, having a single drilled hole of a 3 mm diameter, which acts as a collimator. The plastic cube in this case also prevents from an undesired bremsstrahlung. The MIP signals are read-out with n-XYTER (neutron-X-Y-Time-Energy Readout) based front-end electronics [62]. The n-XYTER is a 128 channel self-triggering readout ASIC, originally developed as a part of the EU-FP6 NMI3 project DETNI to readout solid converter based neutron counting area detectors. The ASIC provides both analogue signal amplitude and timing information. Due to its wide dynamic range, a bipolar front-end and a low-noise design, it is well suited for the measurements of charge collection from MIPs.

A coincidence scheme containing a planar silicon diode of a $3 \times 3 \text{ mm}^2$ size and a 2 mm thick aluminum absorber is used to determine the signal amplitude of the β^- particles and to cut the low-energy particles of less than 1.5 MeV energy, which cannot be considered as MIPs. Here, the n-XYTER is operated in a self-triggered mode. The coincidence is achieved on a software level using a GO4 analysis [63]. The front-end board (FEB) that hosts the n-XYTER ASIC is located inside the refrigerator, coupled directly to the test box. The FEB is shielded from an electromagnetic pickup with a thin copper cover. After the signal is registered and digitized, it is transferred from the FEB to the Read-Out Controller (ROC). The ROC provides an interface between the FEB and the PC and by design can support 4 n-XYTER ASICs simultaneously. The so-called DABC data acquisition system is used to store the data for offline analysis as well as to broadcast the data to the GO4 software for the online data acquisition [66]. Configuration of the FEB and the ROC is done via the *rocutil* console program. For a detailed description of the readout chain components and for the results of the calibration of the ASIC see [64].

Data analysis

The analysis of signal amplitudes is performed by using the output files of the amplitude distributions from the data acquisition system as an input for a ROOT macro,⁶ providing fitting of the amplitude distributions with a Landau-Gauss convolution (Fig. 3.8). Here, as mentioned in Section 1.3.1, the most probable value (MPV) of the distribution defines the charge collection. The results pre-

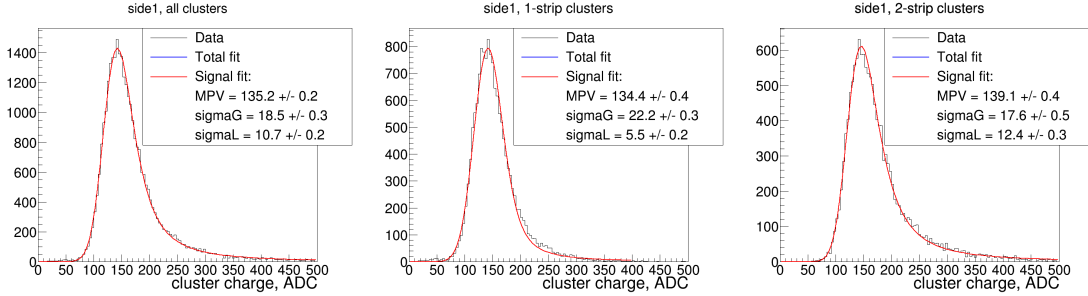


Figure 3.8: Typical signal amplitude distribution at the output of the ADC fitted by Landau-Gaussian convolution as presented for all-strip clusters, single-strip clusters and two-strip clusters cases from left to right.

sented in the following sections, correspond to the most probable value of the *all-cluster charge* distribution, a sum of the signal amplitude distributions for 1- and 2-strip clusters. The total error of the most probable charge extracted from this measurement includes the error of the ASIC calibration, the statistical error and the error of the fit:

$$Err_{tot} = \sqrt{\sigma^2 + Err_{fit}^2 + Err_{cal}^2} \quad (3.1)$$

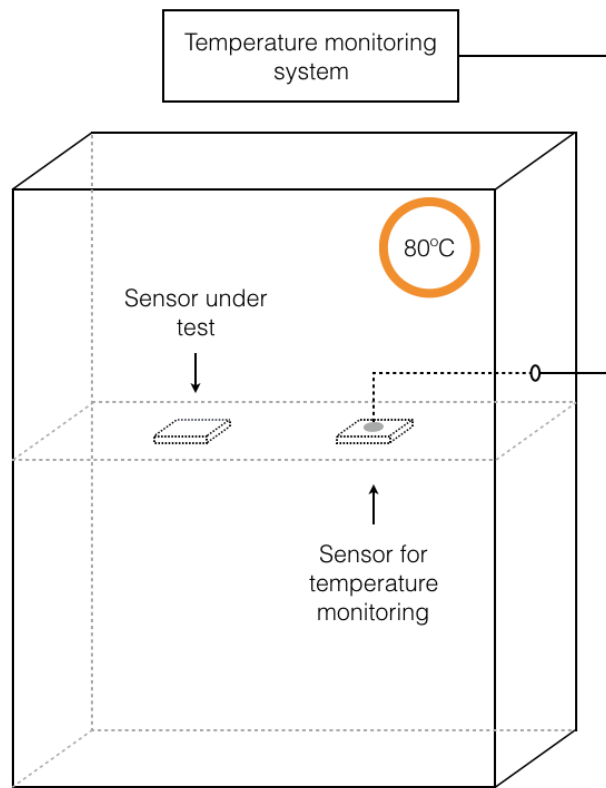
3.3.3 Setup used for annealing studies

Within the annealing studies, the room temperature annealing was performed in a light-tight box in the STS laboratory without any special measures. The accelerated annealing at 80 °C was performed using an oven featuring an air-circulating system.

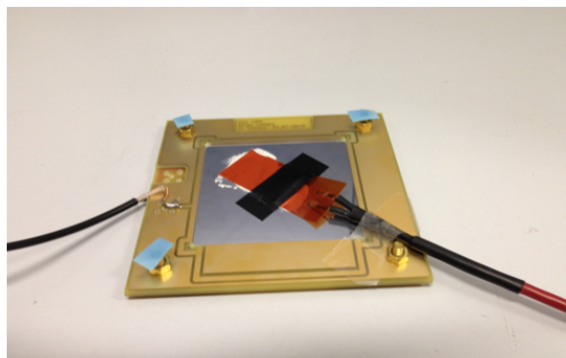
In order to monitor the direct temperature of the sensor surface during annealing, an additional test sensor of a 6.2×6.2 cm² area was used together with a PT100 sensing device attached directly to its surface via a thermoconductive paste (Fig. 3.9). Such a system provides a precise temperature measurement of the sensor surface during annealing. The PT100 device was read-out by a Keithley SMU.

The temperature ramping in the oven up to 80 °C lasted tens of seconds, however, the measured warm-up period of the test sensor's surface was within

⁶Developed by Hanna Malygina [65].



(a)



(b)

Figure 3.9: (a) Schematic view of the setup used for annealing studies at 80 °C; (b) PT100 device attached to the test silicon sensor for direct temperature monitoring.

approx. 3 minutes until the saturation (Fig. 3.10). Here, the considered annealing time was assigned to 11 minutes.

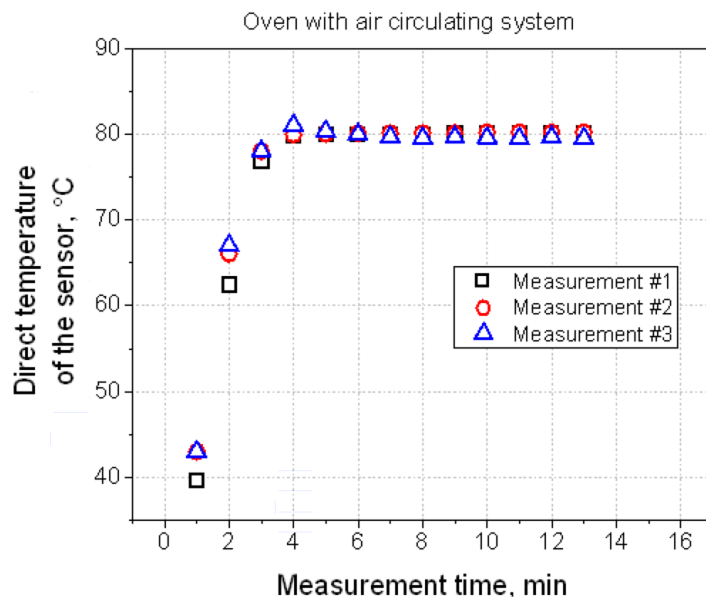


Figure 3.10: Direct temperature of the test sensor surface during annealing in the oven with an air circulating system.

3.3.4 Setup for long-term stability measurements

A schematic representation of the long-term stability setup is shown in Fig. 3.11. In general, this setup uses the same components as the setup for charge collection measurements. The sensors under test are mounted inside the test box located inside the refrigerator. Temperature and humidity monitoring devices are read-out via the NI-USB 6009 data acquisition system connected to the PC. The Keithley 2410 power supply provides the bias voltage for the sensors under test. The test box is coupled to the dry nitrogen supply. A custom-made software providing the measurement interface and control of the instruments was developed on a LabView base. The interface of the developed program is represented in Appendix B.

A reverse bias voltage of 350 V required for overdepletion of each sensor, was applied. Each measurement starts with a bias voltage ramp-up after a 10 minute stabilization delay, following the sensor mounting inside the test box. After reaching the operation voltage, the software monitors the values of the leakage current, the temperature and the relative humidity inside the test box, with a step of 30 seconds, during a selected measurement range. Measurement results are displayed online in a graph mode and also are saved in an ASCII file.

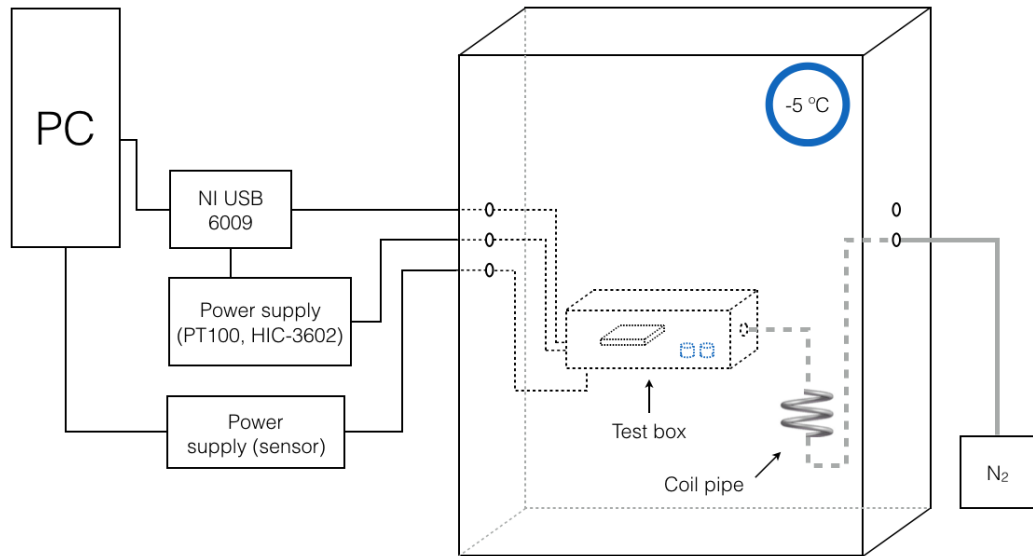


Figure 3.11: Schematic view of the setup used for long-term stability measurements.

3.4 Measurements on miniature STS sensors

A set of sensors examined in this section includes double-sided miniature sensors irradiated with reactor neutrons, presented in Table 3.1 within the *batch A*.

3.4.1 Sensors before irradiation

Before irradiation, the devices were characterised in terms of their electrical properties. Leakage current and bulk capacitance scans were performed at room temperature up to 300 V. The leakage current values lay in the range of tens of nanoamperes and differ from wafer to wafer (Fig. 3.12a). The depletion voltage values were extracted from the $1/C^2$ -V plots (Fig. 3.12b). The sensors that showed a normal I-V curve but a non-standard $1/C^2$ -V curve, such as the w8sn3 sensor in Fig. 3.12b, were rejected during the selection.

Due to resistivities, according to the manufacturer, varying from wafer to wafer from 2.08 k Ω ·cm to 4.32 k Ω ·cm, the extracted V_{fd} values also vary from approx. 80 V to 90 V (Tab. 3.1).

The charge collection tests before irradiation would have required a massive wire bonding of the readout strips and a subsequent removal of the latter as well as disengagement of the sensors from the PCBs due to irradiation specifics⁷. However,

⁷Due to a limited size of the irradiation tube, the sensors clipped in the PCBs would not fit in it (Fig. 3.1a)

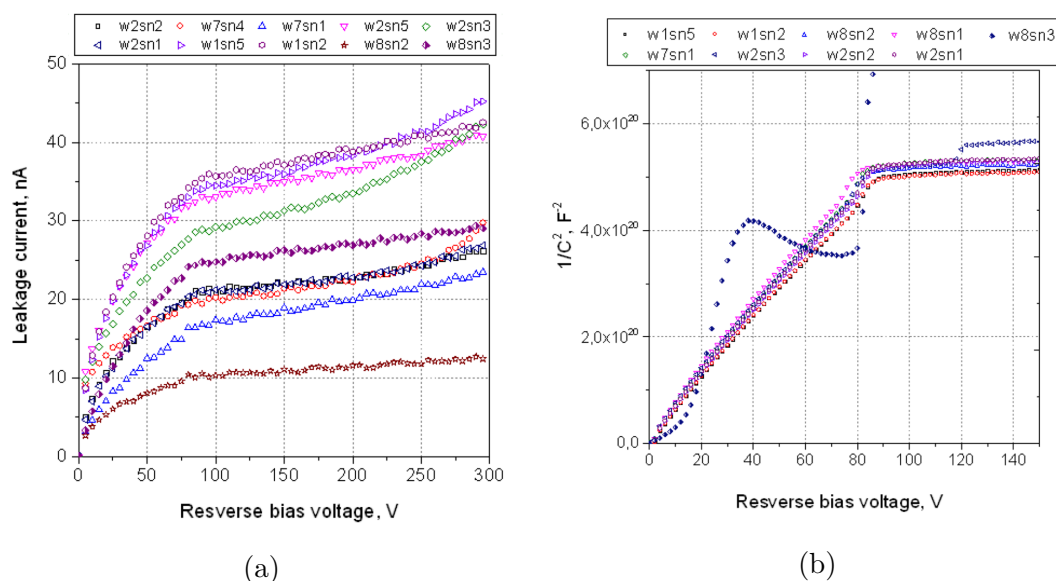


Figure 3.12: (a) I-V scans for the sensors before irradiation; (b) $1/C^2$ -V scan shapes for selected sensors and a rejected sensor (w8sn3).

removal of the micro-wires is very much undesired as it may cause damage of the readout pads' aluminum coating and create difficulties for the repeated bonding required for the tests after irradiation. Therefore, the charge collection tests of the selected sensors were not performed before irradiation. Instead, non-irradiated baby sensors from the same batch were used for the charge collection measurements providing a reference point.

3.4.2 Results after irradiation: leakage current density and full depletion voltage

Leakage current

The irradiated sensors were characterized in terms of leakage current as a very first step. The measured I-V curves were obtained at approx. -5°C within the setup described in Section 3.3.2.

Figure 3.13 exhibits the measured I-V curves normalized to a constant temperature of -5°C . The plot shows the leakage current increase with fluence and an increasing difference of the leakage current values for the sensors irradiated to the same fluence due to the fluence uncertainty.

Using the measured leakage current values at the 300 V bias voltage before and after irradiation, an increase of the bias current caused by irradiation was calculated. Then, the ratio of the bias current increase over volume was determined using the measured values of the sensor thicknesses (Table 3.1). The obtained ratio

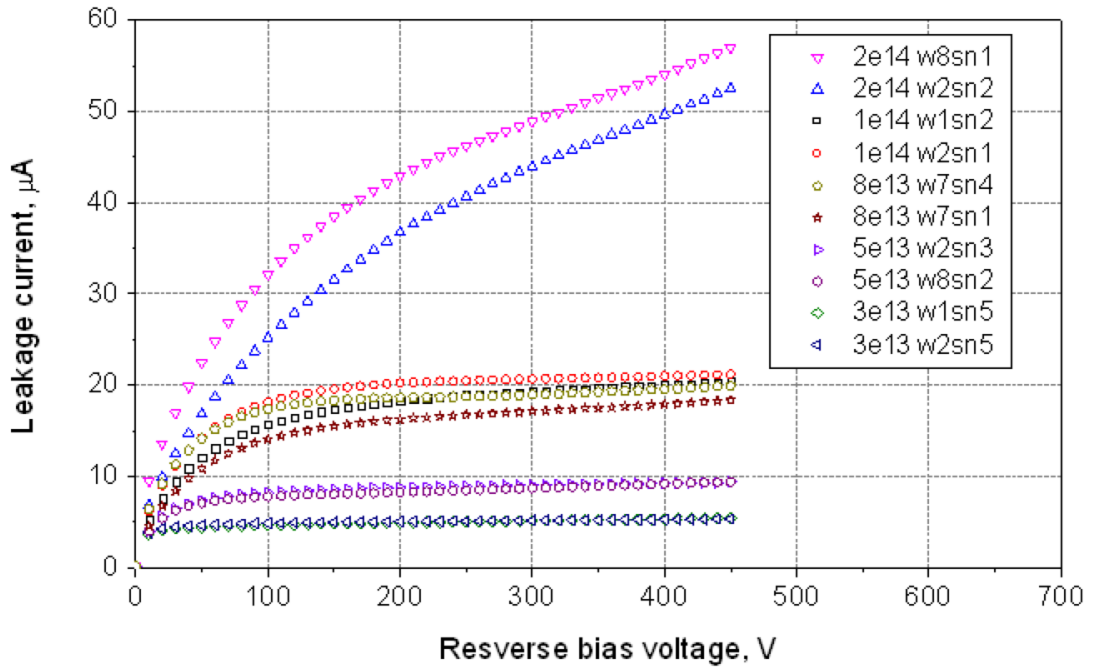


Figure 3.13: I-V curves of the irradiated CBM05 miniature sensors (*batch A*) measured at $-5\text{ }^{\circ}\text{C}$.

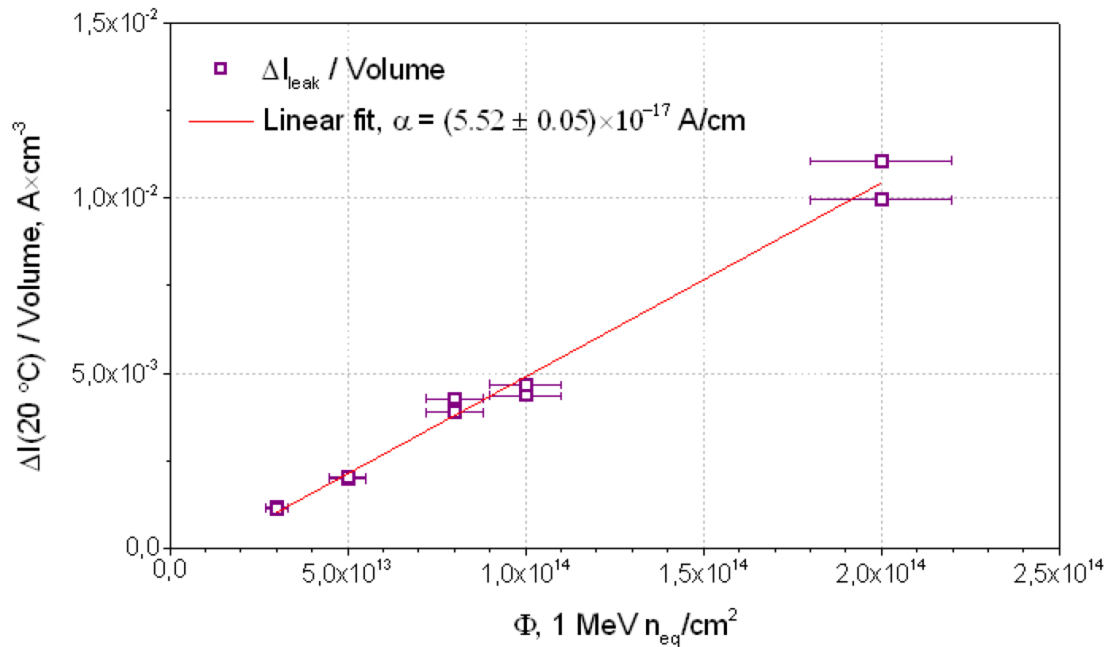


Figure 3.14: Fluence dependence of the leakage current density for neutron irradiated STS miniature sensors. The data points are scaled to $20\text{ }^{\circ}\text{C}$.

must be proportional to the accumulated equivalent fluence as $\frac{\Delta I}{Volume} = \alpha \cdot \Phi_{eq}$, where α is a current damage rate (Section 2.4).

Figure 3.14 illustrates the dependence of the leakage current density as a function of accumulated fluence for neutron irradiated STS sensors. The values of the leakage current density were scaled to 20 °C using the temperature relation of the leakage current [67]:

$$I(T_{meas}) \propto T_{meas}^2 \times \exp\left(-\frac{E_g}{2k_B T_{meas}}\right), \quad (3.2)$$

where $E_g = 1.12$ eV is an effective energy gap and k_B is the Boltzmann constant. The 10% systematic error of the fluence is included in the plot. The data points were fitted by a linear function and the experimental value of the current related damage rate was extracted: $\alpha = (5.52 \pm 0.05) \times 10^{-17}$ A/cm. The literature value for α , measured directly or shortly after irradiation, lies in a range of $5 \div 6 \times 10^{-17}$ A/cm for different substrate types [37]. Additionally, the current related damage rate after annealing at 80 °C is determined in the following sections.

Full depletion voltage and effective doping concentration

The effective doping concentration⁸ N_{eff} of n -type silicon sensors undergoes a considerable evolution under irradiation. Experimental data shows a dependence of N_{eff} on the substrate material and irradiation type⁹.

The full depletion voltage of a silicon sensor is proportional to its effective doping concentration as:

$$V_{fd} = \frac{qd^2|N_{eff}|}{2\varepsilon}, \quad (3.3)$$

where $\varepsilon = 2 \varepsilon_0 \varepsilon_{Si}$, d - sensor thickness, q - elementary charge. Figure 3.15 depicts the evolution of the full depletion voltage for neutron irradiated miniature STS sensors¹⁰.

Using the Hamburg model equations (Section 2.4) and the values of the full depletion voltage before irradiation $V_{fd,0}$ as well as the experimentally measured thicknesses of the sensors (see Table 3.1), a parametrization of the V_{fd} was performed. In particular, the averaged value of the initial effective doping concentration $|N_{eff,0}| = 1.34 \times 10^{12}$ cm⁻³, corresponding to the initial $V_{fd,0} = 85$ V was used in the calculation as well as the average sensor thickness of 290 μ m. The model parameters, corresponding to these initial values, were taken from [37]. For calculation of the annealing components N_a and N_Y , 6 hours of annealing at 20 °C that

⁸Also, *effective impurity concentration* and *space charge density*.

⁹In case of oxygen enriched substrates.

¹⁰Data points corresponding to the data from both batches *A* and *B* are presented.

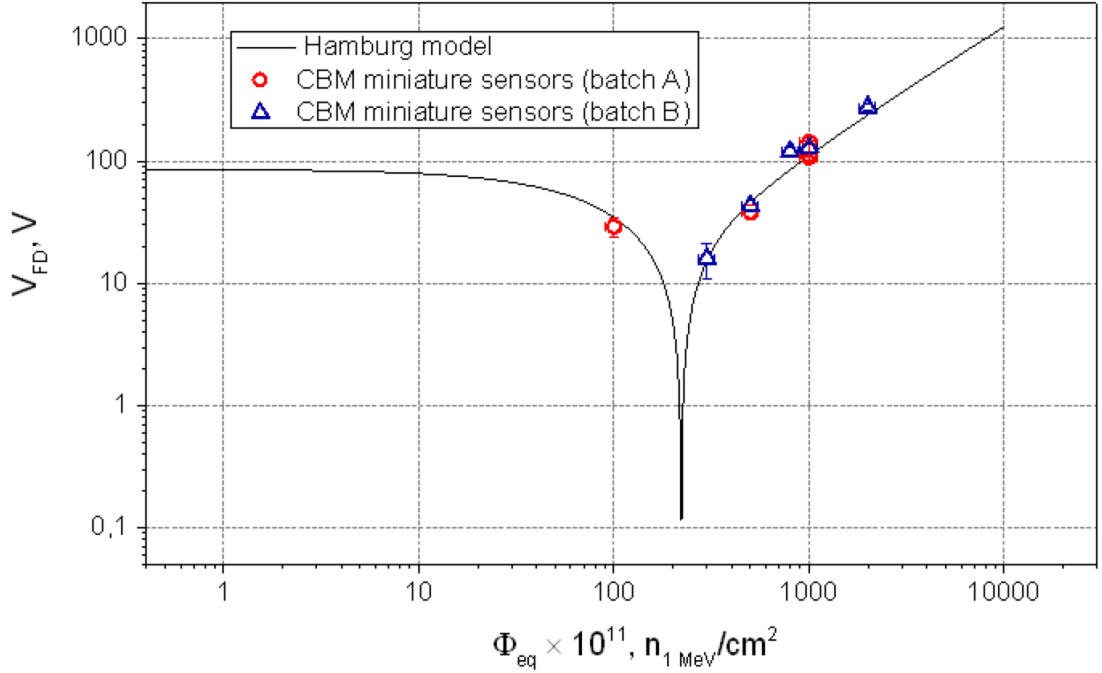


Figure 3.15: Full depletion voltage as a function of accumulated fluence. Experimental data for the STS sensors is shown together with the Hamburg model calculation (see Section 2.4), performed considering the initial space charge density of the STS sensors.

the sensors experienced during the bonding and assembly procedures, was considered. The model parameters are listed in Appendix D. A good agreement with the model is observed using the parameters corresponding to the initial parameters of the STS sensors as an input data in the regions of the plot before and after the inversion of the space charge. The experimental and the model data confirm the point of inversion of the space charge at about $2.25 \times 10^{13} \text{ n}_{eq}/\text{cm}^2$. The fluence uncertainties ($\approx 10\%$) and the V_{fd} point determination errors are included in the plot and partially are smaller than the symbol size.

3.4.3 Charge collection results

The sensors were characterized in terms of charge collection as a function of the reverse bias voltage, ranging from 100 V to 495 V (in absolute values) with a step of 100 V and, in special cases, a number of intermediate points. The setup used for charge collection measurements is described in Section 3.3.2, where the ^{90}Sr source provides β^- radiation considered as minimum ionizing particles.

Only one side of the sensor was read-out at a time due to the setup specifics. Therefore, the measurements of the p - and the n -side of a sensor under test were

carried out sequentially. The readout side was kept at the ground potential. The last measured point was set to 495 V due to the operational limit of 500 V of the capacitor included in the noise reduction filter. In this section, the most probable values of the signal amplitude distribution corresponding to all-strip cluster charge, are presented.

Measurement results

Table 3.2: Division of sensors into two sets for representation of the charge collection results.

$\Phi, n_{eq}/\text{cm}^2$	Set 1	Set 2
3×10^{13}	w2sn5	w1sn5
5×10^{13}	w2sn3	w8sn2
8×10^{13}	w7sn4	w7sn1
1×10^{14}	w2sn1	w1sn2
2×10^{14}	w2sn2	w8sn1

The measurement results are presented in two sets for better perception of the data. As two sensors were irradiated per fluence, each set represents five sensors irradiated to different fluences in the way as presented in Table 3.2. The first set comprises 4 sensors that were produced within the same wafer, namely wafer 2, and one sensor from wafer 7. The set 2 is formed with two sensors coming from wafer 1, two sensors from wafer 8 and one sensor from wafer 7.

Overall p -side readout trend

After space charge sign inversion, the pn -junction is relocated to the n -side. The p -side of the sensor becomes the opposite to that with the pn -junction, therefore, the electric field at it is minimal¹¹. The measurement results obtained at the p -side for the sensors from *set 1* are presented in Fig. 3.16. Here, the most probable charge shows a saturation at various points depending on the fluence but demonstrates comparable values for the sensors irradiated up to $1 \times 10^{14} \text{ n}_{eq}/\text{cm}^2$ at the highest bias voltage. In addition to that, the most probable charge of these sensors at this point is comparable to the one obtained for a non-irradiated device (w06), within the error bars.

The results obtained for the w2sn2 sensor, which accumulated the highest fluence of $2 \times 10^{14} \text{ n}_{eq}/\text{cm}^2$, demonstrate a notable charge collection degradation. The measured MPV for this sensor show a steep enhancement in the voltage range

¹¹Up to approx. $10^{14} \text{ n}_{eq}/\text{cm}^2$. Beyond this point the electric field has a non-linear profile [68].

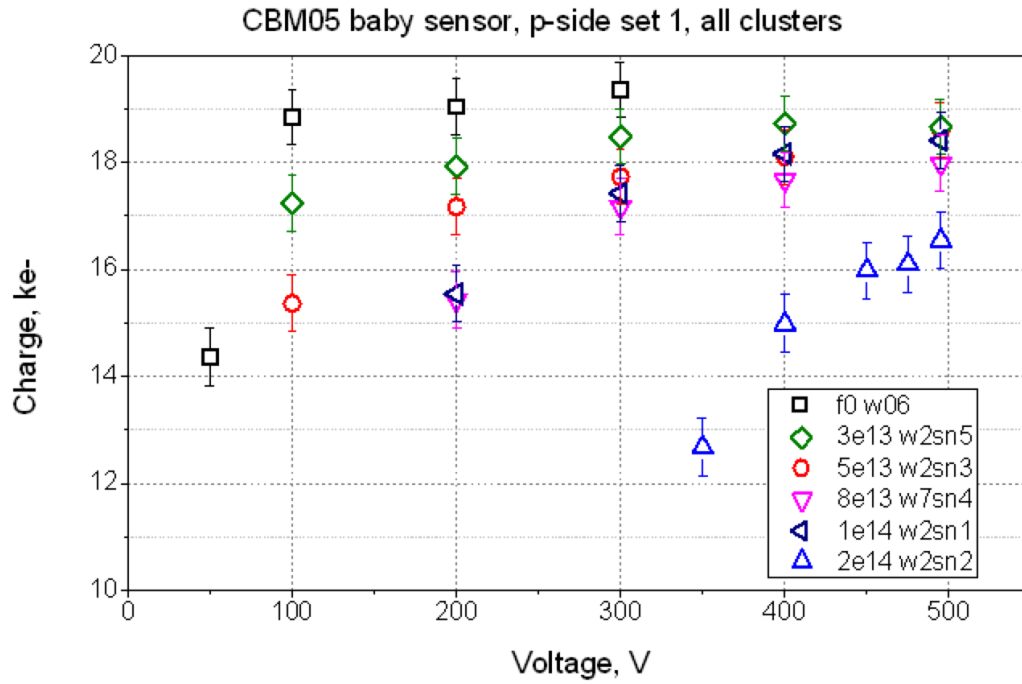


Figure 3.16: Charge collection results for the p -side of the sensors from the *set 1*.

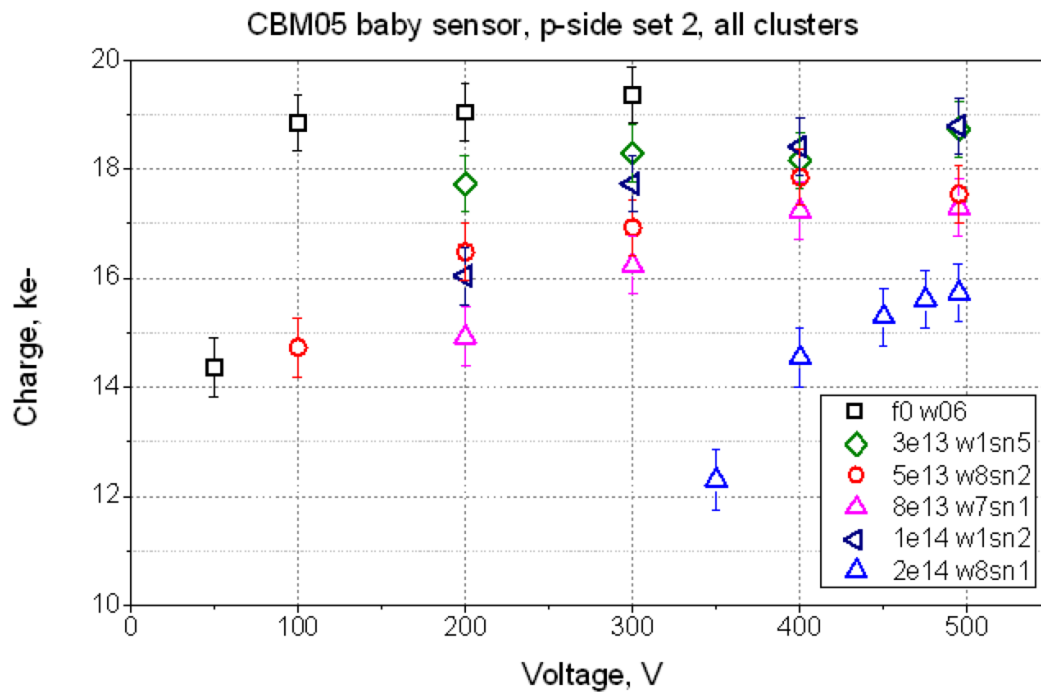


Figure 3.17: Charge collection results for the p -side of the sensors from the *set 2*.

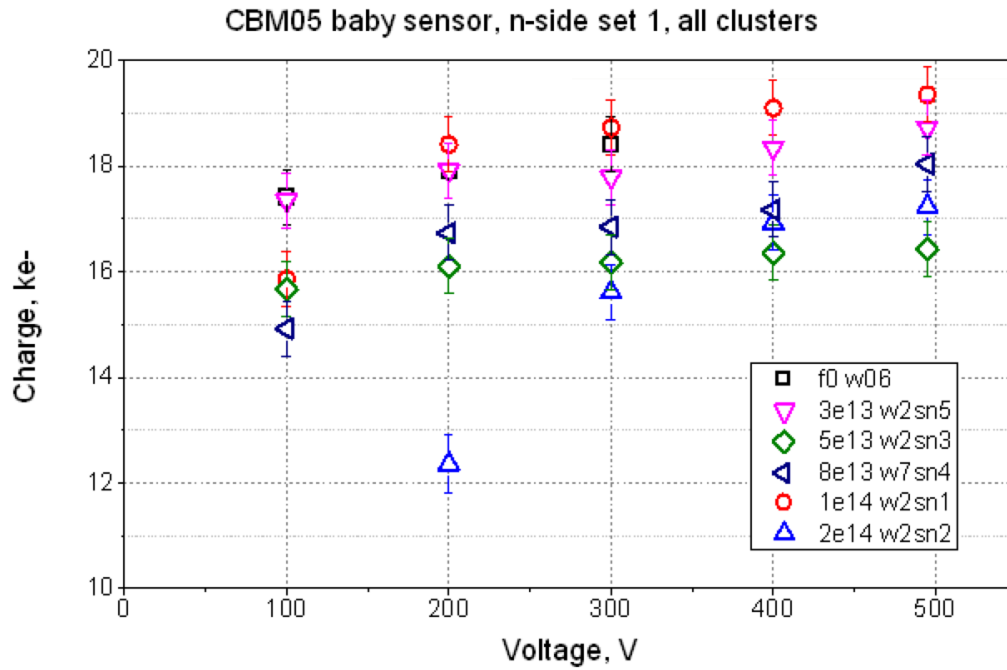


Figure 3.18: Charge collection results for the n -side of the sensors from the *set 1*.

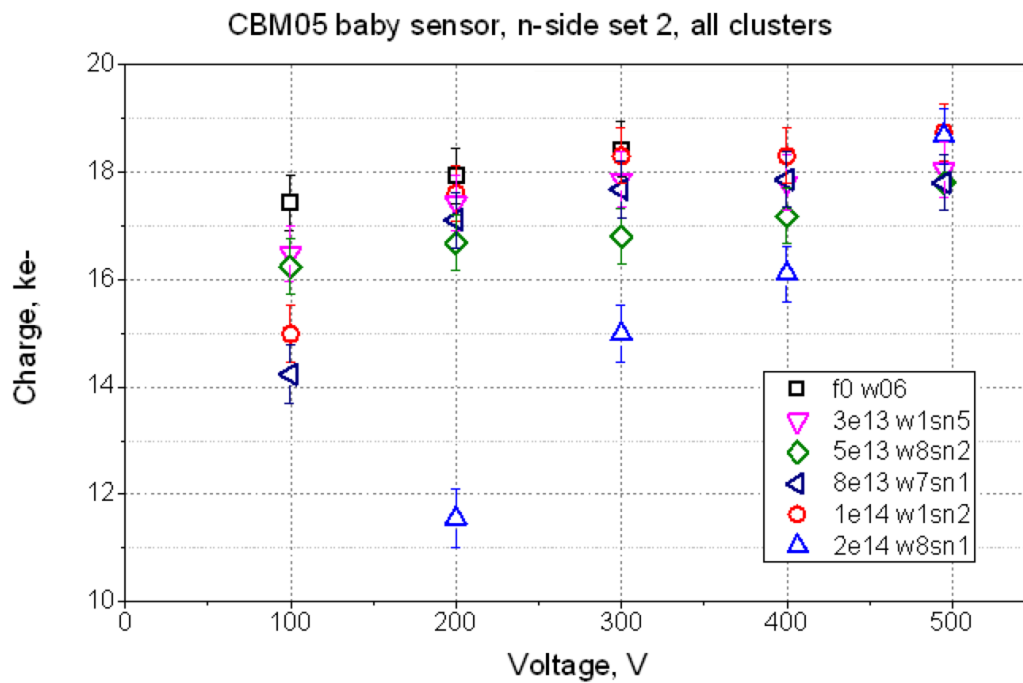


Figure 3.19: Charge collection results for the n -side of the sensors from the *set 2*.

of 350 V - 450 V. The maximum collected charge of approx. $16.5 ke^-$ at the highest applied voltage is observed for this sensor. In other words, the charge collection of the sensor that accumulated twice the STS lifetime fluence is approximately 15% less than that for a non-irradiated device. It is worth noting that the slope of the charge collection as a function of the bias voltage increases proportionally with the fluence.

The measurement results obtained for the sensors from the second set (Fig. 3.17) show somewhat similar charge collection performance to those from the first set. However, here the difference in collected charge at the highest bias voltage point is more pronounced than for the sensors from the first set, due to the values of the w8sn2 and w7sn1 sensors which saturate slightly lower than those for the w1sn2 and w1sn5 sensors. Here, the w1sn2 sensor ($\Phi = 1 \times 10^{14} \text{ n}_{eq}/\text{cm}^2$) exhibits high charge collection performance at the same level as the sensor irradiated to $3 \times 10^{13} \text{ n}_{eq}/\text{cm}^2$ in a 300 V - 495 V range.

Overall n -side readout trend

The measurement results obtained at the n -side of the sensors from the *set 1* demonstrate a diversity of different trends (Fig. 3.18). Here, the w2sn3 sensor exhibits almost no increase in collected charge over the whole bias voltage range and the worst performance at 495 V. Also, the maximum charge collection of this set is demonstrated by the w2sn1 sensor irradiated to $1 \times 10^{14} \text{ n}_{eq}/\text{cm}^2$. Other sensors demonstrated an increase of various slopes with increased bias. For the majority of the sensors including the sensor irradiated to $\Phi = 2 \times 10^{14} \text{ n}_{eq}/\text{cm}^2$, the most probable charge measured at 495 V is comparable to the one of the non-irradiated sensor within the error bars.

The n -side measurements of the sensors from the *set 2*, at 100 V demonstrated the most probable charge proportional to the accumulated fluence (Fig. 3.19). Further increase of the voltage exhibit an increasing trend of the most probable charge even for the sensors having their V_{fd} below 100 V, in particular, w1sn5 and w8sn2. The strongest increase in collected charge with increasing V_{bias} is observed for the sensor accumulated the maximum fluence, w2sn2. Also, no saturation of charge collection is observed for this sensor. Within this measurement set, the most probable charge at the maximum applied bias is comparable to that for the non-irradiated device, for each sensor.

3.4.4 Comparative analysis of charge collection for p - and n -side readout at various levels of irradiation

The measurement results of both the p - and the n -side readout sides of the sensors irradiated to $\Phi = 3 \times 10^{13} \text{ n}_{eq}/\text{cm}^2$ are depicted in the top of Fig. 3.20. The full

3.4 Measurements on miniature STS sensors

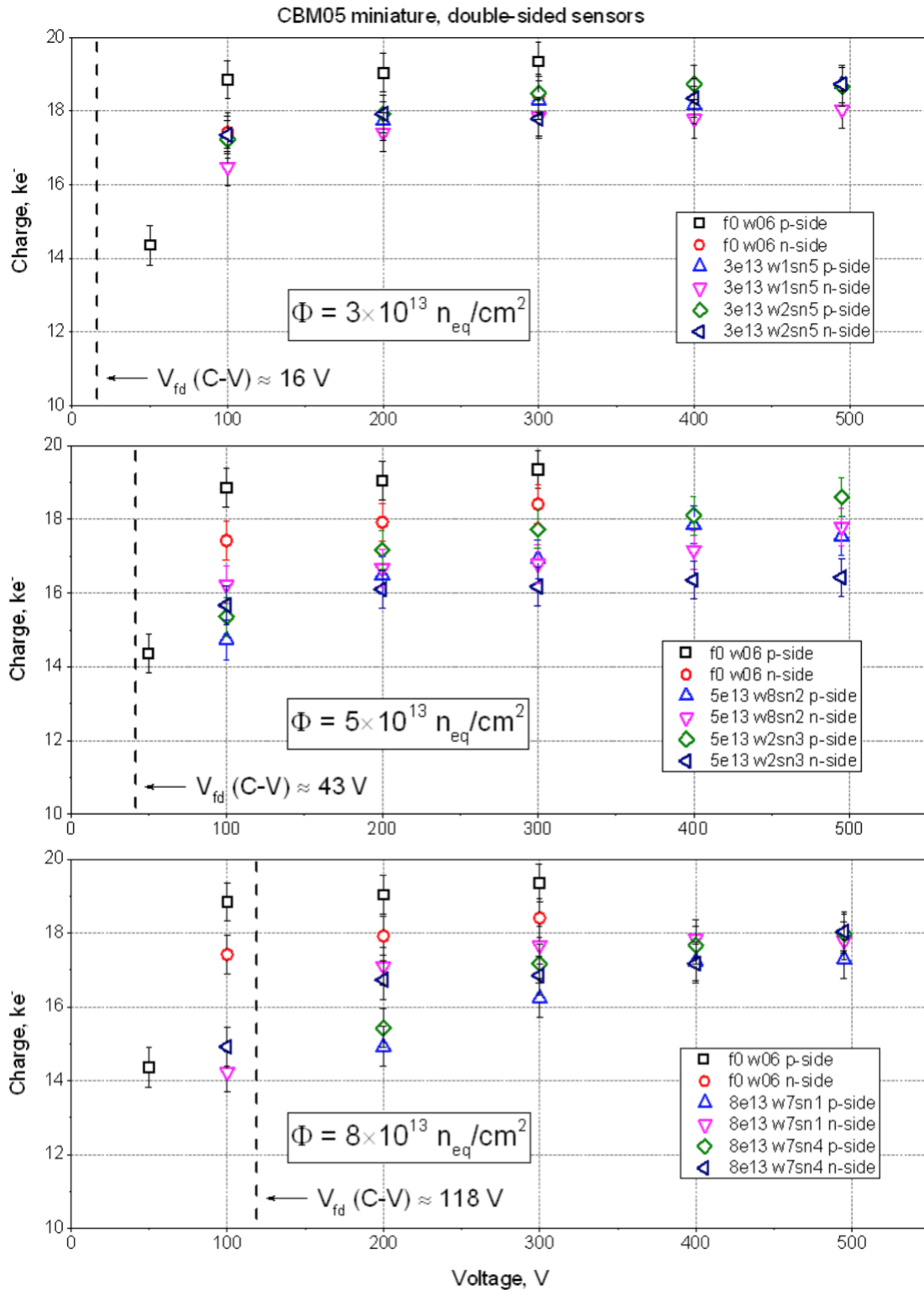


Figure 3.20: Charge collection results for the p - and n -sides of the sensors irradiated to $3 \times 10^{13} \text{ n}_{eq}/\text{cm}^2$ to $8 \times 10^{13} \text{ n}_{eq}/\text{cm}^2$.

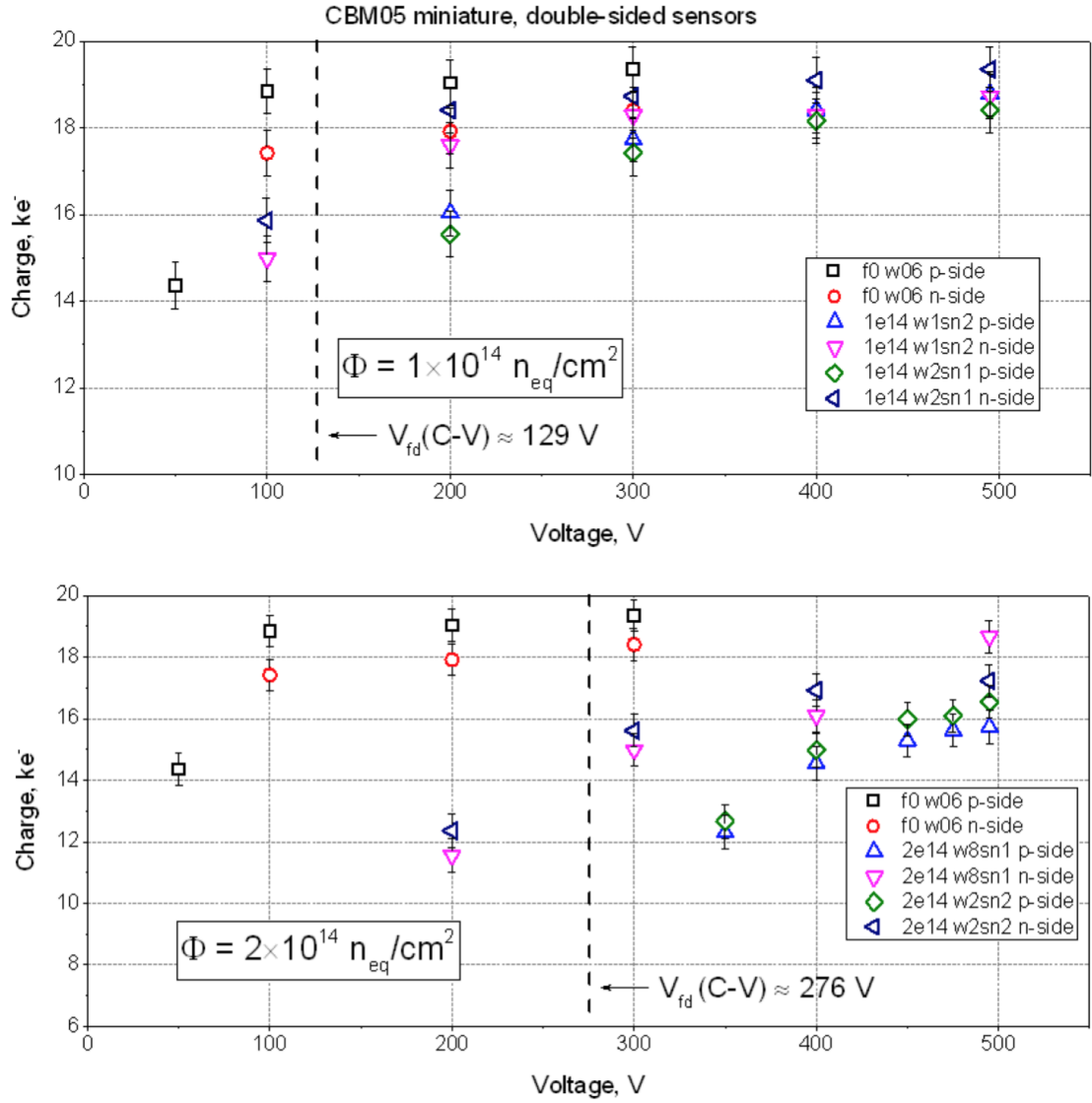


Figure 3.21: Charge collection results for the *p*- and *n*-sides of the sensors irradiated to $1 \times 10^{14} \text{ n}_{eq}/\text{cm}^2$ to $2 \times 10^{14} \text{ n}_{eq}/\text{cm}^2$.

depletion voltage for these sensors is approx. 16 V. It is notable that these sensors were operated at up to 495 V, which is more than 30 times higher than the depletion voltage. The performance of both sensors demonstrates comparable most probable charge values within the error bars over the whole bias voltage range. The data points exhibit a slow enhancement from 100 V to 300 V and a further saturation up to 495 V of applied bias. Also, noteworthy is that overdepletion is required for saturation of the charge collection for both p - and n -sides. Finally, operation of sensors irradiated to 3×10^{13} n_{eq}/cm^2 already at 300 V provides full charge collection efficiency¹².

The measurement results for the sensors irradiated to 5×10^{13} n_{eq}/cm^2 are presented in the center of Fig. 3.20. For the w8sn2 sensor, the signal obtained at both readout sides is equal within the error bars. The behaviour of the w2sn3 sensor is different. At low voltages the most probable charge measured at both sides is comparable within the error bars. However, in the range of 300 V - 495 V a significant, increasing difference is observed. A closer view showed that for this particular sensor the guard rings were not produced at its n -side. The results demonstrate that more than a 200 V overdepletion is required for high charge collection performance at this fluence.

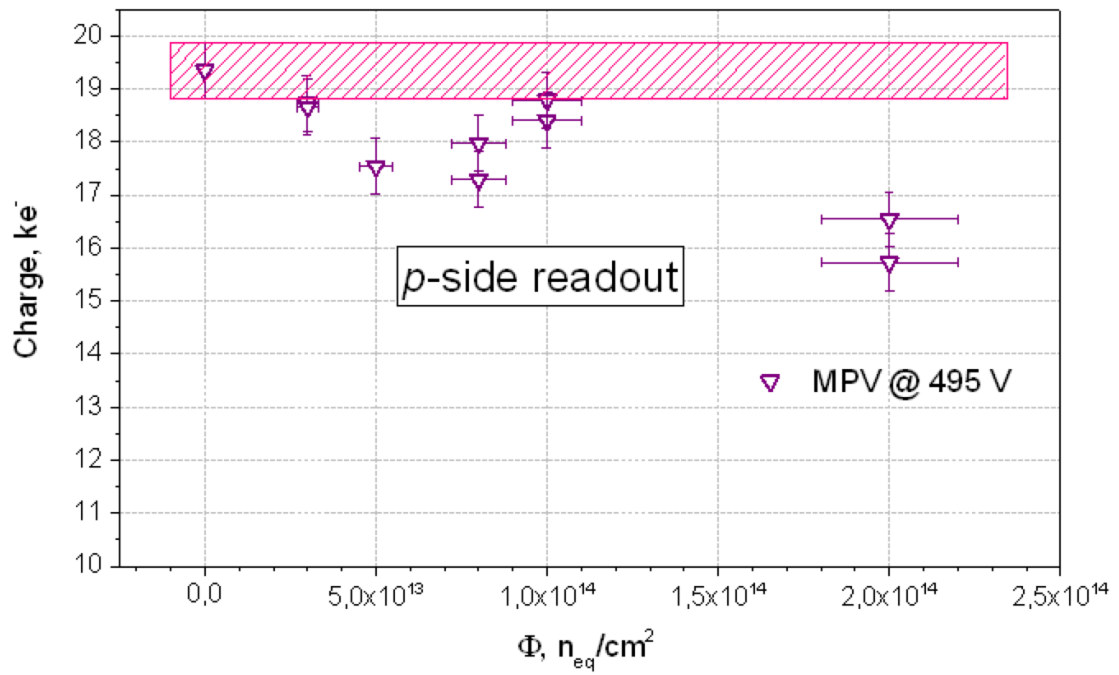
Both the w7sn1 and the w7sn4 sensors, irradiated to 8×10^{13} n_{eq}/cm^2 , demonstrate a dominant charge collection at their n -side at lower bias voltages (up to 300 V). With further increase of the bias, the values become comparable within the error bars for the p - and the n -side readout (bottom of Fig. 3.20). Here, more than 250 V of overdepletion is needed for full charge collection efficiency for the n -side readout. For the p -side strips, a 5% charge collection loss w.r.t. to the non-irradiated sensor is present even at 495 V.

For both the w1sn2 and the w2sn1 sensors of a 1×10^{14} n_{eq}/cm^2 fluence¹³, the most probable charge at their n -sides dominates at low bias voltages (100 V to 300 V). With further increase of the voltage, the most probable charge at both readout sides becomes comparable within the error bars (Fig. 3.21), top. Already at 400 V, the full charge collection is obtained at both readout sides. However, more than a 200 V overdepletion is required for that.

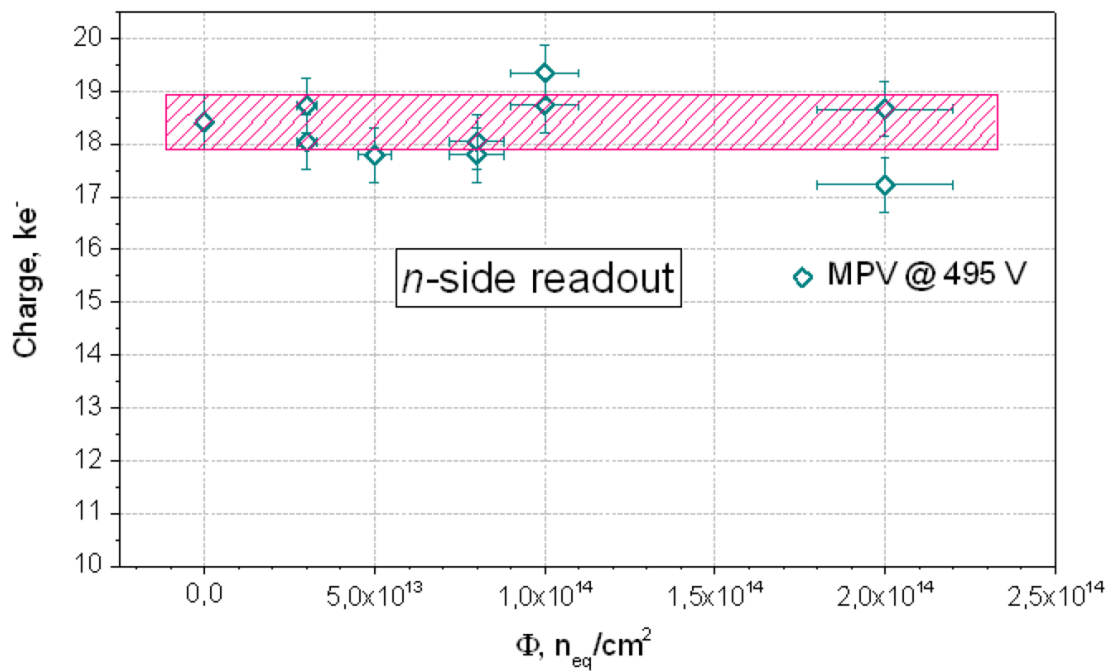
For the w8sn1 and the w2sn2 sensors, which accumulated the highest fluence, the charge collected at the n -side dominates over the whole bias voltage range, most significantly below 400 V. Also, sensors from both wafers show similar levels of charge collection at both p - and n - readout sides. For the n -side reading of the w8sn1 sensor at 495 V, the full charge collection is obtained. Other readings obtained at the highest bias voltage demonstrate approximately a 8% - 16% loss in

¹²As a ratio of the collected charge after and before irradiation, $CCE = \frac{Q_{irr}}{Q_0}$.

¹³Defines the lifetime fluence.



(a)



(b)

Figure 3.22: Most probable charge as a function of the fluence for the p^+ (a) and the n^+ (b) readout sides, measured at 495 V of applied bias voltage.

charge collection. In this case, the highest possible bias voltage should be applied to achieve the highest charge collection.

3.4.5 Charge collection as a function of the fluence

In order to observe the charge collection tendency as a function of the fluence, the results obtained at both readout sides at the maximum applied bias of 495 V, are presented in Fig. 3.22. Here, for the p -side the explicit decreasing trend of the most probable charge is observed with an outstanding point of $\Phi = 1 \times 10^{14} \text{ n}_{eq}/\text{cm}^2$. In particular, at this point the MPV demonstrate a higher value than expected from the overall trend.

The charge collection obtained at the n -side shows less degradation as a function of the fluence w.r.t. to the p -side. Up to $\Phi = 1 \times 10^{14} \text{ n}_{eq}/\text{cm}^2$, the most probable signal amplitude is comparable to that of the non-irradiated sensor within the uncertainties. Also, the data points obtained at this fluence show higher values than those corresponding to the lower fluences. At the highest fluence, the most probable charge of one sensor is comparable to the MPV for the non-irradiated sensor, and in case of the second sensor it is approx. 6% lower.

3.5 Measurements on miniature STS sensors: annealing studies

Irradiated silicon sensors demonstrate a change in their characteristics as a function of time due to annealing of radiation induced defects. Here, depending on the temperature and elapsed time, these changes may have either a beneficial or an undesired effect on the sensor performance (Section 2.4).

According to the CBM running scenario, the experiment will be operated for approximately 2 months per year. During the maintenance period until the next operational year, the detectors will be evaluated and maintained. As the nominal operational temperature of the STS is $-5 \text{ }^\circ\text{C}$, during the maintenance period the sensors will be exposed to room temperatures for a certain period.

In this section, the changes in characteristics of the STS sensors irradiated with reactor neutrons are studied as a function of annealing time at various temperatures. The maintenance period conditions for the sensors exposed to various equivalent fluences are suggested (in the discussion section).

3.5.1 Sensors involved in the annealing studies

Annealing studies were carried out on four STS miniature sensors¹⁴ irradiated with reactor neutrons. After irradiation, the sensors were transported to GSI in a sealed box filled with dry ice, featuring a temperature and humidity monitoring system, in order to suppress annealing effects during the transportation. The temperature history of the shipment exhibited a negative temperature inside the package during the whole transportation time, starting from -37 °C and ending up with -1 °C at arrival. After the arrival the sensors were stored in a freezer at -27 °C. The leakage current, measured after the arrival, demonstrated a linear dependence on the fluence. The full depletion voltage values were extracted from

Table 3.3: Sensors involved in annealing study.

Sensor name	Fluence Φ , n_{eq}/cm^2	Annealing temperature T_a , °C
w6sn2	1×10^{14}	80
w12sn2	5×10^{13}	80
w25	1×10^{13}	80
w6sn1	1×10^{14}	25

the C-V measurements. The measured values were in agreement with the Hamburg model calculation (Fig. 3.15). Table 3.3 shows the naming of the sensors under study, their corresponding fluences and the temperatures selected for annealing.

3.5.2 Annealing procedures

The setup used for annealing studies is described in Section 3.3.3. A group of three sensors (w6sn2, w12sn2 and w25) experienced an exposure at 80 °C in order to accelerate the effect of annealing of the radiation induced defects and to study the effects of annealing on a long-term scale¹⁵. An oven with an air-circulating system was used for storage of the objects in order to provide high temperature stability (Fig. 3.10). Each step lasted for 13 minutes including the temperature ramping, considering 11 minutes of real annealing time at 80 °C, confirmed by the direct measurement of the sensor surface (Fig. 3.9b). After each exposure, measurements of the full depletion voltage V_{fd} were performed for all sensors, the charge collection measurements were performed for the w6sn2 and w12sn2 sensors, measurements of the leakage current were performed for all sensors with various steps.

The w6sn1 sensor was kept at room temperature (approx. 25 °C) in a light-tight box for 61 days. Measurements of the leakage current and the depletion

¹⁴The general properties of the sensors are listed in the *batch B* section of Table 3.1.

¹⁵One minute of annealing at 80 °C is equivalent to approx. 5.14 days at 20 °C [37].

voltage were performed with a 3 to 5 day step until the 48th day. The next and the last measurement was performed on the 61st day.

All the measurements were performed at -5 °C using the setup described in Section 3.3. In order to avoid a high contrast temperature stress, the sensors were kept at room temperature for approximately 5 minutes after releasing from the oven. Also, inside the refrigerator the sensors were kept for at least 5 minutes for temperature and humidity stabilization.

3.5.3 Annealing of the leakage current

After the initial increase under irradiation, the leakage current is expected to exhibit a continuously decreasing tendency¹⁶ as a function of time (see Fig. 2.6).

The leakage current of irradiated STS sensors was monitored during an 80 °C and a 25 °C temperature storage at various steps, measured at -5 °C. Figure 3.23 shows the leakage current measured at various steps as a function of elapsed time in minutes for the sensors exposed to 80 °C and in days for the sensor kept at 25 °C. As expected, the measured data shows a graduate decrease over the whole annealing range in both cases.

Figure 3.24 shows the leakage current density¹⁷, measured after 11 minutes of annealing at 80 °C as a function of accumulated fluence. Here, the I_{leak} values, measured at -5 °C, were scaled to 20 °C using the Equation 3.2. The current related damage rate extracted from the fit of the experimental data equals to: $\alpha(11 \text{ min}, 80 \text{ °C}) = (5.32 \pm 0.05) \times 10^{-17} \text{ A/cm}$.

3.5.4 Annealing of effective impurity concentration

The absolute effective impurity concentration was monitored as a function of time by measuring the full depletion voltage values. The measurement results were compared to the Hamburg model parametrization.

Accelerated annealing at 80 °C

Figure 3.25 summarizes the time evolution of the full depletion voltage for the w25, w12sn2 and w6sn2 sensors exposed to $1 \times 10^{13} \text{ n}_{eq}/\text{cm}^2$, $5 \times 10^{13} \text{ n}_{eq}/\text{cm}^2$ and $1 \times 10^{14} \text{ n}_{eq}/\text{cm}^2$ fluences, respectively.

Here, for the w25 sensor which did not experience the type-inversion (Fig. 3.15), the depletion voltage demonstrates almost non-noticeable increase after the first 11

¹⁶A saturation tendency was observed after storing the detectors at high temperatures (e.g., 106 °C) on long time scales (> 2 months) [37].

¹⁷Calculated as the difference of the leakage current after and before irradiation per unit of volume.

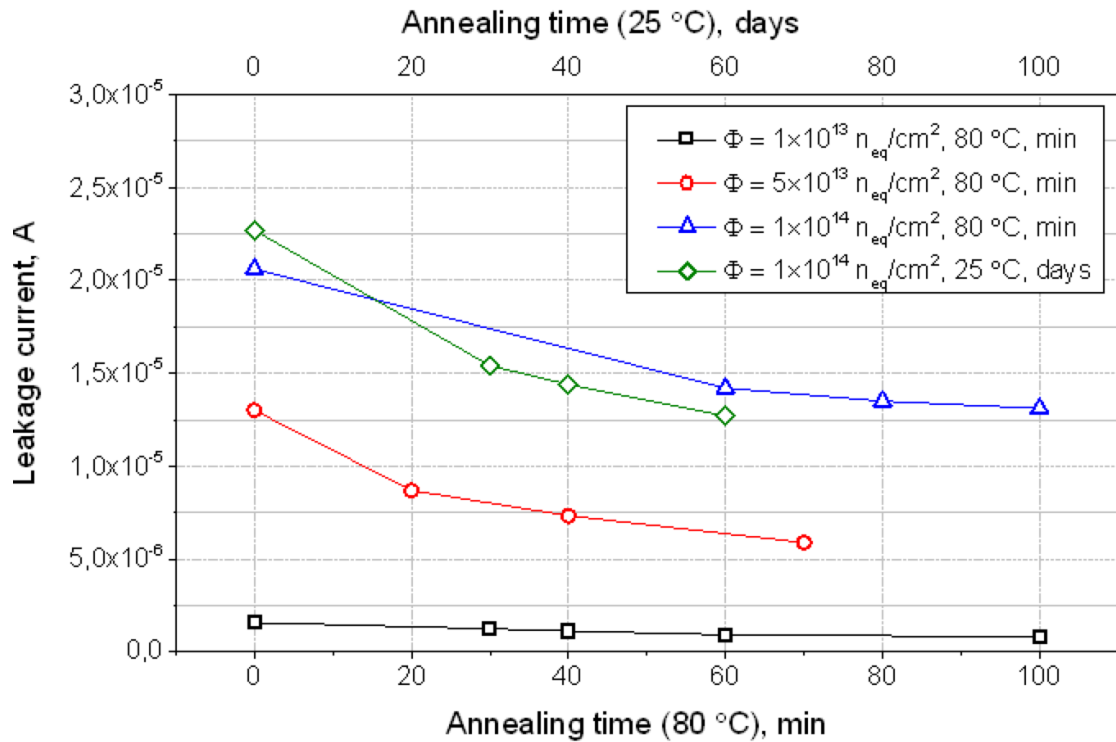


Figure 3.23: Leakage current of the STS sensors as a function of time at 80 °C and 25 °C after neutron irradiation.

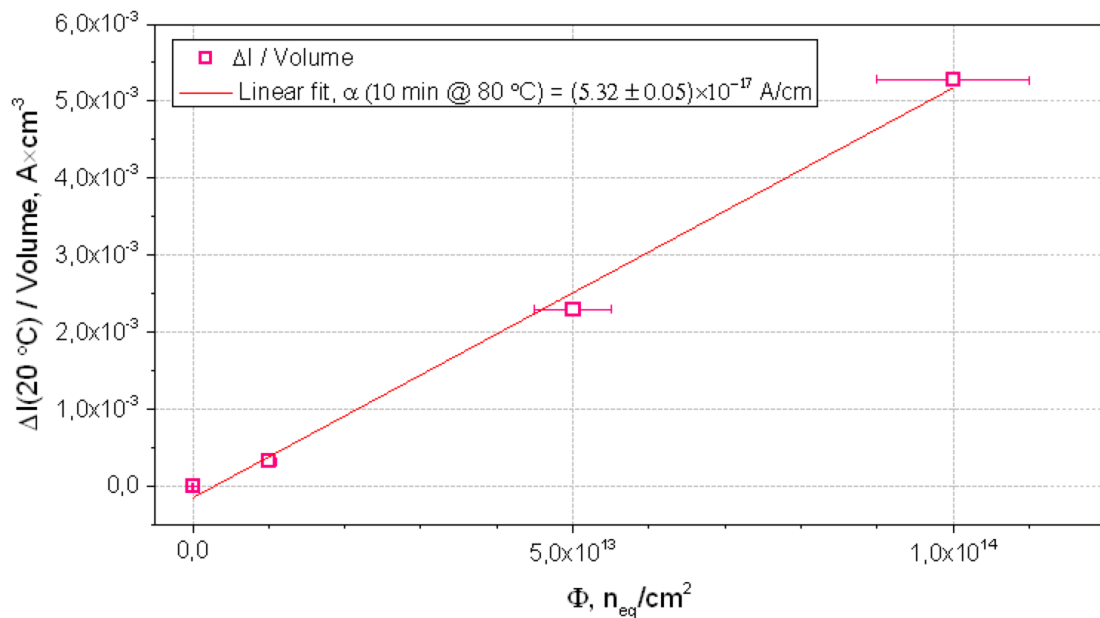


Figure 3.24: Leakage current density plotted after 11 minutes of annealing at 80 °C. The current damage rate value is extracted from the fit.

minutes of exposure, and further continuous decrease with a long time constant. The accelerated annealing at 80 °C performed for 143 minutes is equivalent to approximately 735 days in terms of 20 °C exposure.

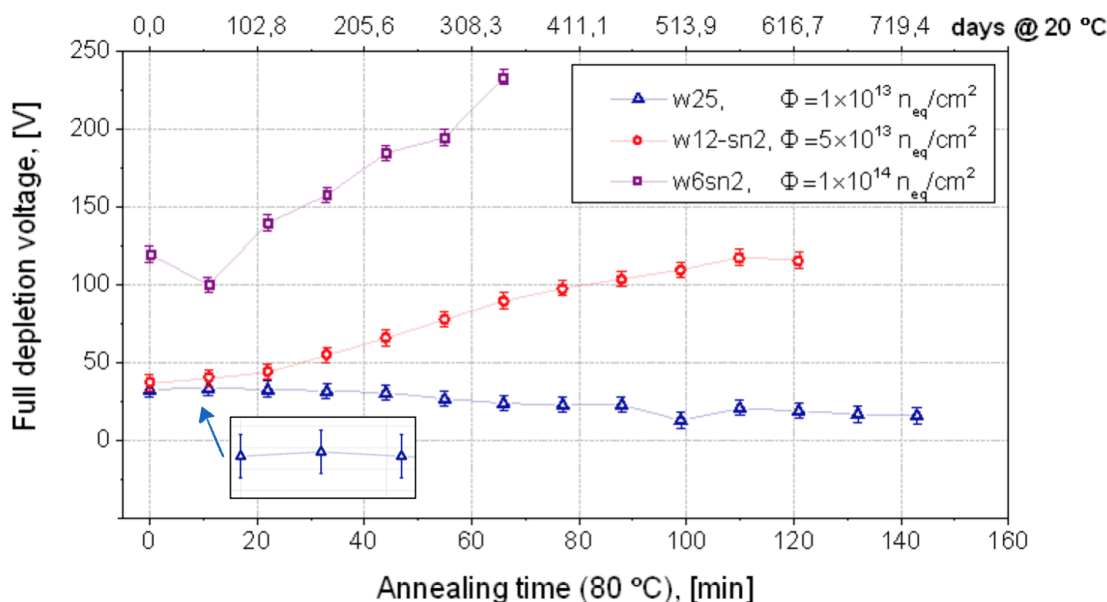


Figure 3.25: Full depletion voltage of the STS sensors as a function of time at 80 °C. The upper X scale shows the equivalent time in days if stored at 20 °C.

The w12sn2 sensor exhibits a continuous increase of the V_{fd} over the whole measurement range. This sensor underwent a type-inversion at approximately $2.2 \times 10^{13} \text{ n}_{eq}/\text{cm}^2$ fluence.

The w6sn2 sensor, having its V_{fd} of approximately 120 V after accumulating $\Phi = 1 \times 10^{14} \text{ n}_{eq}/\text{cm}^2$, demonstrated a decrease of the depletion voltage down to about 100 V after the first 11 minutes of annealing. With further temperature exposure, a fast enhancement of the depletion voltage is observed for this sensor. It rises up from 100 V to almost 250 V after 55 minutes of further annealing.

The full depletion voltage behaviour of the w25 and w12sn2 sensors confirm the location of the type-inversion point between $1 \times 10^{13} \text{ n}_{eq}/\text{cm}^2$ and $5 \times 10^{13} \text{ n}_{eq}/\text{cm}^2$: the same annealing process leads to the opposite change in the effective impurity concentration. This is true only if the sensors have opposite signs of the space charge.

25 °C annealing

The w6sn1 sensor, irradiated to $1 \times 10^{14} \text{ n}_{eq}/\text{cm}^2$, was kept at room temperature in order to determine the annealing behaviour at conditions close to that during the maintenance period of the experiment. Data were taken with a step of 3 to

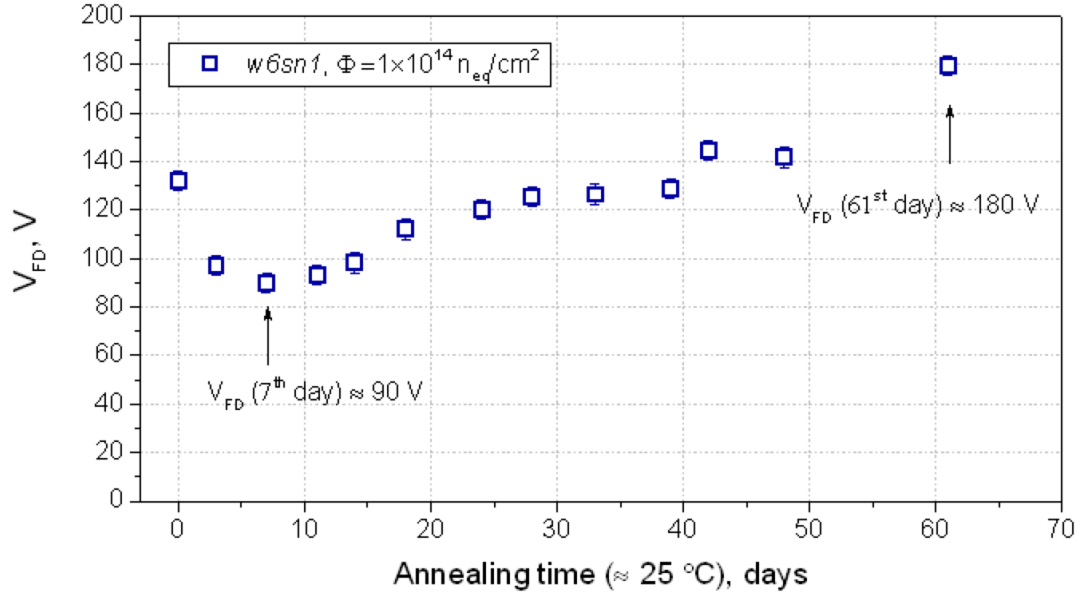


Figure 3.26: Full depletion voltage of the STS sensor as a function of time at 25 °C.

5 days during the first 48 days, and an additional data point was taken on the 61st day. The temperature was measured several times during the procedure, exhibiting variations from approximately 23 °C to 26 °C.

Figure 3.26 exhibits the measured full depletion voltage V_{fd} as a function of time. Here, both the short-term “beneficial” and the long-term “reverse” annealing phases are clearly observed. During the first 7 days of exposure, a decline of the V_{fd} is observed with a high magnitude and a short time constant. Starting from the 11th day and until the end of the measurement range, the depletion voltage exhibits a continuous growth with a long time constant. Here, an increase of the V_{fd} between the minimum and the last measured point equals to approximately 90 V. Wherein, the minimum V_{fd} value obtained on the 7th day of the procedure equals to 90 V. Thus, for a sensor irradiated to $1 \times 10^{14} \text{ n}_{eq}/\text{cm}^2$ fluence, 54 days of reverse annealing at 25 °C increases the full depletion voltage by 100%.

3.5.5 Parametrization of annealing data for effective impurity concentration

Using the experimental values of V_{fd} and the initial values of the full depletion voltage, the change in absolute effective impurity concentration was calculated as $\Delta N_{eff}(\Phi_{eq}, t(T_a)) = N_{eff,0} - N_{eff}(\Phi_{eq}, t(T_a))$ (see Section 2.4). In order to compare the experimental data with model expectations, a parametrization of the change in space charge density was performed using the Hamburg model. The model parameters for the calculation of the stable damage, short-term and long-

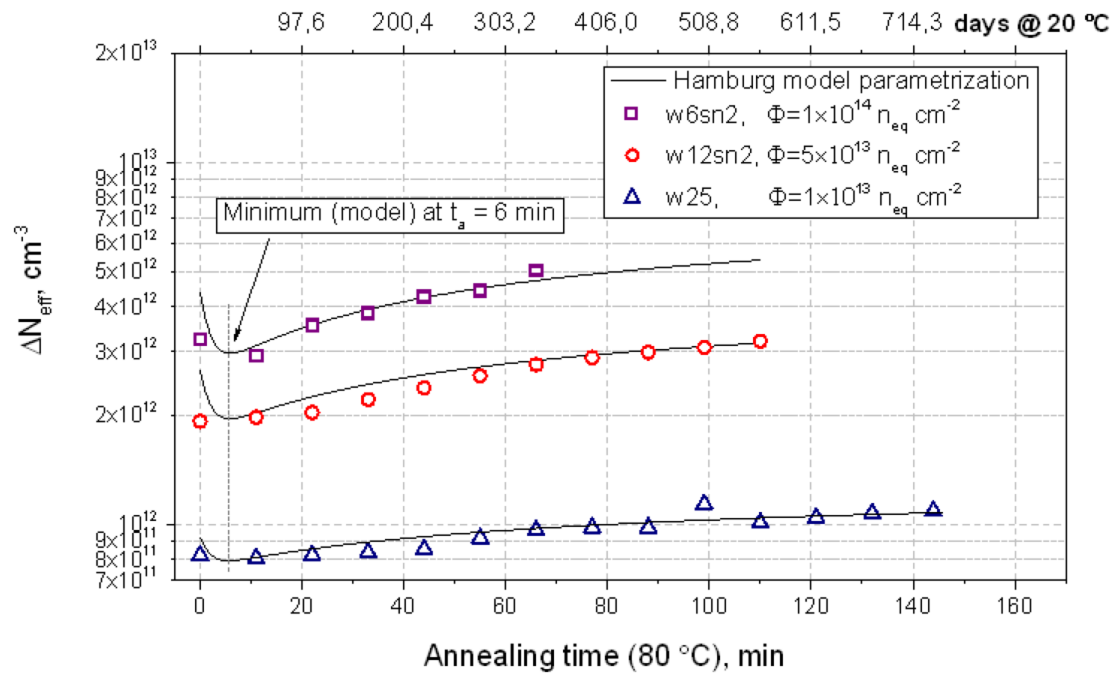


Figure 3.27: Change in effective impurity concentration for the STS sensors as a function of time at 80 °C. The lines represent the Hamburg model parametrization.

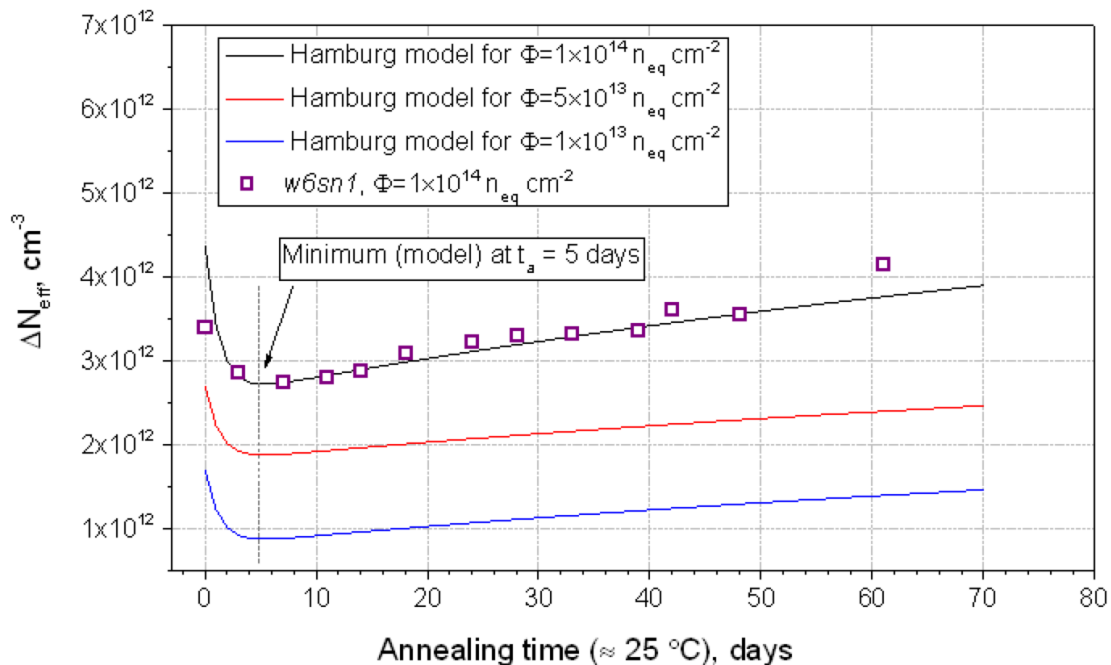


Figure 3.28: Change in effective impurity concentration for the STS sensors as a function of time at 25 °C. The lines represent the Hamburg model parametrization.

term annealing components were selected according to the average initial space charge density of the CBM sensors selected for the study: $N_{eff,0} \approx 1.34 \times 10^{12} \text{ cm}^{-3}$. The equations for calculation of the ΔN_{eff} evolution, used in the Hamburg model, are listed in Section 2.4.

Parametrization of annealing results at 80 °C

Figure 3.27 demonstrates the change in absolute effective impurity concentration ΔN_{eff} as a function of time at 80 °C. The experimental points for the ΔN_{eff} were calculated using the measured V_{fd} values before irradiation and after each annealing step. Here, as the ΔN_{eff} is in absolute values, it will exhibit an increase during the long-term period even for the w25 sensor, which demonstrated a decreasing behaviour for the full depletion voltage during this period.

The Hamburg model calculation describes well the trend of the experimental data. However, the decrease of the ΔN_{eff} during the short-term annealing for the w6sn2 and w25 sensors is lower for the experimental data compared to the model. For the w12sn2 sensor, no short-term annealing is observed. The reverse annealing data is described very well. According to the model, the dependence reaches its minimum¹⁸ at $t_a = 6$ min while the minimum in case of the experimental points is located at $t_a = 11$ min.

Parametrization of annealing results at room temperature (25 °C)

The experimental data for 25 °C was parametrized using the Hamburg model in similar way like presented in the previous paragraph, but using the model parameters for the corresponding temperature. The parameter values are listed in Appendix D. The parameters for the short- and long-term annealing were obtained from the fits of the corresponding Arrhenius plots¹⁹.

Figure 3.28 shows the resulting experimental points for the ΔN_{eff} and the model calculation performed for various fluences. The experimental data agree with the model prediction. Here, the expected decrease of the ΔN_{eff} during the short-term annealing is higher than that observed experimentally. The minimum of the ΔN_{eff} , (and, therefore, the minimum of the full depletion voltage) is expected by the model after 5 days of storage at 25 °C. However, it is notable that the difference between the values corresponding to the 5th and the 7th days is less than 1%.

¹⁸Which is the point when the V_{fd} reaches its minimum for type inverted sensors and its maximum for the ones with positive space charge.

¹⁹The fits were performed by M. Moll [37].

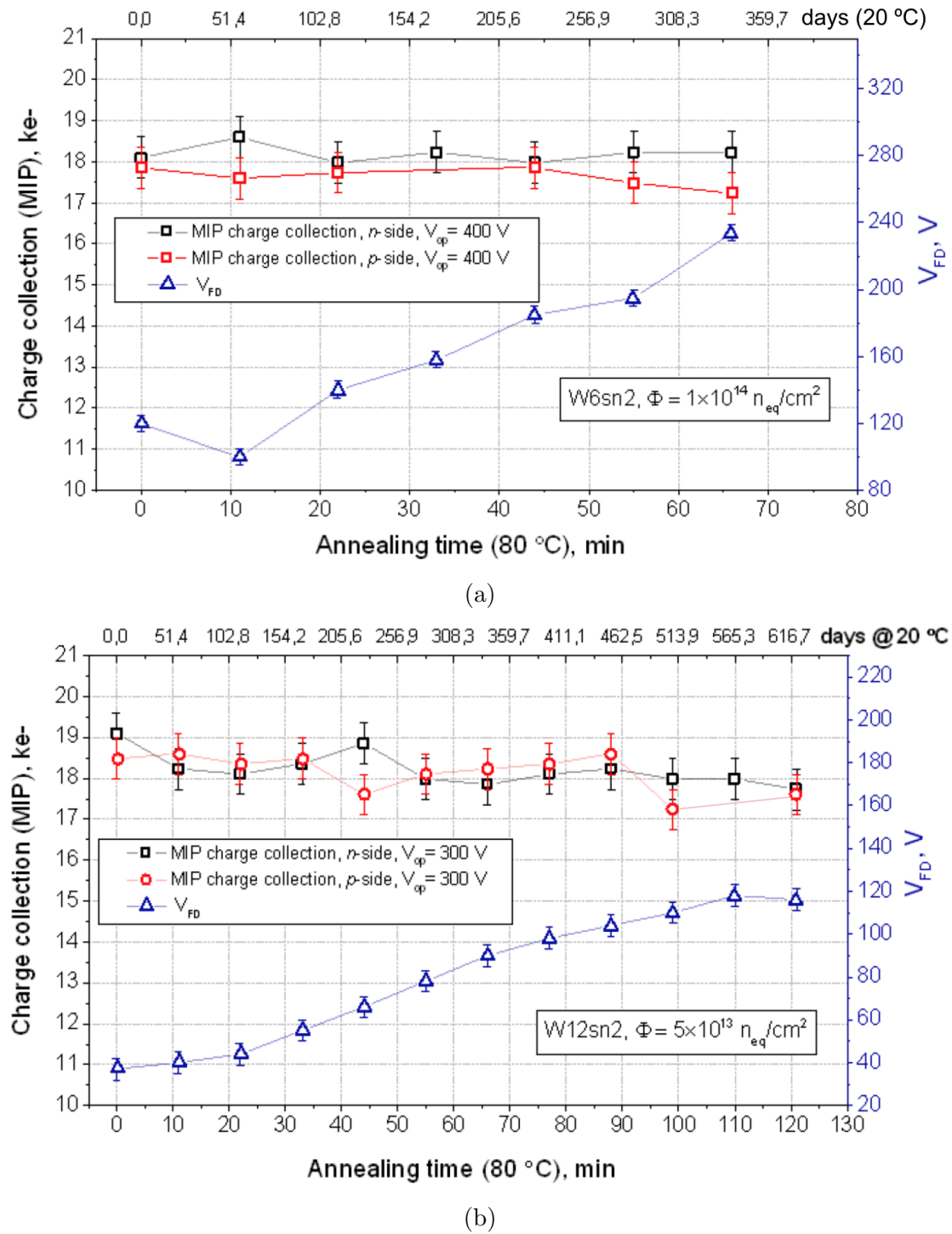


Figure 3.29: Measured most probable charge for the w6sn2 (a) and w12sn2 (b) sensors as a function of time at 80 °C.

3.5.6 Charge collection as a function of annealing time

Measurements of the most probable charge as a function of time at 80 °C were performed for the w6sn2 and w12sn2 sensors, in order to monitor the change in the charge collection during annealing. For this, the setup described in Section 3.3.2 was used. The operational voltages chosen for these measurements were far beyond the depletion voltages extracted from the C-V measurement²⁰. For a more convenient representation, the results are plotted together with the corresponding V_{fd} values.

The measurement results are presented in Fig. 3.29. As mentioned above, both sensors underwent the space charge sign inversion. Here, for the n -side of the w6sn2 sensor the collected charge increases by approx. 3% after the first annealing step ($t_a = 11$ min.) with further return to lower value and remains stable within the error bars until the end of the measurement range. For the p -side of this sensor, the most probable charge shows a slow decline with a long time constant.

Figure 3.29b shows the time evolution of the most probable charge acquired for the w12sn2 sensor. Here, the observed overall trend shows a slow reduction of the MPV at both readout sides. However, certain deviations from the overall trend are noticeable (e.g., at 44 min. and 99 min. points).

For both plots, the upper X axes show the corresponding time in days for an equivalent annealing time at 20 °C. Thus, the charge collection is not expected to be decreased significantly during long time periods if the sensors will be stored at 20 °C. On the other hand, no improvement of such treatment is observed.

3.6 Measurements on prototype sensors

During the R&D and prototyping phases, several generations of prototype sensors were produced by two vendors, CiS and Hamamatsu (or HPK). In order to study the characteristics of prototype sensors after irradiation, four prototype sensors, produced by both vendors, were exposed to a 23 MeV proton fluence of 2×10^{14} n_{eq}/cm^2 , which is twice the maximum fluence expected for the sensors located in the innermost areas of the STS stations. Moreover, the sensors under test were produced with two different strip interconnection schemes (Fig. 1.10). First, so-called “double-metal”, provides the interconnection of the corner strips via an additional metal layer produced during the sensor fabrication. The second scheme uses an external microcable attached to a sensor via the TAB bonding.

The sensors were characterized after irradiation in terms of their main characteristics. In this section, the results of this study are presented.

²⁰ $V_{op} = 400$ V for the w6sn2 sensor and $V_{op} = 300$ V for the w12sn2 sensor.

3.6.1 Sensors selected for irradiation

The selected sensors produced by CiS were of $6.2 \times 6.2 \text{ cm}^2$ size while those produced by Hamamatsu had a size of $6.2 \times 4.2 \text{ cm}^2$. At the moment when the irradiation was performed the sensors of $6.2 \times 6.2 \text{ cm}^2$ had not been produced by Hamamatsu yet. The external microcables were produced by LTU in Kharkiv, Ukraine and TAB bonded in GSI. The sensors had different values of the full depletion voltage V_{fd} and the leakage current I_{leak} before irradiation due to differences in fabrication technologies and also in size (Table 3.1). Thicknesses of the sensors were measured using the TESA GIGICO1 precision device [69]. The measured thickness of the sensors produced by Hamamatsu is approx. $330 \pm 3 \text{ }\mu\text{m}$ while for CiS sensors it is approx. $290 \pm 3 \text{ }\mu\text{m}$.

3.6.2 Results after irradiation

Leakage current density

Measurements of the leakage current were performed at $-5 \text{ }^\circ\text{C}$ using the setup described in Section 3.3.2. As all the sensors were irradiated to a single fluence, the linear dependence of the leakage current density is not available. Instead, using the measured leakage currents before and after irradiation the leakage current density was calculated and plotted as a function of the reverse bias voltage.

In an ideal case, if the sensors did receive identical fluence, the curves would have been identical within the error bars. However, the observed behaviour of the curves demonstrated that the CBM05C6-DM, CBM05H4-SMwC and CBM06C6-SMwC sensors exhibit comparable values of the leakage current density over the whole voltage range. The CBM05H4-DM sensor does not follow the path of the previous sensors, showing a stronger enhancement of the data points and, therefore, disagreement with the rest of the sensors (Fig. 3.30). As the leakage current undergoes an approximately 3 orders of magnitude increase after receiving a fluence of $2 \times 10^{14} \text{ n}_{eq}/\text{cm}^2$, the leakage current measured after irradiation mostly determines the leakage current density. Thus, to exclude the measurement error possibility for the I-V curve of the CBM05H4-DM sensor, it was measured several times after irradiation. Figure 3.31 illustrates the variety of the measured I-V curves for this sensor demonstrating a good agreement and reproducibility of the measured data. Thus, the observed difference in the leakage current density for the CBM05H4-DM sensor may issue from a higher amount of the integrated fluence. Another explanation of such a different behaviour could be a mechanical stress caused due to the PCB mounting. It is well known that mechanical stress leads to an increase of the leakage current.

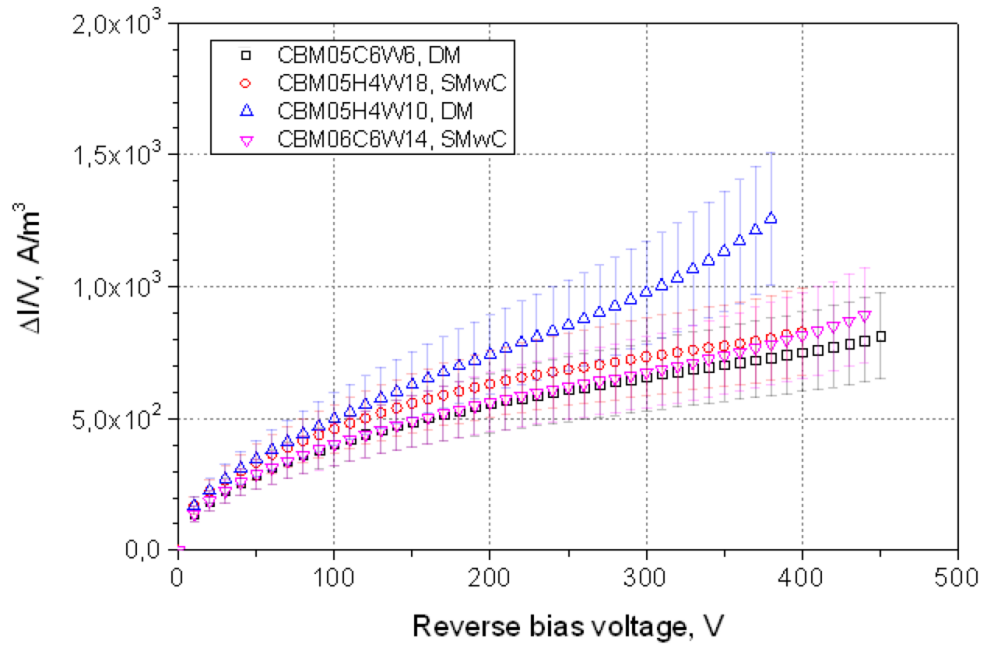


Figure 3.30: Leakage current densities as a function of the reverse bias voltage for proton irradiated STS prototype sensors.

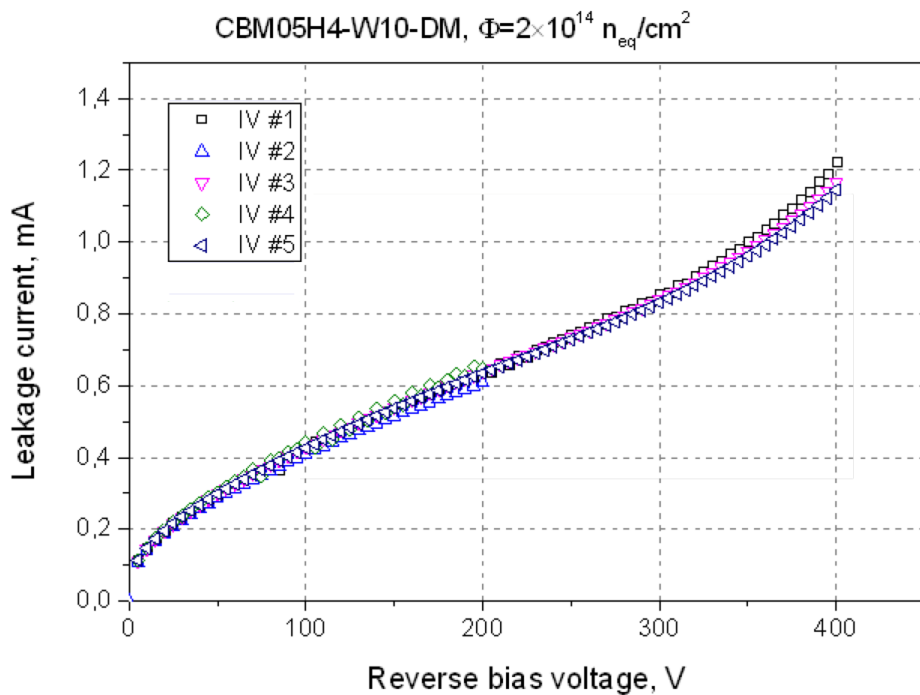


Figure 3.31: I-V measurement reproducibility for the CBM05H4-DM sensor after irradiation.

Full depletion voltage

As described in Section 3.3.1, the depletion voltage measurement of irradiated sensors at $-5\text{ }^\circ\text{C}$ has to be performed at test frequencies of $\approx 950\text{ Hz}$. The C-V curves at a given frequency were obtained, but the analysis of the $1/C^2$ curve did not show a typical behaviour up to 400 V of the applied bias. The measurement was distorted by a high leakage current²¹. Therefore, the depletion voltage values were not extracted from the C-V measurement. The V_{fd} values for each sensor were estimated using the Hamburg model²² (Fig. 3.32). The initial effective impurity concentration that is required for the model calculation was calculated from the measured initial V_{fd} values. The following model parameters were used

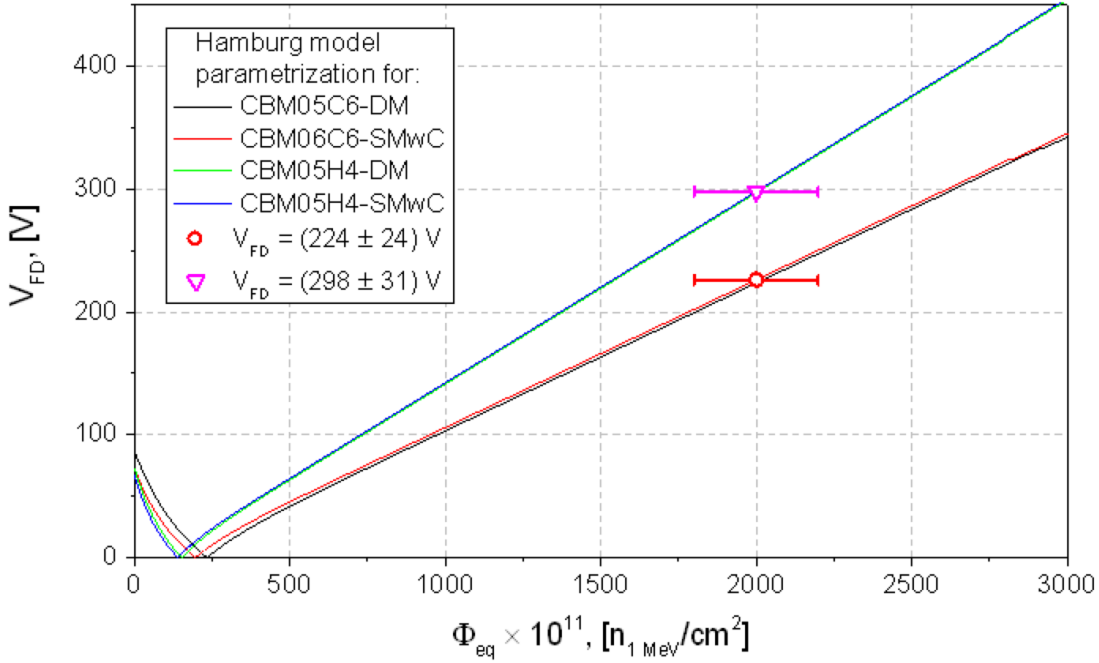


Figure 3.32: Evolutions of the full depletion voltage as a function of the fluence, calculated according to the initial properties ($N_{eff,0}$, $V_{fd,0}$) of the investigated sensors. The V_{fd} values at $\Phi = 2 \times 10^{14}\text{ n}_{eq}/\text{cm}^2$ are given in the legend considering the fluence error of approx. 20%.

in the calculation: the donor removal rate c was calculated for each sensor individually from $N_{eff,0} \times c = (10.9 \pm 0.8) \times 10^{-2}\text{ cm}^{-1}$ [67], the introduction rate of acceptors $g_c = 1.9 \times 10^{-2}\text{ cm}^{-1}$. The initial effective impurity concentration was calculated for Hamamatsu sensors with a $330\text{ }\mu\text{m}$ thickness and for CiS sensors with a $290\text{ }\mu\text{m}$ thickness. The V_{fd} values estimated with the Hamburg model at

²¹Of the order of 1 mA measured at $-5\text{ }^\circ\text{C}$.

²²Calculation was performed considering the stable damage term.

$\Phi = 2 \times 10^{14} \text{ n}_{eq}/\text{cm}^2$ equal to (298 ± 31) V for Hamamatsu sensors and (224 ± 24) V for CiS sensors.

From Fig. 3.32 one can notice that due to the lower initial V_{fd} values and higher thickness, the Hamamatsu sensors are expected to undergo the space charge sign inversion at lower levels of irradiation than those fabricated by CiS. Also, the HPK sensors are expected to experience a faster growth of the V_{fd} after the type inversion. Such a difference arises from the difference in thicknesses and lower values of the initial effective impurity concentration for the Hamamatsu devices.

Charge collection performance of prototype sensors

For an evaluation of the charge collection performance, the sensors were tested with a ^{90}Sr source using the setup described in the Section 3.3.2. The measurements were performed at -8°C . The obtained signal amplitude histograms were fitted with the Landau-Gaussian convolution, where the most probable values that define the *charge collection*, were extracted. The measurements were performed at 470 V of applied bias voltage which is more than 100 V higher than the V_{fd} values estimated in the previous paragraph. The charge collection results presented in this section correspond to the full-length strips located in the middle of the sensor.

Figure 3.33 demonstrates the measurement results of the most probable charge for both p^+ and n^+ readout sides before and after irradiation. Here, the upper X axis shows the corresponding strip interconnection scheme. The collected charge corresponding to thicker²³ Hamamatsu sensors is approx. 15% to 20% higher than for the CiS sensors before irradiation. However, after irradiation the observed most probable charge of the Hamamatsu sensors is reduced in a greater degree than for irradiated CiS devices. Also, no significant difference is observed in the collected charge corresponding to the double-metal and external microcable strip interconnection schemes.

Using the values measured before and after irradiation, the charge collection efficiency (CCE) was calculated as a ratio of the charge collection after irradiation (Q_{irr}) to the value observed before irradiation (Q_0):

$$CCE = \frac{Q_{irr}}{Q_0} \quad (3.4)$$

Figure 3.34 demonstrates the charge collection efficiency for the prototype sensors. Here, the CiS sensors demonstrate the CCE in the range of 80% to 95% depending on the readout side, while the CCE values of the Hamamatsu sensors lay in the range of 70% to 80%. The errors of CCE were calculated as:

$$\Delta CCE = \sqrt{\left(\frac{\Delta Q_{irr}}{Q_0}\right)^2 + \left(\frac{Q_{irr} \cdot \Delta Q_0}{Q_0^2}\right)^2} \quad (3.5)$$

²³The difference in thickness between the CiS and Hamamatsu sensors is approx. 14%.

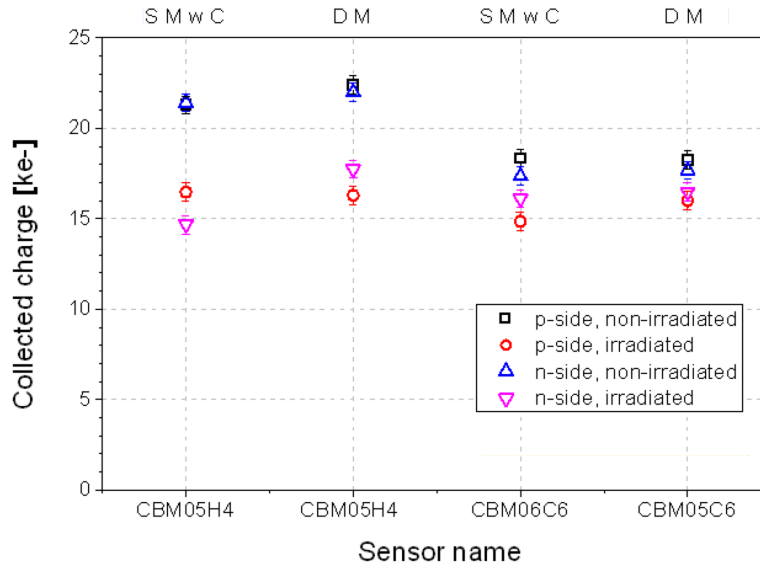


Figure 3.33: Charge collection results before and after irradiation for proton irradiated prototype sensors produced by CiS and Hamamatsu, featuring double-metal (DM) and external microcable (SMwC) strip interconnection schemes. $V_{bias} = 470$ V.

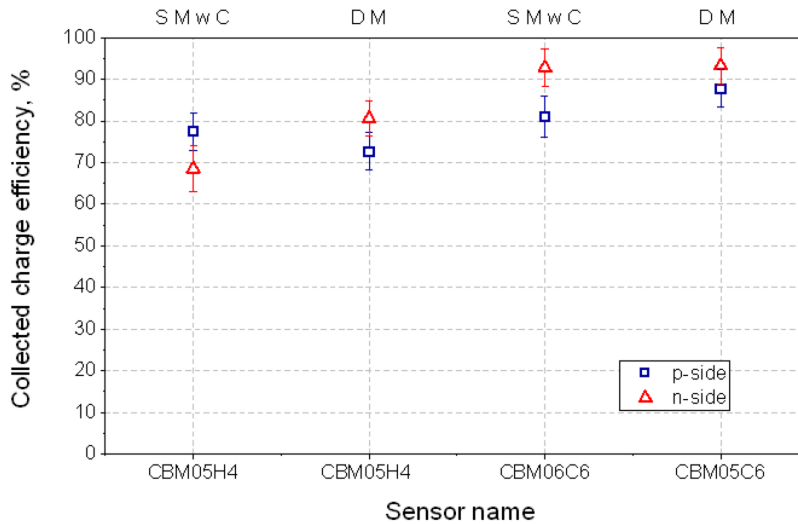


Figure 3.34: Charge collection efficiency results after irradiation for proton irradiated prototype sensors produced by CiS and Hamamatsu, featuring double-metal (DM) and external microcable (SMwC) strip interconnection schemes. $V_{bias} = 470$ V.

3.7 Long-term stability performance of prototype sensors

Stable operation of each sensor of the system is a key requirement for stability and decent operation of the whole detector. The long-term stability of the STS sensors is verified as a part of the QA program on a fraction of the sensors. However, during the operation of the experiment in a high radiation environment the leakage current of silicon sensors undergoes a considerable increase that is proportional to the accumulated fluence (Eq. 2.5). For the successful operation of the CBM experiment the STS sensors are required to maintain their stability over their whole lifetime period. In Section 3.6.2, the leakage current of the prototype sensors irradiated to twice the lifetime fluence was found at a level of milliamperes, which is approx. three orders of magnitude higher compared to that before irradiation.

In order to be sure that the STS sensors exhibit a required operational stability after heavy irradiation, their long-term stability was studied as presented in this section. Also, the sensors having different strip interconnection schemes were compared in terms of their long-term stability in the current study. The measurements were performed on the prototype sensors irradiated to $\Phi_{eq} = 2 \times 10^{14} \text{ n}_{eq}/\text{cm}^2$ at approx. $-5 \text{ }^\circ\text{C}$, a temperature corresponding to the operational temperature of the CBM experiment. A 350 V bias voltage was applied.

3.7.1 Measurement results of long-term stability

Measurement conditions

The measurement setup for long-term stability measurements is described in Section 3.3.4. Within this setup, the following parameters were monitored: the leakage current of the sensors under test, the temperature and the humidity of the surrounding air.

The operational principle of a refrigerator implies periodic variations of the temperature with a certain period. The temperature variation inside the refrigerator used in the current study is $\pm 1 \text{ }^\circ\text{C}$. However, inside the test box (Fig.3.5b), due to a continuous flow of the cooled nitrogen, the measured temperature variation equals to $\pm 0.3 \text{ }^\circ\text{C}$. The leakage current, having a strong temperature dependence, is expected to follow the periodic behaviour of the temperature. The relative humidity follows the periodic behaviour as being temperature dependent by definition.

A zoomed area of the measurement section demonstrates the periodic behaviour of all the monitored parameters (Fig. 3.35a). Moreover, every approx. 8 hours due to an anti-condensate procedure of the refrigerator, an additional temperature enhancement of $0.5 \text{ }^\circ\text{C}$ is observed for a short period with the following recovery

3.7 Long-term stability performance of prototype sensors

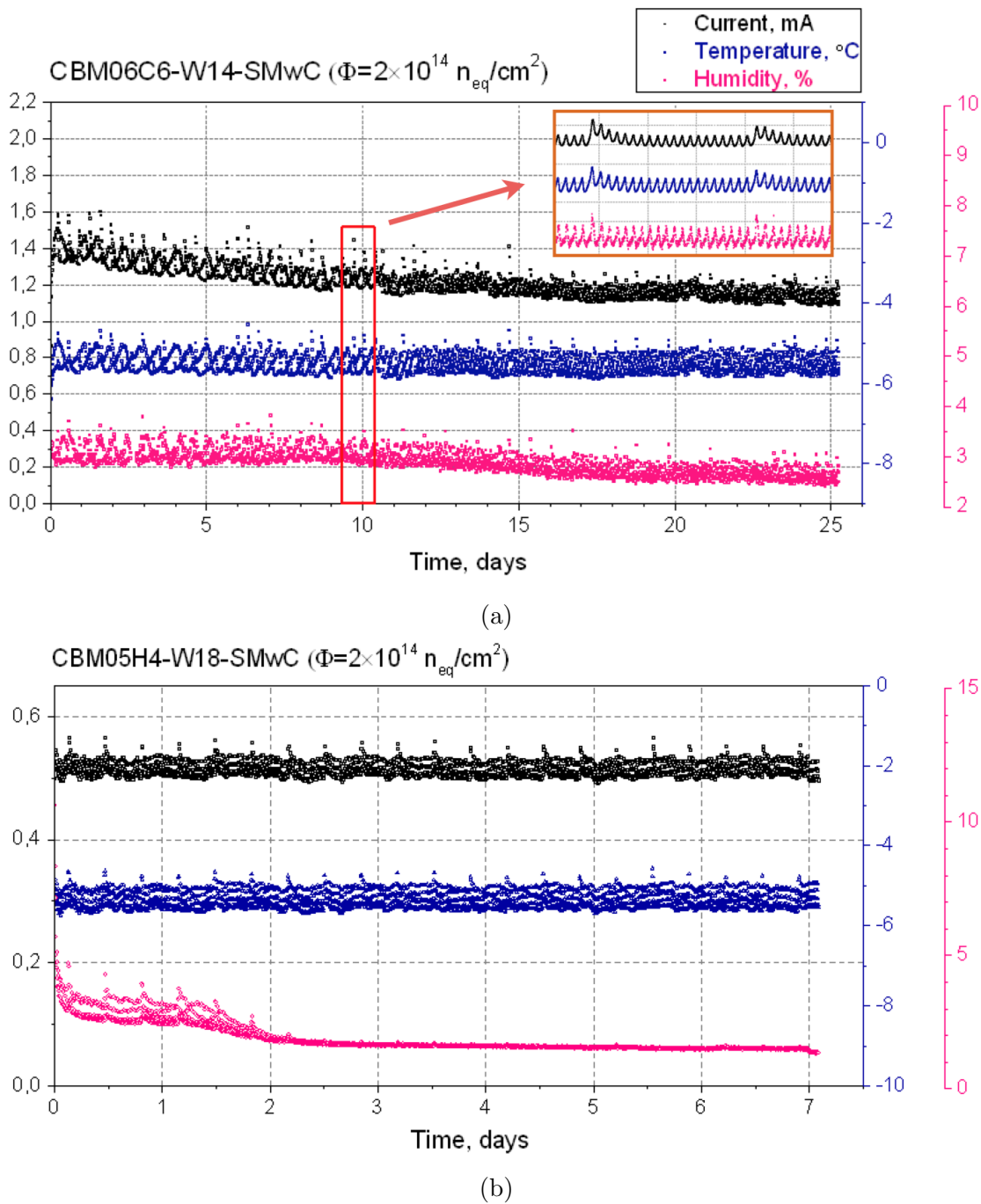


Figure 3.35: Long-term stability results for the STS prototype sensors with external microcable strip interconnection design: (a) CBM06C6-SMwC sensor (CiS); The zoomed area shows the periodic behaviour of the monitored parameters; (b) CBM05H4-W18-SMwC sensor (Hamamatsu).

to the nominal value within approx. 1 hour. During this period, the leakage current also undergoes an enhancement as well as the relative humidity.

Sensors with external cable strip interconnection design

Figure 3.35a illustrates the result of the long-term stability test for the CBM06C6-SMwC sensor. After a 25 day long test, this sensor showed a stable operation with a slow decrease of the leakage current. Here, during the first 10 days of the measurement, the leakage current decreased from 1.5 mA at the starting point down to 1.2 mA, which is approx. 20% of the initial value. During the next 15 days, it decreased from 1.2 mA to 1.1 mA, featuring a lower slope. The temperature recording during the whole measurement period showed a very stable behaviour with a mean value of -5.5 °C. The relative humidity experienced a slow and a low-value descent from approx. 3 % down to about 2.7 %.

The long-term test result for the CBM05H4-W18-SMwC sensor is shown in Fig. 3.35b. From the starting point of approximately 0.51 mA²⁴ the mean value of the leakage current remained stable without any deviation during one week. The temperature during the measurement remained constant without any deviations as well. The humidity recording showed an approximately 2.5 day descending behaviour from about 5% down to 1.5% with further stabilization until the end of the measurement. Due to the continuous blow of the nitrogen for a long period, it stabilizes at a low level and do not exhibit high variations.

Sensors with double-metal strip interconnection design

Figure 3.36a shows the stability measurement results for approx. 4.5 days of operation of the CBM05C6-W6-DM sensor. During the first day of the measurement, the leakage current demonstrated a stabilization from approx. 1.4 mA to 1.2 mA, then remained stable for almost 4 days until the moment when the leakage current runaway occurred. The detailed view of the last moments of the measurement showed that during the last hour due to an unexpected nitrogen supply shutdown, the leakage current experienced a rapid runaway until it reached the compliance limit that forced the measurement software to stop the test as a protection measure. Analysis of the temperature recording did not show any deviation from the mean value during the whole measurement period until the very end. The quantitative increase of the humidity level was approximately 50% of its nominal value before the gas supply shutdown.

²⁴This test was performed after approximately 1 year of the moment of irradiation. The leakage current of this sensor measured shortly after irradiation equaled to approx. 0.7 mA. Even though the sensor was kept at -5 °C, annealing effects took place that lead to a decrease of the leakage current.

3.7 Long-term stability performance of prototype sensors

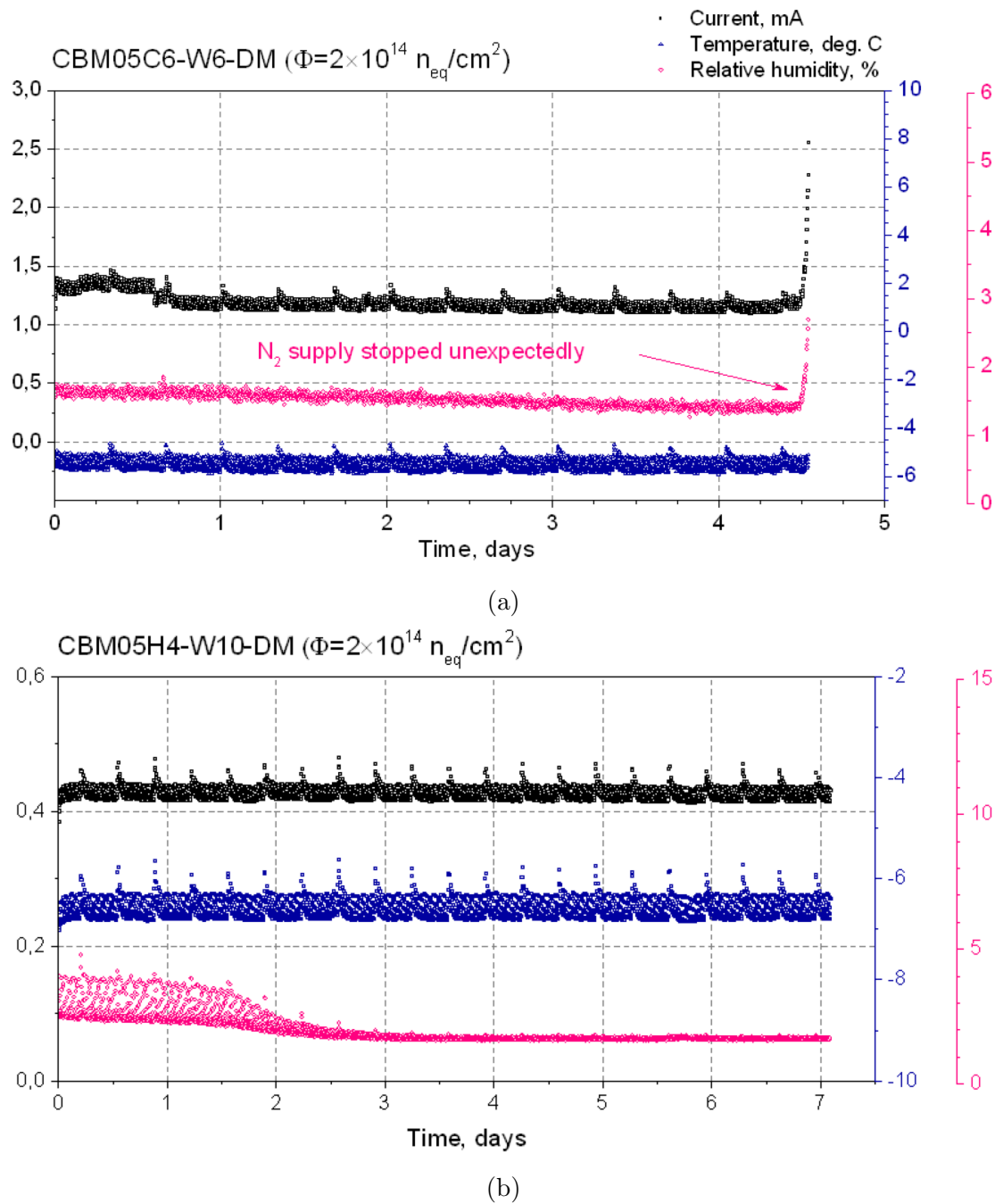


Figure 3.36: (a) Long-term stability test for a $6.2 \times 6.2 \text{ cm}^2$, $\approx 290 \text{ }\mu\text{m}$ thick CBM05C6-DM sensor with double-metal strip interconnection scheme, irradiated to $2 \times 10^{14} \text{ n}_{eq}/\text{cm}^2$; (b) Long-term stability test for a $6.2 \times 4.2 \text{ cm}^2$, $\approx 330 \text{ }\mu\text{m}$ thick CBM05H4-DM sensor with double-metal strip interconnection scheme, irradiated to $2 \times 10^{14} \text{ n}_{eq}/\text{cm}^2$

Figure 3.36b illustrates the measurement result for the CBM05H4-W10-DM sensor. The measurement was carried out for 7 days of continuous operation. The sensor showed a perfect operational stability over the whole measurement range without any deviations from the mean value. The temperature during the measurement did not exhibit any variation as well, keeping the mean value stable at approx. -6.5 °C. The relative humidity recording showed a stabilization of the mean value after approximately 2.5 days of operation at the level of less than 2%.

3.7.2 Operational stability under changing environmental conditions

After the observed leakage current runaway due to a rapid increase of humidity, caused by the N_2 supply shutdown, it was decided to reproduce this situation and to study the humidity influence on the stability. The shutdown of the nitrogen was performed in this case on purpose.

Sensors with external cable strip interconnection design

The CBM06C6-W14-SMwC sensor that showed stable operation on a 25 day timescale under stable environmental conditions, exhibits a moderate rise of the leakage current right after the N_2 supply shutdown while the relative humidity experienced an enhancement from less than 3% to more than 7% in approximately 10 minutes (Fig. 3.37a). Also, the moment of the N_2 supply shutdown coincided with the moment of the fridge anti-condensation procedure that lead to an additional rise of the temperature. The sensor, however, did not experience a rapid runaway of the leakage current during the humidity test.

The measurement of the CBM05H4-W18-SMwC sensor was carried out over approx. 7 days with the humidity test in between (Fig. 3.37b). The recordings of all three monitored parameters before the humidity supply shutdown showed a stable operation of the sensor with a slight decrease of the leakage current, a stable temperature, and a slow humidity decrease. After more than 5.5 days of operation, the nitrogen supply was switched off and the system was left free for about a day, during which the humidity level rose up to 35%. It lead the leakage current to increase by approx. 10% from it's stable value. A stable sensor operation was observed during the nitrogen shutdown period. Almost 20 hours later the nitrogen supply was brought into operation, rapidly dropping the humidity level down to less than 5%. The leakage current of the sensor exhibited a recovery the previous level before the nitrogen shutdown and further stable operation until the end of the measurement. The temperature during the whole measurement was stable, with a very low and almost non-noticeable enhancement during the humidity rise with

3.7 Long-term stability performance of prototype sensors

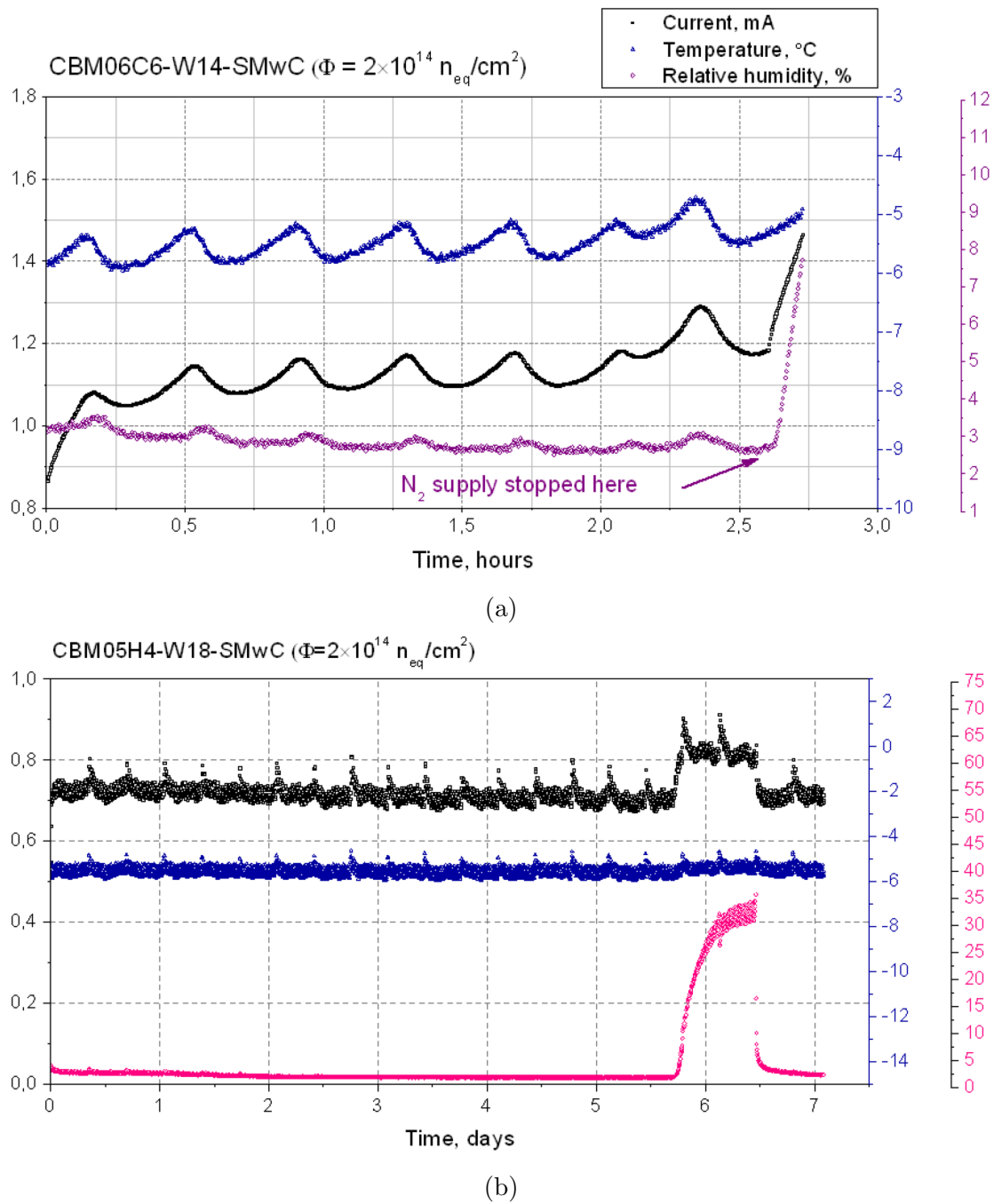


Figure 3.37: Repeated long-term stability tests featuring the nitrogen supply shut-down for: (a) CBM06C6-W14-SMwC sensor irradiated to $2 \times 10^{14} \text{ n}_{eq}/\text{cm}^2$; (b) CBM05H4-W18-SMwC sensor irradiated to $2 \times 10^{14} \text{ n}_{eq}/\text{cm}^2$.

a return to the previous level after stabilization of the humidity and the leakage current.

Sensors with double-metal strip interconnection design

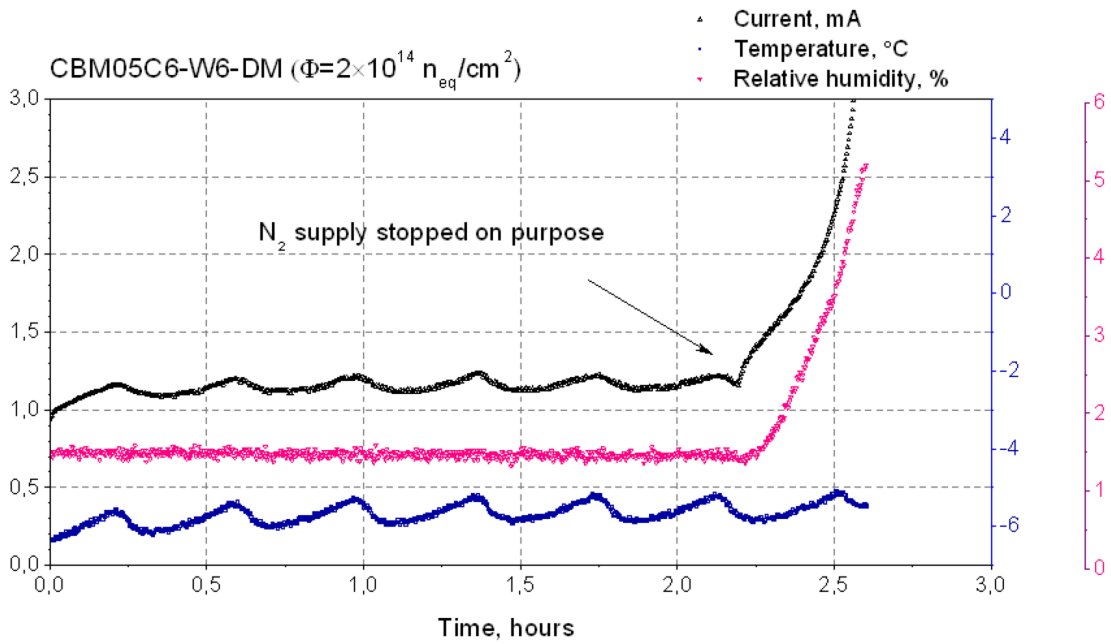
Conditions for the CBM05C6-W6-DM that already showed the leakage current runaway after the rapid increase of humidity, were repeated (Fig. 3.38a). Here, after 2 hours of a stable operation, the leakage current experiences a rapid increase again, right after the nitrogen supply shutdown occurs. The leakage current reaches the compliance limit of 3 mA in this case in 15 minutes after the gas supply was switched-off. During this period, the humidity increased up to 5% from a stable value of approx. 1.5%. The temperature recording did not show any deviation from the mean value of -5.5 °C.

Measurement of the CBM05H4-W10-DM sensor was carried out for approximately 6 days with a test of the nitrogen supply shutdown in the end (Fig. 3.38b). Before the N_2 shutdown, the sensor showed a very good operational stability. The temperature recording demonstrated a constant mean value without notable deviations. The humidity was kept at a few percent level. After the N_2 supply shutdown, the leakage current increased by approx. 50% in several hours while the relative humidity and the temperature rose up to 25% and -4.5 °C, respectively. It is remarkable that there was no obvious reason for the temperature to rise. It could have been increased due to the heat produced by the sensor suffering from a high level of the leakage current. It is also notable that the sensor did not experience the runaway and remained its operation after such a significant rise of the humidity, compared to the CBM05C6-W6-DM sensor. After several hours of waiting, the humidity supply was switched on that immediately reflected in a drop of the leakage current and the relative humidity values with their following stabilization. However, the temperature remained at the value that was reached after the N_2 supply shutdown. The leakage current was found to be stabilised at a level located higher than the one before the humidity supply shutdown. After the humidity test, the sensor demonstrated a stable operation for 1 day.

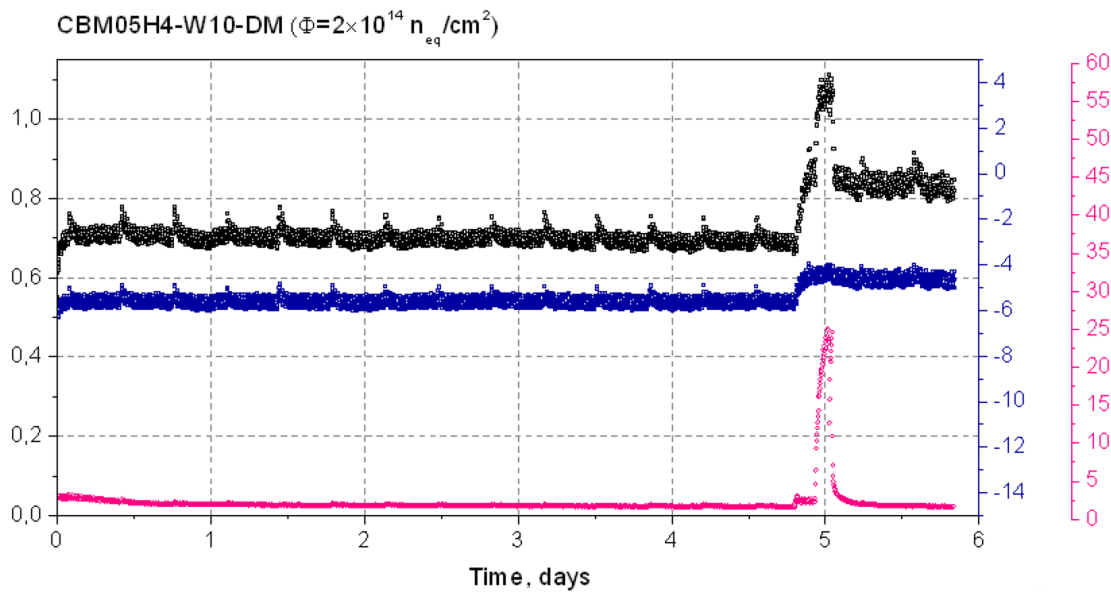
3.8 Discussion on measurement results

Measurements on irradiated miniature STS sensors

The leakage current measurements demonstrated the expected linear increase of I_{leak} with irradiation. The measurements were performed at -5 °C and were corrected to a fixed temperature of 20 °C in order to calculate the current related damage rate α . The latter equals to $(5.52 \pm 0.05) \times 10^{-17}$ A/cm, which is in agreement with



(a)



(b)

Figure 3.38: Repeated long-term stability tests featuring the nitrogen supply shutdown for: (a) CBM06C6-W6-DM sensor irradiated to $2 \times 10^{14} \text{ n}_{eq}/\text{cm}^2$; (b) CBM05H4-W10-SMwC sensor irradiated to $2 \times 10^{14} \text{ n}_{eq}/\text{cm}^2$.

the measurements performed by other collaborations²⁵. Using the obtained value, the leakage current can be estimated at various levels of irradiation.

The measurements of the full depletion voltage of the sensors irradiated to various fluences, demonstrated an expected evolution for an n -type silicon detector. The experimental data was found to be in agreement with the Hamburg model parametrization. The point of type-inversion was identified at approx. $2.2 \times 10^{13} \text{ n}_{eq}/\text{cm}^2$.

Measurement results of the most probable charge, corresponding to the non-irradiated sensor, demonstrate a noticeable difference: the charge collection obtained at the p -side is approx. 5% higher. Several effects may lead to such a difference: a weaker electric field at the n -side may lead to a higher charge sharing for signals in the interstrip region as the drifting electrons can diffuse and induce a fraction of the signal on the neighbouring strips which might be cut by a threshold²⁶. Also, the signals could be induced on the p -spray isolation structure between the n -side implants, which, for instance, has a longer time constant for a “discharge” than the integration time of the readout electronics, therefore, this fraction of the signal is not integrated [70]. Measurements of a non-segmented test structure can be performed to exclude the influence of segmentation as well as the impact of the strip isolation.

The low charge collection obtained from the n -side of the w2sn3 sensor may originate from the lack of guard rings at this side of this particular sensor. When the n -side is read out, its potential is at ground²⁷, and, if the signals are induced on the isolation structure, without the guard rings they can be leaked to ground through a periphery.

The overall charge collection deterioration after irradiation is attributed to the reduction of the carrier lifetime due to trapping of the carriers by the radiation-induced deep level traps. Because of the same reason, the charge collection increases with increase of the bias voltage: the higher electric field increases the drift length thus increases the charge collection. It was observed that more than 200 V of overdepletion is required for the charge collection to saturate for the majority of the sensors. The overall charge collection performance up to the lifetime fluence is 90% – 95% depending on the readout side, which confirms that the sensors are able to withstand the expected radiation environment.

The fact that after irradiation the n -side readout demonstrates higher charge collection at low bias voltages (but higher than the V_{fd} obtained from the C-V measurement), which is observed for the sensors of a $8 \times 10^{13} \text{ n}_{eq}/\text{cm}^2$ fluence and higher, is attributed to the fact that electrons, which are collected at the

²⁵Here, measured directly after irradiation.

²⁶An approx. 1 fC threshold was applied to each channel of the n-XYTER.

²⁷Due to the setup specifics, each side, when read-out, was kept at ground.

n -side, have lower trapping probability and higher mobility w.r.t. to holes. Also, as the strongest electric field after the type-inversion is located at the n -side, the charge is more efficiently induced on the n -side readout strips. The dominant signal from the n -side readout is also observed after irradiation in [71],[72]. The observed gain for the sensors irradiated to a fluence of 1×10^{14} n_{eq}/cm^2 may be attributed to the effect of charge multiplication: such effects were observed at fluences of 1×10^{14} n_{eq}/cm^2 and higher [68]. A certain gain is also present for the sensors of a 2×10^{14} n_{eq}/cm^2 fluence, however, it is suppressed due to trapping of the carriers by the deep level states, which becomes significant at this fluence.

Discussion on annealing studies

The leakage current values were monitored as a function of time at 80 °C and 25 °C. At both temperatures, a decrease of the reverse current is observed as expected from the measurements performed by other groups. The decrease of the leakage current will have a beneficial effect on operation of the sensors as the shot noise of the readout electronics will decrease with it.

The measurements of the full depletion voltage V_{fd} as a function of time demonstrate a different behaviour of this parameter depending on the fluence. At 80 °C, the beneficial annealing was observed for the w6sn2 sensor ($\Phi = 1 \times 10^{14}$ n_{eq}/cm^2), while for the sensors irradiated to lower fluences it was either much less pronounced (w25) or not observed at all (w12sn2). Such a difference is expected as the higher the number of the introduced defects (i.e., the fluence), the stronger is the effect of annealing. Here, the w25 sensor did not experience the type-inversion and, therefore, remains the positive space charge. The same processes that lead to a decrease of the full depletion voltage for the sensors that underwent the type inversion, lead the V_{fd} of this sensor to increase during the short-term annealing phase. This is true for a sensor irradiated to any fluence below the type inversion.

During the long-term phase, the effect of annealing is again more pronounced for the w6sn2 sensor as the amplitude of the long-term annealing $N_{Y,\infty}$ is directly proportional to the fluence (Eq. 2.10). Here, after 55 min. of exposure at 80 °C, it's V_{fd} increases by approx. 134%. This conditions are equivalent to approx. 300 days of exposure at 20 °C. For the same period, the full depletion voltage of the w12sn2 and w25 sensors increased by approx. 120% and decreased by approx. 30%, respectively. Here, even though for the w25 sensor the V_{fd} decreases during the long-term annealing, in practice it just brings the full depletion voltage closer to the point of space charge sign inversion, after which it will rapidly increase like for the w12sn2 and w6sn2 sensors. Thus, in order to keep the operational voltage low, the sensors are recommended to be kept at low temperatures to avoid the

reverse annealing effects.

The 25 °C exposure of the w6sn1 sensor ($\Phi = 1 \times 10^{14} \text{ n}_{eq}/\text{cm}^2$) for 61 days, which is close to the real conditions of the maintenance period of the experiment, have clearly shown the short-term and the long-term phases of the full depletion voltage time evolution. The V_{fd} decreases by approx. 30% during the first 7 days of storage down to its minimum and increases afterwards until the end of the measurement range. The absolute increase of the full depletion voltage during 54 days of long-term annealing equals to approx. 100%.

The parametrization of the V_{fd} evolution in terms of the change in effective impurity concentration ΔN_{eff} , performed using the Hamburg model, describes well the experimental data at both temperatures. Here, the change of ΔN_{eff} demonstrate a lower decrease during the short-term phase than that expected from the model. The long-term annealing data is described well. The minimum of the ΔN_{eff} evolution is expected from the model after 6 min. of exposure at 80 °C and 5 days at 25 °C. Both minimums expected from the model are located between the experimental points. However, in case of 25 °C exposure, the difference between the ΔN_{eff} on the 5th and the 7th day is less than a percent.

The charge collection was monitored for the w6sn2 and the w12sn2 sensors as a function of time at 80 °C in order to determine its trend on a long-time scale in terms of 20 °C exposure. For both sensors, the most probable charge demonstrated a slow decreasing tendency, at a level of a few percent, during more than 300 days for the w6sn2 device and more than 600 days for the w12sn2 sensor, in terms of equivalent annealing at 20 °C. As presented in Section 2.4, the difference in trapping probabilities for electrons and holes was observed after irradiation and during the subsequent annealing at various temperatures. However, no significant difference is observed in collected charge at the p^+ and n^+ readout sides. A slow decrease of the most probable charge can originate from the fact that the readings were obtained at a fixed bias voltage, but the full depletion voltage increased by more than 100% for the w6sn2 and by approx. 200% for the w12sn2 sensors (Fig. 3.29). As observed in Section 3.4.3, a certain overdepletion is required for the charge collection to saturate. CCE evolution can be studied at short-term scales. For this, it is recommended to use lower temperatures.

Thus, during the maintenance period of the experiment, the sensors can be kept at 25 °C for a period of 5-7 days in order to minimize the full depletion voltage of type-inverted detectors. The equivalent time at lower temperatures can be estimated using the Hamburg model. Thus, for a 20 °C temperature it equals to 10 days (see Appendix D). Obviously, the lower the temperature of the exposure, the longer time is required for both the short-term and the long-term annealing. It is therefore recommended to reduce the temperature after the sensors reach the minimum of V_{fd} , to 5 °C or lower. According to [97], the reverse annealing

becomes negligible below $T = 5$ °C. Already at 10 °C, the reverse annealing time constant τ_Y equals to 8 years [37].

Discussion on measurements of irradiated prototype sensors

The leakage current of the prototype sensors, irradiated to twice the lifetime fluence, increases up to a mA level (for the sensors of 6.2×6.2 cm² and 6.2×4.2 cm² sizes). Here, it has to be taken into account that after mounting and glueing of the sensors on the supporting carbon fiber structures, the leakage current of non-irradiated sensors can be increased by several times [73], [74] due to mechanical stress. Therefore, the I_{leak} can be even higher than that observed at this fluence. This has to be considered when evaluating the total noise of the readout module after irradiation. The leakage current, estimated using the current related damage rate, extracted from the measurements with miniature sensors, equals to (1.15 ± 0.23) mA for a 6.2×6.2 cm² sensor, and (0.85 ± 0.17) mA²⁸ for a 6.2×4.2 cm² sensor, which is in agreement with the experimental data.

The full depletion voltage of the prototype sensors was not extracted from the C-V measurement due to a distortion because of high leakage currents. A solution could be a measurement at lower temperatures, down to -20 °C or lower. In this case, the test frequency of the LCR-meter need to be adjusted according to [58]. The full depletion voltages after irradiation, estimated with the Hamburg model, demonstrate an approx. 75 V difference for the sensors fabricated by CiS and Hamamatsu vendors, due to their difference in thickness and initial doping concentration. The V_{fd} of the sensors produced by Hamamatsu demonstrates an earlier type-inversion and a faster enhancement with irradiation.

The charge collection measurements demonstrate a difference for the sensors produced by CiS and Hamamatsu. Due to a higher thickness, the Hamamatsu sensors exhibit higher charge collection before irradiation. However, after irradiation, the most probable charge is comparable within a few percent in absolute values for the sensors produced by both vendors. In terms of charge collection efficiency, the CiS sensors show a 80% – 90% level of CCE and the Hamamatsu ones show a 70% – 80% of CCE. Here, due to differences in thickness and initial doping concentration, the difference in V_{fd} is present after irradiation, as mentioned above. As the sensors were measured at a fixed bias voltage of 470 V, the effective overdepletion for the CiS and the Hamamatsu sensors was different. The electric field distribution which, according to [70], influences the charge collection efficiency as well, is also different for these sensors as their thickness is different. Taking into account the above considerations, the difference in charge collection efficiency can be explained by performing additional measurements, e.g., transient

²⁸The values are scaled to -5 °C.

measurements for determination of the electric field profile.

Summarizing this section, the prototype sensors demonstrated a good charge collection performance of 70% – 90%, after irradiation to twice the lifetime fluence. As a next step, the performance of the whole readout module has to be evaluated after various levels of irradiation, using the latest prototype components.

Discussion on long-term stability operation of irradiated STS prototype sensors

Series long-term stability studies, performed on the STS prototype sensors irradiated to twice the lifetime fluence, demonstrated high operational stability during long timescales at stable parameters of surrounding environment. Additionally, the sensors exhibited a leakage current dependence on a rapid variation of humidity. For the sensors featuring an external cable strip interconnection scheme, manufactured by both vendors, this sensitivity is found to be less pronounced than for those featuring a double-metal strip interconnection. In addition to that, the Hamamatsu sensors are found to be less sensitive to this effect in general: full or partial recovery of the leakage current was observed after stabilization of the humidity back to a low level. The best performance is demonstrated by the sensor with external cable design produced by Hamamatsu. The most pronounced sensitivity to the humidity variation is shown by the double-metal sensor produced by CiS.

Additional measurements on CiS sensors (see Appendix A) have shown that a slow increase of humidity leads to a slow increase of the leakage current, and an eventual thermal runaway at approx. 5.2×10^{-2} mA/cm². Also, a measurement of a non-irradiated prototype CiS sensor exhibited the sensitivity observed for the irradiated sensors.

The observed sensitivity, therefore, is neither attributed to radiation damage nor to high leakage currents. Presumably, it can be a result of an introduction of negative charges on the sensor surface in humid conditions which leads to a surface depletion and subsequent increase of the leakage current [75], [77]. The lower sensitivity for the sensors with an external cable may be due to the fact that the surface of their *p*-side is covered by the microcable. Also, the differences in size and fabrication technologies of the CiS and Hamamatsu sensors can be a possible reason for observed differences in their stability.

It was observed that in most of the cases the leakage current stabilizes at higher values than those observed in the corresponding I-V curves. Additionally, the above mentioned increase of the leakage current of non-irradiated sensors is expected due to mechanical stress. Thus, considering the facts mentioned above, it is recommended to reduce the operational temperature down to -10 °C in order

3.8 Discussion on measurement results

to avoid possible thermal runaways.

Chapter 4

Quality Assurance of the STS sensors

The latest high energy physics experiments address higher and higher requirements for tracking systems and, consequently, for their main units - silicon sensors. Operation at high luminosities and particle multiplicities require stable, long-lived, radiation hard sensors. Thus, silicon sensors become more and more complex objects with high standards of operation. The technological progress in the past decades allows to produce silicon sensors of high quality and yield but still various defects can be developed during fabrication, transportation or handling. As a result, the performance of sensors or their individual strips can be degraded. The components of the STS detector (sensors, cables, readout ASICs etc.) will be produced in cooperation with industry. To verify the quality of the STS components, the Quality Assurance (QA) procedures will be applied at various stages of the STS detector construction. The QA program for the STS sensors is currently being developed. In this chapter, the scope of the QA program to be applied to the STS sensors is presented.

4.1 Production and distribution of the STS sensors

The construction of the STS detector is a complex procedure that involves many research and industrial facilities around the world. Silicon sensors for the STS will be fabricated in cooperation with industry with their design and specifications provided by the STS group. For the production of the STS sensors, two manufacturer companies are being considered at the moment of completing this thesis, namely CiS, Germany and Hamamatsu, Japan. Several generations of prototype sensors have been and are being produced by both vendors. Approximately 900 double-

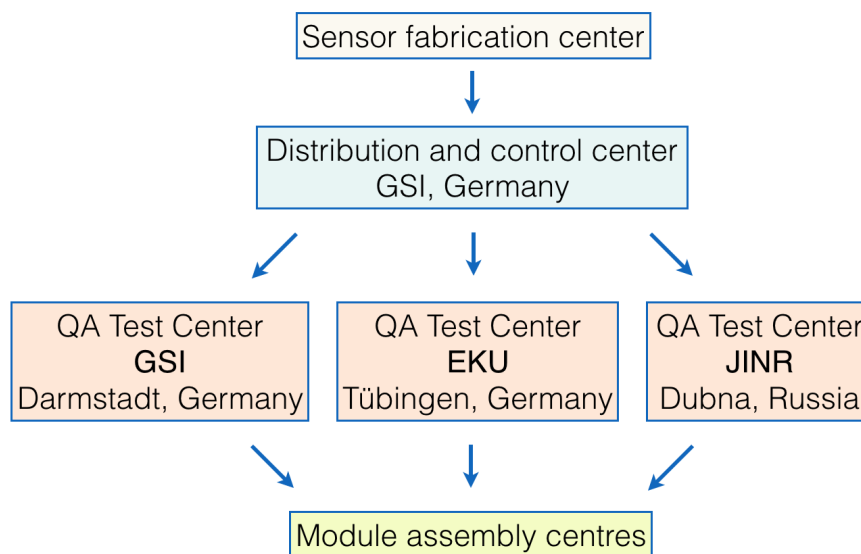


Figure 4.1: Distribution of sensors in CBM among the Quality Test Centers.

sided silicon sensors in four different sizes will be produced for the STS tracker. The produced sensors will be delivered in batches to the Distribution and Control center located in GSI, Germany, where they will be registered and recorded into a database. After that, the sensors will be distributed among three Quality Test Centers (QTC) for a detailed characterization (Fig. 4.1):

- GSI Helmholtzzentrum für Schwerionenforschung GmbH, Darmstadt, Germany;
- Eberhard Karls Universität (EKU), Tübingen, Germany;
- Joint Institute For Nuclear Research (JINR), Dubna, Russia.

The operability of each single sensor is one of the major requirements that determines the successful detector performance. Thus, an efficient quality assurance and characterization of silicon sensors has a decisive role during the sensor series production and module assembly periods.

4.2 Quality assurance program at the Quality Test Centers

Due to a large-scale sensor production, the effective sensor QA can be achieved by a collective effort among the Quality Test Centers. Figure 4.2 indicates the variety of quality assurance tests and the corresponding Quality Tests Centers in charge. The overall quality assurance program can be represented as a combination of the

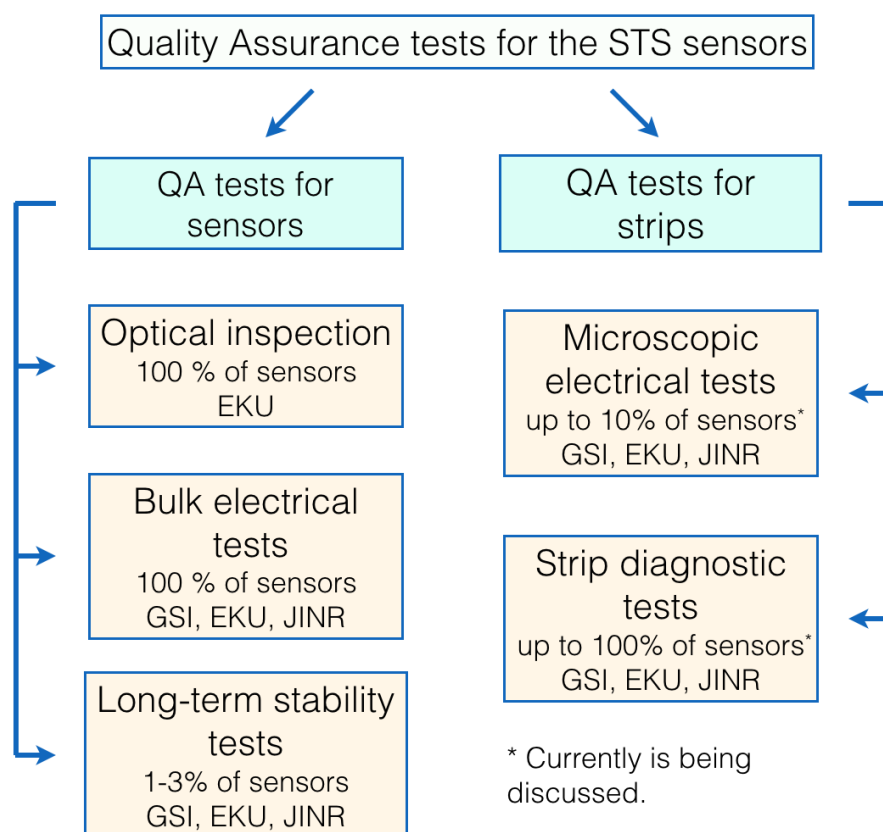


Figure 4.2: Schematic representation of the quality assurance program for the STS sensors.

quality assurance tests performed on a sensor level and the quality assurance tests performed on a strip level.

Optical inspection is intended to identify any kinds of surface defects. This test will be performed on 100% of the sensors at the EKU test center. Sensors with identified defects will undergo further electrical tests.

Bulk electrical tests are performed to determine the overall sensor behaviour at the operational conditions. Current-voltage (I-V) and capacitance-voltage (C-V) tests are conducted after the optical inspection. The I-V test determines the leakage current of a sensor. The C-V test determines the full depletion voltage of a sensor.

Long-term stability tests will be performed on a fraction of the sensors. The leakage current of the sensors will be monitored for a time period of 48-72 hours in order to evaluate their stability.

Microscopic electrical tests focus on determination of various sensor parameters and their correspondence with specifications, mainly coupling capacitance C_c , interstrip capacitance C_{is} , interstrip resistance R_{is} , and bias resistance R_{bias} .

Strip diagnostic tests aim to identify strip defects originating from the complex

fabrication processes that cannot be identified by the optical inspection [76]. These defects comprise mainly ohmic contacts or short circuits between the strip implant and the readout strip (so-called “pinholes”), short circuits between two or more readout strips, and strips exhibiting high leakage current.

The following sections describe these QA tests in details. Measurement conditions and acceptance criteria are discussed. Before that, the infrastructure and the laboratory equipment required for the QA tests, are described.

4.3 Infrastructure and laboratory equipment

4.3.1 Testing conditions

A cleanroom with temperature and humidity control is a standard requirement for quality assurance tests of silicon sensors. The cleanroom at the GSI QTC, where all the measurements of this chapter have been performed, features a standard class of ISO 4 [79]. The temperature in the cleanroom is kept at 23 °C and the relative humidity is approx. 20%.

4.3.2 Storage conditions

Silicon sensors can be stored on a shelf without limitations. However, certain conditions for the humidity should be obeyed in the storage section. According to [26], the humidity should not be too low due to a risk of static electrical discharges and a possible charge-up of the passivation oxide that can affect the properties of sensors. For the STS sensors a storage place has been established in the cleanroom areas of the testing and assembling centers, providing moderate humidity and constant room temperature.

4.3.3 Sensor handling

Silicon sensors require delicate handling due to a risk of surface scratches or other surface damages that can affect the characteristics of the sensors or introduce difficulties for bonding of the microcables or wire-bonds. Any direct contact with human hands is strictly forbidden. The sensors are handled with vacuum pens, providing a small contact area, far from the bonding and testing pads.

Special care should be taken of the sensor packaging to avoid any mechanical stress during transportation. Figure 4.3 shows the packaging of the STS prototype sensors produced by two vendors, Hamamatsu and CiS. Both companies provide safe packaging using the cleanroom paper or a set of cleanroom tissues inside the plastic packaging. Any direct contact with plastic packaging must be avoided due to a high risk of surface defects production and an undesired charge-up.



Figure 4.3: Sensor packaging by Hamamatsu (left) and CiS (right).

4.3.4 Equipment and testing tools

The core element of the QA test setup is a probe station with high movement precision. In the GSI QTC, the Süss PA300PS probe station featuring a $1\ \mu\text{m}$ movement precision in X-Y-Z directions and a chuck rotation option of $\pm 7.5^\circ$ is arranged in the cleanroom (Fig. 4.4). It provides by design a light-tight and electromagnetically shielded environment for the measurements.

The probe station is equipped with four probe needles that are mounted on special movable manipulators which can be reliably fixed in a desired position. The device under test is fixed on a precision table, so-called “chuck”, using the vacuum system. Needles with $5\ \mu\text{m}$ and $7\ \mu\text{m}$ tips are used to be able to probe the sensor’s DC-pads¹. The needles are mounted at a 45° angle in order to probe the pads safely and not to pierce the thin aluminum coating. The needles are brought to a desired position above the pad under test manually. After the position of the manipulator is fixed the needles are aligned using the mechanical precision controllers of the manipulator.

The probe station is equipped with a so-called ProberBench PC that hosts the ProberBench operating system, a control panel with a joystick controller (Fig. 4.5) with integrated display for prober control with or without a PC, and a PC based graphical user interface (GUI). This standard configuration allows to perform measurements in a semi-automatic mode (e.g., each movement of the chuck requires

¹Typical dimensions of the DC pad are $45 \times 87\ \mu\text{m}^2$.

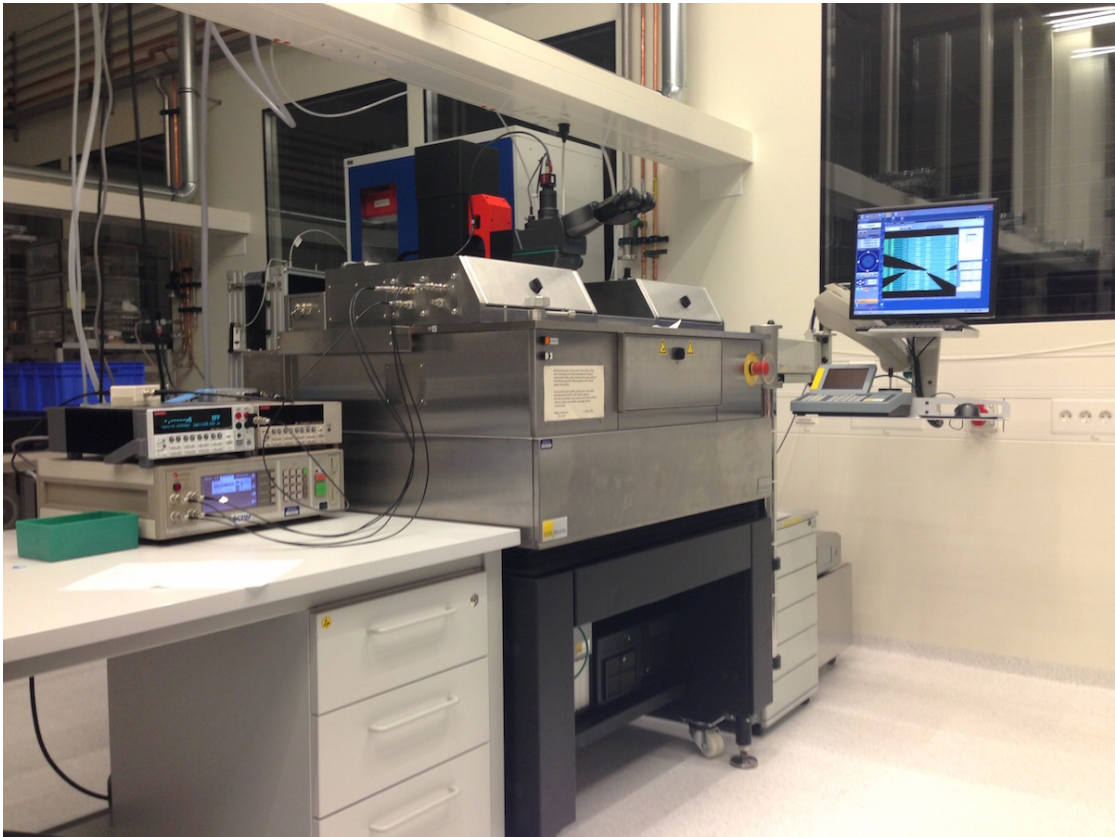


Figure 4.4: General view of the probe station at the GSI QTC.



Figure 4.5: General view of the Süss Expert Control Panel (left); Chuck controls of the PC based operating system (right).

pressing of a control button (Fig 4.5, right).

To be able to perform the full quality assurance program the following measurement instruments are used:

- Keithley 2410 SourceMeter unit (SMU) providing high-voltage up to ± 1100 V and current resolution of 10 pA;
- Keithley 6487 picoammeter/voltage source having a 2 nA - 20 mA current range and a high-resolution voltage source up to 505 V;
- QuadTech 7600 precision LCR-meter with customized external biasing up to 500 V, wide frequency range from 100 Hz to 2 MHz, 0.05 % measurement accuracy, programmable test voltage and current;
- Keithley 708B switching matrix (multiplexer) mainframe with a high-voltage (up to 1100 V) switching card (Keithley 7072-HV) for automation of the measurements (discussed in Chapter 5).

Standard BNC, LEMO and triaxial cables and connectors are used to establish the required connections.

The body of the probe station is used for grounding when required. In order

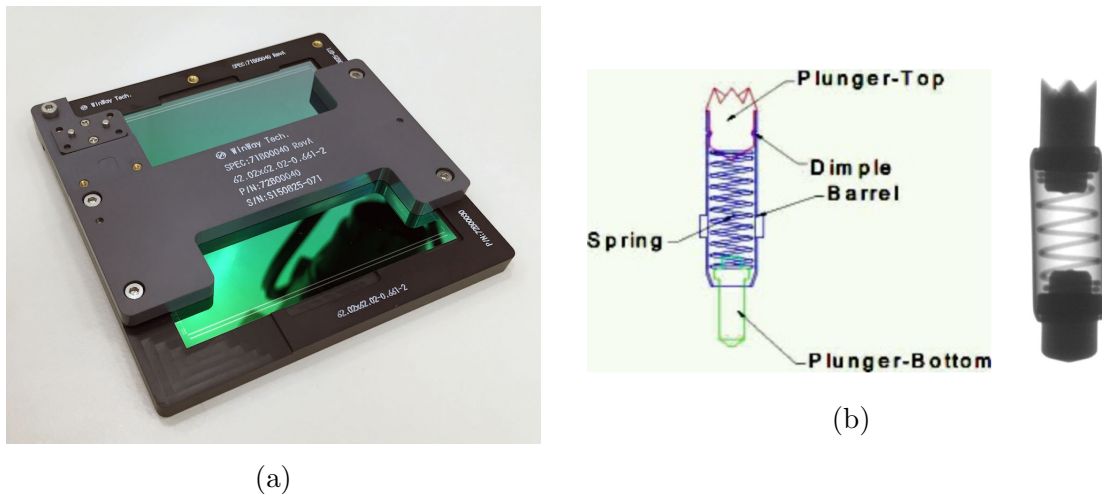


Figure 4.6: (a) General view of the STS test socket, (b) Cross-section and X-ray views of the Spring Probe Pin technology.

to provide the bias voltage to a double-sided sensor without wire bonding², a dedicated test socket has been designed in cooperation with GSI Detector Laboratory and produced by APS Solutions GmbH [80]. The socket consists of two parts, bottom and top, that are coupled together and held by metal screws (Fig. 4.6a).

²For time saving and safety reasons.

The sensor under test is placed in the bottom part of the socket which is milled out with a high precision to ensure proper positioning of the sensor. The bias contact is provided via so-called Spring Probe Pins (also known as "Pogo-pins") having a 30 μm diameter and being located precisely in the area corresponding to the middle of the bias pads. This technology provides a maximum spring force of 20 g at 0.5 mm. Using the test socket, the time required for the test preparation is strongly reduced in comparison with other test frames that require wire-bonding. Also, the test socket allows for a quick and easy exchange of the sensors under test, which is very important during the mass testing. For trained personnel the exchange of the sensors takes approx. 1-2 minutes.

4.4 Quality assurance tests on a sensor level

4.4.1 Optical inspection

Fabrication of a silicon sensor is a complex technology that comprises more than 10 technological operations. During the fabrication, various defects or fabrication impurities can be created, including the surface defects, which can affect the characteristics of the sensors. Also, some surface defects can be introduced due to intolerant handling. The goal of the optical inspection is to identify these defects as most often electrical defects are reflected in optical ones [26]. The following list exhibits the most common defects and impurities that may occur during the manufacturing or handling:

- Chipped/damaged corner or edge;
- Disruption of the poly-Si resistor;
- Lack of aluminum coating on pads or bias/readout lines;
- Unprecise dicing;
- Surface scratches.

The microscopic pictures of some of these defects are depicted in Fig. 4.7.

In addition, several defects may appear during transportation. Nowadays, manufacturing companies offer several types of the sensor packaging including plastic boxes filled with bubble wrap, thick paper packaging and others, where sensors are usually tightly fixed between several layers of the cleanroom paper (Section 4.3.3). Nevertheless, sensors may suffer from the mechanical stress and vibrations.

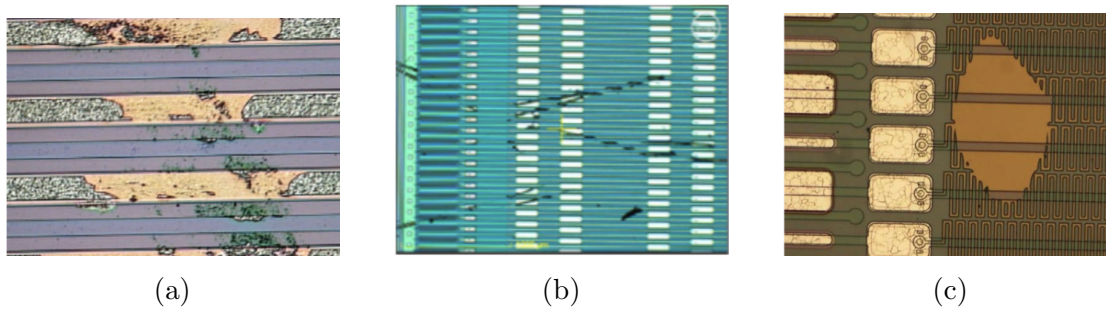


Figure 4.7: Microscopic view of different strip defects: (a) aluminum strip disruption [81], (b) surface scratches, (c) Poly-Si resistor brake [82].

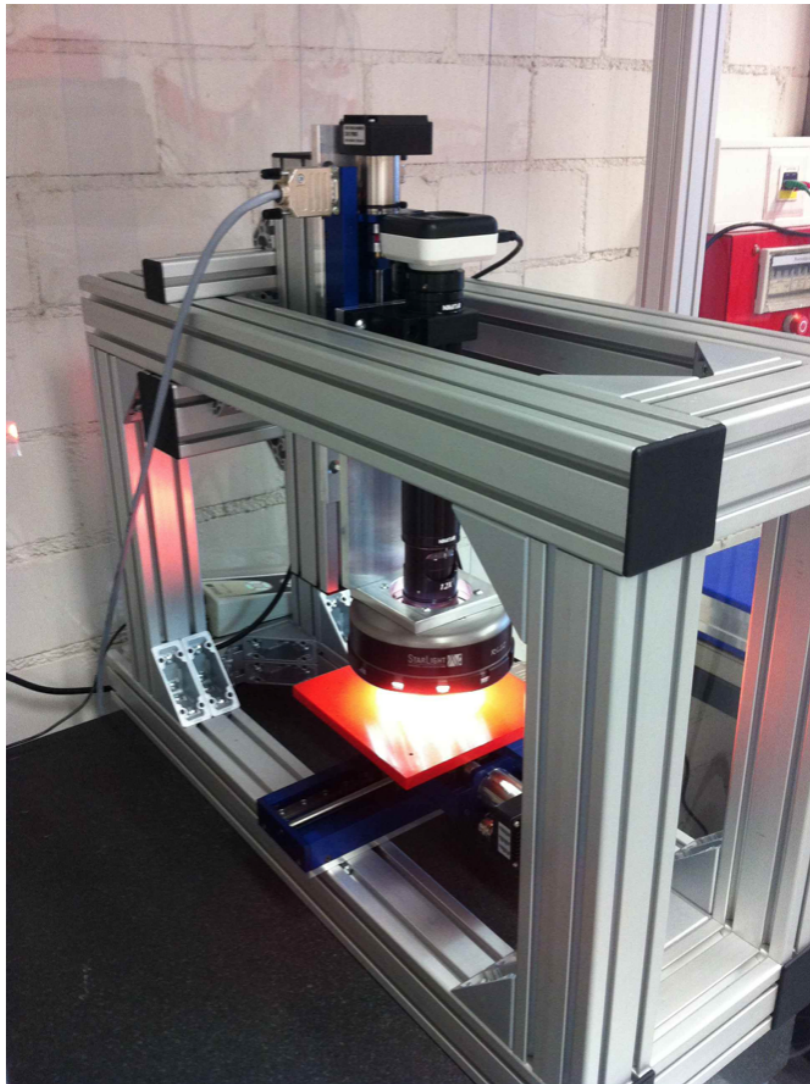


Figure 4.8: General view of the optical test stand at EKU.

For the optical inspection of the STS sensors, a dedicated test stand has been assembled at the EKU QTC by the Tübingen group (Fig. 4.8). The stand features a movable custom made vacuum chuck with a $2\ \mu\text{m}$ position accuracy, a 5 megapixel Moticam microscope camera with up to $12\times$ magnification, an LED light source, and a software for the setup control and automation based on the National Instruments Vision package.

Each delivered sensor is planned to undergo the optical inspection. The acceptance criteria and damage grading are currently being developed. The sensors having explicit surface damages have to be investigated further electrically.

4.4.2 Current-voltage (I-V) test

The I-V test is a bulk quality assurance test that shows the overall sensor health. It determines the total leakage current I_{leak} of a silicon sensor. The leakage current defines the shot noise of the readout system, thus desired to be as low as possible [83]. At the STS quality test centers, the I-V test will be performed using a probe station, the STS test socket (Fig. 4.6a) and a source-measurement unit (SMU). A schematic view of the test is shown in Fig. 4.9. Here, using a Keithley

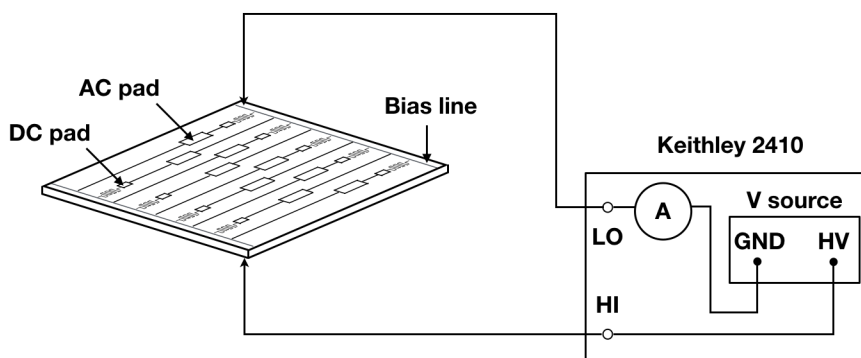


Figure 4.9: I-V test measurement scheme.

2410 SMU, the reverse bias voltage is applied in small steps to the bias pads³ of a sensor while the current flowing through the sensor bulk is measured. The measured leakage current includes a bulk generation current⁴ and surface currents.

The bulk generation current has a strong temperature dependence (see Eq. 3.2). If the measurements are performed at different temperatures, results have to be normalized to a fixed temperature, for instance, $20\ ^\circ\text{C}$. At the GSI quality test

³Bias pads are located on the bias line.

⁴In a reverse biased sensor, it originates from the drift of electron-hole pairs generated by various impurities in the silicon bulk.

center, the measurement software allows to perform the normalization automatically.

By conducting the I-V test the following sensor parameters can be also identified:

- Breakdown voltage V_{bd} (Fig. 4.10);
- If irradiated, the equivalent fluence can be estimated;
- The full depletion voltage V_{fd} can be roughly estimated.

The breakdown voltage defines the voltage limit up to which a sensor can be operated without a risk. Along with the full depletion voltage, it is used to estimate the optimal operational voltage. As the difference in the leakage current before and after irradiation is proportional to the received fluence, the latter can be estimated as well (see Section 2.4). The full depletion voltage can be roughly determined observing the I-V curve as the leakage current follows a $\propto V_{fd}^{1/2}$ dependence until the point of full depletion.

Typical I-V scan curves of the STS prototype sensors are depicted in Fig. 4.10. Here, the W03 sensor exhibits a non-standard behaviour and will be rejected. The W04 and W22 sensors exhibit either an early breakdown or an effect of a fast ramp-up. Thus, the IV-test serves as a first level selection procedure.

Sometimes, the I-V curve behaviour depends on the measurement details, in particular, the ramp-up step value and the time delay between the steps. As presented in Fig. 4.11, the same sensor has been tested at Hamamatsu and, when delivered, at GSI, showing a significant difference in the behaviour. The reason of the fast increase of the leakage current observed in the measurement at Hamamatsu can be attributed to the movement of the built-in oxide charges causing an additional current under fast ramping. Thus, the measurement settings should be selected carefully. Currently, the acceptance for the leakage current is the following: below⁵ $0.25 \mu\text{A}/\text{cm}^2$ at 120 V and below $0.8 \mu\text{A}/\text{cm}^2$ at 300 V. The final criteria will be updated after the evaluation of the signal-to-noise ratio of the readout module after irradiation.

4.4.3 Capacitance-voltage (C-V) test

The capacitance-voltage test (C-V) is performed to determine a full depletion voltage V_{fd} of a silicon sensor. In addition to that, a bulk capacitance C_{bulk} is determined. The V_{fd} of a silicon sensor is a quantity of the bulk material. It is proportional to an effective doping concentration in the sensor bulk (Eq. 3.3). The effective doping concentration and, respectively, the V_{fd} , undergoes a considerable

⁵At room temperature.

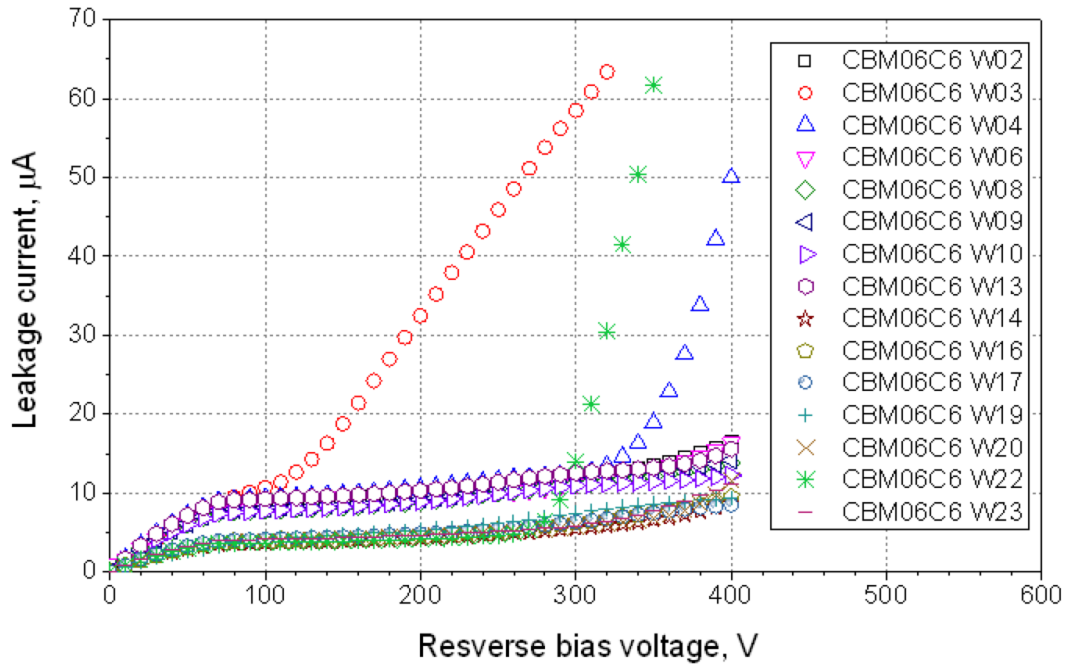


Figure 4.10: I-V test results for the STS prototype sensors. The W03 sensor exhibits a non-standard behaviour. The W04 and W22 sensors exhibit either an early breakdown or an effect of fast ramping (see Fig. 4.11).

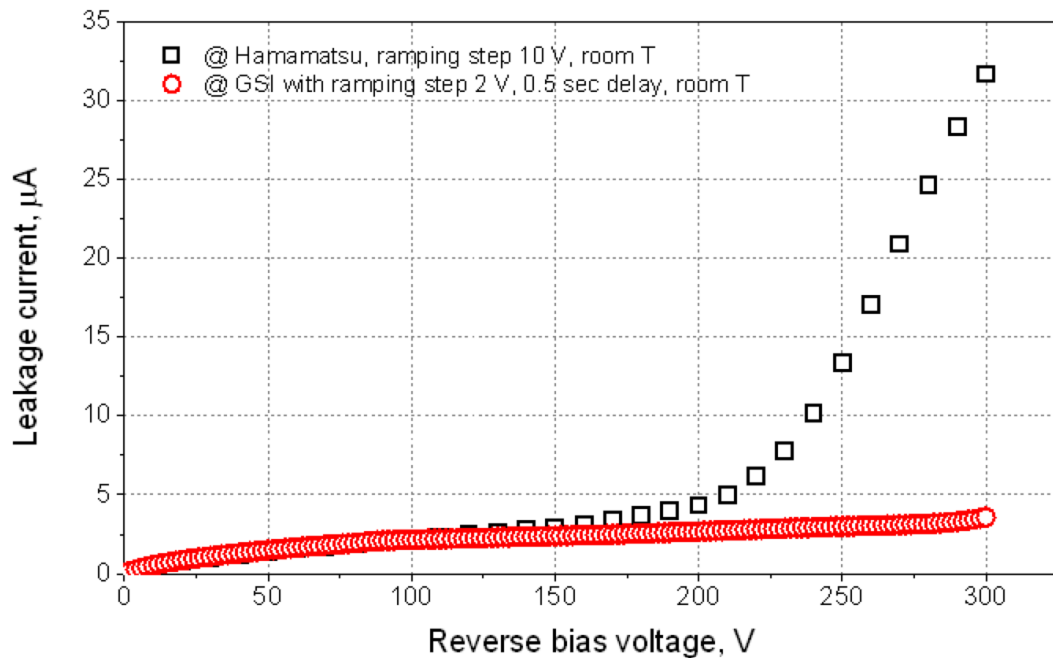


Figure 4.11: I-V test results obtained at the Hamamatsu and the GSI test centers. Diversity is observed due to different measurement settings (see text).

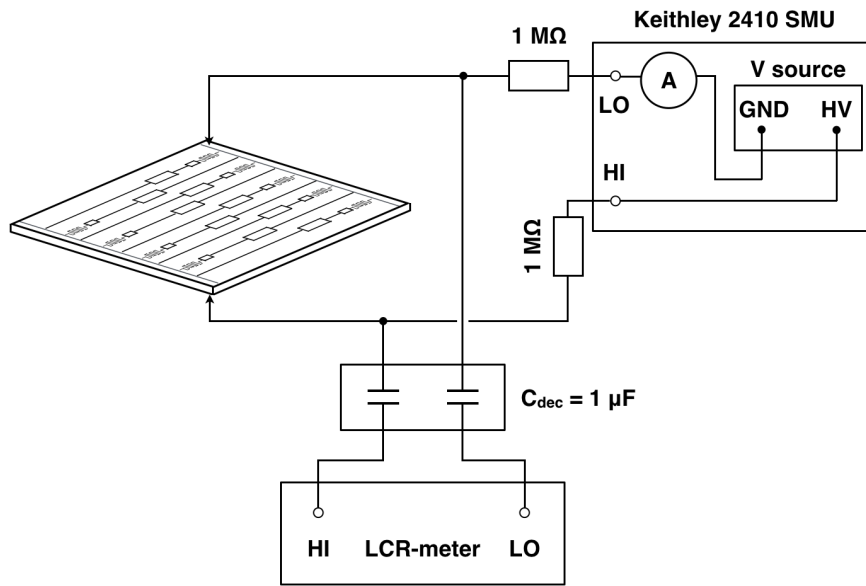


Figure 4.12: C-V test measurement scheme.

change during irradiation (see Section 2.4). Therefore, depending on the V_{fd} value, the sensors should be selected carefully and accordingly to the radiation damage expected in the corresponding areas of the stations.

A schematic view of the C-V measurement is represented in Fig. 4.12. The measurement requires an LCR-meter and a voltage source connected simultaneously to a sensor under test. The voltage source ramps-up the bias voltage in steps of several volts while the LCR-meter measures the capacitance of the depleted region by applying a sinusoidal voltage and measuring the induced current and its phase shift w.r.t. the applied voltage. Here, in order to decouple the LCR-meter from high voltage, two capacitors of a μF level are introduced to the measurement circuit. On the other hand, the AC test current should not flow into the power supply but only through the device under test. Therefore, two resistors of $1\text{ M}\Omega$ are introduced into the circuit.

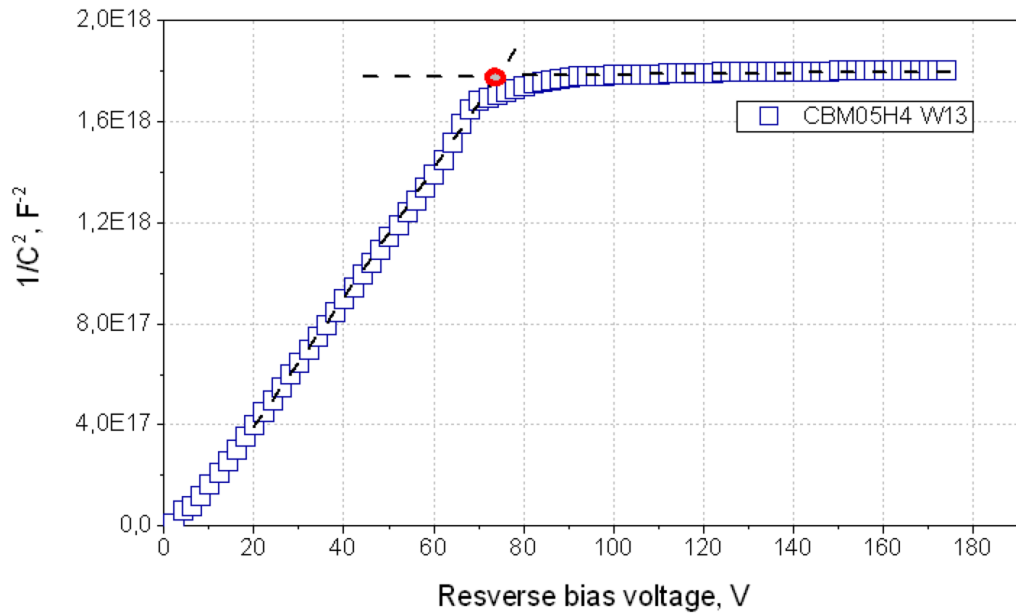


Figure 4.13: C-V measurement result of a prototype sensor represented by means of $1/C^2$ -V. The value of the full depletion voltage is obtained in the point of intersection of two straight lines following the experimental points.

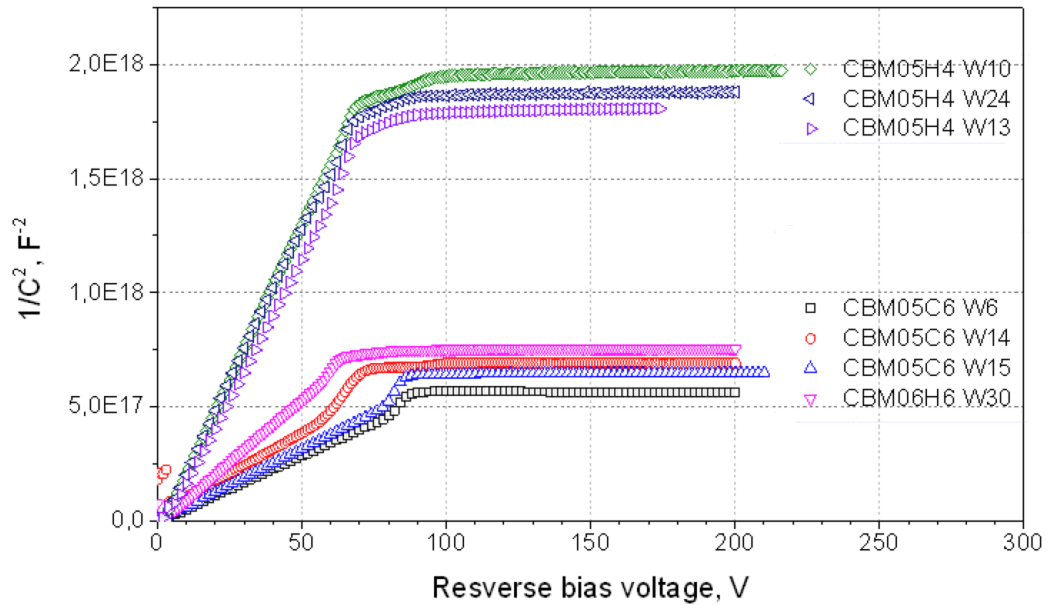


Figure 4.14: $1/C^2$ -V measurement scans for the STS prototype sensors.

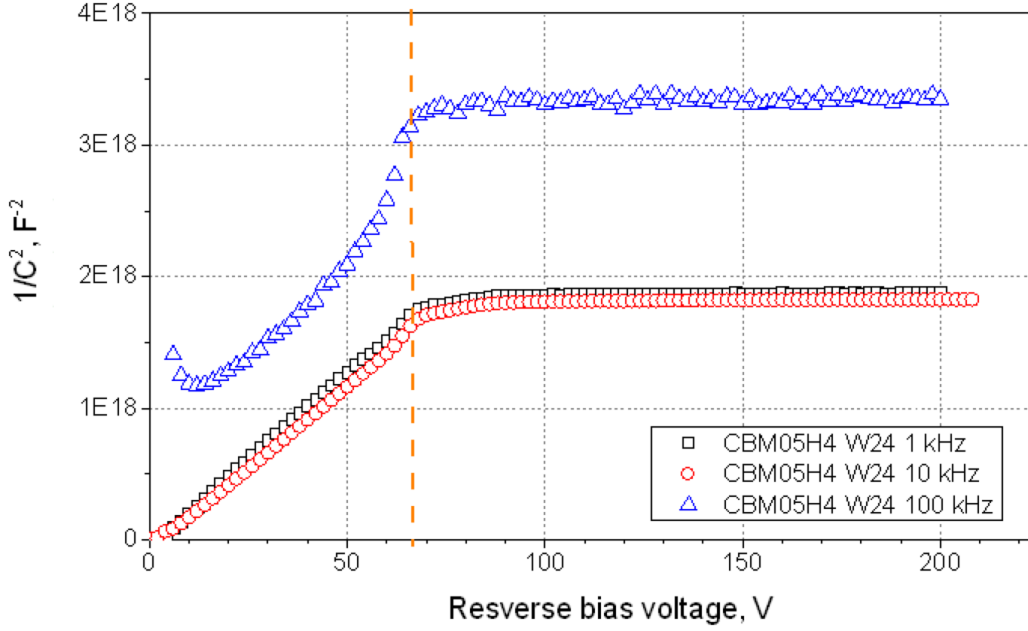


Figure 4.15: $1/C^2$ - V curves measured at various test frequencies.

The C-V measurement results is convenient to observe and process in a “ $1/C^2 - V$ ” representation, as the capacitance of a pn -junction depends on applied bias voltage as $C_{pn} \propto V_{bias}^{-1/2}$ up to the point of full depletion [84], after which remains constant (Fig. 4.13). Here, the value of full depletion voltage is obtained in a point of intersection of two straight lines following the experimental points. The experimental dependence of $1/C^2$ vs. V_{bias} for various STS prototype sensors is shown in Fig. 4.14. The measurement frequency is set to 10 kHz as suggested as optimal by the RD50 collaboration [85]. However, for non-irradiated sensors it is not crucial as illustrated in Fig. 4.15. In contrast, measurements of irradiated sensors have to be performed at lower frequencies, depending on the temperature (see Section 3.3.1).

Acceptance of the sensors should be based on their initial V_{fd} value. Figure 4.16 shows the evolutions of the effective doping concentration N_{eff} and the full depletion voltage V_{fd} as a function of the equivalent neutron fluence for a 300 μm thick sensor with various initial full depletion voltages, calculated using the Hamburg model. The full depletion voltage after irradiation is desired to be as low as possible⁶. This corresponds to the highest V_{fd} before irradiation (Fig. 4.16). The STS prototype sensors usually have their full depletion voltage in a range of approx. 60 to 100 V (Fig. 4.14). All sensors having their V_{fd} within this range can be accepted, however, allocation of the sensors inside the stations have to be

⁶In order to keep the operational voltage, which may equal up to $V_{fd} + 200$ V (Section 3.4.3), as low as possible.

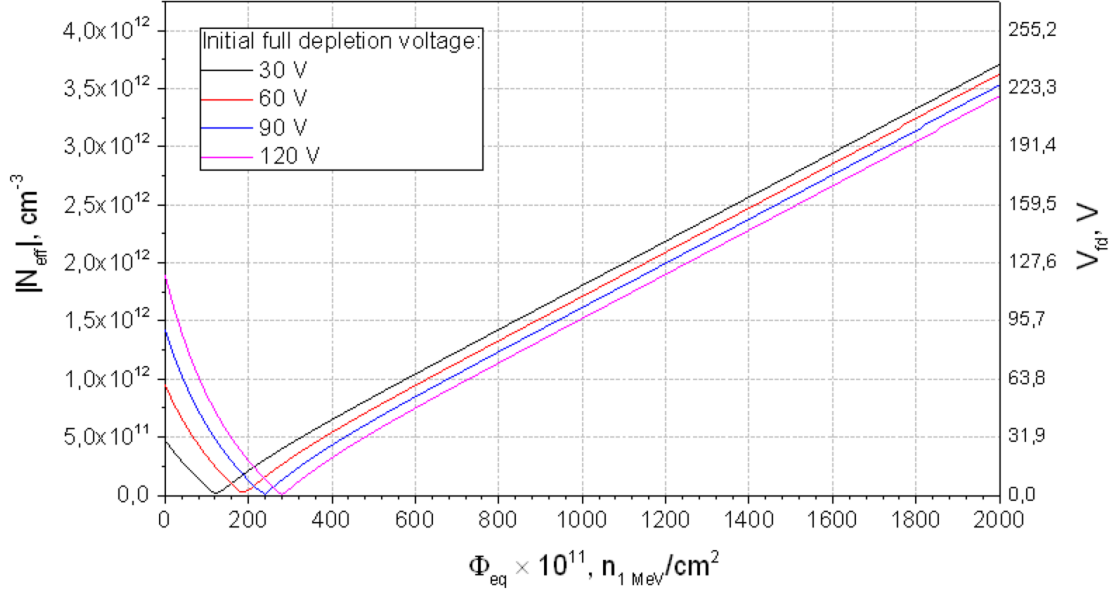


Figure 4.16: Evolution of V_{fd} as a function of the equivalent neutron fluence Φ_{eq} for a 300 μm thick sensor with various initial full depletion voltages. Calculation is performed using the Hamburg model, considering the stable damage.

performed such that in the regions, where the highest irradiation is expected the sensors with the highest V_{fd} values should be installed.

Therefore, the lower limit of the V_{fd} is defined at 60 V. The upper limit is defined at 200 V.

4.5 Long-term stability tests

During the experiment, the sensors will be operated continuously for several months. Therefore, their stability needs to be ensured. Several sensors from each batch will undergo the long-term test. Moreover, those sensors that showed an early breakdown or a non-standard leakage current behaviour (Fig. 4.11) should be tested as well as can exhibit such a behaviour due to a charge-up of the passivation layer that can disappear after a certain time.

A schematic view of the long-term test is depicted in Fig. 4.17. In order to perform a long-term test, the SMU connected to the sensor under test, is controlled remotely from a PC using a LabView software. Here, temperature and humidity deviations affect the leakage current, therefore, should be monitored during the measurement. The measurement setup is described in details in Section 3.3.4 of Chapter 3. In Section 3.7 the measurement results for the prototype sensors are presented.

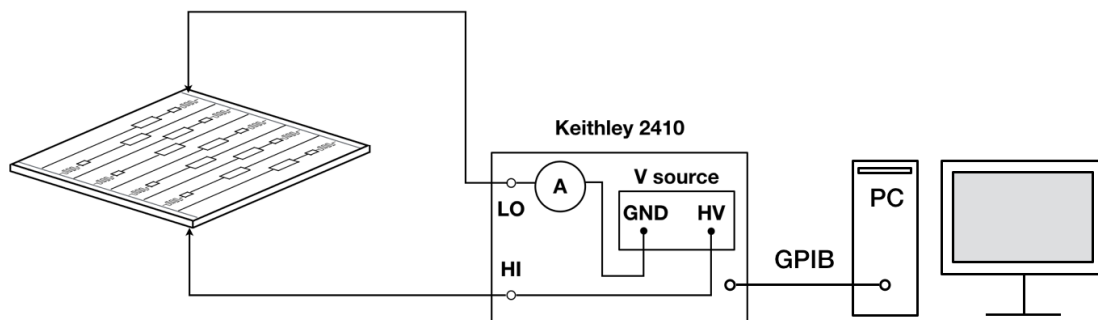


Figure 4.17: Schematic view of the long-term test.

4.6 Microscopic electrical tests

4.6.1 Coupling capacitance

The STS sensors have a capacitively coupling readout, i.e. the signals are read-out from an aluminum readout line⁷ implemented on top of the strip implant (Fig. 4.18), and insulated from it through a thin dielectric layer [31]. Such a design prevents the leakage current flowing into the charge sensitive amplifier (CSA) and provides the signal readout without a direct current compensation scheme.

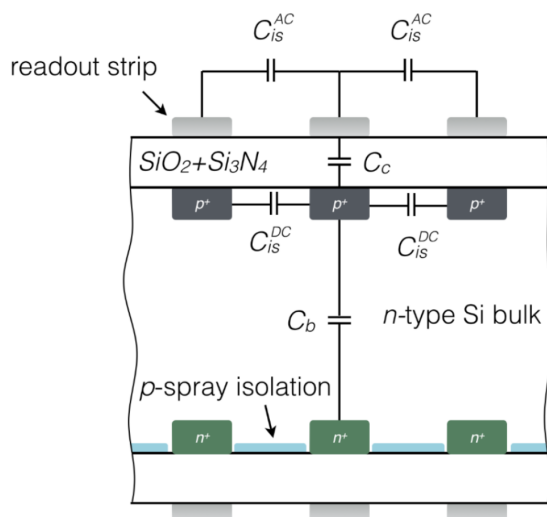


Figure 4.18: Schematic view of the capacitances in a double-sided segmented silicon sensor.

In order to ensure the vast majority of the charge to flow into the CSA, the coupling capacitance C_c should be much larger than the parasitic capacitances, in particular, the interstrip capacitance C_{is} . In practice, high values of the coupling

⁷Also called a *readout strip*.

capacitance can be achieved by reducing the thickness of the dielectric layer. However, technologically it is very difficult to obtain very thin layers without defects. Therefore, the dielectric layer actually consists of two layers: a bottom layer of SiO_2 and a top layer of Si_3N_4 . The latter is used to fill the possible pores in the silicon dioxide and, on one hand, is a preventing measure against coupling capacitor failures and, on the other hand, as the dielectric constant of silicon nitride is higher, it serves as an additional enlargement of the coupling capacitance [86].

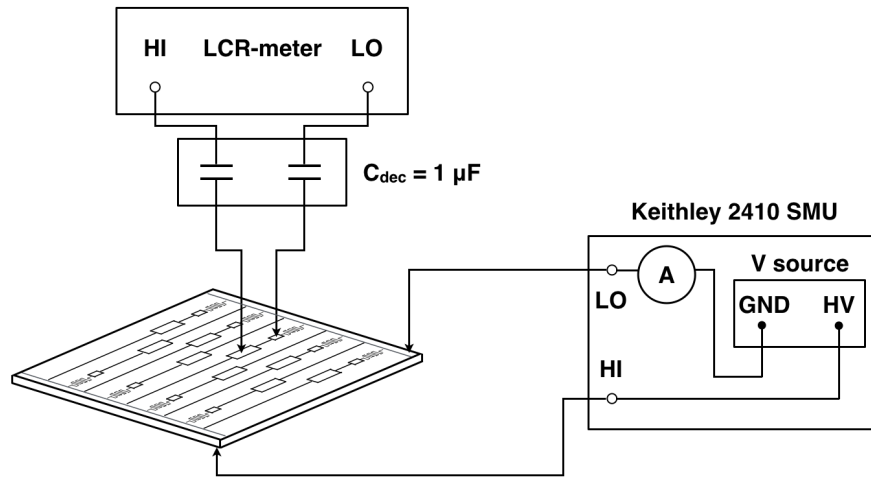


Figure 4.19: Coupling capacitance measurement scheme.

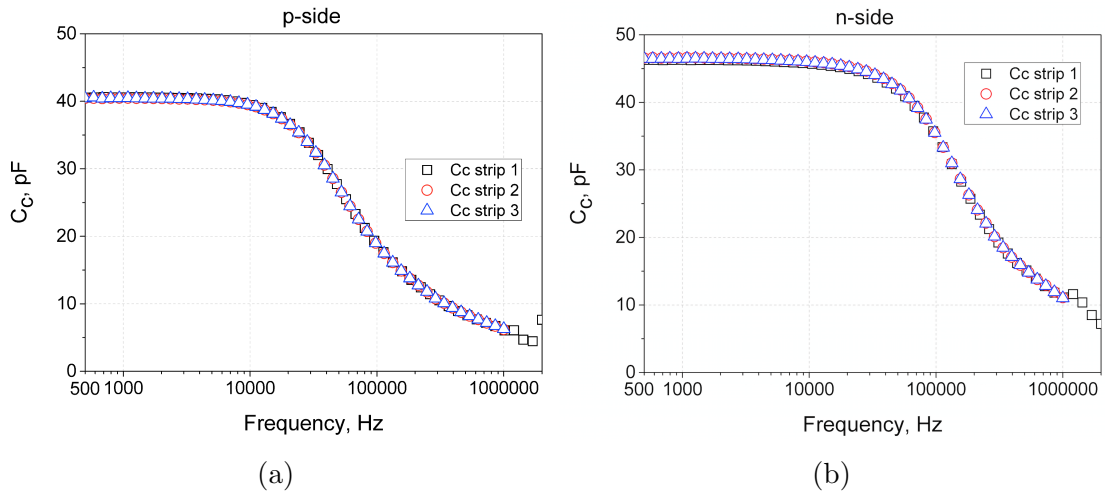


Figure 4.20: Frequency scan of the coupling capacitance for (a) p-side (b) n-side of a prototype sensor of a $6.2 \times 4.2 \text{ cm}^2$ size.

The scheme of the coupling capacitance measurement is illustrated in Fig. 4.19. The terminals of the LCR-meter are connected to the DC and the AC pads of the

a selected strip of a biased sensor or, if possible, to the AC pad and the bias line. In [64] it has been shown that grounding of the neighbouring strips during the measurement does not significantly affect the measurement results.

The coupling capacitance has a strong frequency dependence. Figure 4.20 shows the measured coupling capacitance as a function of the test frequency for both p - and n -sides of a prototype sensor. In a frequency range from 500 Hz to approximately 10 kHz a plateau is observed while afterwards the capacitance drops down until the end of the frequency range. In order to understand this effect one can think of the implant and the metal strip as a system comprising a series of finite but small resistors with distributed capacitors to the other electrode forming a high-pass filter [87]. In such a system, at high frequencies only a small fraction of the implant length will be “seen” by the LCR-meter due to finite resistance of the implant; thus the observed value of the capacitance will be reduced. Subsequently, the C_c should be measured at a frequency within the plateau region. Therefore, the measurements are performed at a 1 kHz frequency.

As mentioned above, the C_c value should be much larger than the parasitic capacitances of the strip, mainly the interstrip capacitance C_{is} . This requirement imposes the coupling capacitance for the STS sensors to exceed 10 pF/cm.

4.6.2 Interstrip capacitance

The measurement of the interstrip capacitance has to be performed on a fraction of the sensors from each batch, like C_c , selecting up to 10 strips per sensor side. C_{is} is a main component of the total capacitance w.r.t. the ground, it contributes to the load capacitance of the pre-amplifier, therefore, should be low to keep the noise of the system in a reasonable limit. Also, it is preferred to be low enough to provide good coupling of the signal into the readout electronics and to avoid the charge sharing among the strips. On the other hand, the charge sharing between the neighboring strips is required to improve the spatial resolution of the system. Therefore, the following expression describes the compromised requirement for the ratio of C_c and C_{is} for the STS sensors:

$$\frac{C_c}{C_{is}} > 10 \tag{4.1}$$

Different experimental groups have made several suggestions on how to measure the interstrip capacitance. For example, [88], [89]. The measurement method of the C_{is} that was used in this work is described below. The measurement arrangement of the chosen method is shown in Fig. 4.21. During the measurement, the sensor was kept at the operational voltage, $V_{fd} + 20$ V. As a preparation of the measurement, two neighbouring strips on each side of the strip under test were connected to each other via wire bonding, and afterwards both groups were interconnected

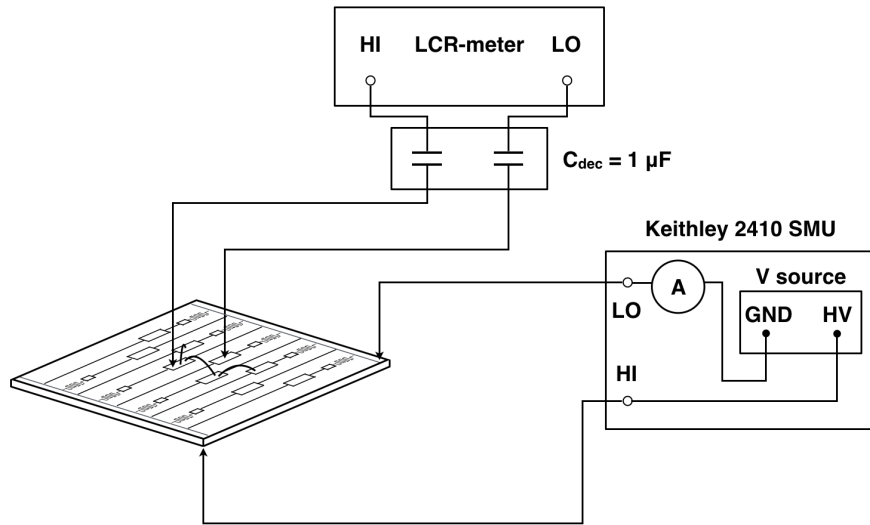


Figure 4.21: Interstrip capacitance measurement scheme.

together (Fig. 4.22). This connection provides a comprehensive measurement of the C_{is} as the interstrip capacitance includes all capacitances from the strip under test to the rest of the strips on the measured side⁸. The measured value in this case equal to twice the interstrip capacitance. One terminal of the LCR-meter

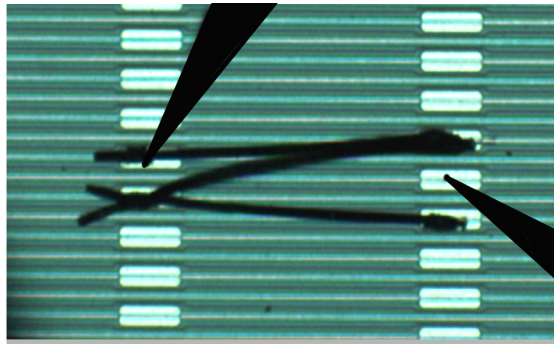


Figure 4.22: Strip interconnection for interstrip capacitance measurement. Two groups comprising the first two neighbouring strips of the strip under test are interconnected via wire-bonds. One probe needle contacts the AC pad of the strip under test, the second one contacts one of the AC pads of the neighbouring group.

was connected to the AC pad of the strip under test and the other one to the neighbouring AC pad representing a group of neighbouring strips. A frequency scan was performed for both the junction and ohmic sides of the sensor (Fig. 4.23). Herewith, the following consideration is taken into account: at high frequencies the coupling capacitor behaves as an AC short circuit [90]. This allows to measure

⁸Here, the contribution of the strips beyond the second neighbour is considered as negligible.

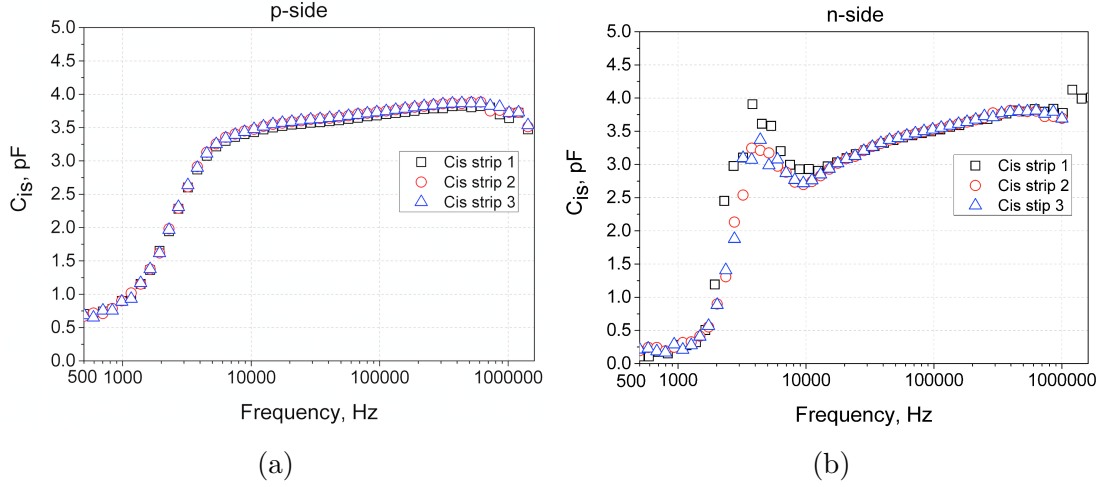


Figure 4.23: Frequency scan of the interstrip capacitance for (a) p-side (b) n-side of a prototype sensor of a $6.2 \times 4.2 \text{ cm}^2$ size

both C_{is}^{DC} and C_{is}^{AC} components of the interstrip capacitance using the presented method. The value obtained in the measurement equals to twice the interstrip capacitance as the strips from both sides of the seed strip are selected. At low frequencies a high pass filter effect is observed, suppressing the low frequencies by shunting them to ground through the polysilicon resistors [87]. Moreover, the measurement at the n-side of the sensor exhibits a peak in a frequency range of 4 to 9 kHz which is most probably attributed to an effect of the isolation structure between the n^+ strips. The value to be considered as C_{is} lies in the high frequency, close-to-plateau area starting from 10 kHz. The value of the C_{is} should obey the Eq. 4.1 and typically do not exceed 1 pF/cm for the STS sensors.

4.6.3 Interstrip resistance

Interstrip resistance R_{is} is a resistance between two neighbouring implants. It defines the integrity of the charge collected on individual strips and its subsequent flow into the readout electronics, and prevents the charge spreading among the neighbouring strips.

The value of R_{is} is desired to exceed tens or even hundreds of $\text{G}\Omega$ due to its irradiation sensitivity. The bottom limit of R_{is} can be estimated from the following consideration. It is required that the charge stays at the readout strip for a time considerably longer than the signal processing time $\tau = R_{is} \cdot C_{is} \gg \tau_{el}$ [91]:

$$R_{is} \gg \frac{\tau_{el}}{C_{is}}, \quad (4.2)$$

where C_{is} is the interstrip capacitance. Considering $C_{is} = 1 \text{ pF/cm}$ and the signal processing time $\tau_{el} = 1 \text{ }\mu\text{s}$, for a 6.2 cm long sensor we obtain $R_{is} \gg 161 \text{ k}\Omega$.

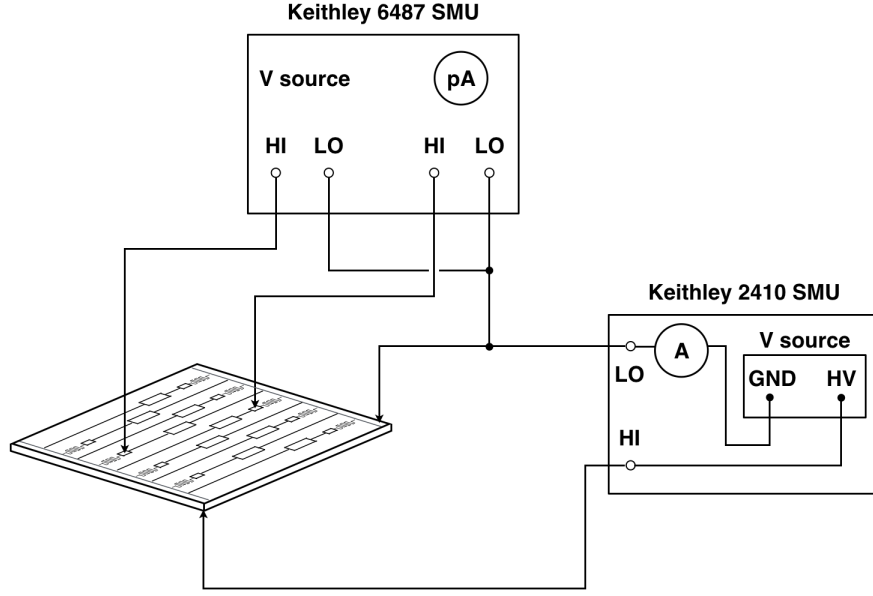


Figure 4.24: Interstrip resistance measurement scheme.

However, the requirements for R_{is} are usually such that it should exceed tens of $\text{G}\Omega$ as it decreases with irradiation. In [92] it has been shown that starting from well above $10 \text{ G}\Omega$ before irradiation, R_{is} decreases to few hundreds $\text{M}\Omega$ already at $5 \times 10^{13} \text{ n}_{eq}/\text{cm}^2$ and degrades down to tens of $\text{M}\Omega$ with further irradiation. However, this value is still acceptable if the bias resistors are on the level of a few $\text{M}\Omega$.

Measurement of the interstrip resistance using different methods is well described in [93]. For sensors having a *poly-Si* biasing mechanism, R_{is} should be measured in the way excluding the influence of the poly-silicon resistors R_{poly} since the latter is connected in series and has a value which is orders of magnitude lower than the interstrip resistance. The connection scheme for the R_{is} measurement is depicted in Fig. 4.24.

The interstrip resistance is defined as a ratio of the change in the strip current caused by the change of the testing voltage:

$$R_{is} = \frac{\Delta I_{strip}}{\Delta V_{test}} \quad (4.3)$$

As the STS sensors are expected to be exposed to a maximum of $1 \times 10^{14} \text{ n}_{eq}/\text{cm}^2$ the R_{is} is required to exceed $10 \text{ G}\Omega$ for non-irradiated sensors. The measurements on the latest prototype sensors are currently being performed.

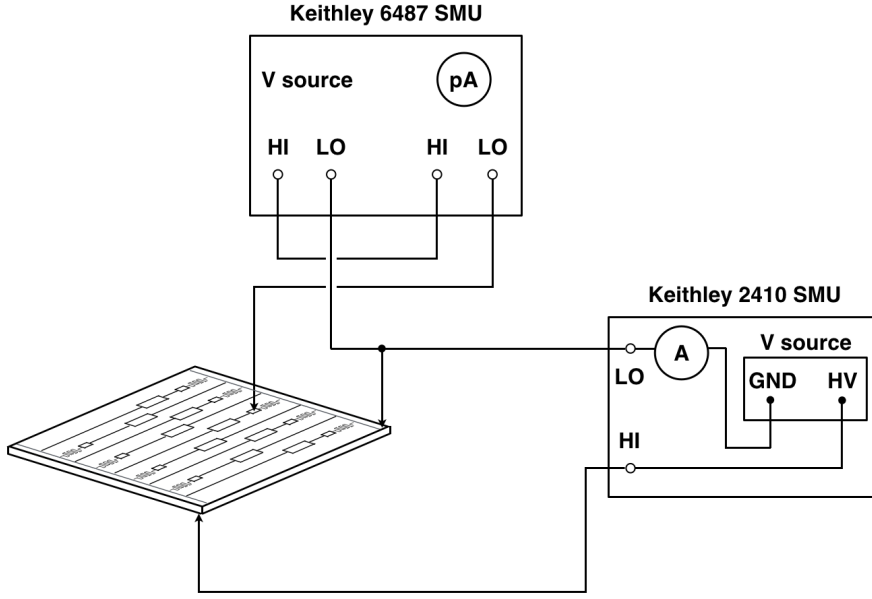


Figure 4.25: Bias resistance measurement scheme.

4.6.4 Bias resistance

The bias voltage can be provided to each strip of the sensor via punch-through [91] and FOXFET [94] techniques, or via poly-Si resistors. In the STS sensor design, poly-Si resistors are implemented. Poly-Si resistors R_{poly} have a high linearity along a wide range of voltages in contrast to the punch-through and FOXFET contacts and exhibit higher stability after irradiation [96]. The last feature becomes important particularly for the STS sensors with their expected irradiation beyond the point of type inversion where the properties of punch-through and FOXFET structures are not sufficiently studied yet. The disadvantage of the poly-Si biasing method is its production complexity comprising around 10 technological operations [95] which may lead to a variation of R_{poly} values within a sensor and, as a result, distortion of the electric field in the sensor bulk. For this reason, a deviation from the nominal value of R_{poly} should not exceed 15% within a single sensor.

The poly-Si resistor, connected in parallel to the pn -junction, produce a parallel thermal noise which contributes to the overall equivalent noise charge (ENC) and is inversely proportional to the square root of R_{poly} :

$$ENC_{R_{poly}} \propto \sqrt{\frac{k_B \cdot T}{R_{poly}}} \quad (4.4)$$

This expression therefore imposes R_{poly} to be high for lower noise contribution. On the other hand, with irradiation the leakage current of the sensor increases proportionally with the fluence (see Section 2.4) and in case of high-ohmic bias

resistor the voltage drop may become significant. As a compromise, the value of $1\text{ M}\Omega$ is chosen for the STS sensors. Additionally, at the CBM operational temperature $T_{op} = -5\text{ }^\circ\text{C}$, the parallel thermal noise contribution will be reduced.

The CMS and ATLAS collaborations have reported on observed defects of poly-Si resistors such as disruption of the resistor structure (see Figure 4.7). During the production of the STS prototype sensors, this defect has not been observed so far. The optical inspection procedure described in section 4.4.1 performs an analysis of the integrity of the poly-Si resistors. Nevertheless, the poly-Si resistor values have to be controlled on a fraction of sensors from each batch, following the optical tests.

The method of the poly-Si resistor measurement is depicted in Fig. 4.25. Here, the bias resistor is connected in parallel with the resistance of the depleted pn -junction. As the resistance of the latter is much larger than R_{poly} , the measurement accuracy in such a connection is not affected by it. A test voltage between the poly-Si resistor and the bias line should be applied with a step of a 0.1 V ending up with 1 V . The value of R_{poly} is obtained from the slope:

$$R_{poly} = \frac{dV_t}{d(I_{meas} - I_{strip})} \quad (4.5)$$

For the STS sensor the nominal value of R_{poly} equals to $1.5\text{ M}\Omega$. The deviation from this value within one sensor should not exceed 1%.

4.7 Strip diagnostic tests

4.7.1 “Pinhole” test

A “pinhole” is a short circuit or an ohmic contact between the strip implant and the aluminum readout line in case of capacitively coupled read-out. As the STS sensors have a capacitive coupling readout, such a defect leads to a leakage current flowing directly into the readout electronics, therefore can cause a severe effect on circuiting of the channel up to saturation, or even inoperability of the whole ASIC. Therefore, the strips with identified pinholes must not be connected to the readout ASIC.

Pinholes can originate during the sensor manufacturing as well as because of intolerate shipping or handling. Thus, the pinhole test must be performed after the delivery of the sensors, even if it has been already done by the company. The pinhole test is performed by connecting the outputs of the SMU to the DC and the AC pad of a strip under test or, if allowed by design, to the AC pad and the bias line. A test voltage up to 20 V is applied and the current through the dielectric layer is measured. The connection scheme is depicted in Fig. 4.26.

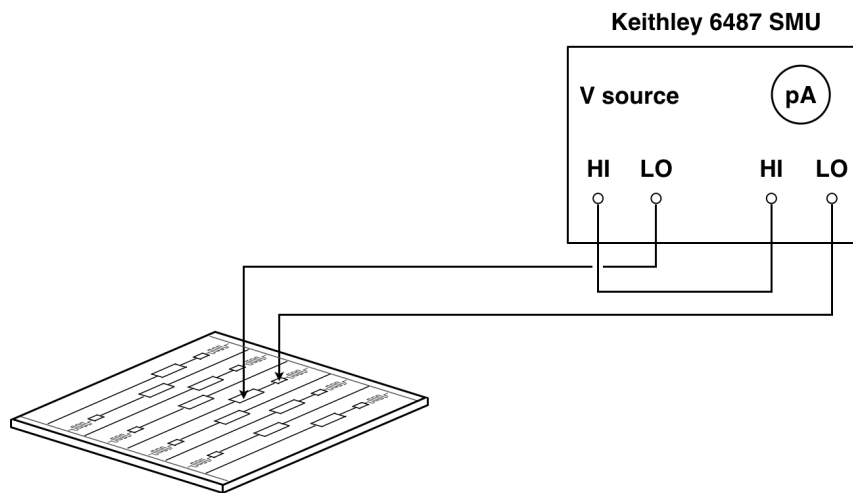


Figure 4.26: Pinhole test measurement scheme.

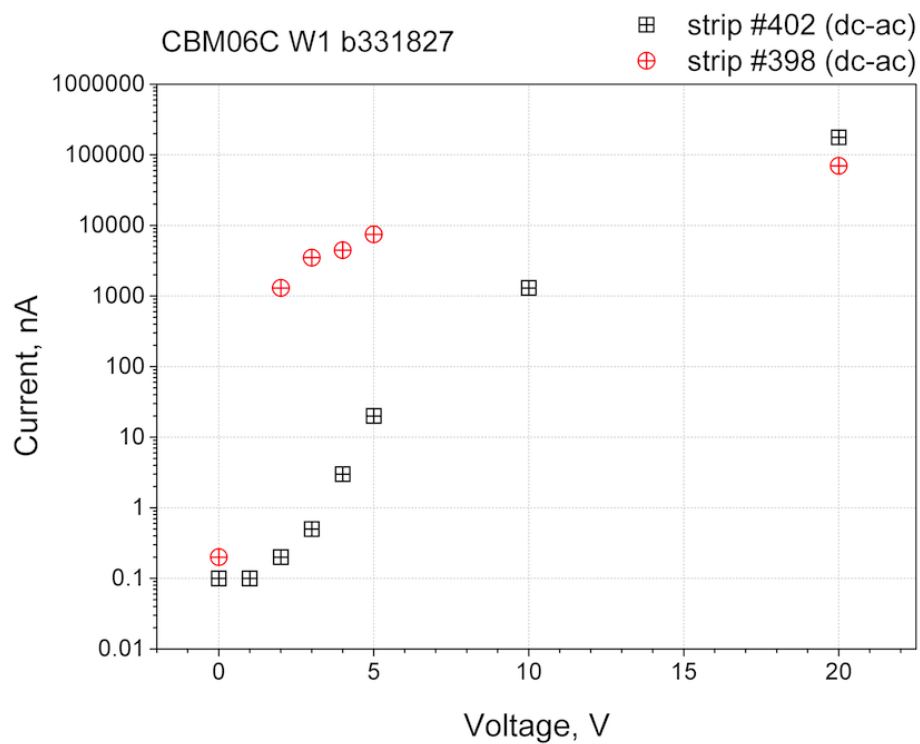


Figure 4.27: Two types of pinholes: ohmic (red circles) and non-ohmic (black squares).

Here, two types of pinholes were identified. First, an ohmic-type pinhole, is observed already at test voltages of a few volts. This type is either a result of incomplete etching or a hole in the dielectric layer developed due to a defect of the photomask. The second type of pinholes is created if the dielectric layer is too thin. The measured value for the second type of pinhole is several times higher than the average measured value⁹ for a normal strip at low test voltages but increases dramatically when higher voltages are applied (Fig. 4.27). In order to identify both types of pinholes the test must be performed at the 20 V test voltage.

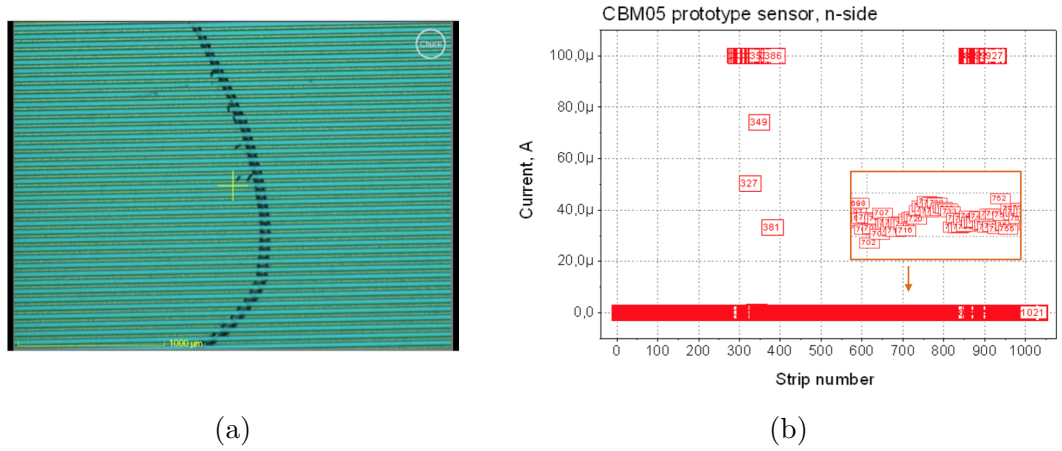


Figure 4.28: (a) Scratch of the sensor surface; (b) Pinhole scan: 62 pinholes developed due to the scratch.

Table 4.1: Pinhole test results for the STS prototype sensors.

Sensor	Type	Wafer number	Number of pinholes	
			p-side	n-side
CBM03'	Single-sided	7	0	-
CBM03'	Single-sided	10	5	-
CBM03'	Single-sided	13	0	-
CBM05	Double-sided	4	0	4
CBM05	Double-sided	6	0	0
CBM05	Double-sided	13	1	62
CBM05	Double-sided	0	0	0
CBM05	Double-sided	0	0	0
CBM05	Double-sided	0	0	0

⁹Of the current through the dielectric layer.

Transportation can be another reason for pinholes to appear. For instance, the DELPHI experiment experienced a significant pinhole development during transportation because of a chemical reaction of plastic packaging with the silicon dioxide [26]. Thus, the packaging should be selected carefully avoiding materials that can chemically or electrostatically interact with the sensors.

Also, intolerate handling may result in a considerable pinhole development. Figure 4.28a shows the surface of a scratched sensor that was damaged during a handwork accident in the assembly lab. The pinhole test performed afterwards identified 62 pinholes in the area of the scratch (Fig. 4.28b). Pinhole test results for the STS prototype sensors are given in Table 4.1.

4.7.2 Readout strip short circuit test

This test aims to identify “shorts”, i.e. ohmic connections between two or more readout strips. Such a defect is usually produced during the final stage of sensor production. Proper materials, e.g., a thick cleanroom paper is therefore employed.

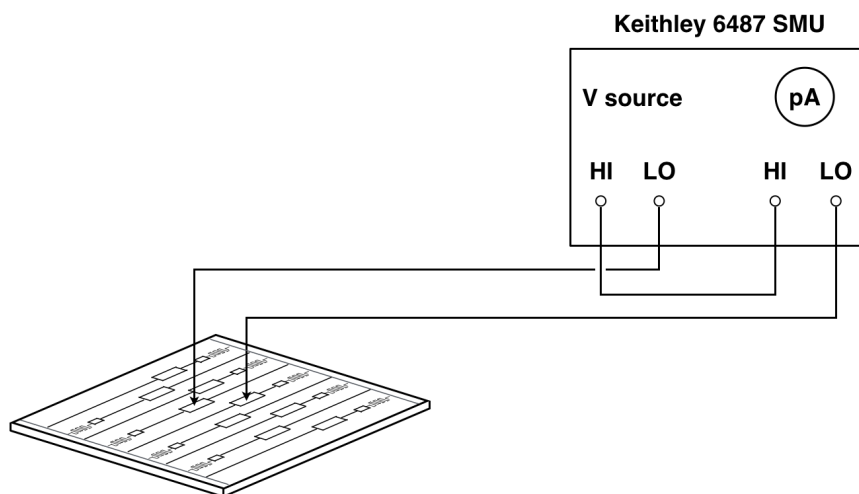


Figure 4.29: Measurement scheme for the readout short strip test.

If two or more strips are coupled together, the capacitive load of the electronics channel becomes several times higher than the nominal value, increasing the noise of the preamplifier. Also, due to connection of multiple strips, the position resolution will be corrupted. The sensors having shorted strips must be arranged, if at all, in the remote parts of the stations where the hit occupancy is lower compared to the innermost areas. Therefore, the readout strip short test should be performed for all the sensors following the pinhole test.

Figure 4.29 represents the measurement scheme of the test. The terminals of the SMU are connected to two neighbouring AC pads. The measurement is performed by applying a voltage ramp and measuring the resulting current. A stable ohmic connection gives a current of the order of microamperes at low test voltages while the current through a normal insulator stays below 1 nA.

There are also another methods of identifying the shorts between the readout strips including the measurement of the total strip capacitance or the measurement of the capacitance between the AC pad and the bias line during the operation of the sensor in a forward biased mode [86]. The method described in this section is easy to realize and gives an unambiguous result for ohmic connections, compared to capacitive measurements.

4.7.3 Strip leakage current test

Strips having high leakage current may be dangerous for operation of the readout chip. Also, the information in the neighbouring strips can be affected due to this defect [97]. Therefore, strips suffering from high leakage current must be identified and should not be coupled to the readout electronics. Measurement of the strip

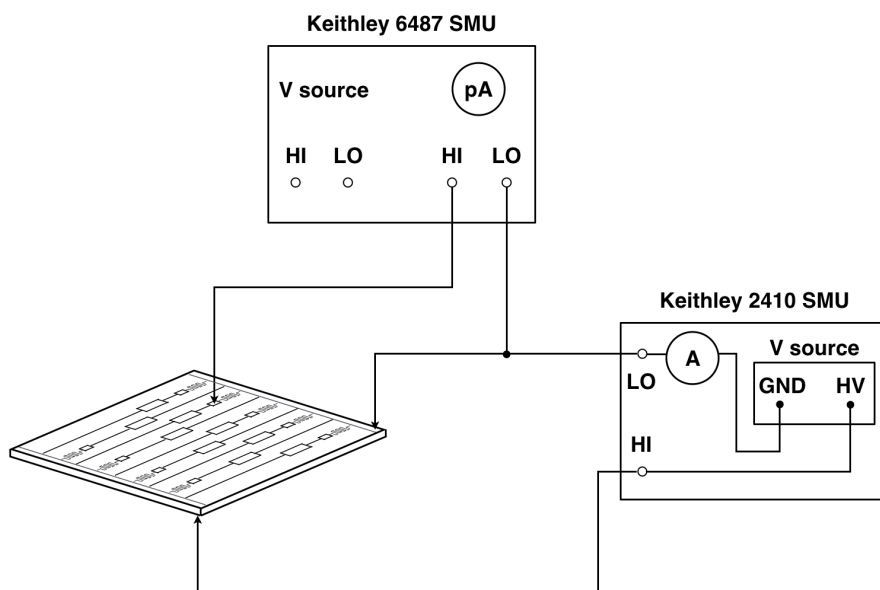


Figure 4.30: Strip leakage current test measurement scheme.

leakage current requires the sensor under test to be kept at the operational voltage, and the terminals of the picoammeter connected to the DC pad and the bias line (Fig. 4.30).

The measured values of the strip current usually ranges from 1 to 10 nA depending on the sensor. A strip having the leakage current of one order of magnitude

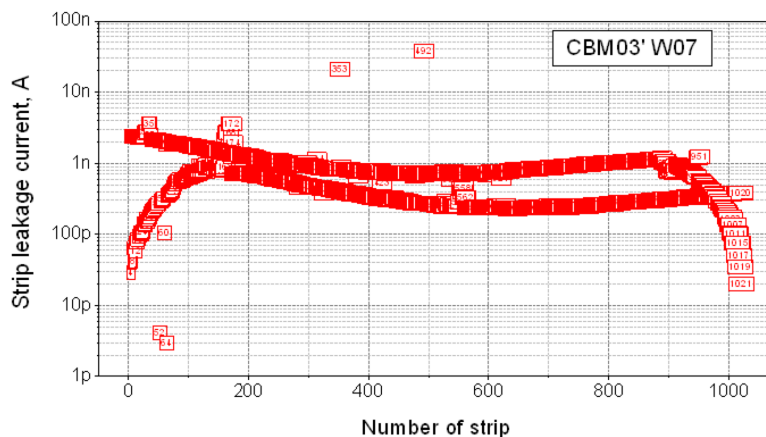


Figure 4.31: Strip current for a junction side of an STS prototype sensor.

or higher than the average value for this very sensor is considered as problematic and should not be connected to the readout electronics.

A typical strip current distribution for the junction side of a prototype sensor is depicted in Fig. 4.31. One can notice that the measured value gradually decreases towards the first and the last strips. This is due to a decrease of the strip length towards the corners of a sensor at the junction side (see Fig. 1.9).

4.8 Quality of the sensors

Based on the inspection data provided by the vendors, strip fault statistics was analyzed. Several batches of the latest prototype sensors were considered. Here, inspection performed by CiS include the “pinhole” test, while Hamamatsu conducted the “pinhole” and the readout strip short tests.

The sensor quality in terms of strip faults is found to be very high. Considering 2048 strips per sensor¹⁰, less than 0.3% of strip faults are observed for the majority of CiS sensors, and less than 0.7% for the majority of Hamamatsu devices. Currently, the acceptance criterion for the total number of strip defects is 1% per sensor. The strip leakage current test is not performed at the fabrication sites. The quality tests to be performed by the vendors are being discussed presently. If the strip leakage current test will not be performed by the vendors, it has to be performed at the CBM Quality Test Centers. Therefore, in order to be able to identify the most common strip defects (pinholes and the readout strip shorts), and the strip leakage current, an automated test stand has been assembled in the

¹⁰In practice the number of strips per sensors is higher. Due to a stereo angle at the p^+ side, the corner strips at both edges must be counted separately. Thus, for a 6.2×6.2 cm² sensor, the actual number of strips is 2182. For a 6.2×4.2 cm² sensor it equals to 2134.

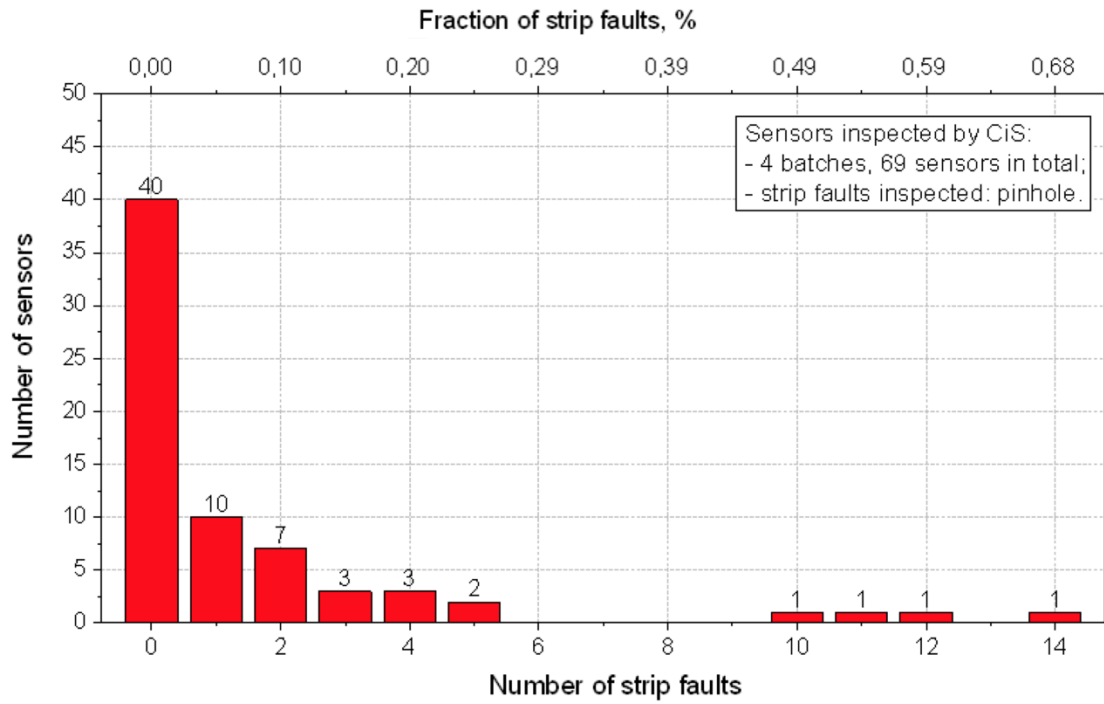


Figure 4.32: Statistics on strip faults of several batches of the prototype sensors, inspected by CiS.

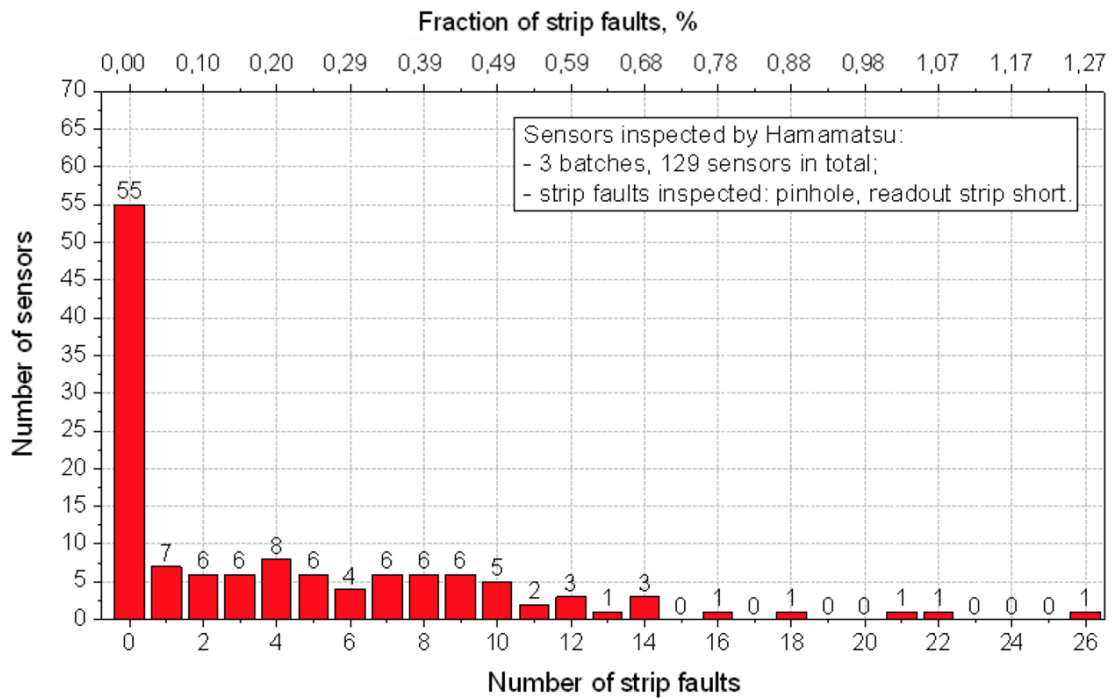


Figure 4.33: Statistics on strip faults of several batches of the prototype sensors, inspected by Hamamatsu.

cleanroom of the GSI QTC. The next chapter describes the development of a test stand for automated strip diagnostic tests.

Chapter 5

Development of the test stand for automated strip diagnostic tests

In the previous chapter the quality assurance tests that will be applied on the STS sensors were overviewed, the methods and measurement equipment were defined. Here, the strip diagnostic tests are required to ensure the quality of each strip of the sensor. In this case, automation of the strip diagnostic tests is crucial in terms of large-volume production. Also, by reducing the human error factor that can lead to damage or even destruction of the objects, it serves as an additional safety aspect.

Beyond that, the automated strip diagnostic tests can reduce the mechanical damage of the testing pads surfaces caused by multiple probing, saving the channel yield as well. Automated measurements require a software control of the hardware elements of the setup including the measurement units, the probe station electronics and the data acquisition system. In this Chapter, the development of the automated strip diagnostic test system for the GSI Quality Test Center, is described.

5.1 Remote control of the probe station electronics

In order to automate the tests performed on the probe station, the remote control of the hardware units should be established. The probe station's electronics module (Fig. 5.1) manages the main operational functions of the probe station: control of the chuck and the microscope movements in X-Y-Z directions, rotation of the chuck, vacuum control and communication with the ProberBench PC. The ProberBench firmware installed on the ProberBench PC provides the operation of the probe station in a semi-automatic mode. The communication between the



Figure 5.1: The probe station electronics module.

ProberBench PC and the probe station electronics module is provided via Ethernet. Therefore, to be able to control the probe station remotely, an instrument communicating with the ProberBench operating system is required.

5.2 Software tools for remote control of the probe station and the measurement units

The ProberBench firmware installed on the ProberBench PC is suitable for a stand-alone operation using the joystick of the Expert Control Panel, shown in Fig. 4.5, as well as the graphical user interface of the ProberBench PC. However, this configuration has limited capabilities and allows a user to work in a semi-automatic mode, e.g. each movement of the chuck or the microscope is performed by pressing a button.

Simultaneous control of the probe station electronics and the measurement units, required for automated tests, is only possible using an additional software. Due to specifics of the application, such a software is not available on a commercial market. The ProberBench firmware supports the following programming tools: Agilent Vee, Borland Delphi 7, Borland C++ Builder, Borland C# Builder, Microsoft Visual Basic 6, CEC TestPoint, TransEra HTBasic 90, National Instruments LabVIEW versions 7.0 and upper, and others [98]. The National Instruments LabVIEW software platform has been chosen as a base for the software development among other programmer tools due to availability of the programmer tools for both the measurement units and the probe station electronics.

LabView is a system-design platform and development environment based on a graphical programming interface (Fig. 5.2). The programming language used in LabView is a dataflow programming language. Execution is determined by the structure of a graphical block diagram on which various function-nodes are connected by drawing the “wires” which propagate variables and any node can

5.3 Concept of the automated test system

execute as soon as all its input data becomes available [99]. LabView programs

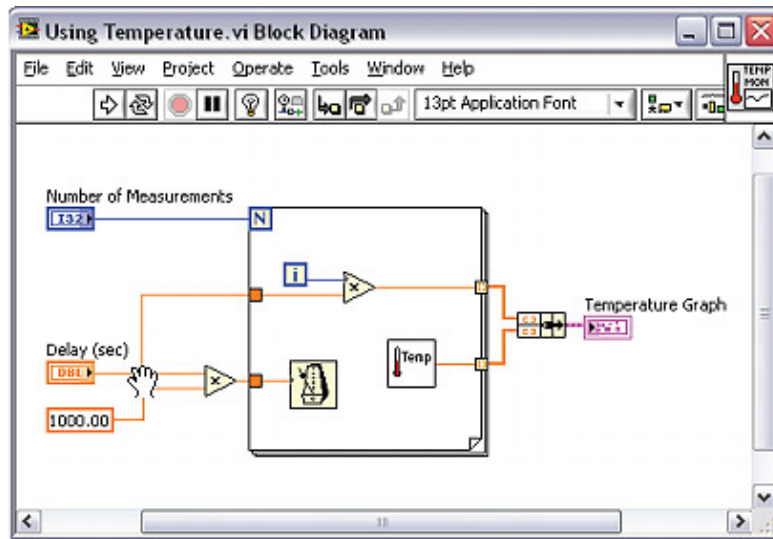


Figure 5.2: Example of a block diagram in LabView.

and subroutines are called Virtual Instruments (VI). Each VI has a block diagram and a front panel.

Basic sets of virtual instruments for the probe station and the measurement units' remote control are provided by the manufacturer companies and are available for download online [100]. However, in many cases, the VIs provided by a manufacturer do not allow for a full functionality of the hardware units or they are not optimal for a dedicated task or a command. Therefore, some of the VIs provided by the manufacturer were modified by the author for better productivity of the software, or developed from scratch.

5.3 Concept of the automated test system

The following concept of the automated test setup is proposed using the considerations mentioned above. A stand-alone Master PC was proposed as a host of the software and the GUI as well as a main communication hub providing the remote control of all the measurement units. The ProberBench PC, which is disconnected from the local network for security reasons, in this case only keeps a function of controlling the probe station electronics.

Figure 5.3 illustrates the communication between the units of the setup in details. The Master PC establishes a connection to the ProberBench PC via a serial port (RS-232). This communication type is reliable and fast enough to provide the command exchange and the data transfer between two PCs. Moreover,

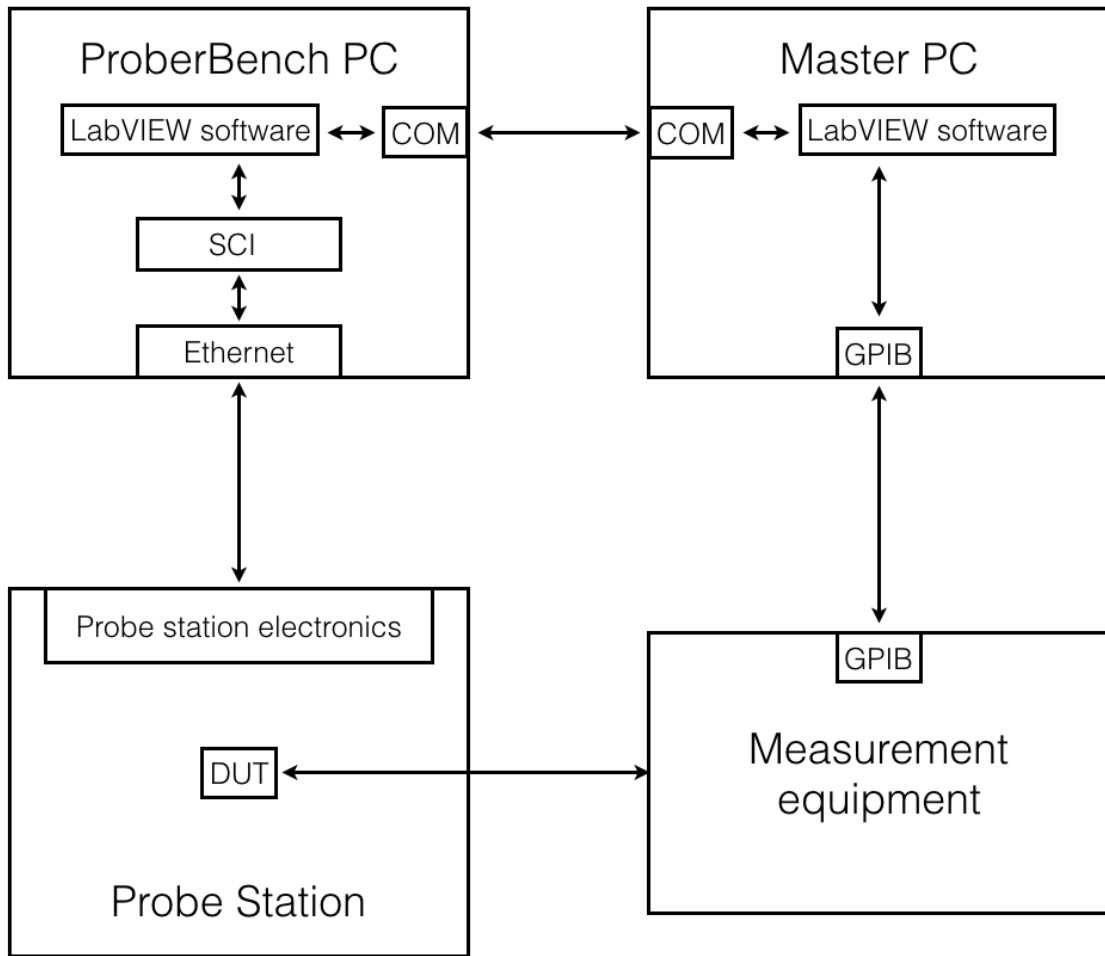


Figure 5.3: Concept of the communication with the test setup components.

it does not depend on network availability¹.

The concept suggests the Master PC to be the main and the only control and data processing unit. It communicates both with the measurement units connected to a device under test at the probe station via sending the commands to the ProberBench PC. Here, the commands between the two PCs are exchanged through a custom made communication/data transfer protocol developed in the LabView environment. The development of the protocol is described in details in Appendix C.

¹As network failures occur sometimes, the communication and data transfer system should not depend on the network connection in order to avoid the delay of the test workflow if the latter takes place.

5.4 Automation of the probe station operation

An automated stepping procedure that allows to probe the strips sequentially was realized via a combination of several commands²:

1. *SetChuckHeight* defines the current height of the chuck as a contact height. Wherein, the alignment and separation heights are calculated automatically.
2. *SetChuckIndex* is used to set the index size of the wafer along the X and Y axes. Due to the layout of the probing pads the index value is set to twice the strip pitch;
3. *MoveChuckIndex* is used to move the chuck stage in index steps along the X or Y axes. This command moves the chuck down to the separation height, then performs a step to the next strip equals to the index value and finally sets the contact height;
4. Steps 1-2 are performed once before starting the stepping procedure;
5. Execution of the step 3 in a loop provides stepping over the desired number of strips³;

The commands are sent via the developed communication protocol from the Master PC to the ProberBench PC using a set of developed virtual instruments.

5.5 Remote control of the measurement instruments

Remote control of the measurement instruments was established using the package of standard virtual instruments, provided by the manufacturer, and custom made virtual instruments, developed by the author. It comprises a library of virtual instruments for initialization, configuration and reading of the measured parameters. Special attention was paid for configuration of the Keithley 6487 SMU as it defines the measurement speed and its accuracy. The details of this configuration are discussed in Section 5.10.

²The commands are compatible with the Süss ProberBench firmware.

³Equal to the index value of the loop.

5.6 Development of an automated pinhole and readout strip short circuit test system

After the stepping procedure was realized and the virtual instruments for the remote control of the measurement units were prepared, a software for an automated pinhole and readout strip short circuit test was developed as a base for further development.

In order to synchronize the measurement and the chuck stepping the built-in LabVIEW structures known as the “Flat sequence structure” were used. This structure, as shown in Fig. 5.4, executes commands from left to right. It ensures that the right subdiagram is not executed until the left one is executed. An

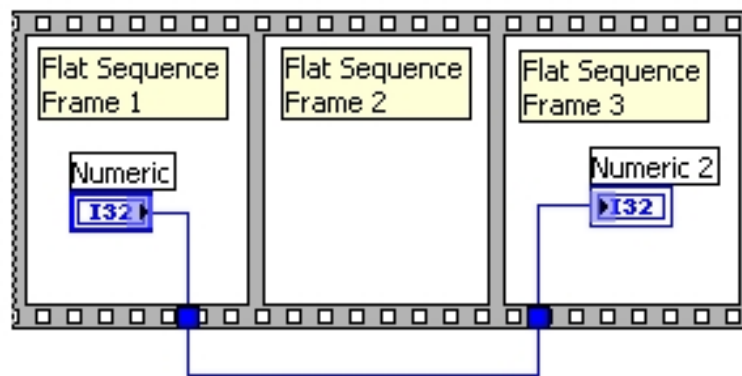


Figure 5.4: Flat sequence structure in LabView.

interface of the developed program is depicted in Fig. 5.5. It features two tabs, one for the measurement configuration and the execution control and the second one for handling the errors. The front panel feature several buttons to start and stop the measurement, and also a standby button that allows to pause the measurement and to continue it from the last point. The number of strips to measure is set before the start button is pressed in a corresponding field. The block diagram of the program contains several structures for synchronization, event handling, online display of the measured parameters, sorting of the data and others.

Due to the fact that the pinhole and the readout strip short circuit tests are similar with the only difference of the probing needles arrangement, both measurements are possible to be performed. During the test, the measured parameter is indicated in an auto-updated table. Each measured value is compared with a pre-defined compliance value. If the latter is exceeded, a “Defect” result is printed in a third column in front of the corresponding strip. Otherwise, the “Ok” message is printed. The bottom panel allows to set the location of the text file with the measurement results. The right bottom field indicates the number of identified defects.

5.6 Development of an automated pinhole and readout strip short circuit test system

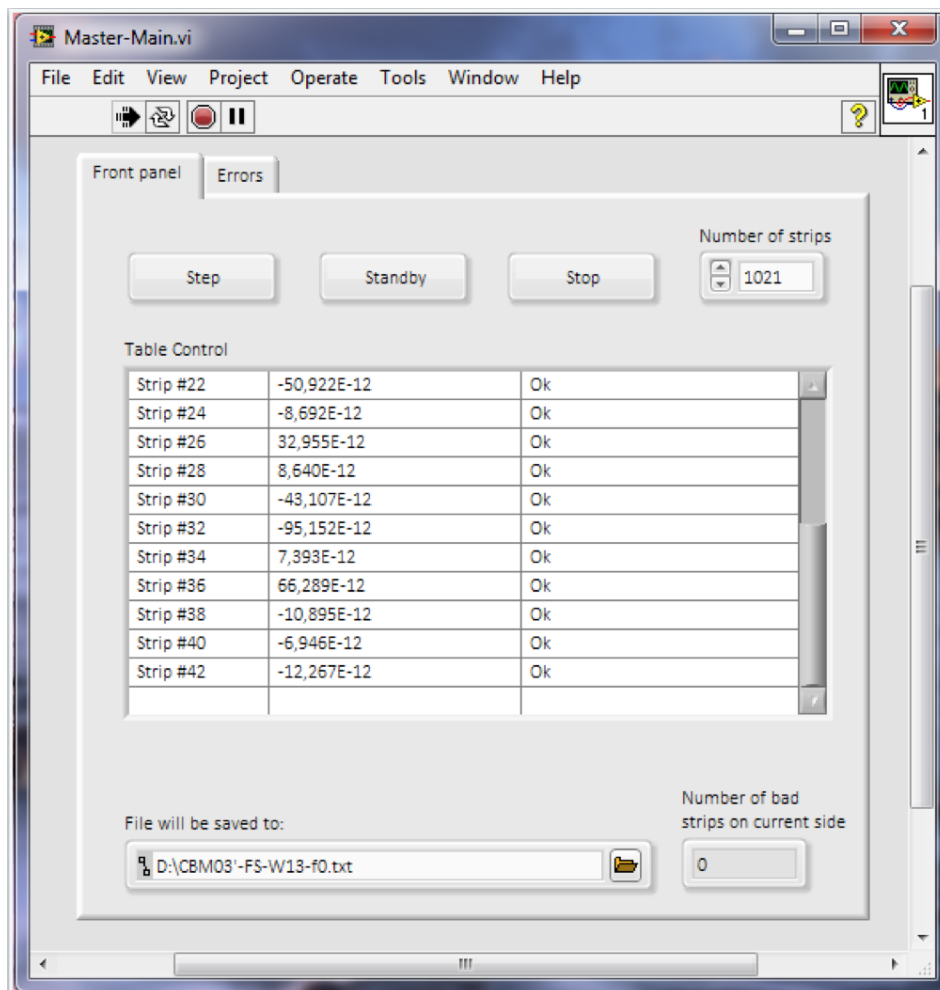


Figure 5.5: Interface of the automated software for the pinhole and the readout strip short tests.

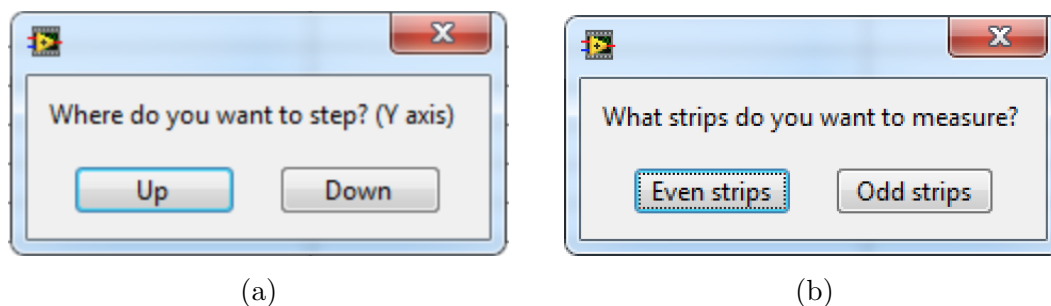


Figure 5.6: (a), (b): pop-up windows with options for the measurement configuration.

After the "Step" button is pressed, two pop-up window containing the additional measurement configurations are displayed (Fig. 5.6). Typical pinhole test result is illustrated in Fig. 5.7. The pinhole test results for the STS prototype sensors of various families are presented in Table 4.1.

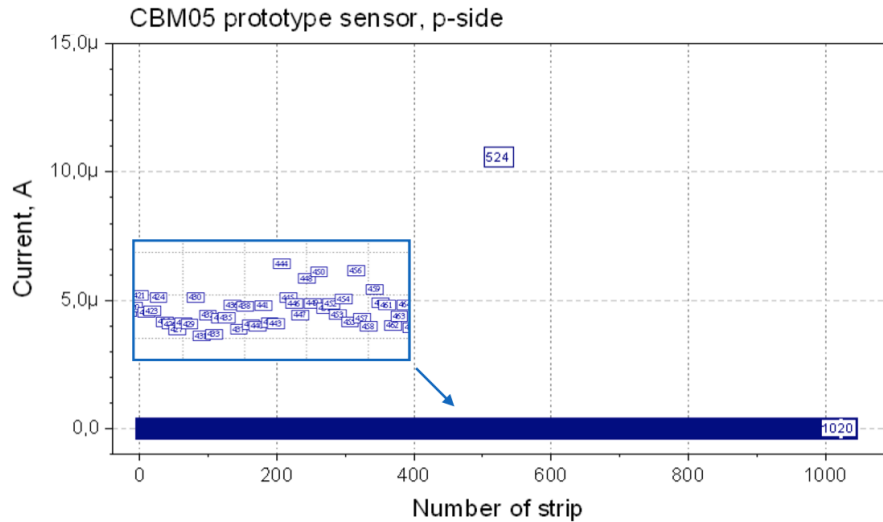


Figure 5.7: Pinhole scan of a prototype sensor. A single pinhole defect was identified for the strip number 524.

5.7 Development of an extension for a strip current measurement

As mentioned in Section 4.7.3, measurement of the strip current is particularly important as if high current is observed, the strip should not be connected to the readout electronics. A set of virtual instruments was developed for configuration and operation of the measurement unit used in the strip leakage current measurements - the Keithely 6487. An extension was implemented such that a pop-up window appears, asking for the type of measurement to start with (Fig. 5.8). Typical results of the strip current scan are presented in Fig. 5.9.

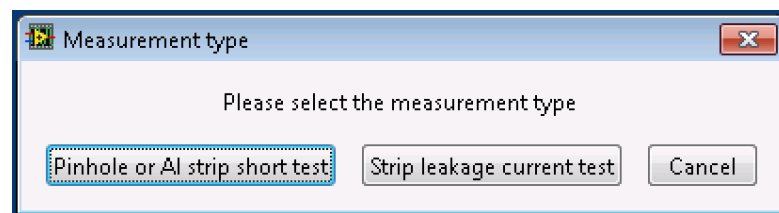


Figure 5.8: Selection of the measurement type

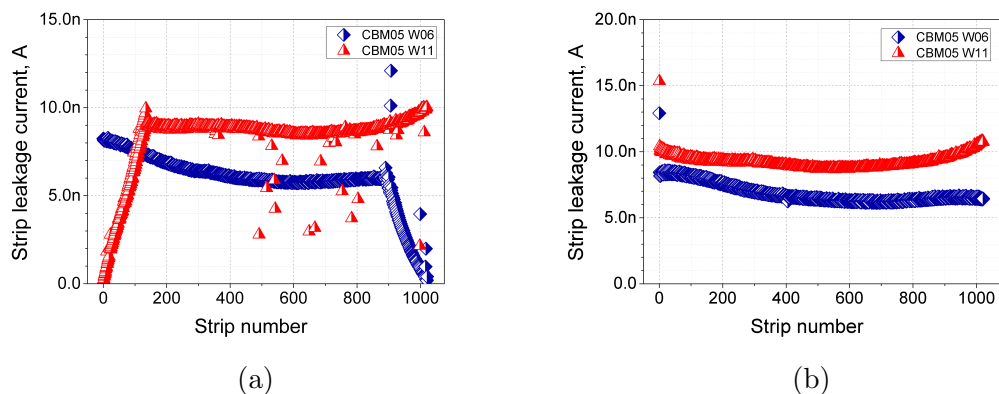


Figure 5.9: Automated measurements of the strip leakage current for STS prototype sensors: a) p-side b) n-side.

5.8 Optimization of the measurement setup by using a switching matrix

A switching matrix or multiplexer is a device that has a certain number of input and output channels where any input channel can be connected to any output channel. Different kinds of switching matrices are available commercially. By



Figure 5.10: Front and rear views of the Keithley 708B mainframe with the switching card 7072-HV installed [101].

introducing a switching matrix the following improvements can be realized:

- reduction of the measurement time by performing multiple measurements;
- reduction of the damage probability of the sensor by testing personnel due to numerous handling of the sensors;

- reduction of the surface damage of probing pads surface damage due to less probing violation.

For optimization of the STS QA setup, the Keithley 708B unit mainframe equipped with the Keithley 7072-HV switching card (Fig. 5.10) was chosen according to their following benefits:

- Availability of the LabView programmer tools package;
- Compatibility with Keithley 2410 and 6487 instruments by design;
- High single-command execution speed;
- Low offset of the measured parameters;
- High voltage operation for selected channels up to 1100 V;
- Special paths for low-current and capacitive measurements (Fig. 5.11).

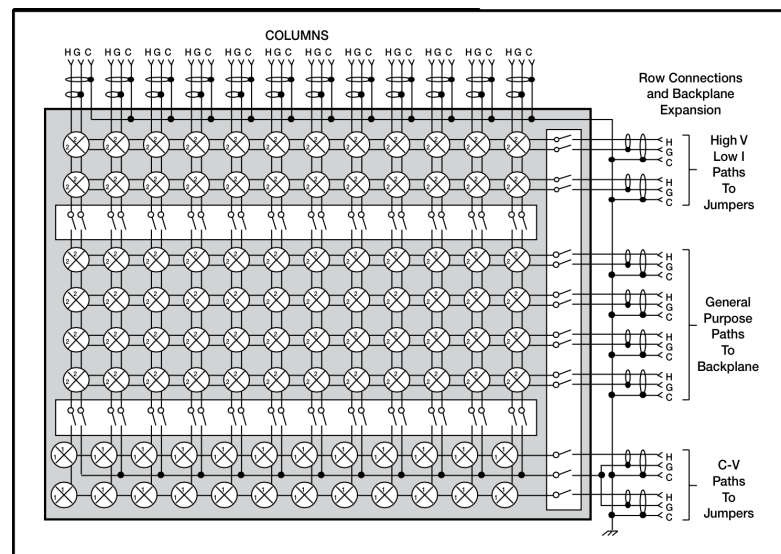


Figure 5.11: Schematic view of the Keithley 7072-HV switching card [101].

As the probe station hosts four manipulators with probe needles, all of them can be involved in the test procedure. Figure 5.12 shows an arrangement of the probing needles that allows to probe the AC and DC pads of a central strip and the AC pads of the neighbouring strips. The picture shows that two neighbouring DC pads cannot be probed simultaneously due to design specifics. The advantage of using a switching matrix is seen as a possibility to use various needle combinations to perform a full set of strip diagnostic tests in a row.

Each needle connected to the output of the switching unit can be linked to any of the measurement devices' output. The following tests can be performed using the combination of needles shown in Fig. 5.12:

5.8 Optimization of the measurement setup by using a switching matrix

- The sensor under test is biased after the C1 and D2 connections are established. The strip leakage current test is performed using the needle number 4. To complete the measurement circuit according to section 4.7.3 the 4A and 2B connections should be closed.
- Using the needles number 4 and 5 the pinhole test is performed. Here, the 4A and 5B connections are closed. Also, using the same combination, the coupling capacitance can be measured (Section 4.6.1);
- The needles number 5 and 6 are used to conduct the readout strip short circuit test between the central strip and it's upper neighbour with the connections 5A and 6B closed;
- The needles number 5 and 3 are used for the readout strip short circuit test between the central strip and it's lower neighbour with connections 5A and 3B closed.

Hence, a switching matrix is a powerful instrument for the automation of strip diagnostic tests that allows to perform multiple measurements in a row. The

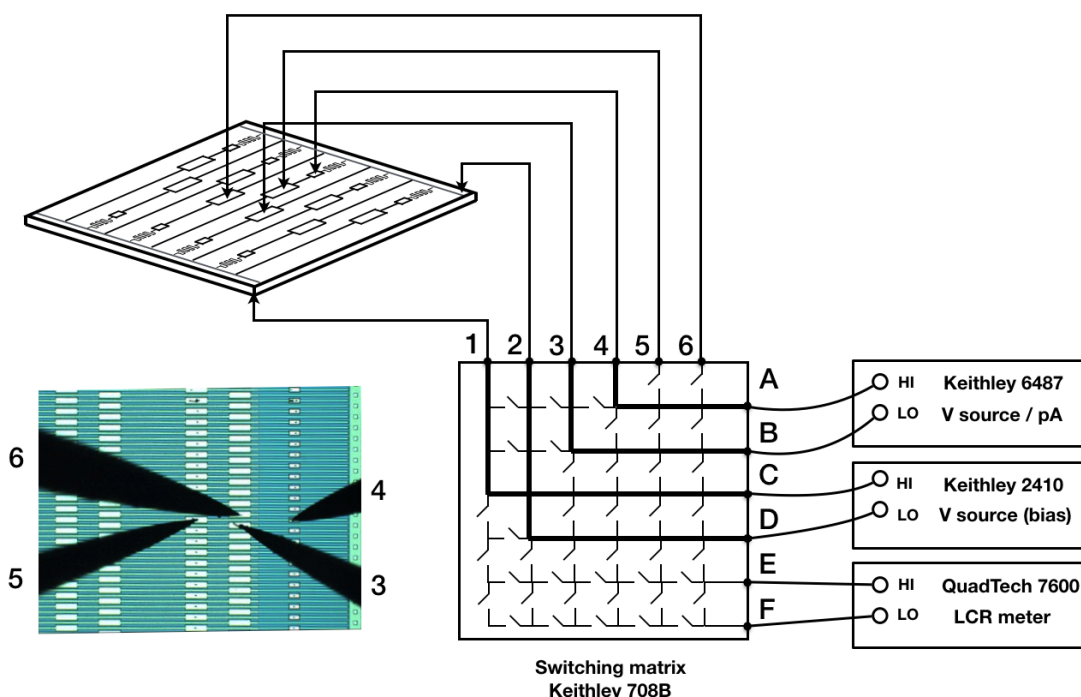


Figure 5.12: Arrangement of the instruments for a multi-purpose strip diagnostic test.

intergration of the switching unit on a software level was realized using the default virtual instruments package providing the virtual instruments for initialization, opening and closing of the desired channels and closing the instrument connection.

5.9 Optimization of the measurement sequence

In order to perform an efficient multi-purpose test, the optimal measurement sequence has to be identified and fixed. It has been shown that the pinhole test is performed by applying a test voltage up to 20 V between the strip implant and the readout strip with a sequential measurement of the resulting current through the dielectric layer. Here, the measured value for a “typical” strip usually reaches a few nA. It is worth noting that this value is mostly composed of a charge-up current of the coupling capacitor. The measured value of the strip current varies from hundreds of pA to up to several nA depending on the sensor size and the purity of the material. In case when the strip current is measured after the pinhole test, the charge-up current may distort the measurement and introduce an offset. Because of that, the strip current has to be measured in the first place when the coupling capacitor is not charged. Afterwards, the pinhole and the readout strip short circuit tests have to be performed.

The current range of the measurement unit was set to 200 nA and is fixed for all of the tests in order to prevent an additional delay due to a change of the measurement range for different measurements. Also, re-zeroing of the device is not required in this case, which also saves approximately a second⁴. The 200 nA range is high enough to be able to identify the strip failures. Also, within this range, the measurement precision is enough to distinguish the typical measured values and the values which correspond to a loss of the contact to the probing pads. The following measurement sequence is therefore established:

1. Current range is set to 200 nA;
2. Measurement of the strip current;
3. Gradual ramp-up of the test voltage to 20 V, applied between the AC and the DC pad;
4. Measurement of the current through the coupling capacitor;
5. Gradual ramp-down of the test voltage to 0 V;
6. Gradual ramp-up of the test voltage between neighbouring AC pads to 20 V;
7. Measurement of the resulting current;
8. Gradual ramp-down of the test voltage to 0 V;

⁴According to [102], it is advisable to perform re-zeroing if the instrument range is down-ranged. The estimated time for switching of the current range along with re-zeroing is approximately 1.5 seconds. For 1024 strips per side, it gives about 50 minutes per sensor.

9. Repeat steps 2-8 for the next strip.

Moreover, a dedicated virtual instrument that allows to perform the graduate ramping faster than using the one provided by the manufacturer is used, has been developed and implemented in the test software.

5.10 Optimization of the measurement speed

The measurement speed is defined according to the configuration of the main measurement unit - the Keithley 6487. By default many parameters of the instrument that define the measurement speed and the accuracy of the measurement are set to pre-defined values. To be able to tune each setting of the SMU the virtual instrument package for an advanced configuration was developed. The following settings of the measurement unit were varied in order to obtain the optimal measurement speed and accuracy ratio:

- *Zero correct.* Subtracts the voltage offset from the measurement.
- *Autozero.* Maintains stability and accuracy over time and changes in temperature. The device periodically measures internal voltages corresponding to offsets and amplifier gains. When disabled, the offset and gain measurement are not performed.
- *Digital filter.* Averaging of selected number of readings.
- *Damping.* Helps to reduce noise caused by input capacitance.
- *Median filter.* Used to determine the “middle-most” reading from the group of readings.
- *Rate or number of power line cycles (NPLC).* Selects the integration time of the analogue/digital converter, affects the amount of reading noise as well as the ultimate reading rate of the instrument.

A series of measurements have been made with varied settings. The measurement speed was stored as well as the measured data. Table 5.1 summarizes the results for different instrument settings. Here, the measured values were compared to the values of the configuration 5 featuring most of the settings enabled that provides the most precise but long measurement. The compromise settings between the measurement speed and accuracy have been found as configuration 8. In this case, it takes approx. 4 seconds to perform three strip diagnostic tests, yielding approximately 68 minutes for a scan of one side of the sensor.

Table 5.1: Instrument configuration as function of the measurement speed.

Configuration	Zero correct	Autozero	Digital filter	Readings to average	Damping	Median filter	Median filter rank	NPLC	Measurement time, sec
1	yes	yes	yes	3	yes	no	-	1	2
2	yes	yes	yes	3	yes	yes	3	1	2
3	yes	yes	yes	5	yes	no	-	5	6
4	no	yes	no	-	yes	no	-	5	3
5	yes	yes	yes	20	yes	no	-	5	20
6	yes	yes	yes	3	yes	no	-	3	3
7	yes	yes	yes	3	yes	yes	3	3	3
8	yes	yes	yes	3	yes	no	-	2	4

5.11 Development of the software interface

The interface of the software was developed following the idea that possible mistakes of the operator should be minimized. The software does not allow the operator to start the measurement before the configurations of the measurement and the instruments are set and saved. Only then the “Start” button becomes available to press and the user is allowed to start the measurement. The software errors are

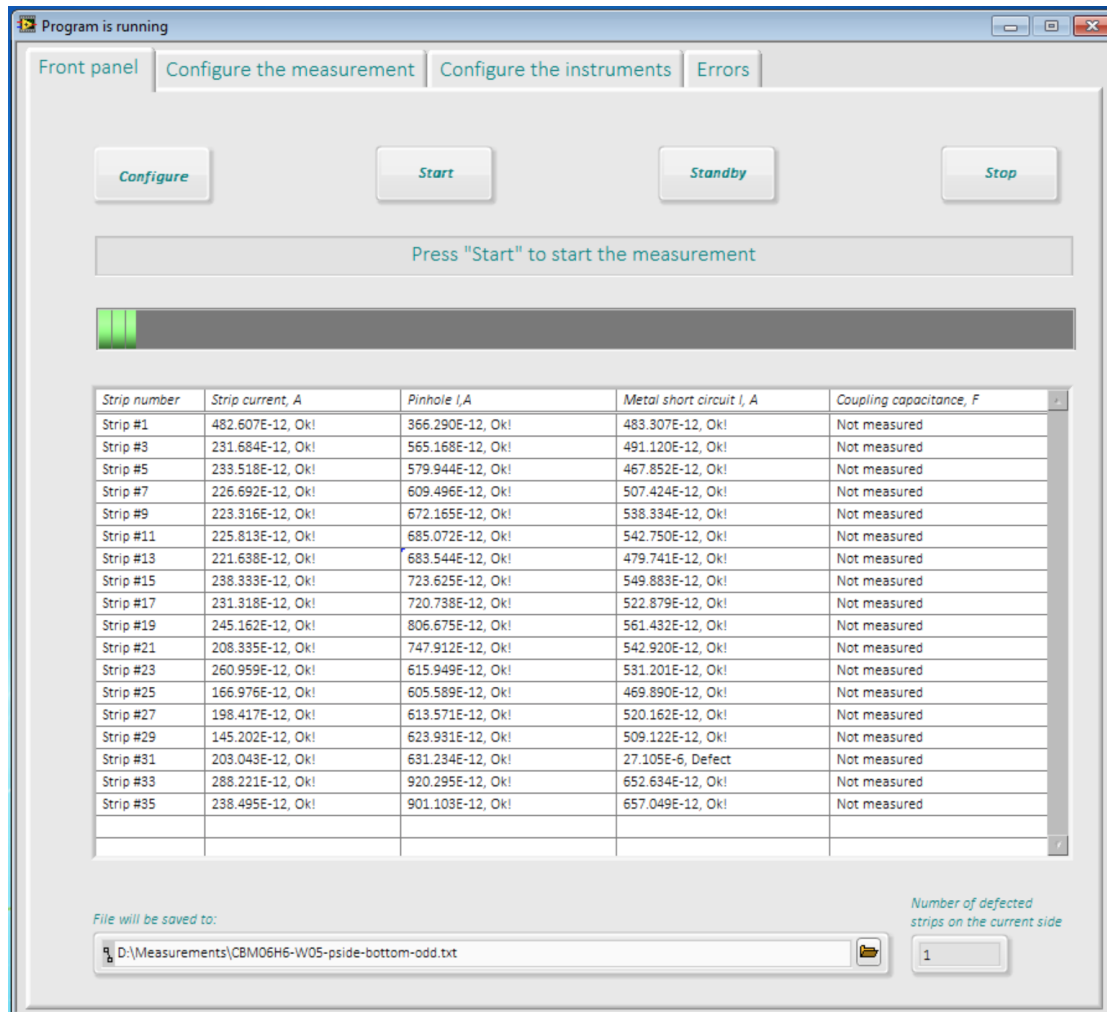


Figure 5.13: Interface of the software for automated strip diagnostic tests shown during the operation.

being handled at each stage of the measurement. If occurs, the error message is printed in the “Errors” tab, while the measurement is sent into a standby mode. The corresponding views of the software interface including the measurement and the instrument configuration panels are presented in Appendix B.

The main panel of the program features buttons to start, stop and stand-by the

measurement, an auto-updated table showing the measurement results in real time and a field to define a path for the resulting storage file (Fig. 5.13). A “Standby” button was implemented in order to be able to pause the measurement and to start it again from the point of pausing. Configurations of the stepping direction, type of the strips under test (even or odd) and others, are performed using the pop-up windows as presented in Fig. 5.6.

5.12 Components of the developed test stand

The developed test stand includes the following components:

- Süss PA300PS probe station with 4 needle manipulators;
- Keithley 6487 SMU is used for measurements of the strip faults;
- Keithley 2410 SMU provides a bias voltage of the device under test;
- Keithley 708B mainframe with Keithley 7072-HV switching card provide multi-purpose measurements;
- Quad Tech 7600 LCR-meter for capacitance measurements (optional);
- ProberBench PC with the Süss firmware installed, for the communication with the probe station electronics;
- Master PC controls the measurement and the instruments;
- Software for automated tests installed on both PCs.

5.13 Output of the automated strip diagnostic scan

A typical output of the automated strip diagnostic scan for a prototype STS sensor is depicted in Fig. 5.14. The test results are presented in the same order as were measured according to Section 5.9. The scan was performed for a junction side of the CBM06 prototype sensor. No strips with high leakage current were found. The measured strip current values vary within several nanoamperes. One pinhole failure was identified during the test (strip #410). The scan for the readout strip short circuit did not show any ohmic connections between the readout strips.

5.13 Output of the automated strip diagnostic scan

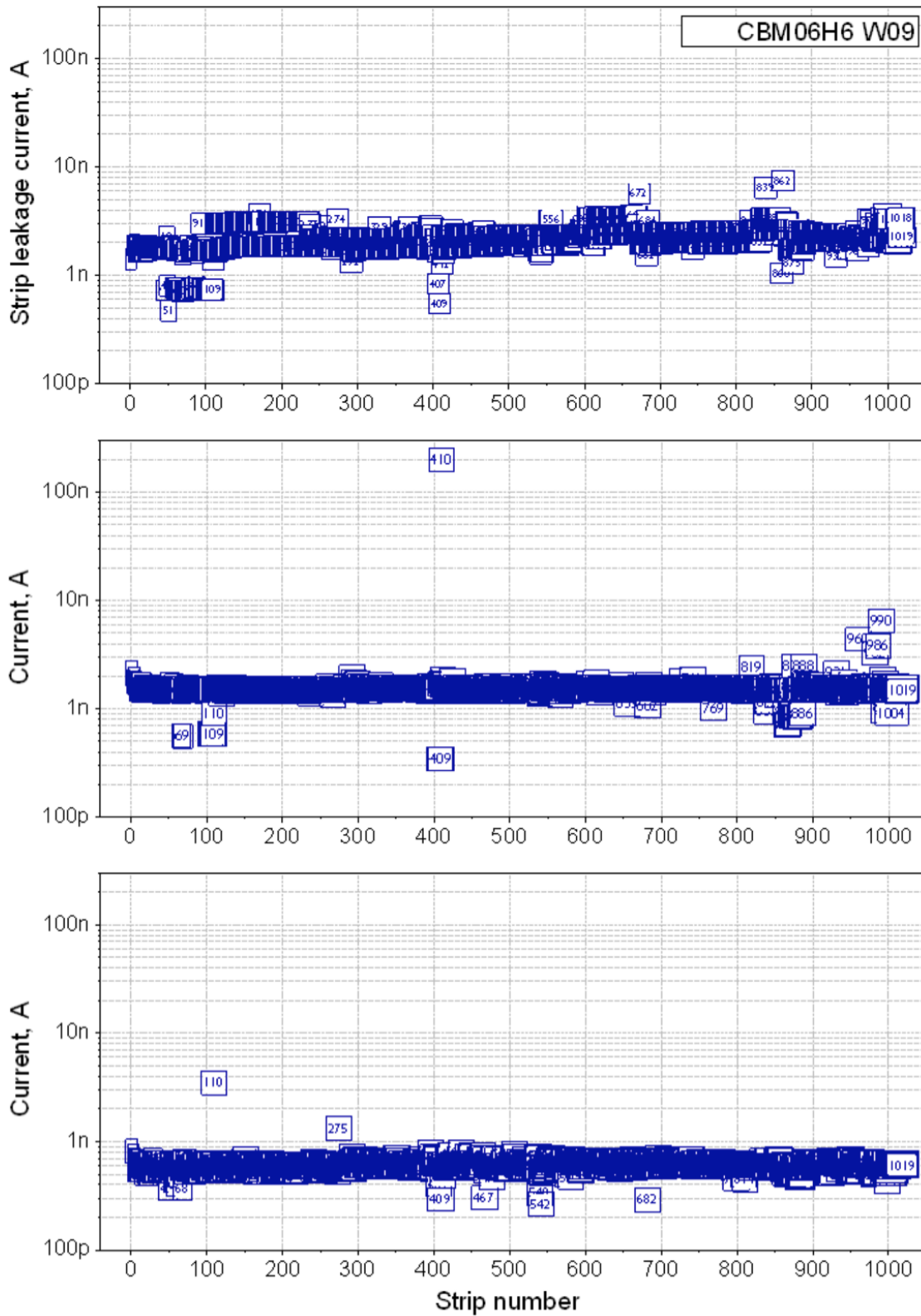


Figure 5.14: Full strip diagnostic scan of an STS prototype sensor. Top: strip current scan; Center: pinhole test scan; Bottom: readout strip short circuit scan.

5.14 Experience with automated testing

In order to perform an efficient testing, many aspects have to be taken into consideration. The sensor under test have to be aligned precisely to allow the probe needles to contact the probing pads along the sensor edge. For this, a manual alignment is performed using a built-in “2 point alignment” procedure by selecting two points at the opposite edges of the sensor.

The needles should be cleaned after testing several sensors. Due to probing a large amount of strips, an aluminum chip scrap is being accumulated at the tips of the needles, which can deteriorate the contact. A special brush wetted with isopropanol is used for cleaning.

The flatness of the sensor surface is crucial during the tests. If the flatness is violated, either a loss of the contact or surface scratching will take place. The present design of the STS test socket (Fig. 4.6a) allows to perform the tests on a fraction of the sensors, which have the most precise dicing⁵. Moreover, the pogo pins contact the bias pads only at one corner. Due to their pressure, the opposite corner located diagonally is slightly lifted up. In order to avoid the present problems, a new design of the socket has been proposed. Here, it is suggested to implement two pairs of the bias pads in the middle of the bias line, and to improve the design of the socket in order to be able to probe these bias pads.

The microscope light, if used in a standard brightness, should be switched off as causing an additional leakage current. However, this will make the visual monitoring of the testing procedure not possible. If reduced to the minimum, the scope light can be used during the testing procedure, which is recommended even for well trained personnel.

⁵If the sensor have a slightly larger size after dicing, it will bend when put in the socket, therefore, it's surface is not anymore flat. Here, bending even at a level of tens of μm is crucial.

Summary and Conclusion

The CBM experiment aims to study the phase diagram of strongly interacting matter at neutron star core densities. For this, CBM will focus on investigation on the signatures sensitive to the dense phase of the fireball evolution, such as multi-strange (anti-) hyperons, lepton pairs and particles containing charm quarks. In order to investigate this rare observables with high precision, the experiment will be operated at extremely high interaction rates, up to 10^7 collisions/sec, and will be composed of several detector systems for an extensive particle identification.

The main tracking detector of the CBM experiment is the Silicon Tracking System, designed as a low mass, highly granular system with fast readout, and required to provide a momentum resolution of $\Delta p/p \approx 1\%$ and $> 95\%$ track reconstruction efficiency for charged particles with momenta > 1 GeV/c. In order to provide the optimal spacial resolution for the particle trajectory reconstruction, fast readout and low material budget, approximately 900 of 300 μm thick double-sided silicon microstrip sensors will be employed in four different sizes.

In the scope of this work, a contribution to the development of the Silicon Tracking System have been made, focused on the following topics:

- A detailed investigation on the radiation tolerance of double-sided silicon strip sensors for the STS;
- The development of the Quality Assurance (QA) test stand for strip quality evaluation on double-sided silicon strip sensors of the STS.

Investigation on the radiation tolerance of the STS sensors

In Chapter 3, the radiation tolerance of the STS sensors was studied using several sets of miniature double-sided sensors of $(1.2 \times 1.2 \text{ cm}^2)$ size as well as the latest full-size prototype sensors of various sizes ($6.2 \times 6.2 \text{ cm}^2$ and $6.2 \times 4.2 \text{ cm}^2$). After irradiation, a characterization of the sensors was performed in terms of their main characteristics: leakage current I_{leak} , full depletion voltage V_{fd} , and charge collection.

Results obtained on irradiated miniature sensors. The miniature sensors were irradiated with reactor neutrons at the JSI irradiation facility,

Ljubljana, Slovenia, to various fluences in 1 MeV neutron equivalent, ranging from $1 \times 10^{13} \text{ cm}^{-2}$ to $2 \times 10^{14} \text{ cm}^{-2}$. The measurements determined the evolutions of the sensors' characteristics as a function of the fluence. It was found out that the leakage current increases proportionally to the fluence, following the expected behaviour. The current related damage rate that defines the increase of the leakage current with irradiation was determined directly after irradiation: $\alpha = (5.52 \pm 0.05) \times 10^{-17} \text{ A/cm}$. This value is found to be consistent with the measurements performed by other groups. Using the obtained parameter, an estimation of the leakage current can be performed at various levels of irradiation. Consequently, the shot noise of the readout electronics can be estimated as well at various Φ_{eq} .

The full depletion voltage V_{fd} evolution was determined as a function of the equivalent fluence as well. The experimental data was compared to a parametrization performed using the "Hamburg model" and was found to be in agreement with the latter. The model parameters were selected according to the properties of the devices under test. Using both the experimental data and the parametrization, the point of "type inversion"⁶, after which the V_{fd} rapidly increases, proportionally to the fluence, was identified at approximately $2.25 \times 10^{13} \text{ n}_{eq}/\text{cm}^2$. The obtained data gives a valuable information about the development of the full depletion voltage with irradiation, therefore, the operational voltage for various areas of the STS stations during the operation of the experiment can be adjusted accordingly. Also, allocation of the sensors with various V_{fd} within a station should be performed considering the corresponding irradiation level.

First results on the charge collection performance of the STS sensors irradiated to high fluences, up to twice the maximum expected fluence, were obtained. The measurements confirmed that the STS sensors are able to withstand high radiation environment and maintain approx. 95% of the charge collection efficiency⁷ at the n^+ readout side and approx. 90% at the p^+ readout side, in the range up to the maximum expected fluence. The saturation of the most probable charge for the sensors in this fluence range was found to take place at bias voltages more than 200 V exceeding the full depletion voltage⁸. In case of irradiation to twice the lifetime fluence, signs of saturation of the most probable charge were observed at the p^+ readout side while no saturation observed at the n^+ readout side up to the reverse bias voltages of about 500 V. Additionally, measurements revealed that for the sensors irradiated to twice the lifetime fluence, the most probable charge collected at the p^+ side exhibits further stronger deterioration than that at the n^+ readout side.

⁶Or space charge sign inversion (SCSI).

⁷Here, the charge collection efficiency before irradiation is considered as 100%.

⁸Extracted from the C-V measurement.

The sensors' characteristics change as a function of time after irradiation due to annealing of the radiation-induced defects. The annealing rate strongly depends on the temperature. The time development of the sensors' characteristics was investigated in order to determine the conditions for the maintenance period of the experiment.

The measurements demonstrate that the leakage current continuously decreases as a function of time, which confirms the expected behaviour. The full depletion voltage reaches its minimum⁹ during the short-term "beneficial" stage, after 7 days of storage at 25 °C. If stored for longer periods, the V_{fd} demonstrates a significant increase, e.g., increases by 100% after an additional storage for 54 days. Analysis of the long-term "reverse" annealing at 80 °C confirmed the location of the type-inversion point between 1×10^{13} n_{eq}/cm² and 5×10^{13} n_{eq}/cm².

In order to compare the experimental data with the "Hamburg model", the results were also represented in terms of the change in effective impurity concentration ΔN_{eff} , where a good agreement was found, although the observed changes in the V_{fd} and ΔN_{eff} during the short-term annealing are lower than those expected by the model. Also, the V_{fd} minimum predicted by the model was found after 5 days of exposure at 25 °C, located between the experimental points.

Time development of the charge collection was studied using the accelerated annealing data, in order to observe the long-term behaviour¹⁰ of the most probable charge. A slow decreasing tendency of the most probable charge was observed on time scales of more than 300 days for the sensor irradiated to 1×10^{14} n_{eq}cm⁻² and more than 600 days for that irradiated to 5×10^{13} n_{eq}cm⁻², in terms of equivalent storage at 20 °C. However, the decrease in charge collection does not exceed a 5% level. Considering the obtained results, the conditions for the maintenance period were suggested.

Results obtained on irradiated full-size prototype sensors. The full-size prototype sensors, fabricated by CiS and Hamamatsu vendors, were irradiated with 23 MeV protons to twice the lifetime fluence ($\Phi = 2 \times 10^{14}$ n_{eq}/cm²) at KIT Kompakt-Zyklotron, Karlsruhe, Germany. Measurements of irradiated full-size prototype sensors were performed for the first time. The sensors under test feature the double-metal or the external microcable strip interconnection design.

Measurements of the leakage current demonstrated its increase up to 2.86×10^{-2} mA/cm², which corresponds to 1.1 mA for a sensor of a 6.2×6.2 cm² size. This increase is found to be in agreement with the current damage rate

⁹For the sensors which underwent the "type inversion". Otherwise, the V_{fd} increases and reaches the maximum.

¹⁰A 20 °C equivalent of 1 min. of annealing at 80 °C equals to approx. 5.14 days.

extracted from the measurements with the miniature sensors. Due to different thicknesses¹¹ and fabrication technologies the sensors under test exhibited different full depletion voltages before irradiation. The depletion voltage evolution, estimated with the “Hamburg model” have shown differences for the sensors with different thicknesses. Measurement results of the charge collection performance revealed that the dedicated double-sided STS sensors are able to yield 70% to 90% of the charge collection efficiency after irradiation to twice the lifetime fluence. The results differ depending on the manufacturer and the readout side.

Due to the observed high level of leakage current the operational stability of the sensors was investigated in detail. The measurements confirm the stable operation of the prototype sensors under controlled environmental conditions. A sensitivity to the rapid increase of humidity was observed, reflected in an increase of the leakage current for all sensors however, for those produced by Hamamatsu, in a lower degree. The effect is related to the impact of the humid air on the surface depletion. A thermal runaway was observed in several cases when the leakage current, as a result of the humidity enhancement, reaches the level of approx. 5.2×10^{-2} mA/cm². Scenarios of rapid increase of humidity were performed experimentally demonstrating that the sensors featuring the double-metal strip interconnection design are less resistant to this effect than those having the external microcable.

Development of the Quality Assurance test stand for strip quality assessment

Currently under development, the Quality Assurance (QA) program for the STS sensors will include visual inspection, bulk electrical tests, strip diagnostic tests and others. In Chapter 4, the QA tests relevant for the STS sensors are identified in terms of the required hardware, software and measurement procedures. Test results obtained for the latest prototype sensors are presented. The quality of produced sensors is found to be very high. The measured sensor parameters are found to be within the specifications.

For an efficient operation of the system as a whole, the quality of each strip has to be ensured. Due to complexity of the measurement procedures involving several measurement units, the probe station and the amount of strips per sensor (2048), the strip diagnostic tests are very time consuming when performed manually. Thus, automation of the test procedure is crucial in terms of the large-volume sensor production and the limited timeline for the STS detector construction. It also reduces the human factor that can lead to the damage or even destruction of the

¹¹The sensors produced by CiS are 285 ± 15 μm thick, while those produced by Hamamatsu have a 320 ± 15 μm thickness.

devices, serving as an additional safety aspect. In Chapter 5, the development of the quality assurance test stand for strip diagnostic tests is described. It includes development of the software for managing and automation of the test procedure. The developed test-stand allows for an efficient quality evaluation of each strip by determination of the strip failures originating from the manufacturing or handling. The strip quality is evaluated within 4 seconds by performing three tests in a sequence. The developed setup will be used during the sensor mass production phase.

Conclusions and outlook

Up to date, a significant progress have been achieved in the development of the CBM Silicon Tracking System. In particular, several generations of prototype sensors featuring dedicated design specifics have been realized and characterized.

In the scope of this work, systematic studies performed on neutron irradiated miniature sensors have shown that double-sided STS sensors are able to withstand the expected radiation loads and to maintain high charge collection efficiency (90% to 95% depending on the readout side) up to the lifetime fluence. Studies of the performance of the prototype sensors irradiated to twice the lifetime fluence revealed the ability of the sensors to yeild high charge collection (from 70% to 90%) even beyond the expected conditions. The design of the sensors therefore satisfies the requirements in terms of radiation tolerance. For an exhaustive evaluation of the performance of the whole readout module, a signal-to-noise ratio have to be determined after irradiation using the latest prototype components. This is planned to be finished by Q2 2017. The production of the sensors starts in Q4 2017, shortly after the production readiness review.

Stable operation of irradiated sensors is achieved by controlling the operational temperature and humidity at the stable level. It is prefferable to reduce the operational temperature down to -10 °C in order to avoid thermal runaways.

An efficient and safe testing is achieved not only due to decent software and hardware but also requires appropriate conditions concerning the flatness of the sensor surface during the test. In order to achieve this, a dedicated test frame, the “STS test socket”, have been produced and tested but up to date requires an improvement of the design.

The quality of the produced sensors is very high. Less than 1% of strip failures is observed for the latest prototype sensors. The strip quality will be ensured during the sensor production period using the developed test stand. The strip quality is evaluated within 4 seconds by performing three tests in a sequence. The developed software for automated tests can be impoved by implementing an automated database storage and embedding the capacitance related test procedures.

Zusammenfassung

Das Compressed Baryonic Matter (CBM)-Experiment ist eine der wissenschaftlichen Grundsäulen der “Facility for Antiproton and Ion Research” (FAIR), die sich momentan an der GSI in Darmstadt im Bau befindet. Ziel des Experiments ist die Erkundung des Phasendiagramms stark wechselwirkender Materie im Bereich von hohen Baryonendichten bei moderaten Temperaturen. Dieser Bereich wurde bislang nur unzureichend in Schwerionenkollisionen untersucht.

Modellen der Quantenchromodynamik (QCD) zufolge weist das Phasendiagramm in diesem Bereich eine Vielzahl von Strukturen auf, beispielsweise einen Phasenübergang erster Ordnung von hadronischer zu partonischer Materie, einen kritischen Endpunkt, der Regionen unterschiedlicher Phasenübergänge trennt, und einen möglichen neuen Materiezustand - die quarkyonische Materie. Weltweit gibt es verschiedene Forschungsprogramme, die das QCD-Phasendiagramm bei hohen Baryonendichten untersuchen oder untersuchen wollen, z.B. STAR am RHIC, NA61/SHINE am CERN-SPS oder NICA am JINR. Diese Programme werden aber aufgrund von Einschränkungen bezüglich der Luminosität und oder der Detektoren hauptsächlich Teilchen messen können, die in der späten Phase des Stoßes entstehen wenn die Dichte der Reaktionszone aufgrund ihrer Expansion bereits stark abgenommen hat.

Im Gegensatz dazu wird sich das CBM-Experiment auf die Untersuchung von Signaturen konzentrieren, die sensitiv auf die dichte Phase der “Feuerball“-Entwicklung sind. Zu diesen Signaturen gehören unter anderem (Anti-)Hyperonen mit mehrfacher Seltsamkeit, Leptonenpaare und Teilchen, die Charm-Quarks enthalten. Es wird erwartet, dass die Prozesse zur Erzeugung solcher Teilchen nur sehr kleine Wirkungsquerschnitte haben. Um diese Observablen mit hoher Genauigkeit untersuchen zu können, werden bei dem CBM-Experiment sehr hohe Wechselwirkungsraten von 10^7 Kollisionen/Sekunde angestrebt und mehrere Detektorsysteme zur genauen Teilchenidentifikation verwendet.

Der Hauptdetektor zur Spurrekonstruktion beim CBM-Experiment ist das “Silicon Tracking System” (STS). Es ist ein hochgranulares System mit geringer Massenbelegung und sehr hoher Auslesegeschwindigkeit ausgelegt, um eine Impulsauflösung von $\Delta p/p \approx 1\%$ und $> 95\%$ Effizienz bei der Spurrekonstruktion

geladener Teilchen zu erreichen. Der Detektor wird aus acht Tracking-Stationen bestehen, die sich in einem Dipolmagneten befinden und einen Rapiditätsbereich vom Schwerpunktsystem bis nah an die Strahlrichtung heran abdecken werden. Um sowohl eine optimale räumliche Auflösung für die Rekonstruktion der Teilchentrajektorien als auch eine hohe Auslesegeschwindigkeit und geringe Materialkosten zu gewährleisten, werden 300 μm dicke doppelseitige Silizium-Mikrostreifensensoren in vier unterschiedlichen Größen eingesetzt. Etwa 900 dieser Sensoren werden insgesamt hergestellt.

Die im Rahmen dieser Dissertation durchgeführten Arbeiten sind Teil der Entwicklung des sogenannten "Silicon Tracking System", das im CBM-Experiment zum Einsatz kommen wird. Dabei wurden schwerpunktmäßig zwei Themen bearbeitet:

- Die Untersuchung der Strahlentoleranz doppelseitiger Silizium-Streifensensoren für das STS;
- Die Entwicklung eines Teststands zur Qualitätssicherung der Siliziumstreifen.

Aufgrund der Tatsache, dass Strahlenschäden der am stärksten einschränkende Faktor bei Verwendung von Silizium-Sensoren in einem Hochenergiephysik-Experiment sind, muss sichergestellt sein, dass die STS-Sensoren den während der Betriebsphase vorherrschenden Strahlungsbedingungen standhalten können. Simulationen¹² haben gezeigt, dass die Sensoren im Innenbereich der STS-Stationen harschen Strahlungsbedingungen ausgesetzt sein werden, welche einem 1 MeV Neutronenäquivalent von bis zu $1 \times 10^{14} \text{ cm}^{-2}$ (die Fluenz über die Gesamtlebensdauer des Detektors nach mehreren Betriebsjahren, im Folgenden als Gesamtfluenz bezeichnet) entsprechen. Solche Strahlungsbedingungen werden vor allem die Eigenschaften der Sensoren negativ beeinflussen, während andere Systemkomponenten (wie Auslekabel und Elektronik) nicht so stark in Mitleidenschaft gezogen werden. Die Bewertung der Leistungsfähigkeit der Sensoren unter Bestrahlung ist daher eine entscheidende Voraussetzung, um zukünftig einen erfolgreichen Betrieb des Gesamtsystems zu gewährleisten. Ein weiterer limitierender Faktor der Systemperformanz ist die Qualität der verwendeten Komponenten, insbesondere der Siliziumsensoren.

Daher werden die Sensoren bereits beim Hersteller auf eine Vielzahl von Defekten hin untersucht. Allerdings besteht beim Transport, der Handhabung und der Montage die Gefahr, sie zu beschädigen, weshalb ihre Funktionsfähigkeit nach jedem größeren Schritt überprüft werden muss. Insbesondere muss die Qualität jedes einzelnen Streifens mittels automatisierter und zeiteffizienter Methoden festgestellt werden können.

¹²FLUKA-Simulationen des nicht-ionisierenden Energieverlusts.

Untersuchung der Strahlentoleranz der STS-Sensoren

In Kapitel 3 dieser Dissertation wird die Untersuchung der Strahlentoleranz der STS-Sensoren beschrieben. Dazu wurden sowohl mehrere Miniaturversionen ($1.2 \times 1.2 \text{ cm}^2$) Prototyp-Sensoren in Vollgröße ($6.2 \times 6.2 \text{ cm}^2$ und $6.2 \times 4.2 \text{ cm}^2$) verwendet. Nach erfolgter Bestrahlung wurden die Sensoren auf ihre wichtigsten elektrischen Eigenschaften hin untersucht: dem Leckstrom I_{leak} , der Verarmungsspannung V_{fd} und der Ladungssammlungseffizienz.

Ergebnisse mit bestrahlten Miniaturesensoren

Die Miniaturversionen der Sensoren wurden mit Reaktorneutronen an der JSI Irradiation Facility in Ljubljana, Slowenien, bestrahlt. Dabei konnten Fluenzen verwendet werden, die einem 1 MeV Neutronenäquivalent von 1×10^{13} bis $2 \times 10^{14} \text{ cm}^{-2}$ entsprechen. Mit den Messungen wurde die Abhängigkeit der Sensoreigenschaften von der Fluenz bestimmt. Es wurde festgestellt, dass der Leckstrom wie erwartet proportional mit der Fluenz zunimmt. Die Schädigungskonstante α , welche die Zunahme des Leckstroms in Abhängigkeit von der Bestrahlung beschreibt, wurde unmittelbar nach der Bestrahlung zu einem Wert von $\alpha = (5,52 \pm 0,05) \times 10^{-17} \text{ A/cm}$ bestimmt. Dieser Wert ist in guter Übereinstimmung mit den Messergebnissen anderer Forschungsgruppen. Mit Hilfe dieses Parameters kann der Leckstrom bei unterschiedlichen Strahlungsdosen abgeschätzt werden, wodurch auch das Rauschen der Ausseelektronik in Abhängigkeit von Φ_{eq} berechnet werden kann.

Der Verlauf der Verarmungsspannung V_{fd} wurde ebenfalls als Funktion der äquivalenten Fluenz bestimmt. Die experimentellen Daten wurden mit einer dem "Hamburg Model" entsprechenden Parametrisierung verglichen, wobei die Parameter entsprechend der Geräteeigenschaften unter Testbedingungen gewählt wurden. Es konnte hier eine gute Übereinstimmung festgestellt werden. Unter Verwendung der experimentellen Daten und der Parametrisierung konnte der Punkt der "Typ-Inversion"¹³ zu einem Wert von $2.25 \times 10^{13} \text{ n}_{eq}/\text{cm}^2$ bestimmt werden. Nach diesem Punkt steigt V_{fd} proportional zur Fluenz schnell an. Die gewonnenen Daten liefern wertvolle Informationen über den Verlauf der Verarmungsspannung in Abhängigkeit von der Strahlenbelastung, womit die Betriebsspannung für verschiedene Zonen der STS-Stationen während der experimentellen Phase entsprechend angepasst werden kann. Außerdem sollte die Verteilung von Sensoren mit unterschiedlichen V_{fd} innerhalb einer Station die Bestrahlungsstärke berücksichtigen.

Abschließend wurden erste Ergebnisse bezüglich der Ladungssammlungseffizienz unter hohen Fluenzen (bis zu zweifacher erwarteter Fluenz) ermittelt. Diese Ergebnisse bestätigen, dass die STS-Sensoren hohen Bestrahlungsstärken stand-

¹³Auch als "Space Charge Sign Inversion" (SCSI) bezeichnet.

halten können. Es konnte gezeigt werden, dass die Ladungssammlungseffizienz bei Fluenzen bis zur maximal erwarteten Fluenz auf der n^+ -Ausleseseite etwa 95% und etwa 90% auf der p^+ -Ausleseseite beträgt, im Vergleich zur Ladungssammlungseffizienz eines unbestrahlten Sensors. Die Sättigung der am wahrscheinlichsten durch ein detektiertes Teilchen erzeugten Ladung im Sensor in diesem Fluenzbereich findet bei Vorspannungen statt, welche die Verarmungsspannung¹⁴ um mehr als 200 V übersteigen. Im Falle von Fluenzen bis zum Zweifachen der erwarteten Gesamtfluenz wurden auf der p^+ -Ausleseseite Anzeichen von Sättigung der wahrscheinlichsten Ladung beobachtet, während dies auf der n^+ -Ausleseseite bis zu inversen Vorspannungen von 500 V nicht der Fall war. Zusätzlich haben die Messungen gezeigt, dass bei Bestrahlung mit bis zum Zweifachen der erwarteten Gesamtfluenz die am wahrscheinlichsten erzeugte Ladung auf der p^+ -Ausleseseite eine stärkere Minderung erfährt als auf der n^+ -Ausleseseite.

Es wurde beobachtet, dass sich die Sensoreigenschaften nach Bestrahlung mit der Zeit wieder verbessern, da Strahlenschäden "ausheilen" können, wobei dieser Effekt stark abhängig von der Temperatur ist. Diese zeitliche Entwicklung wurde untersucht, um die Bedingungen für die Wartungsphasen während des Experiments zu bestimmen. Hierbei wurde festgestellt, dass der Leckstrom als Funktion der Zeit kontinuierlich abnimmt. Die Verarmungsspannung erreicht ein Minimum¹⁵ während einer kurzzeitigen vorteilhaften Ruhephase von 7 Tagen bei 25 °C. Bei längeren Ruhephasen steigt V_{fd} wieder signifikant an - nach zusätzlichen 54 Tagen um 100%. Eine Untersuchung des lang andauernden "umkehrenden Ausheilens" bestätigt, dass der Punkt der "Typ Inversion" zwischen $1-5 \times 10^{13}$ n_{eq}/cm^2 liegt. Um die experimentellen Daten mit dem "Hamburg Model" vergleichen zu können, wurden die Ergebnisse auch als Änderung der effektiven Konzentration von Störstellen ΔN_{eff} dargestellt. Hier stellte sich eine gute Übereinstimmung heraus, obwohl die Änderungen von V_{fd} und ΔN_{eff} beim kurzfristigen Ausheilen niedriger waren, als das Model es vorhersagt. Das mit dem Model berechnete Minimum von V_{fd} konnte nach 5 Ruhetagen bei 25 °C beobachtet werden.

Die zeitliche Entwicklung der Ladungssammlungseffizienz wurde anhand von Daten des beschleunigten Ausheilens untersucht, um das Langzeitverhalten der am wahrscheinlichsten erzeugten Ladung zu ermitteln¹⁶. Dabei wurde eine langsame Verringerung der wahrscheinlichsten Ladung beobachtet, auf Zeitskalen von über 300 Tagen bei mit 1×10^{14} n_{eq}/cm^2 bestrahlten Sensoren und von über 600 Tagen bei mit 5×10^{13} n_{eq}/cm^2 bestrahlten Sensoren. Die Abnahme der Ladungssamm-

¹⁴Extrahiert aus der C-V-Messung.

¹⁵Unter Voraussetzung, dass der Sensor eine "Typ Inversion" unterlief; sonst steigt V_{fd} an und erreicht ein Maximum.

¹⁶1 min Ausheilen bei 80°C entspricht etwa 5.14 Tagen bei 20 °C.

lungseffizienz übersteigt jedoch nicht die 5%-Marke. In Anbetracht dieser Ergebnisse wurden Rahmenbedingungen für die Wartungsperioden vorgeschlagen.

Ergebnisse mit bestrahlten Prototyp-Sensoren in Vollgröße

Die von CiS und Hamamatsu hergestellten Prototyp-Sensoren wurden am KIT Kompakt-Zyklotron in Karlsruhe, Deutschland, mit 26 MeV Protonen und zweifacher erwarteter Gesamtfluenz ($\Phi = 2 \times 10^{14} \text{ n}_{eq}/\text{cm}^2$) bestrahlt. Hierbei handelt es sich um erstmals durchgeführte Messungen mit Sensoren in Vollgröße. Untersucht wurden Sensoren mit Doppelmetall-Lagen und Sensoren mit externem Mikrokabel. Diese alternativen Technologien haben die Aufgabe, die Streifen mit Stereowinkel im Bereich der Sensorecken miteinander zu verbinden.

Messungen des Leckstroms haben gezeigt, dass dieser bis auf $2.86 \times 10^{-2} \text{ mA}/\text{cm}^2$ ansteigt, was bei einer Sensorgröße von $6.2 \times 6.2 \text{ cm}^2$ 1.1 mA entspricht. Dieser Wert ist in Übereinstimmung mit der Schädigungskonstante, die bei den Miniaturesensoren ermittelt wurde.

Aufgrund von unterschiedlichen Herstellungsprozessen und Dicken¹⁷ hatten die getesteten Sensoren schon vor Bestrahlung unterschiedliche Verarmungsspannungen, was auch vom "Hamburg Model" vorhergesagt wird. Messergebnisse der Ladungssammlungseffizienz haben gezeigt, dass diese bei doppelseitigen STS-Sensoren nach Bestrahlung mit dem Zweifachen der erwarteten Gesamtfluenz 70-90% beträgt, abhängig vom Hersteller und der Ausleseseite.

Da ein hohes Niveau an Leckströmen beobachtet wurde, wurde die Betriebstfestigkeit der Sensoren genau studiert. Dabei konnte ein stabiler Betrieb der Prototyp-Sensoren unter kontrollierten Umgebungsbedingungen festgestellt werden. Aufgefallen ist die Empfindlichkeit der Sensoren auf einen schnellen Anstieg der Luftfeuchtigkeit, wodurch bei allen Sensoren der Leckstrom ansteigt - jedoch weniger ausgeprägt bei denen von Hamamatsu. Der Grund dafür liegt in dem Einfluss der Luftfeuchtigkeit auf die Oberflächendepletion. Insbesondere konnte ein thermisches Durchgehen aufgrund von hohen Leckströmen durch Luftfeuchtigkeit ab etwa $5.2 \times 10^{-2} \text{ mA}/\text{cm}^2$ beobachtet werden. Szenarien einer plötzlich anwachsenden Luftfeuchtigkeit haben gezeigt, dass die Sensoren mit externem Mikrokabel hierauf weniger anfällig sind, als die Sensoren mit Doppelmetall-Lage.

¹⁷Die Sensoren von CiS sind $285 \pm 15 \mu\text{m}$ dick, wogegen die von Hamamatsu $320 \pm 15 \mu\text{m}$ dick sind.

Entwicklung des Teststands zur Qualitätssicherung der Siliziumstreifen

Das sich momentan in Entwicklung befindende Programm zur Qualitätssicherung (“Quality Assurance”, QA) der STS-Sensoren wird unter anderem eine visuelle Inspektion, elektrische Tests und Streifendiagnostik-Tests umfassen. In Kapitel 4 werden die für die STS-Sensoren relevanten QA-Tests aufgeführt, unter Angabe der benötigten Hardware und Software und der Messprozeduren. Die Testergebnisse der neuesten Prototyp-Sensoren werden vorgestellt. Es hat sich gezeigt, dass die Herstellungsqualität der Sensoren sehr gut ist und die Sensorparameter innerhalb der Spezifikationstoleranzen liegen.

Für einen effizienten Betrieb des Gesamtsystems ist die Qualität jedes einzelnen Silizium-Streifens zu gewährleisten. Da das Messverfahren, bei dem mehrere Messapparaturen und der Teststand benötigt werden, sehr komplex ist und eine große Anzahl von Streifen pro Sensor (2048) getestet werden müssen, ist die Testprozedur sehr zeitaufwändig, wenn sie von Hand erfolgt.

Eine Automatisierung der Tests ist also unerlässlich, um die große Menge an Sensoren unter Einhaltung des Zeitplans für den STS-Detektorbau bewältigen zu können. Ferner werden menschliche Fehler minimiert, die die Sensoren beschädigen oder zerstören könnten. In Kapitel 5 wird die Entwicklung des Teststands zur Qualitätssicherung beschrieben. Dies umfasst auch die Entwicklung der Software, die für das Management und die Automatisierung des Testprozesses verantwortlich ist.

Der Teststand zur Qualitätssicherung erlaubt eine effiziente Qualitätskontrolle jedes einzelnen Streifens, indem er unterscheiden kann, ob ein Defekt aus der Produktion oder von der Handhabung stammt. Die Qualität eines Streifens wird innerhalb von 4 Sekunden bewertet, indem 3 Tests nacheinander ausgeführt werden. Die entwickelte Messapparatur kommt in der Serienproduktionsphase der Sensoren zum Einsatz.

Appendix A

Additional plots and figures

A.1 Hamburg model parametrization

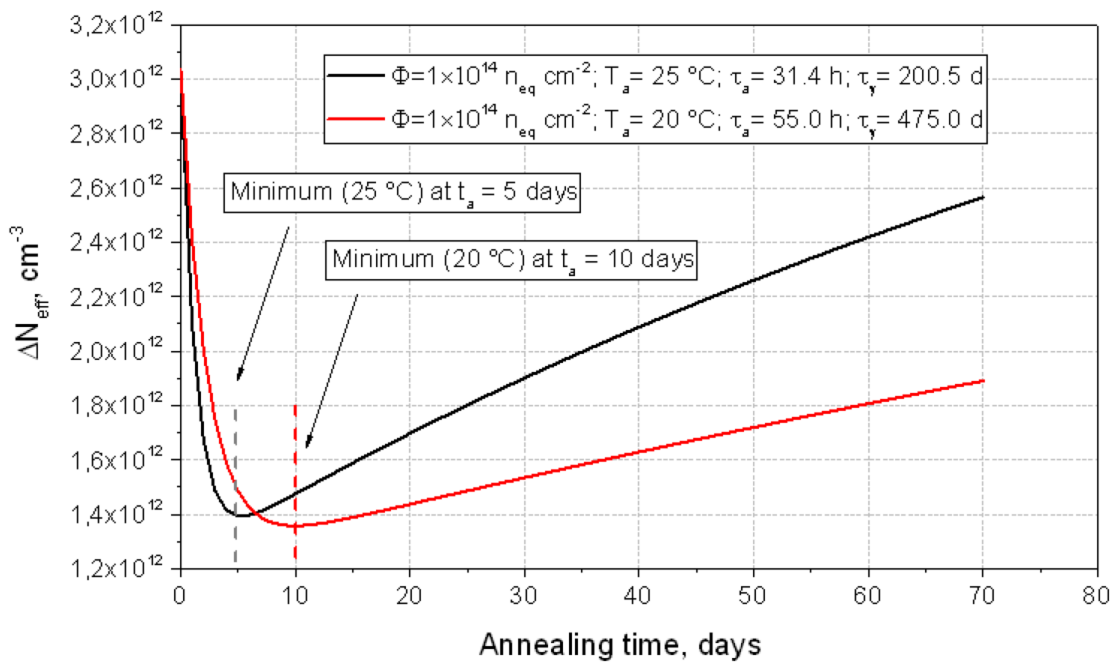


Figure A.1: Parametrization of the change in effective impurity concentration ΔN_{eff} as a function of time at $20\text{ }^{\circ}\text{C}$ and $25\text{ }^{\circ}\text{C}$ for a $300\text{ }\mu\text{m}$ sensor irradiated to $1 \times 10^{14}\text{ n}_{eq}/\text{cm}^2$.

A.2 Long-term stability measurements

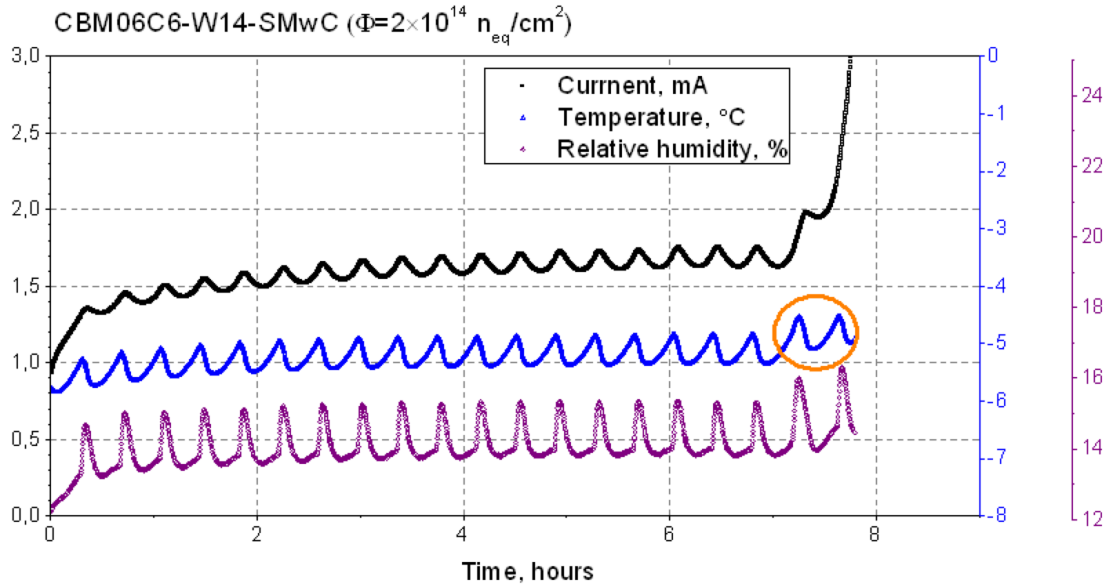


Figure A.2: Long-term stability measurement of the CBM06C6W14-SMwC sensor, started at approx. 12% of the relative humidity and reduced nitrogen flow. A slow increase of the humidity lead to a slow increase of the leakage current. After an additional temperature spike due to an internal process of the refrigerator, a thermal runaway occurred. It is notable that the temperature was increasing during the measurement as well. Presumably, the heat produced due to the increasing leakage current is the reason for this enhancement.

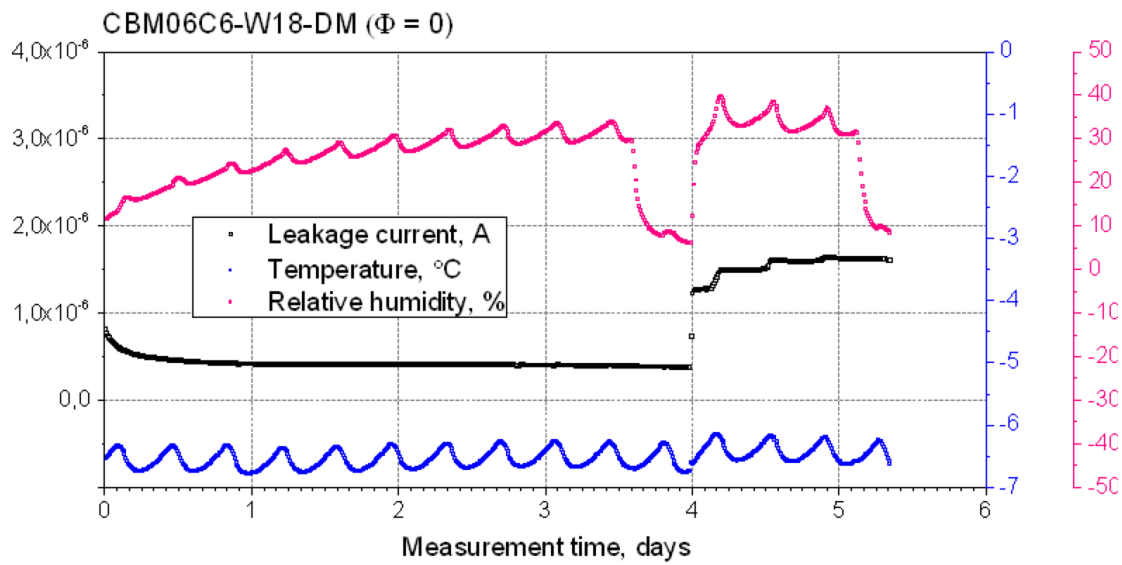


Figure A.3: Long-term stability measurement of a non-irradiated prototype sensor. The leakage current exhibits a slow decrease at a constant level of the temperature and an increasing level of the relative humidity. The leakage current did not react on the decrease of the humidity started after approx. 3.5 days of operation. The rapid increase of the humidity causes an increase of the leakage current by approx. 300%. With the subsequent decrease of the humidity the leakage current remains at the same level.

Appendix B

Interfaces of the developed LabView software

B.1 Software interface for temperature corrected I-V measurements

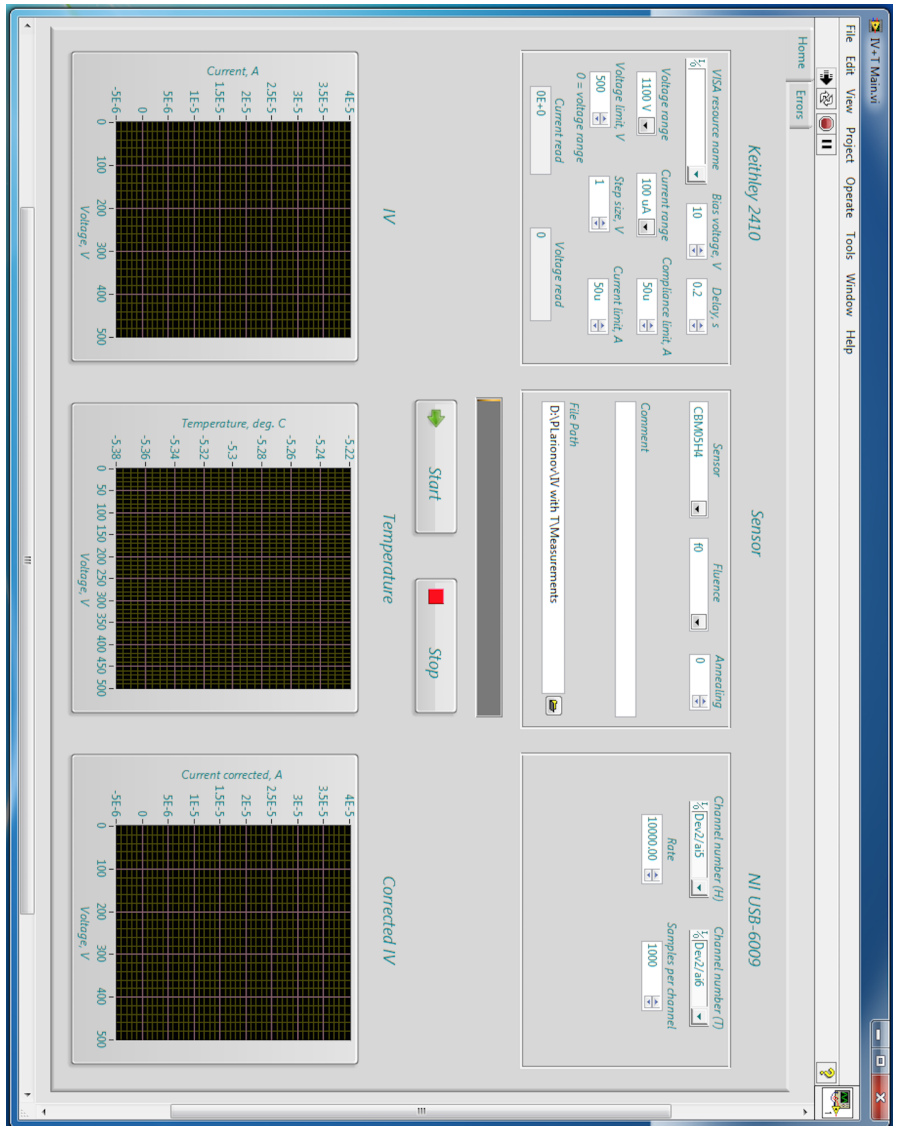


Figure B.1: Software interface for temperature corrected I-V measurements. In the upper part of the front panel, two blocks for the instruments configuration and a block for configuration of the measurement are located. The graphs in the bottom visualize the raw I-V curve (left), the measured temperature (middle) and the corrected I-V curve (right).

B.2 Software interface for long-term stability measurements

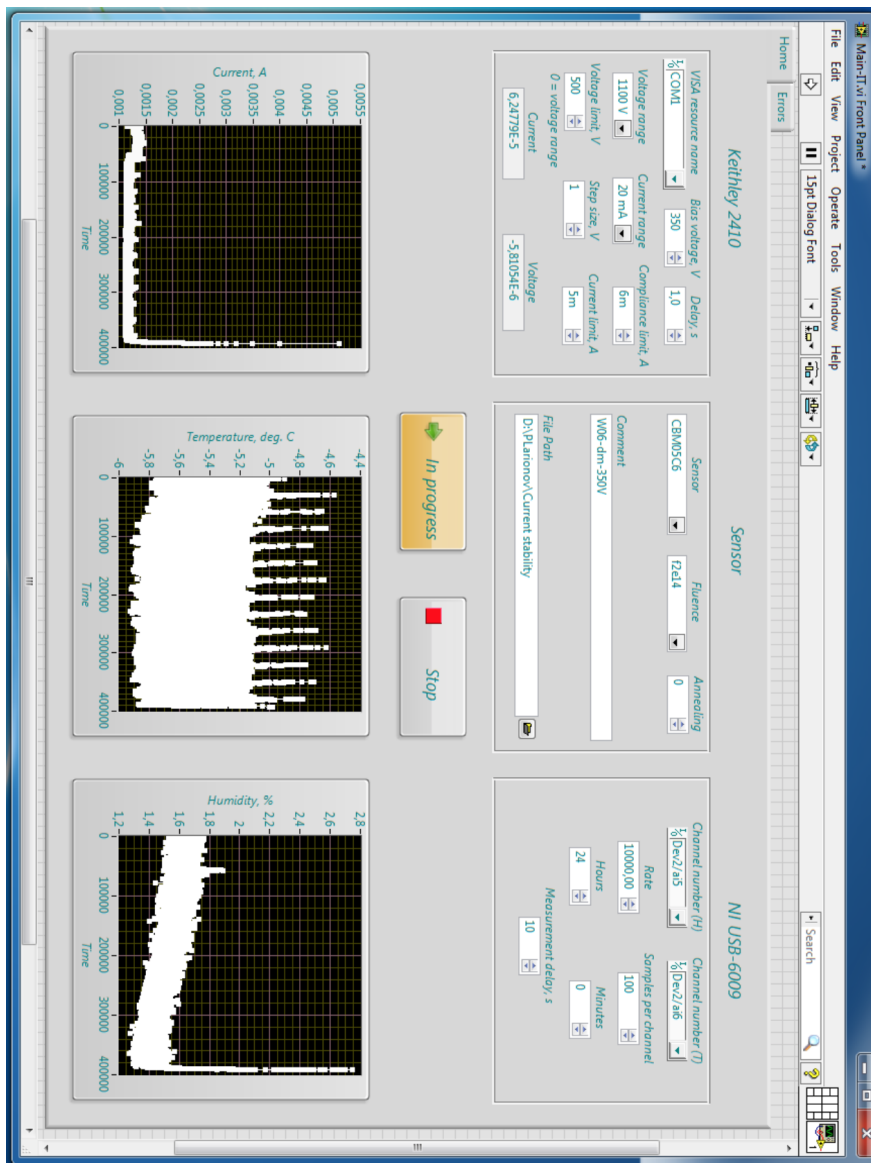


Figure B.2: Software interface for long-term stability measurements. In the upper part of the front panel, two blocks for the instruments configuration and a block for configuration of the measurement are located. The graphs in the bottom visualize the measured leakage current (left), temperature (middle) and relative humidity (right) values.

B.3 Software interface for C-V measurements

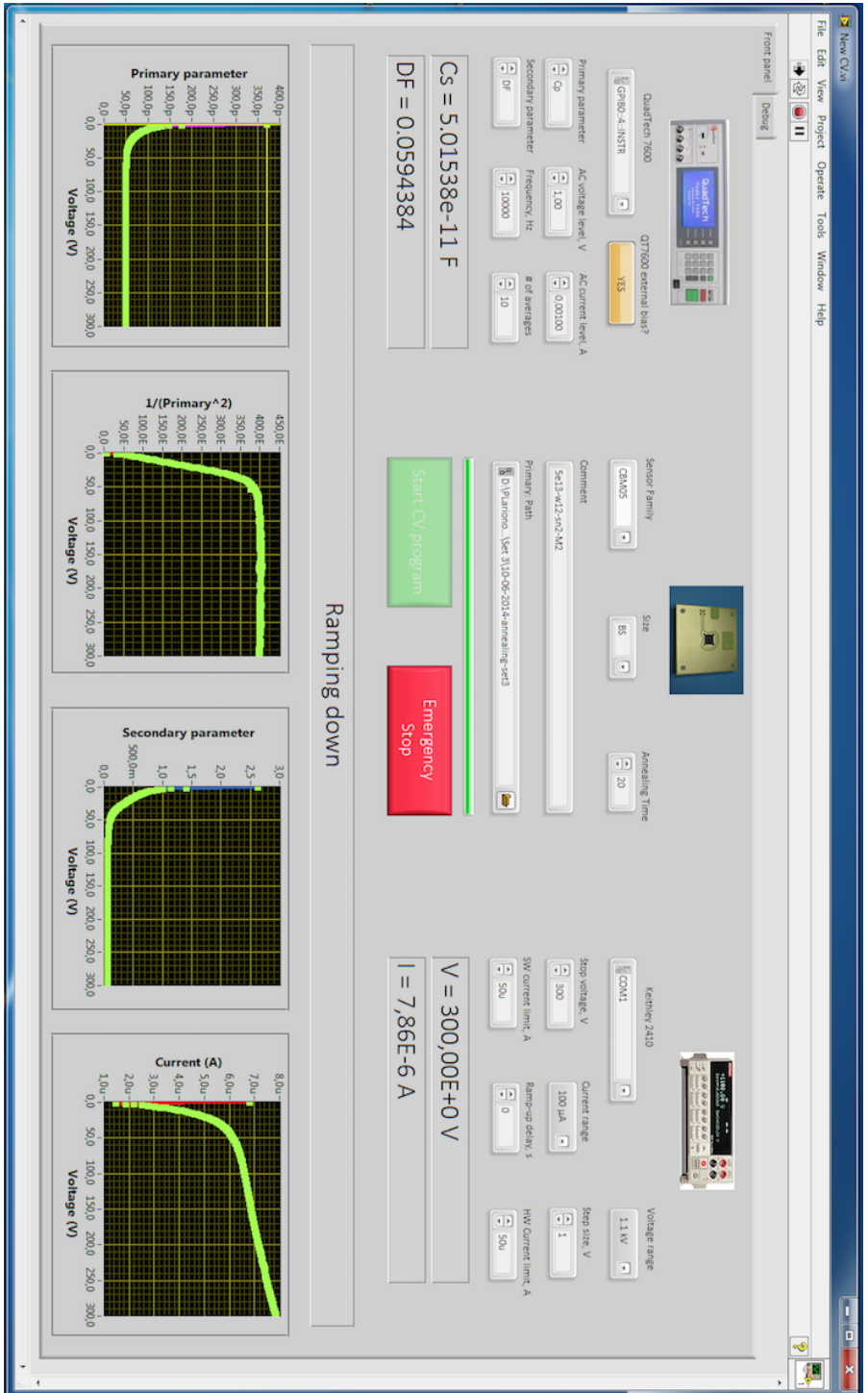


Figure B.3: Software interface for C-V measurements. In the upper part of the front panel, two blocks for the instruments configuration and a block for configuration of the measurement are located. The graphs in the bottom visualize the measured primary parameters (bulk capacitance C), calculated $1/(\text{primary parameter})^2$ ($1/C^2$), secondary parameter (dissipation factor DF), and additionally the leakage current I_{leak} values.

B.4 Software interface for automated strip diagnostic tests

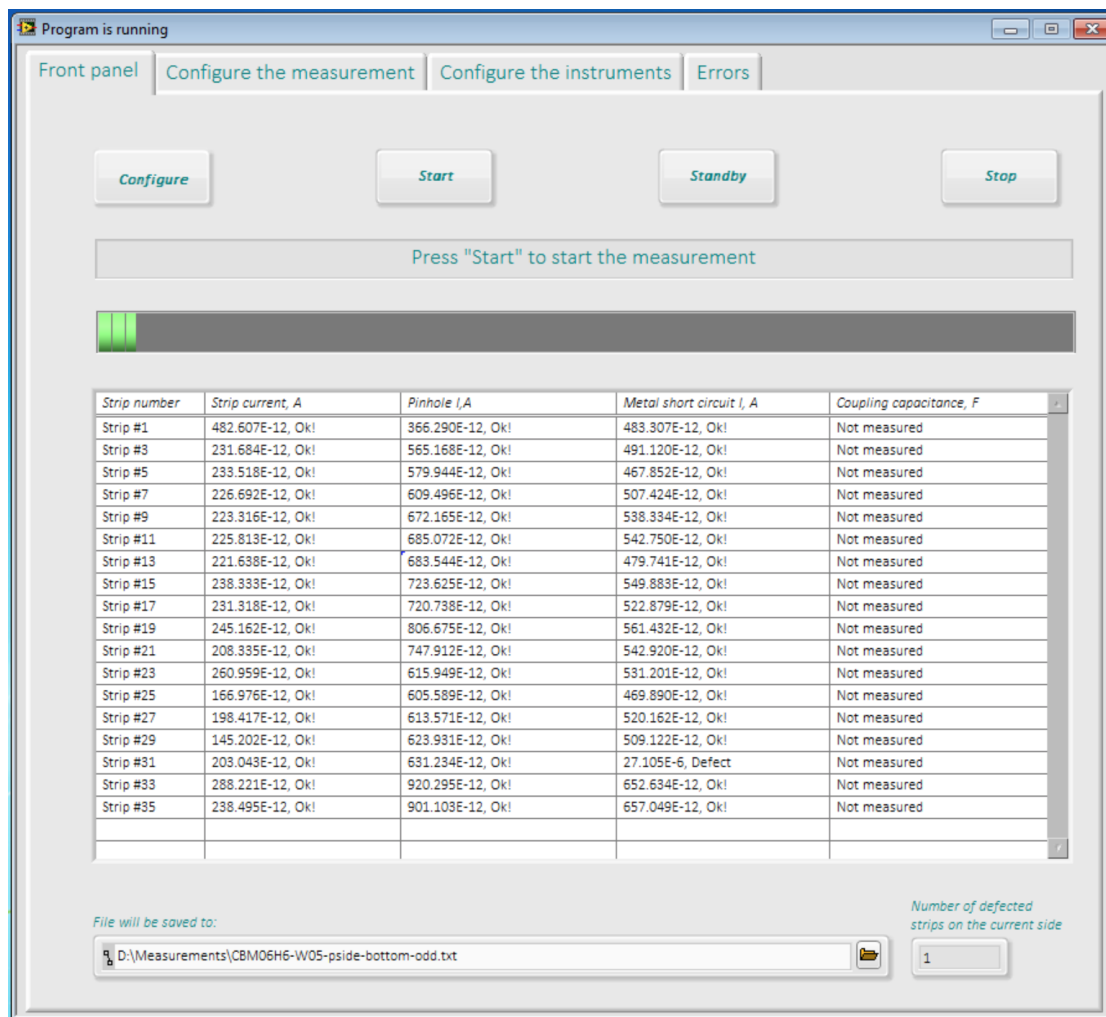


Figure B.4: Main panel of the software for automated strip diagnostic tests, shown during the test. One defect (a readout strip short circuit) has been identified so far for the strip #31. In the upper part, a set of buttons for configuration and operation of the test is implemented. In the middle part of the panel, an auto-updated table is located, showing the test results in real time. The bottom fields show a path for an ASCII file with results and a number of identified defects.

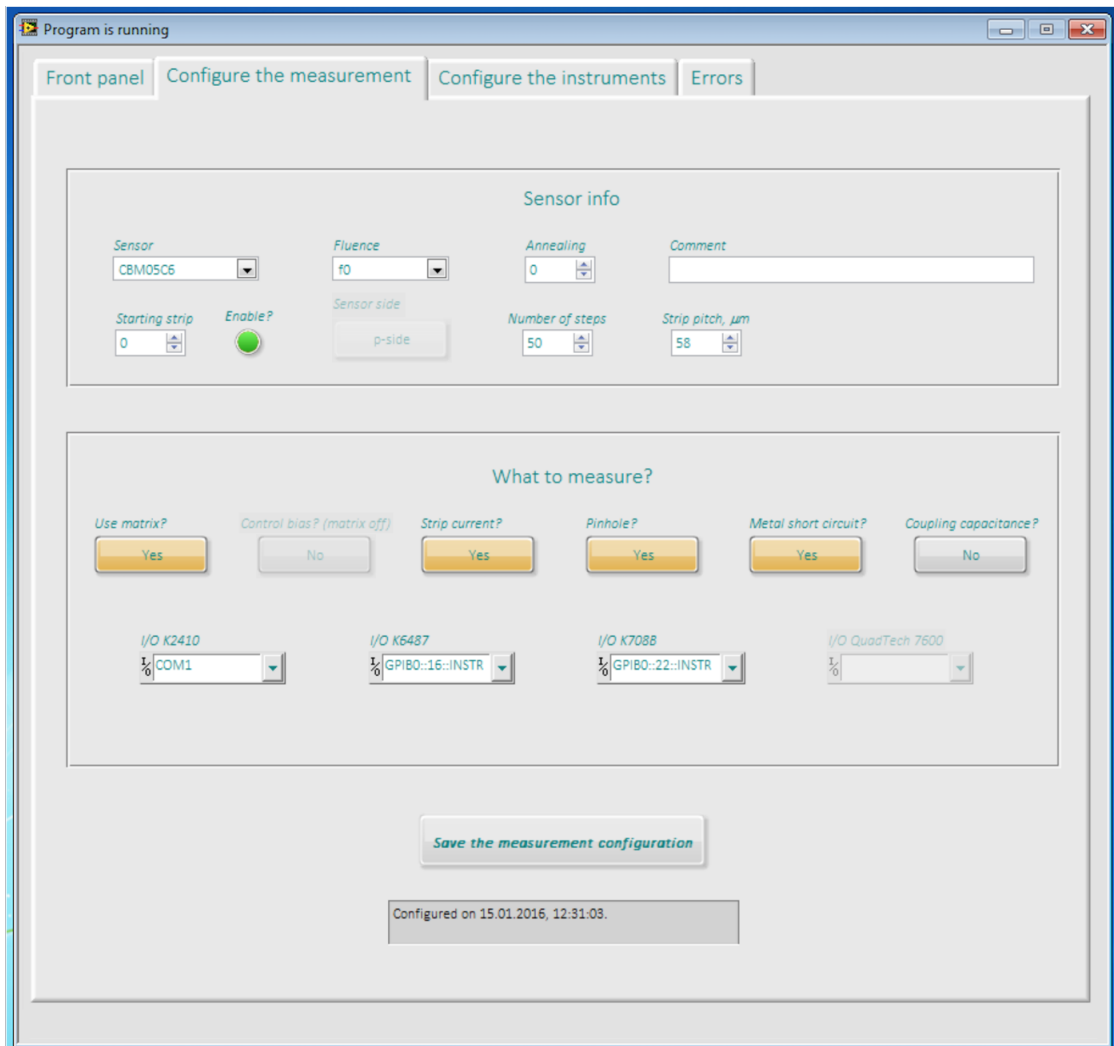


Figure B.5: Measurement configuration panel of the software for automated strip diagnostic tests. The upper block includes input fields for the sensor information. In the lower block, various types of tests to be performed, are selected. When the required information is entered and the desired tests are selected, the configuration is saved by clicking the “Save the measurement configuration” button. When the measurement configuration is saved, the next tab is opened.

B.4 Software interface for automated strip diagnostic tests

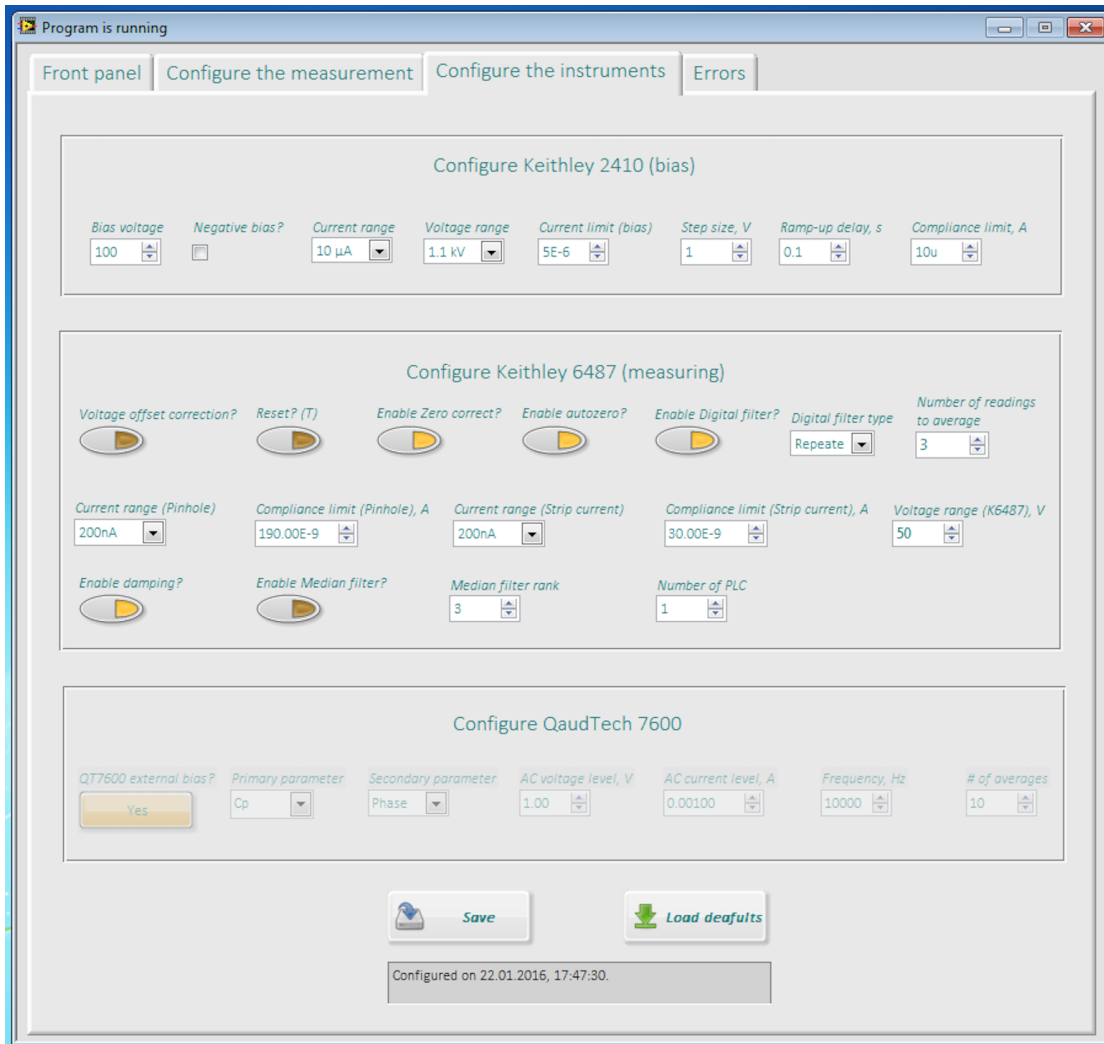


Figure B.6: Instrument configuration tab. Includes configuration buttons and fields for the instruments involved in the selected tests. Here, the coupling capacitance test was not selected in the measurement configuration tab, therefore, the corresponding configuration buttons are disabled. After the configuration is performed, the “Save” button is clicked. The software will allow to start the test only if both the measurement and the instrument configurations are saved.

Appendix C

Communication/data transfer protocol for the test stand

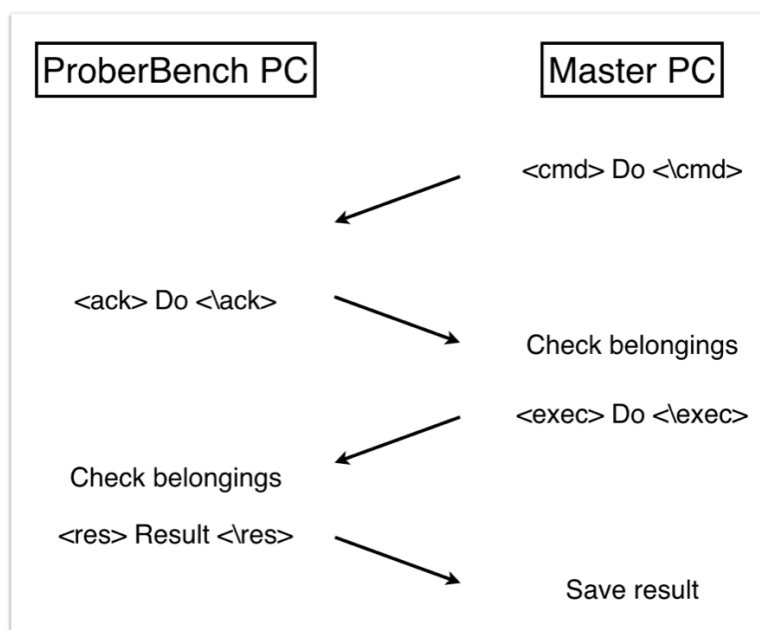


Figure C.1: Schematic representation of the communication protocol.

The communication protocol realizes a secure exchange of the commands and data between the Master PC and the ProberBench PC. The important features of the communication protocol are reliability, high command execution speed and absence of data loss. As mentioned in the Section 5.3, the connection is established via the serial port. The RS-232 connector is being used for decades and revealed itself as very reliable. Due to the fact that the amount of transferred data is on the order of bytes per second, the data rate of the serial port connection is appropriate. The protocol was developed using the LabView built-in programmer

tools and packages. The communication is realized on a Master (Master PC) and Slave (ProberBench PC) principle in a following way:

1. Both Master and Slave are in a listening/standby mode by default;
2. Master sends a "Command" to the Slave. Then, switches into the listening/standby mode;
3. Slave receives the data and verifies if the received data is a "Command". If the data is a "Command" it sends back an "Acknowledgement" that the command has been received, then switches into the listening/standby mode;
4. Master receives the "Acknowledgement" and verifies that the received "Acknowledgement" belongs to the command that was sent. If it matches, sends an "Execute" message, then switches into a listening/standby mode;
5. Slave receives the data and verifies if the execution message belongs to the received command. If it matches, executes the command on the probe station and sends the result with a "Result" stamp. If an error occurred, the Slave sends a message with an "Error" stamp. Then, it turns into a listening/standby mode;
6. Master receives the data. If "Result" is received, the data is stored and processed. If "Error" is received, the program declares an error and switches into the listening/standby mode;
7. If a mismatch or an error occurred during the communication the error is declared. Further communication stops with notification of the opposite side.

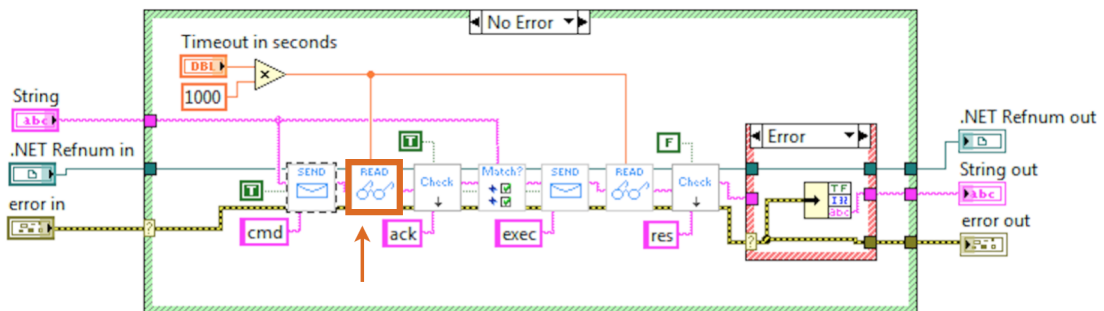


Figure C.2: Virtual instrument representing the communication sequence for the Master PC.

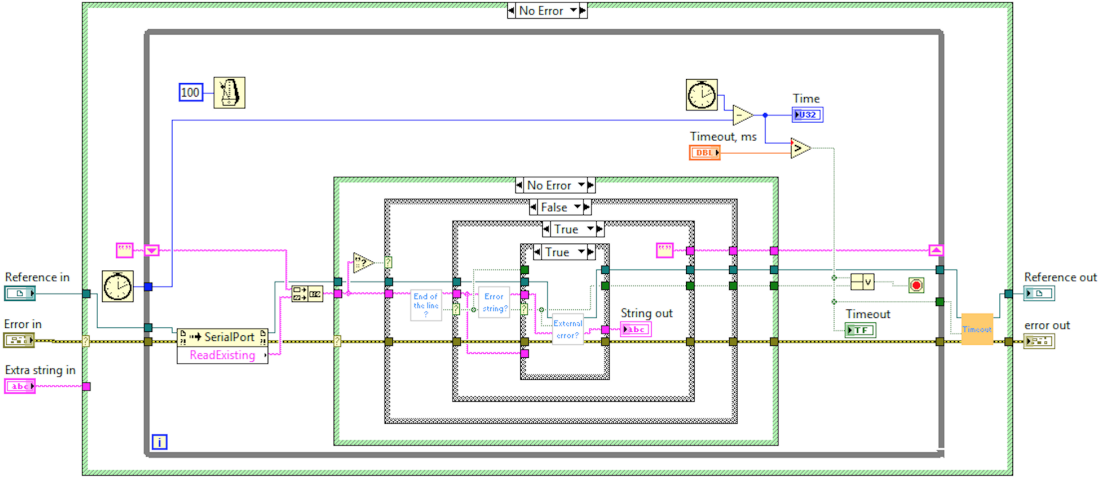


Figure C.3: Structure of the sub-virtual instrument representing the “READ” VI from Fig. C.2

The schematic representation of the protocol is depicted in Figure C.1. Such a multiple verification system allows to perform data transfer with a high reliability. If an error occurs during the communication, an error message is declared on both machines and no command is executed at the probe station. Thus, a safe operation of the measurement is achieved. Also, a timeout of one second is implemented into the protocol sequence. If any part does not receive a required message within one second, an error message pops up and both systems are forced to return to the first stage of the communication. In this case, a notification that the timeout occurred is declared and sent to the opposite side also. With this approach, despite a large number of messages sent, the execution speed of one command (measured experimentally) equals to a fraction of a second which is well acceptable. Sets of virtual instruments have been developed for both Master and Slave. Figure C.2 shows the sequence of the block diagrams of one of the developed virtual instruments for the communication protocol for a Master PC. A sub-virtual instrument responsible for reading of incoming data, is depicted in Fig. C.3.

Appendix D

Parameters of the Hamburg model used for calculations

Table D.1: Model parameters for a calculation performed in Fig. 3.15. $T = 20$ °C.

$N_{eff,0}$ [10^{12} cm $^{-3}$]	c [10^{-14} cm 2]	g_c [10^{-2} cm $^{-1}$]	$\frac{N_{C0}}{N_{eff,0}}$	g_a [10^{-2} cm $^{-1}$]	τ_a [h]	g_Y [10^{-2} cm $^{-1}$]	τ_Y [d]
1.34	8.2	1.9	0.8	1.81	55	5.16	475

Table D.2: Model parameters for a calculation performed in Fig. 3.28. $T = 25$ °C.

Φ_{eq} [10^{13} cm $^{-2}$]	N_C [10^{11} cm $^{-3}$]	g_a [10^{-2} cm $^{-1}$]	τ_a [h]	g_Y [10^{-2} cm $^{-1}$]	τ_Y [d]
1	7.53	1.81	31.44	5.16	201
5	19.4				
10	25.6				

Table D.3: Model parameters for a calculation performed in Fig. 3.27. $T = 80$ °C.

Φ_{eq} [10^{13} cm $^{-2}$]	N_C [10^{11} cm $^{-3}$]	g_a [10^{-2} cm $^{-1}$]	τ_a [min]	g_Y [10^{-2} cm $^{-1}$]	τ_Y [min]
1	7.53	1.81	2	5.16	92
5	19.4				
10	25.6				

Bibliography

- [1] K. Fukushima and T. Hatsuda: Rept. Prog. Phys. 74 (2011) 014001.
- [2] F. Becattini *et al.*, Phys. Rev. Lett. 111 (2013) 082302.
- [3] S. Borsanyi *et al.*, JHEP 1009 (2010) 073.
- [4] A. Basavov *et al.*: Phys. Rev. D85 (2012) 054503.
- [5] Y. Aoki *et al.*, Nature 443 (2006) 675.
- [6] J. Luecker *et al.*, arXiv:1308.4509v1 [hep-ph].
- [7] STAR collaboration, <https://www.star.bnl.gov>
- [8] NA61/SHINE experiment, <http://shine.web.cern.ch>
- [9] NICA facility, <http://nica.jinr.ru>
- [10] M. Orsaria, H. Rodrigues, F. Weber, G.A. Contrera: PRC 89 (2014)015806.
- [11] P. Chung *et al.*, Phys. Rev. Lett. 91 (2003) 202301.
- [12] C. Pinkenburg *et al.*, Phys. Rev. Lett. 83 (1999) 1295.
- [13] S. Chattopadhyay *et al.*, Challenges in QCD matter physics - The Compressed Baryonic Matter experiment at FAIR, arXiv:1607.01487v1.
- [14] P. Hohler and R. Rapp, Phys. Lett. B 731 (2014) 103-109.
- [15] The CBM Physics Book, B. Friman *et al.*(eds): Series: Lecture Notes in Physics, Vol. 814 (2011).
- [16] S. Chattopadhyay, Physics at FAIR, Nucl. Phys. A 931 (2014) 267-276.
- [17] <http://www.fair-center.eu/en/for-users/experiments/cbm/documents.html>

-
- [18] The CBM Collaboration, The Compressed Baryonic Matter experiment, GSI Progress Report 2015.
- [19] P. Senger, The Compressed Baryonic Matter Experiment at FAIR, JPS Conf. Proc. 8, 022001 (2015).
- [20] P. Senger, Probing Dense Baryonic Matter, Prog. in Part. and Nucl. Phys. 62 (2009) 375-380.
- [21] J.M. Heuser for the CBM collaboration, The Silicon Tracking System of the CBM Experiment at FAIR, JPS Conf. Proc. 8, 022007 (2015).
- [22] P. Larionov for the CBM collaboration, Overview of the Silicon Tracking System for the CBM experiment, J. Phys.: Conf. Ser. 599 012025, 2015.
- [23] S. A. Bass *et. al.*, Microscopic Models for Ultrarelativistic Heavy Ion Collisions, Prog. Part. Nucl. Phys. 41 (1998) 225-370.
- [24] GEANT - toolkit for the simulation of the passage of particles through matter, <https://geant4.web.cern.ch/geant4/>
- [25] O. Sokolov, Prototyping of Silicon Strip Detectors for the Inner Tracker of the ALICE Experiment, PhD thesis, University of Utrecht, 2006.
- [26] Frank Hartmann, Evolution of Silicon Sensor Technology in Particle Physics, Springer 2009, ISBN 978-3-540-44774-0.
- [27] M. Moll, Radiation Hardness of Semiconductor Detectors - Radiation Effects and Detector Operation, presentation, 3rd MC-PAD Network Training Event, 2010.
- [28] A. Furgeri, Quality Assurance and Irradiation studies on CMS silicon strip sensors, PhD thesis, Karlsruhe University, 2006.
- [29] J. Beringer et al. (Particle Data Group), Review of Particle Physics, Phys. Rev. D, 86:010001, 2012 and 2013 partial update for the 2014 edition.
- [30] A. Kotynia, J. M. Heuser, CBM Progress Report 2011, (2012) 14.
- [31] CBM Collaboration, Technical Design Report for the CBM Silicon Tracking System, GSI Report 2013-4, www.fair-center.eu/fileadmin/fair/publications_exp/TDR-STs.pdf
- [32] M. Singla, P. Larionov *et. al.*, for the CBM Collaboration, Radiation tolerance studies of neutron irradiated double sided silicon microstrip sensors, Nucl. Instr. Meth. Phys. Res. A824, pp. 462–464, 2016, doi: 10.1016/j.nima.2015.09.003.

- [33] G. Kramberger, Signal development in irradiated silicon detectors, Doctoral Thesis, University of Ljubljana, 2001.
- [34] V.A.J van Lint, T.M. Flanagan, R.E. Leadon, J.A. Naber, V.C. Rogers, Mechanisms of Radiation Effects in Electronic Materials, John Wiley & Sons, 1980.
- [35] D. Zontar, Study of radiation damage in silicon detectors for high luminosity experiments at LHC, Doctoral thesis, University of Ljubljana, 1998.
- [36] M. Huhtinen, Simulation of non-ionising energy loss and defect formation in silicon, Nucl. Instr. Meth. in Phys. Res. A 491, pp. 194-215, 2002.
- [37] Michael Moll, Radiation Damage in Silicon Particle Detectors - microscopic defects and macroscopic properties, PhD Thesis, Universität Hamburg, 1999.
- [38] H. Feick, Radiation Tolerance of Silicon Particle Detectors for High-Energy Physics experiments, PhD thesis, University of Hamburg, 1997.
- [39] Y. Shi *et. al.*, A numerical study of cluster center formation in neutron-irradiated silicon, J. Appl. Phys., 67:1116, 1990.
- [40] F. Hönniger, Radiation Damage in Silicon - Defect Analysis and Detector Properties, PhD thesis, Universität Hamburg, 2007.
- [41] D. V. Lang, Deep-level transient spectroscopy: A new method to characterize traps in semiconductors, J. Appl. Phys., vol. 45 (1974) 3023.
- [42] Z. Li *et. al.*, Development of transient current and charge techniques for the measurement of effective net concentration of ionized charges (N_{eff}) in the space charge region of p-n junction detectors, Nucl. Instr. Meth. Phys. Res. Sect. A 372, pp. 388-398, 1996.
- [43] L. Forbes, et al., Solid-State Electron, 14 (1971) 182.
- [44] J. Stahl, Defect Characterisation in High-Purity Silicon after γ - and Hadron Irraditation, PhD thesis, University of Hamburg, 2004.
- [45] W. Shockley, W.T. Read, Phys. Rev. 87 (1952) 835.
- [46] G. Lindström *et. al.*, ROSE Report, CERN, 28-Nov-01.
- [47] RD48 Status Report, CERN/LHCC 97-39, 1997.
- [48] E. Fretwurst *et. al.*, Radiation Damage in Silicon Detectors Caused by Hadronic and Electromagnetic Irradiation, DESY02-199 note, 2002.

-
- [49] A. Dierlamm, Studies on the Radiation Hardness of Silicon Sensors, PhD thesis, University of Karlsruhe, 2003.
- [50] G. Kramberger *et. al.*, Annealing studies of effective trapping times in silicon detectors, Nucl. Instr. and Meth. A 571 (2007) 608-611.
- [51] R. Eber *et. al.*, Annealing study of a highly irradiated FZ CMS mini sensor with the ALiBaVa setup at KIT, 17th RD 50 Workshop, 2010.
- [52] L. Snoj *et. al.*, Computational analysis of irradiation facilities at the JSI TRIGA reactor, Applied Radiation and Isotopes 70 (2012) 483-488.
- [53] Ljubljana Neutron Irradiation Facility, <http://www-f9.ijs.si/~mandic/Reactor.html>
- [54] A. Vasilescu, G. Lindström, Notes on the fluence normalisation based on the NIEL scaling hypothesis, ROSE/TN/2000-02, 2000.
- [55] Irradiation Center Karlsruhe website, www.ekp.kit.edu/english/irradiation_center.php
- [56] A. Dierlamm, Irradiations in Karlsruhe, presentation, 16th RD50 Workshop, 2010.
- [57] L. Beattie *et. al.*, Dependence of Depletion Voltage and Capacitance on Temperature and Frequency in Heavily Silicon Diodes, ROSE/TN/97-4, 1997.
- [58] M.K. Petterson *et. al.*, Charge collection and capacitance-voltage analysis in irradiated n-type magnetic Czochralski silicon detectors, Nucl. Instr. Meth. A583 189-194 (2007).
- [59] Honeywell HIH series monolithic integrated circuit humidity sensor http://www.emesystems.com/rhtd_dat_files/HIH-3602-C.pdf
- [60] <http://sine.ni.com/nips/cds/view/p/lang/de/nid/201987>
- [61] MECH-EL Industries, Inc., <http://www.mech-el.com/1204w.htm>
- [62] A.S. Brogna *et al.*, Nucl. Instr. and Meth. in Physics Research Section A 568 (2006) 301-308.
- [63] <http://go4.gsi.de>
- [64] Iurii Sorokin, Characterization of silicon microstrip sensors, front-end electronics, and prototype tracking detectors for the CBM experiment at FAIR, PhD thesis, Goethe Universität, Frankfurt am Main, 2013.

- [65] Hanna Malygina, PhD thesis, in preparation.
- [66] J. Adamczewski-Musch, H.G. Essel, S. Linev, IEEE TNS Vol. 58, No. 4, August 2011, pp. 1728-1732.
- [67] M. Moll *et. al.*, Leakage current of hadron irradiated silicon detectors - material dependence, Nucl. Instr. and Meth. A 426 (1999) 87-93.
- [68] V. Eremin *et. al.*, Double peak electric field distortion in heavily irradiated silicon strip detectors, Nucl. Instr. Meth. A535 622-631 (2004).
- [69] <http://www.tesatechnology.com>
- [70] V. Eremin, private communication.
- [71] A. Affolder *et. al.*, Studies of charge collection efficiencies of planar silicon detectors after doses up to 10^{15} n_{eq}/cm² and the effect of varying diode configurations and substrate types, Nucl. Instr. Meth. A 604 (2009) 250-253.
- [72] G. Casse *et. al.*, Nucl. Instr. and Meth. A 581 (2007) 318.
- [73] M. Merkin, private communication.
- [74] Alexander J. Furgeri *et. al.*, Leakage current of CMS single-sided strip sensors under neutron irradiation, Nucl. Instr. Meth. Phys. Res. A 560 (2006), pp. 108-111.
- [75] M. Laakso *et. al.*, Field oxide radiation damage measurements in silicon strip detectors, Nucl. Instr. Meth. Phys. Res. A327 (1993) 517-522.
- [76] P. Larionov for the CBM collaboration, Automated quality assurance for silicon microstrip sensors of the CBM Silicon Tracking System, JINST 11 C01033, 2016.
- [77] A. Chilingarov *et.al*, Interstrip capacitance stabilization at low humidity, Nucl. Instr. Meth. Phys. Res. A 560 (2006), 118-121.
- [78] Thomas Bergauer, Quality Assurance of the Silicon Strip Sensors for the CMS Tracker, presentation, QA Workshop, CERN, 2011.
- [79] ISO/TC 209 Standard catalogue, Cleanrooms and associated controlled environments. http://www.iso.org/iso/home/store/catalogue_tc/catalogue_detail.htm?csnumber=53394
- [80] APS Solutions GmbH, <http://www.aps-munich.com>

-
- [81] A. Tarchini, Production tests of silicon strip detectors of STAR SSD layer, presentation, CERN QA Workshop, 2001.
- [82] G. Baumann *et. al.*, Quality assurance of 100 CMS-OB2 sensors, LHCb note 2004-105.
- [83] Minni Singla, The Silicon Tracking System of the CBM experiment at FAIR - Development of microstrip sensors and signal transmission lines for a low-mass, low-noise system, PhD Thesis, Goethe Universität, Frankfurt am Main, 2013.
- [84] S.M. Sze, Physics of Semiconductor Devices, 2nd edition, Wiley, New York, 1981.
- [85] Recommendations towards a standardisation of the macroscopic parameter measurements, RD50 Technical Note 2003/03.
- [86] Dmitry Karmanov, Development and construction of the forward tracker for the D0 experiment (FNAL) (in Russian), Dissertation, Lomonosov Moscow State University - Skobeltsyn Institute of Nuclear Physics, Moscow, 2008.
- [87] E. Barberis *et. al.*, Measurement of interstrip and coupling capacitances of silicon microstrip detectors, conference record, Nuclear Science Symposium and Medical Imaging Conference, 1992.
- [88] H.F.-W. Sadrozinski *et. al.*, Nucl. Instr. Meth. A342 90-95 (1994).
- [89] N. Bacchetta *et. al.*, Silicon Sensor Quality Assurance for the CDF Run2b Silicon Detector, D0 note CDF/DOC/TRACKING/PUBLIC/6283 V1.0, 2003.
- [90] M. A. Frautschi *et. al.*, Capacitance Measurements of Double-Sided Silicon Microstrip Detectors, CDF Note CDF/DOC/SEC VTX/CDFR/2546, 1995.
- [91] G. Lutz, Semiconductor Radiation Detectors: Device Physics. Springer 2007, ISBN: 978-3-540-71678-5.
- [92] M.M. Angarano, Characterization of neutron irradiated, low-resistivity silicon detectors, CMS conference report 2000/006, 2000.
- [93] Paul Dolejschi, Characterisation of interstrip parameters on silicon sensors for the Belle II vertex detector, Diploma thesis, Technische Universität Wien, 2012.
- [94] P.P. Allport *et. al.*, FOXFET biased microstrip detectors, Nucl. Instr. Meth. Phys. Res. Sect. A 310, pp. 155-159, 1991.

- [95] Helmuth Spieler, Semiconductor Detector Systems, Oxford University Press, 2005.
- [96] Trond I. Westgaard *et. al.*, Radiation hardness of punch-through and FET biased silicon microstrip detectors, Nucl. Instr. Meth. Phys. Res. Sect. A 377, pp. 429-434, 1996.
- [97] M. Merkin, Design, development and application of silicon sensors in high-energy physics and cosmic-ray physics (in russian), habilitational thesis, Moscow State University, 2012.
- [98] Süss MicroTec, ProberBenchTM 7 User Manual - Command and Interface Reference, www.suss.com
- [99] <https://en.wikipedia.org/wiki/LabVIEW>
- [100] National Instruments Corp., www.ni.com
- [101] www.keithley.com
- [102] Model 6487 Picoammeter/Voltage Source Reference Manual, 6487-901-01 Rev. B / March 2011.

Acknowledgement

First and foremost, I would like to express my deep gratitude to my supervisor, Prof. Dr. Peter Senger, for giving me the opportunity to work on such an interesting project, and his support and patience. I'm thankful to Dr. Johann Heuser, for navigating and supporting me during this work. I would like to thank Prof. Dr. Hans Rudolf Schmidt for providing useful feedback as an external supervisor. I am grateful to Dr. Christian Sturm for encouragement and help in improving the quality of this document. I appreciate the assistance of Dr. Ulrich Frankenfeld in managing the hardware and software units and his useful suggestions.

I appreciate the friendly atmosphere and kindness of the whole CBM group in GSI during these years.

Without help and assistance of Dr. Minni Singla and Dr. Iurii Sorokin many measurements in this work would've been missing, thank you guys. I would like to thank Hanna Malygina, Dr. Maksym Zyzak, Dr. Tomas Balog and Dr. Olga Bertini for your help with simulations and for providing useful software tools. I thank Dr. Anton Lymanets for your help with getting familiar with LabView.

I am thankful to Carmen Simons and colleagues from the GSI detector lab for the technical support.

Dr. David Emschermann and Björn Borm, thank you for helping me with the German translation.

For the preparation and carrying out the irradiations, I want to particularly thank Dr. Johann Heuser, Dr. Minni Singla, Dr. Jürgen Eschke, and colleagues from the JSI and KIT irradiation centres.

I would like to thank Dr. Sc. Michael Merkin and Dr. Dmitry Karmanov (MSU), Dr. Sc. Valery Pugatch (KINR), Dr. Vladimir Eremin (Ioffe Institute), Dr. Nikolay Zamyatin (JINR) for interesting discussions that gave me a deeper understanding of the topic.

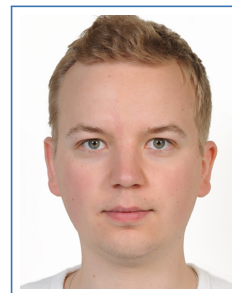
I would like to acknowledge the Helmholtz Graduate School for Hadron and Ion Research (HGS-HIRe) and Helmholtz Research School for Quark Matter Studies in Heavy Ion Collisions (H-QM) for providing interesting events and lecture weeks during my studies. Thanks to the Helmholtz International Center for FAIR (HIC for FAIR) for the financial support of my PhD.

Finally, I would like to thank my family and friends for their continuous support.

Pavel Larionov

Curriculum Vitae

GSI Helmholtzzentrum
für Schwerionenforschung GmbH
Planckstraße 1
64291 Germany
☎ +49-6159-71-1702
✉ P.Larionov@gsi.de



Personal Information

Date of Birth 11.10.1988
Place of Birth Cheboksary, USSR
Citizenship Russian

Education

- 2012–today **PhD Student**, *Johann Wolfgang Goethe University*, Frankfurt am Main, Germany.
Subject: Nuclear Physics
Thesis Title: “Systematic irradiation studies and Quality Assurance of silicon strip sensors for the CBM Silicon Tracking System”
Supervisor: Prof. Dr. Peter Senger
- 2005–2011 **Dipl.-Phys.**, *Nuclear Research National University “MEPHI”*, Moscow, Russia.
Subject: Physics and Technology
Specialization: Physics of Kinetic Phenomena
Thesis Title: “The application of the LaBr₃(Ce) scintillation detector for accounting and control tasks of nuclear materials at the companies of the state atomic energy corporation “Rosatom”
Supervisor: Dr. Oleg Bochkarev
Grade: Excellent
- 2002–2005 **Pupil**, *Lyceum school #2*, Cheboksary, Russia.
- 1995–2002 **Pupil**, *Secondary school #20*, Cheboksary, Russia.

Employment

- 03/2012–09/2012 **Project leader**, *All-Russia Research Institute of Automatics*, Moscow, Russia.
- 2011–2012 **Engineer**, *All-Russia Research Institute of Automatics*, Moscow, Russia.
- 2009–2011 **Intern**, *All-Russia Research Institute of Automatics*, Moscow, Russia.

Awards

- 2011 **First prize**, *Annual Scientific Conference of Young Scientists of All-Russia Research Institute of Automatics*, Moscow, Russia.

